Phosphatation of Zeolites: A Combined Spectroscopy, Microscopy and Catalysis Study

Fosfatering van Zeolieten: Een Gecombineerde Spectroscopie, Microscopie en Katalyse Studie

(met een samenvatting in het Nederlands)

Proefschrift

door

Hendrik Edial van der Bij

geboren op 18 december 1985 te Groningen

Promotor: Prof. dr. ir. B. M. Weckhuysen

Phosphatation of Zeolites: A Combined Spectroscopy, Microscopy and Catalysis Study

Contents

General Introduction

T‍he topic of this PhD thesis, the modification of zeolites by treatment with phosphate precursors, is part of the field of inorganic chemistry and heterogeneous catalysis. While already fascinating from an academic viewpoint alone, there is also a strong incentive from society that drives these fields forward. Knowledge of inorganic chemistry and heterogeneous catalysis is vital in the production of transportation fuels and materials from a wide variety of resources. Even more, discoveries in the field have led to cleaner and more efficient routes toward renewable resources, such as biomass conversion, and gas-to-liquid technology. As demand for these sustainable routes and resources grows every year, the study of the fundamentals of heterogeneous catalysis is of great societal importance. The research presented in this dissertation should be seen as an attempt to contribute to this endeavor.

This introductory Chapter serves to familiarize the reader with some of the concepts and problems addressed in this PhD thesis. In the following sections we intend to answer the following questions, i.e. (i) what are zeolites? (ii) what is their use in catalysis? (iii) what is hydrothermal stability? (iv) what is phosphatation of zeolites? After answering these questions, the scope and outline of the dissertation will be presented.

1.1 Zeolites

Zeolites are crystalline minerals of varying shapes and sizes. For practical applications, the crystal size dimensions are usually a few microns. They can consist of uniform single crystals, twinned crystals, or of various intergrown crystals and aggregates.[1] All zeolites have in common, (i) an ordered micropore system that runs through (ii) an ordered framework, which consists of (iii) interlinked tetrahedral silicon oxides and aluminum oxides.

The fact that zeolites consist of neutral $[SiO_4]$ tetrahedra and negatively charged $[AlO_4]^-$ tetrahedra leads to a net negative charge on the framework. Therefore, the framework needs to be stabilized by counter-cations. This gives zeolites ion-exchanging capacities, which allows

zeolites to be utilized in environmental remediation, such as wastewater treatment.[2] If the counter-cations are protons, strong Brønsted acid sites are formed and the zeolite effectively adopts a solid-acid character. Solid-acid zeolites are widely applied in acid-catalysis processes.[3] For every $[AlO_4]^-$ unit that is substituted in the framework, one proton is needed to counter the charge. Therefore, the framework silicon to aluminum (Si/Al) ratio of a zeolite is an important parameter, as it determines the acid site concentration.

Another important parameter is the so-called framework topology of the zeolite. The framework topology dictates the size, shape and dimensionality of micropores in zeolites. Subsequently, these parameters determine what and how fast molecules can enter, form and exit the zeolite. Therefore, zeolites effectively act as molecular sieves. These shape-selective properties make zeolites also important in separation processes, e.g. O_2 and N_2 separation.[4-5]

However, not only do the channels of zeolites separate molecules on shape and size, they also impose confinement effects on adsorbed molecules.[6] This can lead to decreased or increased heats of adsorption for reactants, intermediates, and products. As a consequence, certain catalytic reaction pathways are preferred or occur at lower temperatures, while others are inhibited, depending on the framework topology type. Therefore, in acid-catalysis the topology of a zeolite is often more important than its chemical composition.[6-7] At the time of writing there are 218 registered framework topologies approved by the Structure Commission of the International Zeolite Association (IZA), each with its own unique shape-selective properties. Framework topologies are denoted with three letter codes.

1.1.1 Zeolite H-ZSM-5

A specific example of a zeolite that is widely applied as an acid-catalyst in industry, is zeolite ZSM-5, which is an abbreviation of Zeolite Socony Mobil 5, named after its inventors at the Mobil Oil Company.[8] The framework topology of ZSM-5 is denoted with the three-letter code MFI (ZSM-FIve). Zeolite H-ZSM-5 is the most extensively studied zeolite of this PhD thesis and Figure 1.1 shows zeolite H-ZSM-5 at different dimension scales.

Single H-ZSM-5 crystals are often coffin- or parallelepiped-shaped and can have sizes ranging from 100 nm to 100 μm.[1, 9-10] Inside the crystal we find a three-dimensional microporous channel system as can be seen in Figure 1b and 1c, which act as transport channels for molecules. The channel system comprises of straight and sinusoidal pores. These pore types run parallel to the [010] and [100] crystallographic planes, respectively. As the two pore types are connected at regular intersections, molecules can diffuse into the [001] direction as well.

The circumference of the pores consists of ten linked [TO$_4$] units, where T stands for tetrahedral atom (T-atom), which can be silicon or aluminum (Figure 1.1 d). We abbreviate tetrahedrally coordinated framework aluminum and silicon as TFAl and TFSi, respectively. In zeolite science one generally refers to the amount of T-atoms in the ring of a pore to describe the pore size, hence 10-member rings (MR) in H-ZSM-5. The average size of the MFI channels in Ångströms is around 5.5 x 5.5 Å.[11] At the positions where the channels intersect, cavities form of 6.36 Å in diameter.[12] Consequently, molecules that exceed the dimensions of the channels are prohibited from entering or exiting the zeolite, however larger molecules can form in the cavities. Figure 1.1 e shows an [AlO$_4$]$^-$ unit in the framework that forms a bridging hydroxyl group with a neighboring [SiO$_4$] unit. These bridging hydroxyl groups are the strong Brønsted acid sites in H-ZSM-5. Very weak Brønsted acid sites can be seen in Figure 1.1 g, where terminal [SiO$_4$] units have terminal Si-OH groups, i.e.
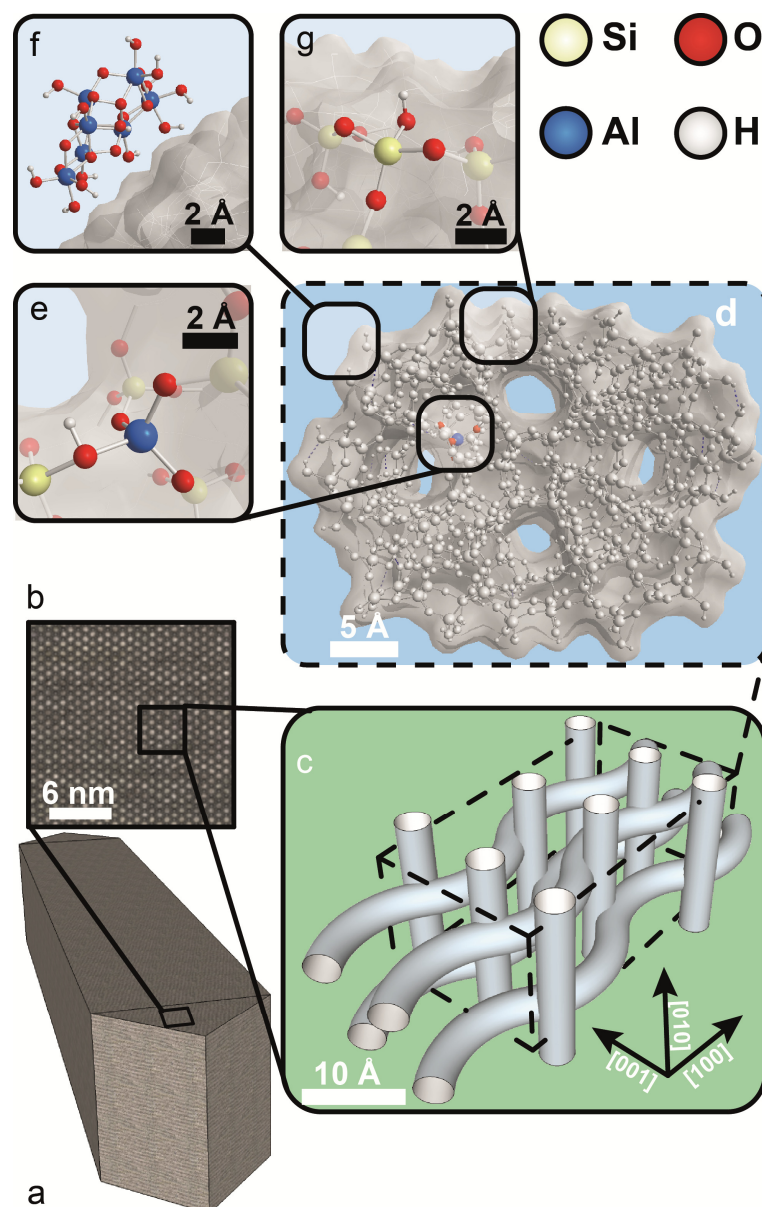
Figure 1.1 Overview of zeolite H-ZSM-5 at different dimension scales. (a) A micron-sized coffin shaped H-ZSM-5 crystal. (b) Closer inspection of the [001][100] plane, revealing the straight pores. (c) The three dimensional channel system of H-ZSM-5 consists of intersecting straight and sinusoidal pores. (d) The channel system follows from the MFI-framework, which comprises of linked silica and alumina tetrahedra. (e) A tetrahedrally coordinated framework aluminum (TFAl) atom leads to a net negative charge on the framework. In H-ZSM-5 this negative charge is compensated by a proton, which leads to a Brønsted acid site. The OH group in SiOHAl is generally referred to as a bridging hydroxyl group. (f) Dealumination leads to the formation of extra-framework aluminum, here shown as boehmite. (g) terminal silicon and aluminum atoms, which are generally found on the zeolite external surface form silanol and aluminol groups.

silanol groups. Extra-framework aluminum as shown in Figure 1.1 f, which can be present in the channels and cages of zeolites, will be discussed in more detail in section 1.3.

The combined shape selectivity and strong acidity of H-ZSM-5 create the desired properties for heterogeneous hydrocarbon catalysis. Industrially, zeolite H-ZSM-5 is used as a catalyst additive in crude oil cracking, known as the fluid catalytic cracking (FCC) process.[8] The addition of H-ZSM-5 to a FCC catalyst leads to an improved octane rating of gasoline and boosts the amount of propylene in the gas effluent.[8] Propylene is an essential component in the petrochemical industry as it forms the starting material for the production of many plastics and polymers, e.g. polypropylene, phenol-based plastics, polyurethane, polyacrylonitrile, etc. [13-14]

Besides being used as a catalyst in the FCC process, zeolite H-ZSM-5 is also used, or has potential use, in many other catalytic processes, including the alkylation of aromatics, methanol and dimethylether conversion to light olefins, aromatics and fuels, the dehydrogenation of paraffins, dehydration of (bio-) alcohols, catalytic fast pyrolysis of biomass, and in photocatalytic reactions.[15-22] Therefore, zeolite H-ZSM-5 is not just an important catalyst for present day crude oil refining purposes, but also a strong candidate for future green/clean hydrocarbon production processes.

[001]

H-mordenite
MOR
12-MR   along [001]
8-MR   along [001]
8-MR   along [010]
Side pockets
1-dimensional

[001]

H-ferrierite
FER
10-MR   along [001]
8-MR   along [010]
2-dimensional

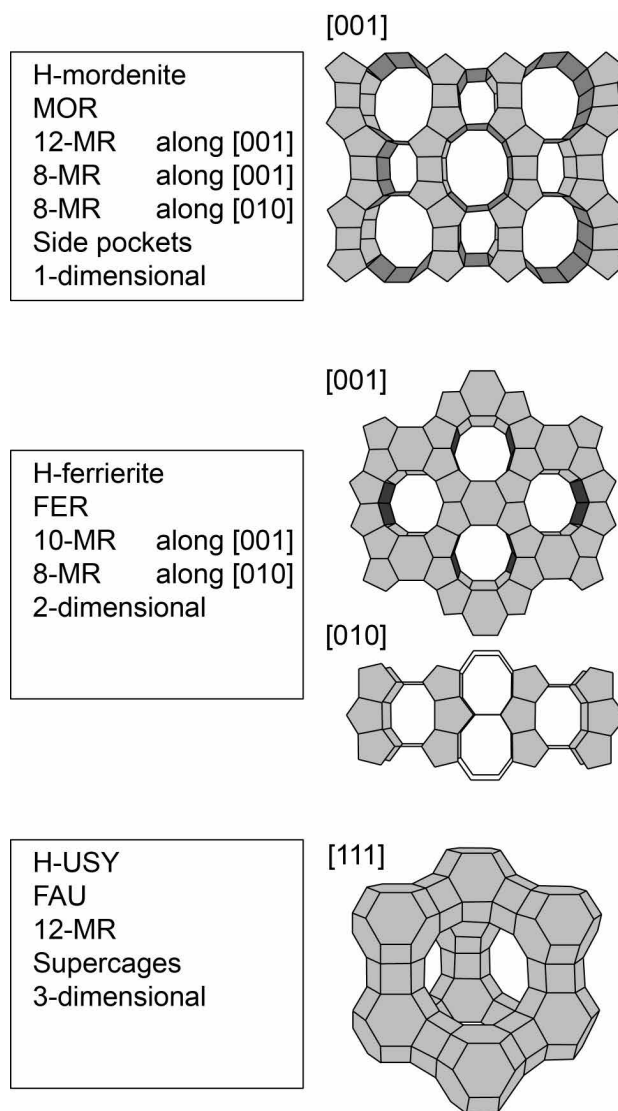[010]

H-USY
FAU
12-MR
Supercages
3-dimensional

[111]

Figure 1.2 Schematic representations of the MOR, FER and FAU topologies, studied in this work. More information and 3-D reconstructions can be found on the website of the International Zeolite Association Database. [12]

1.1.2 Zeolite H-mordenite, H-ferrierite, and H-USY

Three other industrially relevant zeolite topologies that have been studied in this work, although less extensively, are the zeolites H-mordenite (MOR topology), H-ferrierite (FER topology), and the ultra-stable form of zeolite Y (USY) (FAU topology). Figure 1.2 provides a schematic overview of the topologies.

Zeolite H-mordenite has a MOR topology that consists of three straight pore types. Two pore types are 12-MR and 8-MR and run along the [001] plane, the other is 8-MR along [010] which forms side-pockets with the 12-MR channels. The side pockets do not interconnect the 12-MR channels and therefore zeolite H-mordenite is effectively 1-dimensional. In industry, zeolite H-mordenite is used for the isomerization of alkanes and for the alkylation of aromatics.[23-24]

Zeolite H-ferrierite has a FER topology and has two straight channels. One 10-MR channel runs along the [001] plane, while the other 8-MR channel runs along the [010] plane. As these channels intersect, but do not interconnect the channels in the [100] direction, the FER pore system is 2-dimensional. H-ferrierite is suited for dewaxing of hydrocarbon fractions and linear olefin isomerization processes.[25-26]

The final zeolite we have studied in this work is zeolite H-USY. The FAU framework consists of a 3-dimensional pore system of 12-MR that run perpendicular to each other. The pores meet in so-called supercages. While the 12-MR channels can fit molecules up to 7.35 Å in diameter, the supercages can fit molecules up to 11.24 Å in diameter. Zeolite H-Y is the main catalyst in the FCC process and hydrocracking, where it effectively catalyzes the cracking of petroleum into more valuable fractions.[27-29] Unmodified zeolite Y has a very low Si/Al ratio, (2-3 on average). The high amount of aluminum in the framework has several disadvantages for catalytic cracking. For example, the high acid site density leads to weak acid sites, and aluminum is easily expelled from the framework under hydrothermal conditions, which leads to amorphization and deactivation of the material.[30-31] We will discuss the effect of hydrothermal stability in more detail in section 1.3. One of the methods to solve this problem and stabilize zeolite Y is by removing aluminum from the framework before use.[31] Hence, zeolite Y that received such a post-treatment is named ultra-stable zeolite (USY). After the post-treatment, H-USY contains extra-framework aluminum (EFAl), super-acid sites, and mesopores.[31-32]

Chapter 1

1.2 Catalytic cracking

As was touched on in the previous section, catalysis over zeolites is performed by the strongly acidic bridging hydroxyl groups (Si-OH-Al) in the framework. In this section we will discuss one catalytic reaction on the mechanistic level, which is heavily used in oil refining, i.e. catalytic cracking. Crude oil is for a large part composed of (cyclo)alkanes, and cracking is applied to convert long chain alkanes into smaller, more valuable products. [7, 28]

Cracking of hydrocarbons can be performed without a catalyst. Thermal cracking of alkanes already takes place at elevated temperatures above 450 °C and is industrially applied in steam cracking of naphta, which is performed around 850 °C.[33] During thermal cracking, a C-C bond is broken and free-radical intermediates form. The major products of the thermal cracking of e.g. n-hexadecane are low C_1-C_3 species and C_4-C_{15} olefins.[34] This product distribution changes when the cracking reaction is catalyzed by protons. In the case of catalytic cracking mostly C_3-C_5 species form, olefin concentrations above C_4 are low and aliphatic products tend to be branched. [34] Therefore gasoline that is produced by catalytic cracking contains higher fractions of branched alkanes and lower fractions of olefins, which gives it higher octane ratings.

The different product distribution observed for catalytic cracking follows from a different cracking mechanism. Intermediates in catalytic cracking are not free-radical species, but either carbenium or carbonium ions. There are two distinct mechanistic pathways in catalytic cracking. [35-36] The first is the so called monomolecular mechanism, or protolotyic cracking mechanism, and follows the Haag-Dessau mechanism. [37] We will describe this mechanism by example of n-hexane as the reactant.

In a first step n-hexane is protonated by a Brønsted acid site of the zeolite and a chemisorbed carbonium ion is formed, which subsequently collapses into cracking products. If a C-C bond is protonated the following reaction takes place:

$$C_6H_{14} + ZH \quad \rightarrow \quad C_6H_{15}^+ + Z^- \tag{1.1}$$

$$C_6H_{15}^+ + Z^- \quad \rightarrow \quad C_3H_8 + C_3H_7^+ + Z^- \tag{1.2}$$

$$C_3H_7^+ + Z^- \quad \rightarrow \quad C_3H_8 + C_3H_6 + ZH \tag{1.3}$$

Please note that the formed carbenium ion in reaction equation (1.2) remains chemisorbed on the conjugated basic site of the zeolite. Therefore an olefin can only desorb if there is proton back-transfer from the carbenium ion. [38] Another possibility is the protonation of a C-H bond leading to dehydrogenation and subsequent cracking:

$$C_6H_{14} + ZH \rightarrow C_6H_{13}^+ + Z^- + H_2 \tag{1.4}$$

$$C_6H_{13}^+ + Z^- \rightarrow 2\, C_3H_6 + ZH \tag{1.5}$$
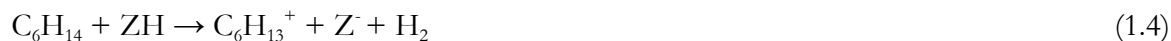
The second cracking mechanism is presented in reaction equations (1.6-1.7) and is known as the bimolecular cracking mechanism, the classical cracking mechanism, the carbenium ion mechanism or the β-scission route.[34-35] This mechanism follows from step (1.2), when the chemisorbed carbenium ion abstracts a hydride from an alkane:

$$C_6H_{14} + C_3H_7^+ + Z^- \quad \rightarrow \quad C_6H_{13}^+ + C_3H_8 + Z^- \tag{1.6}$$

$$C_6H_{13}^+ + Z^- \quad \rightarrow \quad C_3H_6 + C_3H_7^+ + Z^- \tag{1.7}$$
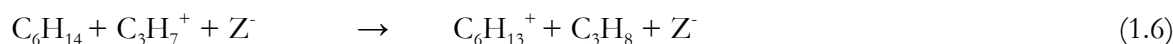
The bimolecular cracking mechanism continues as long as carbenium ions remain chemisorbed on the conjugated base site of the zeolite.[35] Adsorbed carbenium ions can also undergo isomerization, leading to the formation of branched aliphatics.[36]

The product distributions of both reaction mechanisms are quite different. Monomolecular cracking leads to the formation of methane, ethane, propylene, H_2 and high olefin/paraffin ($C^=/C$) ratios.[36, 39] The bimolecular mechanism yields a decreased $C^=/C$ ratio and more (branched) C_{4+} products.[36] Therefore, monomolecular cracking is preferred in the production of light olefins, while bimolecular cracking is preferred in the production of gasoline and diesel.[36] From the reaction equations it can be observed that monomolecular cracking and bimolecular cracking are competing mechanisms. As olefins are better proton acceptors than paraffins, the bimolecular mechanism is favored at high alkene concentrations and high partial pressures of reactants. [35, 40] Since carbenium ions tend to desorb faster or decompose at high temperatures, the monomolecular mechanism becomes more dominant with increasing reaction temperatures.[40] Also, zeolites with low densities of strong acid sites, i.e. high Si/Al ratios, promotes the monomolecular mechanism, as the chance that an alkane and a carbenium ion
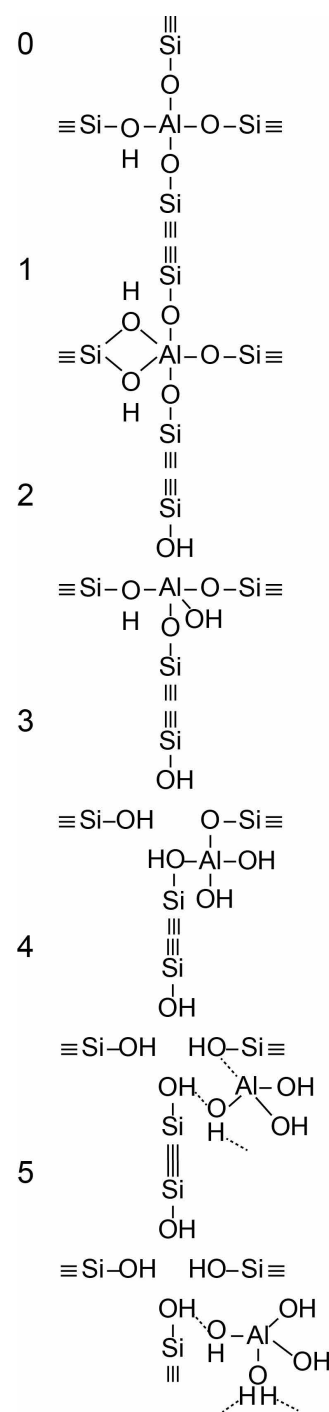
meet and reaction (1.6) takes place becomes smaller.[40] Finally, the topology of zeolites plays an important role. As carbenium ions are bulky intermediates, steric constrains prevents their formation.[35, 40] Therefore, medium-pore zeolites such as H-ZSM-5 inhibit bimolecular cracking to a certain extent.[40]

1.3 Hydrothermal stability

Zeolites form under hydrothermal conditions as a transitory phase of quartz.[41] This metastable nature of zeolites dictates that continued application of hydrothermal conditions eventually leads to the collapse of their framework structure. At elevated temperatures and in the presence of steam, framework Si-O-Al bonds are gradually hydrolyzed and aluminum is expelled from the framework, forming extra-framework aluminum (EFAl) species (Figure 1.3 f). [42-44] It has been shown that silicon is also present in the extra-framework aluminum phase, indicating the presence of extra-framework silica-alumina.[30] Due to the extraction of T-atoms from the zeolite lattice mesopores form and amorphization of the zeolite takes place. Besides the partial destruction of the zeolite lattice, this so-called dealumination also reduces the amount of counter-cations that the zeolitic framework can retain.

In the case of H-zeolites, this means that the active-sites for catalysis are permanently lost. [45] The exact nature of extra-framework aluminum is not clear, but it has been shown to consist of four-, five-, and six-coordinated aluminum species.[46] Furthermore, it has been suggested that extra-framework aluminum can consist of cationic species, which can replace protons in bridging hydroxyl groups. [47] The hydrothermal stability of a zeolite indicates how prone the framework is to dealumination under hydrothermal conditions. Therefore, a zeolite that does not dealuminate and retains acid sites during steam treatment has a high hydrothermal stability. Hydrothermal stability is dictated by the number of aluminum atoms in the framework, the

Figure 1.3 Reaction steps with intermediate configurations found for dealumination. ▬▬ = covalent bonds. ▪▪▪▪ = hydrogen bonds. Based on ref. 43.

framework type, and the type of counter-cations. [48] Increase of temperature, steam volume, or duration of hydrothermal treatment all lead to more severe dealumination.[49]

Dealumination poses a challenge in the industrial application of zeolites as acid catalysts. For example, in the FCC process, a regeneration step of the zeolites is performed at high temperatures and in the presence of steam. While this step is effective in the removal of coke deposits, the dealumination induced by steam leads to gradual deactivation of the catalyst.[28, 45] This catalytic deactivation of zeolites also takes place in high temperature reactions where H_2O forms as a reaction byproduct, examples being the methanol-to-hydrocarbons (MTH) process and the dehydration of alcohols. Therefore, hydrothermal stabilization is paramount for the industrial application of zeolites.

1.4 Phosphatation of zeolites

For zeolite Y, the most important cracking catalyst, rare earth cations and ultra-stabilization by hydrothermal treatment are used to stabilize the material.[50] In the case of zeolite H-ZSM-5, hydrothermal stabilization can be achieved by the addition of phosphorus. [8, 51-54]

After introduction of phosphorus and subsequent heat treatment in air/oxygen, a process better known as calcination, there are several physicochemical effects that take place. On the one hand there is (i) a permanent decrease in acid site number and acid site strength, (ii) a decrease in surface area and micropore volume due to blockage by phosphorus species and, (iii) depending on the phosphatation procedure, Si-O-Al bond loss and even dealumination. [52] These effects can be either advantageous or deleterious for catalytic application. For example, the decrease in strong acid site number and strength is beneficial for the methanol-to-hydrocarbons (MTH) reaction, but detrimental for metal ion-exchanged zeolites used in selective catalytic reduction (SCR) of exhaust gasses, e.g. NO_x.[55-57]

On the other hand, and especially in the case of phosphated zeolite H-ZSM-5, zeolites maintain acid site number, TFAl atoms, and catalytic activity to a significant higher degree than their non-treated counterpart after a steam treatment. [51-54, 58-66] This allows an enhanced temperature range for catalytic applications. The latter phenomenon suggests that phosphorus species formed during phosphatation reinforce the zeolite structure and prevent dealumination. Also, addition of phosphorus to H-ZSM-5 lead to an increase toward propylene selectivity in the MTH reactions and cracking of hydrocarbons. [55, 63, 67-75]

While it needs no further explanation that improved propylene selectivity and hydrothermal stability is beneficial, it is not known how these effects arise, as the exact nature of phosphorus-zeolite interactions is not yet understood. Not surprisingly, many models for possible interactions have been discussed over the years, where the main division of opinion lies between the question whether permanent phosphorus-framework interaction exists or not. [51, 53, 61, 76-80]

In the case of permanent phosphorus-framework interaction the most intuitive explanation would be the incorporation of phosphorus into the zeolitic framework. Examples of these suggestions are shown in Figure 1.4 a-d. These interactions can be subsequently categorized in (a-b) phosphorus bonded to the bridging oxygen group of Si-O-Al, [75-76] (c) Si-O-P bonds, [81] and (d) Al-O-P bonds.[54, 79] Other possible phosphorus-framework interactions have been suggested to be reversible, as

Figure 1.4 Suggestions from the literature for phosphorus-framework interactions. (a-c and f) are most cited. (a) Kaeding et al., [76] (b) Xue et al., [75] (c) Lercher et al., [81] (d) Zhuang et al., Damodaran et al., [54, 79] (e) Abubakar et al. [71] (f) Blasco et al., [53] and (g) Caro et al. [80]

shown in Figure 1.3 e-f. [51, 53, 71] Examples of reversible interactions are (e) intramolecular bonds, [71] or (f) protonation of phosphoric acid by zeolitic bridging hydroxyl groups.[53] It has also been proposed that (g) phosphorus does not interacted at all with the zeolite framework and phosphorus only interacts with extra-framework aluminum, while dealumination is the cause for acid-site decrease.[80]

Elucidation of the kinds of phosphorus-zeolite interactions is expected to reveal the reasons behind hydrothermal stabilization, acid site alteration and changes in catalytic performance.
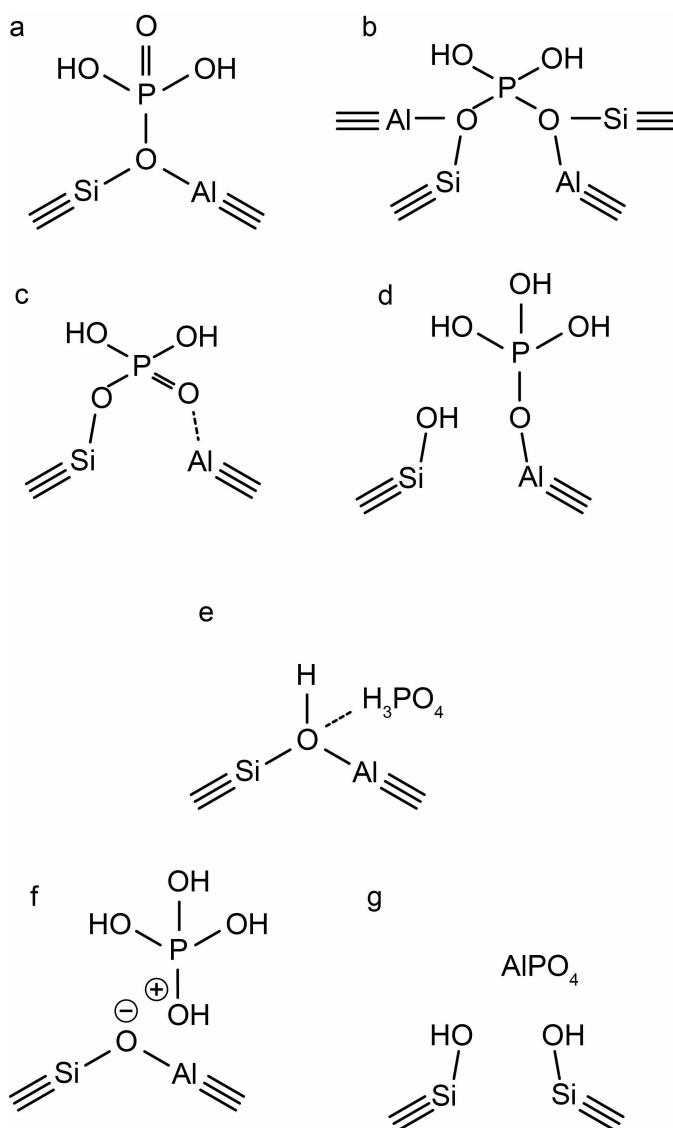
1.5 Scope and outline of the PhD thesis

The scope of this dissertation is to gain a fundamental understanding of phosphorus interaction with zeolites. These interactions can be either promotional or poisonous. Therefore, the main focus of this PhD thesis will be on the understanding of the physicochemical effects that occur upon phosphorus modification of zeolites. The ultimate goal is to elucidate if and what kind of bonds phosphorus forms with zeolite framework atoms, what the nature and location of phosphorus species are, and how these influence the acidity, the accessibility, the shape-selective character and the hydrothermal stability of zeolites. To achieve this goal we will use a combination of spectroscopic and microscopic techniques, complemented with catalytic testing, to study a variety of zeolites to which different pre-, and post-treatments have been applied. The insights gained in this thesis should help with more rationalized designs of phosphated zeolites, which can be used for a variety of applications.

In **Chapter 2** of this dissertation we will present a systematic academic literature survey of phosphated H-ZSM-5. As literature on phosphatation of other zeolite topologies is scarce and H-ZSM-5 is extensively studied, we chose to focus solely on this zeolite topology. Different phosphatation methods will be presented and an extensive in-depth analysis of available results will reveal universal physicochemical, structural and catalytic effects. This Chapter aims to enhance the understanding of phosphatation effects and help the reader with the interpretation of numerous characterization techniques.

An exploratory study of the phosphatation of H-ZSM-5 by combined soft X-ray microscopy and solid-state NMR is presented in **Chapter 3**. The combination of these techniques shows the location and state of phosphorus and aluminum atoms. It will be shown that the use of two differently pre-modified H-ZSM-5 samples, will lead to two very different materials upon phosphatation. The location and types of phosphorus species will be revealed and it will be shown that two distinct types of phosphorus-aluminum interaction exist, i.e. phosphorus interaction with framework aluminum and with extra-framework aluminum.

An extended investigation on the interaction of phosphorus with framework-aluminum is presented in **Chapter 4**. By means of solid-state ^{27}Al-^{31}P hetero-correlation NMR spectroscopy, different stages and parameters of the phosphatation process are studied, i.e. the type of precursor, the effect of thermal treatment and the effect of acidity on the samples. In this manner, it is possible to distinguish between two types of phosphorus interaction with framework aluminum, i.e. permanent interactions and reversible interactions.

Chapter 1

By extending the use of soft X-ray microscopy to tomography, a 3-D reconstruction of a single phosphated and hydrothermally treated H-ZSM-5 aggregate is presented in **Chapter 5**. It will be shown that the use of this technique, complemented with solid-state NMR provides new insights in the origin of hydrothermal stabilization of H-ZSM-5 by phosphorus. Catalytic tests will show that phosphatation leads to an increase in propylene selectivity during *n*-hexane cracking.

Chapter 6 explores the other type of phosphorus-aluminum interactions that are presented in Chapter 3, i.e. the reaction of phosphorus with extra-framework aluminum. Different zeolite topologies are studied in this work, which are zeolites H-mordenite, H-ferrierite and H-USY. A combination of *in-situ* scanning transmission X-ray microscopy, soft X-ray tomography, X-ray diffraction and solid-state NMR will reveal the location, crystallinity, and structure of aluminum-phosphate and the effect that topology has on the successful formation of this phase.

In **Chapter 7** we summarize and reflect on the previous Chapters. A more unified view on the various effects of phosphatation on zeolites will be presented. The dissertation will close with listing some of the important remaining questions, future outlook and suggestions for further research.

References

[1]   L. Karwacki, M. H. F. Kox, D. A. Matthijs de Winter, M. R. Drury, J. D. Meeldijk, E. Stavitski, W. Schmidt, M. Mertens, P. Cubillas, N. John, A. Chan, N. Kahn, S. R. Bare, M. Anderson, J. Kornatowski and B. M. Weckhuysen, *Nat. Mater.* **2009**, *8*, 959-965.

[2]   R. S. Bowman, *Micropor. Mesopor. Mater.* **2003**, *61*, 43-56.

[3]   A. Corma, *Chem. Rev.* **1995**, *95*, 559-614.

[4]   Z. Lai, G. Bonilla, I. Diaz, J. G. Nery, K. Sujaoti, M. A. Amat, E. Kokkoli, O. Terasaki, R. W. Thompson and M. Tsapatsis, *Science* **2003**, *300*, 456-460.

[5]   S. R. Venna and M. A. Carreon, *J. Am. Chem. Soc.* **2009**, *132*, 76-78.

[6]   G. Sastre and A. Corma, *J. Mol. Catal. A-Chem* **2009**, *305*, 3-7.

[7]   C. Marcilly, *Top. Catal.* **2000**, *13*, 357-366.

[8]   T. F. Degnan, G. K. Chitnis and P. H. Schipper, *Micropor. Mesopor. Mater.* **2000**, *35-36*, 245-252.

[9]   G. Reding, T. Mäurer and B. Kraushaar-Czarnetzki, *Micropor. Mesopor. Mater.* **2003**, *57*, 83-92.

[10]   Y. Yan, M. E. Davis and G. R. Gavalas, *Ind. Eng. Chem. Res.* **1995**, *34*, 1652-1661.

[11]   D. H. Olson, G. T. Kokotailo, S. L. Lawton and W. M. Meier, *J. Phys. Chem.* **1981**, *85*, 2238-2243.

[12]   www.iza-structure.org.

[13]   T. A. Hanna, *Coordin. Chem. Rev.* **2004**, *248*, 429-440.

[14]   M. Weber, M. Weber and M. Kleine-Boymann in *Phenol*, Wiley-VCH Verlag GmbH & Co. KGaA, **2000**.

[15]   N. Y. Chen, W. W. Kaeding and F. G. Dwyer, *J. Am. Chem. Soc.* **1979**, *101*, 6783-6784.

[16]   M. Takeuchi, T. Kimura, M. Hidaka, D. Rakhmawaty and M. Anpo, *J. Catal.* **2007**, *246*, 235-240.

[17]   R. K. Grasselli, D. L. Stern and J. G. Tsikoyiannis, *Appl. Catal. A-Gen* **1999**, *189*, 1-8.

[18]   W. O. Haag, R. M. Lago and P. G. Rodewald, *Journal of Molecular Catalysis* **1982**, *17*, 161-169.

[19]   L. B. Young, S. A. Butter and W. W. Kaeding, *J. Catal.* **1982**, *76*, 418-432.

[20]   W. W. Kaeding, C. Chu, L. B. Young, B. Weinstein and S. A. Butter, *J. Catal.* **1981**, *67*, 159-174.

[21]   C. D. Chang and A. J. Silvestri, *J. Catal.* **1977**, *47*, 249-259.

[22]   W. R. Moser, R. W. Thompson, C.-C. Chiang and H. Tong, *J. Catal.* **1989**, *117*, 19-32.

[23]   T. F. Degnan, C. M. Smith and C. R. Venkat, *Appl. Catal. A-Gen* **2001**, *221*, 283-294.

[24]   K. Tanabe and W. F. Hölderich, *Appl. Catal. A-Gen* **1999**, *181*, 399-434.

[25]   H. Mooiweer, K. De Jong, B. Kraushaar-Czarnetzki, W. Stork and B. Krutzen, *Stud. Surf. Sci. Catal.* **1994**, *84*, 2327-2334.

[26]   G. Cao, B. R. Cook, R. H. Ernst, J. W. Johnson and R. A. McEvoy in *Catalytic dewaxing with trivalent rare earth metal ion exchanged ferrierite*, Patent WO2001002514 A1, **2000**.

[27]   C. Plank, E. Rosinski and W. Hawthorne, *Ing. Eng. Chem. Prod. RD.* **1964**, *3*, 165-169.

[28]   J. E. Otterstedt, S. B. Gevert, S. G. Jääs and P. G. Menon, *Appl. Catal.* **1986**, *22*, 159-179.

[29]   J. W. Ward, *Fuel Processing Technology* **1993**, *35*, 55-85.

[30]   T. Chevreau, A. Chambellan, J. Lavalley, E. Catherine, M. Marzin, A. Janin, J. Hemidy and S. Khabtou, *Zeolites* **1990**, *10*, 226-234.

[31]   R. A. Beyerlein, C. Choi-Feng, J. B. Hall, B. J. Huggins and G. J. Ray, *Top. Catal.* **1997**, *4*, 27-42.

[32]   A. H. Janssen, A. J. Koster and K. P. de Jong, *Angew. Chem. Int. Ed.* **2001**, *40*, 1102-1104.

[33]   T. Ren, M. Patel and K. Blok, *Energy* **2006**, *31*, 425-451.

[34]   B. S. Greensfelder, H. H. Voge and G. M. Good, *Ind. Eng. Chem.* **1949**, *41*, 2573-2584.

[35]   S. Kotrel, H. Knözinger and B. C. Gates, *Micropor. Mesopor. Mater.* **2000**, *35–36*, 11-20.

[36]   A. Corma and A. V. Orchillés, *Micropor. Mesopor. Mater.* **2000**, *35–36*, 21-30.

[37]   W. Haag and R. Dessau, *Proceedings of the 8th International Congress on Catalysis* **1984**.

[38]   F. C. Jentoft and B. C. Gates, *Top. Catal.* **1997**, *4*, 1-13.

[39]   A. F. H. Wielers, M. Vaarkamp and M. F. M. Post, *J. Catal.* **1991**, *127*, 51-66.

[40]   N. Rahimi and R. Karimzadeh, *Appl. Catal. A-Gen* **2011**, *398*, 1-17.

[41]   J. Gopalakrishnan, *Chem. Mater.* **1995**, *7*, 1265-1275.

[42]   S. van Donk, A. H. Janssen, J. H. Bitter and K. P. de Jong, *Catal. Rev.* **2003**, *45*, 297-319.

[43]   S. Malola, S. Svelle, F. L. Bleken and O. Swang, *Angew. Chem. Int. Ed.* **2012**, *51*, 652-655.

[44]   T. Fjermestad, S. Svelle and O. Swang, *J. Phys. Chem. C* **2013**, *117*, 13442-13451.

[45]   C. S. Triantafillidis, A. G. Vlessidis, L. Nalbandian and N. P. Evmiridis, *Micropor. Mesopor. Mater.* **2001**, *47*, 369-388.

[46]   T.-H. Chen, K. Houthoofd and P. J. Grobet, *Micropor. Mesopor. Mater.* **2005**, *86*, 31-37.

[47]   J. Jiao, J. Kanellopoulos, W. Wang, S. S. Ray, H. Foerster, D. Freude and M. Hunger, *Phys. Chem. Chem. Phys.* **2005**, *7*, 3221-3226.

[48]   I. Wang, T.-J. Chen, K.-J. Chao and T.-C. Tsai, *J. Catal.* **1979**, *60*, 140-147.

[49]   L. R. Aramburo, E. de Smit, B. Arstad, M. M. van Schooneveld, L. Sommer, A. Juhin, T. Yokosawa, H. W. Zandbergen, U. Olsbye, F. M. F. de Groot and B. M. Weckhuysen, *Angew. Chem. Int. Ed.* **2012**, *51*, 3616-3619.

[50]   A. Corma, M. Faraldos and A. Mifsud, *Appl. Catal.* **1989**, *47*, 125-133.

[51]   G. Lischke, R. Eckelt, H. G. Jerschkewitz, B. Parlitz, E. Schreier, W. Storek, B. Zibrowius and G. Öhlmann, *J. Catal.* **1991**, *132*, 229-243.

[52]   G. Caeiro, P. Magnoux, J. M. Lopes, F. R. Ribeiro, S. M. C. Menezes, A. F. Costa and H. S. Cerqueira, *Appl. Catal. A-Gen* **2006**, *314*, 160-171.

[53]   T. Blasco, A. Corma and J. Martínez-Triguero, *J. Catal.* **2006**, *237*, 267-277.

[54]   J. Zhuang, D. Ma, G. Yang, Z. Yan, X. Liu, X. Liu, X. Han, X. Bao, P. Xie and Z. Liu, *J. Catal.* **2004**, *228*, 234-242.

[55]   J. Liu, C. Zhang, Z. Shen, W. Hua, Y. Tang, W. Shen, Y. Yue and H. Xu, *Catal. Commun.* **2009**, *10*, 1506-1509.

[56]   X. Wang, W. Dai, G. Wu, L. Li, N. Guan and M. Hunger, *Micropor. Mesopor. Mater.* **2012**, *151*, 99-106.

[57]   I. Lezcano-Gonzalez, U. Deka, H. E. van der Bij, P. Paalanen, B. Arstad, B. M. Weckhuysen and A. M. Beale, *Appl. Catal. B-Environ* **2014**, *154*, 339-349.

[58]   A. F. Costa, H. S. Cerqueira, J. M. M. Ferreira, N. M. S. Ruiz and S. M. C. Menezes, *Appl. Catal. A-Gen* **2007**, *319*, 137-143.

[59]   A. Corma, J. Mengual and P. J. Miguel, *Appl. Catal. A-Gen* **2013**, *460–461*, 106-115.

[60]   G. Yang, J. Zhuang, Y. Wang, D. Zhou, M. Yang, X. Liu, X. Han and X. Bao, *J. Mol. Struc.* **2005**, *737*, 271-276.

[61]   M. J. B. Cardoso, D. D. O. Rosas and L. Y. Lau, *Adsorption* **2005**, *11*, 577-580.

[62]   S. M. Cabral de Menezes, Y. L. Lam, K. Damodaran and M. Pruski, *Micropor. Mesopor. Mater.* **2006**, *95*, 286-295.

[63]   G. Zhao, J. Teng, Z. Xie, W. Jin, W. Yang, Q. Chen and Y. Tang, *J. Catal.* **2007**, *248*, 29-37.

[64]   Y.-J. Lee, J. M. Kim, J. W. Bae, C.-H. Shin and K.-W. Jun, *Fuel* **2009**, *88*, 1915-1921.

[65]   Y.-J. Lee, Y.-W. Kim, N. Viswanadham, K.-W. Jun and J. W. Bae, *Appl. Catal. A-Gen* **2010**, *374*, 18-25.

[66]   D. Liu, W. C. Choi, C. W. Lee, N. Y. Kang, Y. J. Lee, C.-H. Shin and Y. K. Park, *Catal. Today* **2011**, *164*, 154-157.

[67]   J. C. Védrine, A. Auroux, P. Dejaifve, V. Ducarme, H. Hoser and S. Zhou, *J. Catal.* **1982**, *73*, 147-160.

[68]   M. Derewinski, P. Sarv, X. Sun, S. Müller, A. C. van Veen and J. A. Lercher, *J. Phys. Chem. C* **2014**, *118*, 6122-6131.

[69]   A. Rahman, G. Lemay, A. Adnot and S. Kaliaguine, *J. Catal.* **1988**, *112*, 453-463.

[70]   A. Rahman, A. Adnot, G. Lemay, S. Kaliaguine and G. Jean, *Appl. Catal.* **1989**, *50*, 131-147.

[71]   S. M. Abubakar, D. M. Marcus, J. C. Lee, J. O. Ehresmann, C. Y. Chen, P. W. Kletnieks, D. R. Guenther, M. J. Hayman, M. Pavlova, J. B. Nicholas and J. F. Haw, *Langmuir* **2006**, *22*, 4846-4852.

[72]   P. Li, W. Zhang, X. Han and X. Bao, *Catal. Lett.* **2010**, *134*, 124-130.

[73]   G. Jiang, L. Zhang, Z. Zhao, X. Zhou, A. Duan, C. Xu and J. Gao, *Appl. Catal. A-Gen* **2008**, *340*, 176-182.

[74]   N. Xue, L. Nie, D. Fang, X. Guo, J. Shen, W. Ding and Y. Chen, *Appl. Catal. A-Gen* **2009**, *352*, 87-94.

[75]   N. Xue, X. Chen, L. Nie, X. Guo, W. Ding, Y. Chen, M. Gu and Z. Xie, *J. Catal.* **2007**, *248*, 20-28.

[76]   W. W. Kaeding and S. A. Butter, *J. Catal.* **1980**, *61*, 155-164.

[77]   M. Göhlich, W. Reschetilowski and S. Paasch, *Micropor. Mesopor. Mater.* **2011**, *142*, 178-183.

[78]   A. Jentys, G. Rumplmayr and J. A. Lercher, *Appl. Catal.* **1989**, *53*, 299-312.

[79]   K. Damodaran, J. W. Wiench, S. M. Cabral de Menezes, Y. L. Lam, J. Trebosc, J. P. Amoureux and M. Pruski, *Micropor. Mesopor. Mater.* **2006**, *95*, 296-305.

[80]   J. Caro, M. Bülow, M. Derewinski, J. Haber, M. Hunger, J. Kärger, H. Pfeifer, W. Storek and B. Zibrowius, *J. Catal.* **1990**, *124*, 367-375.

[81]   J. A. Lercher and G. Rumplmayr, *Appl. Catal.* **1986**, *25*, 215-222.

The Good or the Bad Guy? On the Chemistry between Phosphorus and Zeolite-based Catalysts

P hosphatation of the industrially important zeolite H-ZSM-5 is a well-known, relatively inexpensive and seemingly straightforward post-synthesis modification, not only to alter its hydrothermal stability and acidity, but also to increase e.g. selectivity towards light olefins in hydrocarbon catalysis. Despite this importance and apparent simplicity, the exact physicochemical processes that take place during phosphatation are not well understood. This Chapter provides the reader with a comprehensive and state of the art overview of the academic literature, from the first reports in the early 1980s until the most recent studies. In the first part of the Chapter various phosphatation synthesis parameters and different modification strategies are discussed. The second part presents an in-depth analysis and based on this a comparison of the available characterization results will be made, which reveals universal physicochemical and structural effects of the phosphatation process on the strength, stability and accessibility of acid sites. The third part of the review aims to link the structural and physicochemical effects of phosphorus on zeolite H-ZSM-5 with its catalytic performance in a variety of catalytic processes, including aromatics alkylation, catalytic cracking, methanol-to-olefin processing and ethanol dehydration.

Chapter 2

2.1 Introduction

To prevent permanent deactivation, modification of zeolites by post-synthesis treatments is an effective route to provide hydrothermal stability. As was mentioned in Chapter 1, several studies reported improved hydrothermal stability after the application of a phosphorus modification, i.e. a phosphatation step.[1-4] Phosphated zeolite literature is almost exclusively written on H-ZSM-5. In these studies phosphated H-ZSM-5 has been tested in catalytic reactions like the alkylation of aromatics, methanol-to-olefins (MTO), cracking of paraffins and the dehydration of alcohols. It has been found that phosphatation leads to (i) a decrease in the formation of bulky isomers, (ii) an increase in the formation of light olefins in MTO, dehydration of ethanol, and cracking reactions, (iii) a decrease in coke formation, and (iv) an enhanced stability with time-on-stream, due to the reduced coke formation and the hydrothermal stabilization of framework aluminum.

Despite the many reports on the positive effect of phosphorus modification on the catalytic performance of H-ZSM-5, qualitative insight is lacking. As was mentioned in Chapter 1, there is still discussion and controversy on, if and how phosphorus species interact with the zeolite framework. [1, 3-16] Furthermore, the various synthesis routes and materials used in the literature are expected to have a strong influence on the eventual catalytic properties of a phosphorus-modified zeolite, e.g. Al/P ratio, Si/Al ratio, zeolite crystal size, phosphatation conditions and phosphorus precursor could all have an effect. Therefore, it is difficult to make direct comparisons between different research works.

This introductory Chapter provides the reader with a systematic overview of phosphated H-ZSM-5 literature. As only papers published in the open literature are considered, patent literature is omitted. We furthermore limit ourselves to the phosphatation of a single zeolite type, i.e. zeolite H-ZSM-5, as literature on other topologies is scarce. The main focus of this Chapter is to compare results obtained with structural and chemical characterization techniques. As interpretation of these results differs greatly from paper to paper, we aim to compare the data directly. Our goal is to find structural and chemical trends for phosphated H-ZSM-5. Subsequently, we will aim to link these structural properties to catalytic promotional effects found during catalytic testing results. The Chapter ends with a summary of the universal effects that a phosphatation step has on H-ZSM-5 and will pose some of the questions that will be answered in the course of this PhD thesis.

2.2 Preparation of phosphorus-modified H-ZSM-5

2.2.1 Methods of phosphorus introduction

When considering the vast literature on the modification of H-ZSM-5 with phosphorus, it is clear that there are many variations and parameters to take into account. They include the zeolite Si/Al ratio, loading technique, phosphatation conditions (i.e., solution pH, reaction temperature and phosphatation time), precursor type and P/Al ratio. Unfortunately, it is rarely found that two literature works have a comparable set of all of these parameters, which makes it difficult to compare different articles when considering the effect of phosphatation on e.g. catalytic performance.

The Si/Al ratio in H-ZSM-5 is an important factor, as this ratio influences the amount of acid sites

Figure 2.1 The occurrence of Si/Al ratios found in literature on phosphated ZSM-5 materials. Values are rounded at 5, except for Si/Al = 12.5. The x-axis has a logarithmic scale.
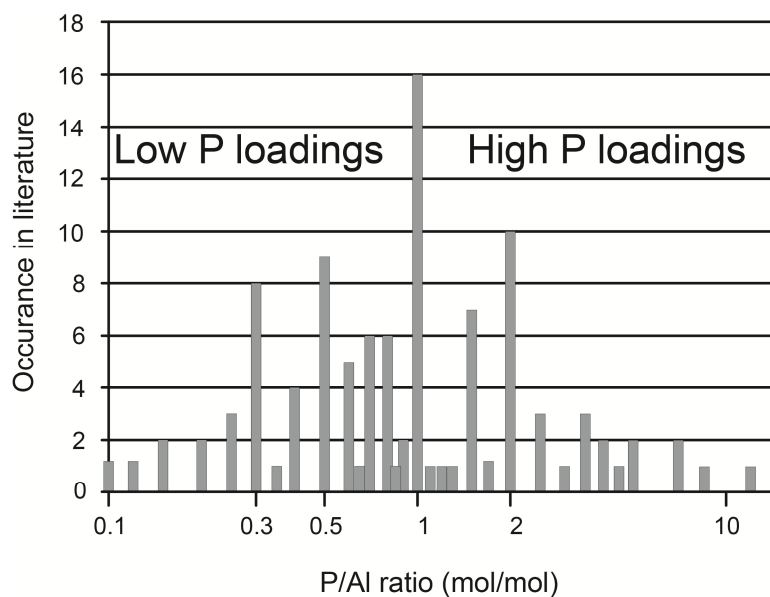
and consequently its catalytic performance. Furthermore, it has an influence on the final P/Al ratio of a sample. From Figure 2.1 it can be seen that the values of Si/Al ratios vary from 12.5 to 360. On average the Si/Al ratios are in the range of 12.5 to 50 and the most recurring values are 15, 25 and 40.

Using H-ZSM-5 as a starting material, the use of incipient wetness impregnation (IWI) or wet impregnation (WI) is the most practiced method of phosphorus introduction. [1-4, 7, 9, 12-13, 16-39] The

Figure 2.2 The occurrence of P/Al ratios found in literature on phosphated ZSM-5 materials. For values below 0.1 numbers are not rounded. Between 0.1 and 1 numbers are rounded at one decimal. Between 1 and 10 numbers are rounded at 0.5. Above 10 numbers are rounded at 1. The x-axis has a logarithmic scale.

precursor of choice is phosphoric acid. [1-4, 7, 9, 14, 16, 18, 20-22, 24, 26-27, 29-31, 34-40] Less acidic precursors such as $NH_4H_2PO_4$ [3, 41-43] and $(NH_4)_2H_2HPO_4$ [12-13, 19, 25, 28, 32-33] are used as well, although sporadically. After impregnation, the materials obtained are first dried at temperatures ranging from 70 °C to 120 °C, sometimes at reduced pressures. Afterwards samples are calcined at elevated temperatures ranging from 450 °C to 650 °C for durations ranging from 1 h to 6 h. Another preparation method of P/H-ZSM-5 is, what we will call now, the reflux method.[8, 10, 15, 44-46] This method is commonly applied by Lercher and co-workers and is quite similar to impregnation. A sample is generally mixed under reflux conditions with an aqueous solution of H_3PO_4, where the concentration of H_3PO_4 corresponds to the desirable phosphorus content. Water is removed by evaporation at reduced pressures. Subsequently, the samples are dried and calcined. This method is also the phosphorus modification technique applied in this thesis.

Besides phosphoric acid and ammonium phosphates, different precursors are used as well. Especially popular in the 1980s was the use of trimethylphosphite (TMPT). This precursor was solved in *n*-octane and mixed with H-ZSM-5. The mixture was stirred under reflux conditions, then filtered, washed with e.g. *n*-pentane and dried at 120 °C. Subsequently, the sample was calcined at elevated temperatures.[5, 10-11, 44, 47-48] Gas-phase deposition is also a technique used to transfer a phosphorus precursor into a H-ZSM-5 zeolite. Precursors reported with this technique are trimethylphosphite (TMPT)[11, 30, 49], triphenylphosphine (TPP)[50-51], trimethylphosphine (TMP)[10, 17, 44-46] and phosphorus pentachloride (PCl₅).[52] H-ZSM-5 was contacted with the vapor phase of these precursors at elevated temperatures ranging from 360 °C to 600 °C. In the case of

TMP a cycle was repeated a couple of times. Afterwards, samples were calcined. Different precursors used in combination with impregnation methods are diphenylphosphinous (DPP) acid, TPP and phosphorus trichloride (PCl_3), dissolved in methylene chloride, carbon tetrachloride and benzene, respectively.[53] It has also been tried to incorporate phosphorus into the MFI framework by synthesizing H-ZSM-5 with a phosphorus precursor in the reaction gel.[54-55] Gao et al. used a phosphatation method which was coined as the hydrothermal dispersion method. Here H-ZSM-5 is mixed with $(NH_4)_2HPO_4$ and reacted at 140 °C and at 0.3 MPa for 2 h.[56-57] As most of these mentioned precursors were subjected to a thermal treatment after introduction to the zeolite, they mainly exist as phosphates.

Most authors have an interest in the effect that the amount of phosphorus content has on zeolite H-ZSM-5. Therefore, samples are often prepared with varying amounts of phosphorus. As can be seen in Figure 2.2 many authors aim for a P/Al ratio of 1. Although the P/Al ratio is a good guideline to compare literature data, since Si/Al ratios vary, we will see over the course of this Chapter that diffusion limitations play a significant role and determine how much phosphorus can enter the zeolite. Therefore, phosphorus weight loading has often a stronger influence on H-ZSM-5 structure and acidity than P/Al ratio.

2.2.1 Treatments following or preceding phosphorus introduction

Additional post- or pre-treatments have been performed as well, with the most common modification being a post-steam treatment. Since it is well known that the addition of phosphorus improves the hydrothermal stability of zeolites, many authors applied such a treatment to investigate this effect. [1-3, 7, 12, 14, 22, 26-27, 30, 32, 37, 39, 56-57] The post-steam treatment is generally performed with 100 vol% steam and at temperatures ranging from 400 °C to 800 °C and for periods of time from 0.5 h up to 72 h.

In certain cases a pre-steam treatment was performed before the addition of phosphorus. Pre-steam treatments were performed at 500 °C for 4 h, 800 °C for 3 h and 800 °C for 4 h. [1, 12, 22] The latter example, which was a work by Xue et al. was in more ways an uncommon modification. During the pre-steam treatment, framework aluminum is partially expelled from the framework to form extra-framework aluminum (EFAl) species. These species were removed by treatment with ethylenediaminetetraacetic acid (EDTA). Then phosphorus was introduced under hydrothermal conditions. $(NH_4)_2HPO_4$ was mixed with the zeolite and placed in an autoclave at 170 °C for 55 h. [12]

Another pre-treatment was the use of a surface-active agent to block the zeolites external surface for phosphorus species before phosphatation. The surfactant used was N-cetylpyridiniumbromide (CPB). [23-25]

Elution of phosphorus species is another post-treatment practiced.[1, 3, 9, 12, 14, 21, 39, 41, 56] If phosphated H-ZSM-5 is washed with hot water and filtered, most phosphorus species that exist as mono-, di-, or polyphosphates are removed from the zeolite, which will be discussed in more detail in section 2.3 of this Chapter.[1]

2.3 Characterization of phosphorus-modified H-ZSM-5

Table 2.1 Characterization methods used in phosphated H-ZSM-5 studies.

Technique	Application
Fourier Transform Infrared Spectroscopy - **FT-IR**	The absorption or diffuse reflectance of infrared light is used to study the O-H stretch vibrations in zeolites. Bridging hydroxyl groups, silanol groups and P-OH groups can be detected using this technique. Qualitative and quantitative information on types of acid sites, extra-framework aluminum and phosphate species can be obtained.
(Multiple Quantum) Magic Angle Nuclear Magnetic Resonance Spectroscopy - **(MQ) MAS NMR**	The interaction of a nuclear spin with a magnetic field can be used to determine coordination states, nearest neighbours, vicinity to other atoms, bond length, and symmetry of surrounding, of atoms. In phosphated H-ZSM-5 studies the atoms of interest are generally ^{1}H, ^{27}Al, ^{29}Si, and ^{31}P. 2-dimensional MQ MAS reveals isotropic line shapes for quadrupolar nuclei such as ^{27}Al. Using this technique it is possible to identify aluminum species that would otherwise not be visible using 1D MAS NMR. By using Cross Polarization (CP) and Insensitive Nuclei Enhanced by Polarization Transfer (INEPT) hetero-correlation (HETCOR) experiments it is even possible to determine interactions through space (CP) and bond (INEPT) respectively, between different atoms, e.g. interactions between ^{31}P and ^{27}Al atoms.
Nitrogen physisorption	The adsorption and subsequent desorption of nitrogen provides insight in the meso- and micropore volume of materials. With this technique it can be determined if dealumination takes place, if phosphorus species block pores or alter pore dimensions. Furthermore, the internal and external surface area of materials can be determined.
Temperature Programmed Desorption - **TPD**	Probe molecules that chemisorb to zeolite acid sites are introduced and desorbed by programmed heating. The number of chemisorbed molecules and temperature of desorption are assumed to correlate with the acid site number and strength respectively. Probe molecules that are usually introduced to zeolites are NH_3, pyridine and propylamine. TPD experiments are generally monitored with a thermal conductivity detector (TCD), but can be followed using FT-IR spectroscopy as well. The latter method adds the possibility to see which OH groups are acidic and if all acid sites are accessible to the probe molecules, so to determine if phosphorus species block pores.
X-ray Diffraction - **XRD**	The diffraction pattern of diffracted X-rays is used to determine the crystal structure and unit cell size of materials. It also provides insight in the crystallinity of a material and if multiple crystal phases exist.
X-ray Photoelectron Spectroscopy/Electron Spectroscopy for Chemical Analysis - **XPS/ESCA**	The energies of electrons that escape the surface of a material that is irradiated by X-rays can be used to determine the element, number, and oxidation state of the atoms that are present on the surface. As this is a surface sensitive technique, it can be used to determine the phosphorus concentration in the first layers ($\pm$ 10 nm) of H-ZSM-5 crystals.

Chapter 2

In this section we will discuss the structural and chemical properties of phosphated H-ZSM-5 materials. The most common characterization techniques that have been applied in the literature on phosphated H-ZSM-5 are summarized in Table 2.1.

2.3.1 Location of phosphorus species

XPS measurements showed a higher concentration of phosphorus surface species compared to phosphorus in the bulk of H-ZSM-5 when the crystals had a homogeneous distribution of aluminum species, as shown in Figure 2.3 a.[48, 50] It was found that with increasing crystal size the ratio of $P_{Surface}/P_{Bulk}$ species increased (Figure 2.3 b).[7] This would suggest that phosphorus species experience diffusion limitations and therefore phosphorus weight loading would be the parameter that rules the phosphorus distribution instead of P/Al ratio. Interestingly, when the concentration of aluminum was higher in the zeolite bulk than the external surface, the distribution of phosphorus was homogeneous (Figure 2.3 c).[48] This latter finding indicates an attraction between framework aluminum and phosphorus.

Furthermore, FT-IR spectroscopy, ^{1}H MAS NMR and ^{27}Al MAS NMR, revealed that at low phosphorus loadings below 2 wt.%, the amount of external Si-OH decreased faster than internal Si-OH-Al groups and only when the surface was covered with surfactant, did phosphorus species enter the zeolite bulk immediately at low loadings, shown in Figure 2.3 d.[10-11, 13, 15, 23-25, 46] When phosphorus loadings are increased the phosphorus species tend to move further into the zeolite, as all aluminum species and corresponding acid sites are affected by the presence of phosphorus (Figure 2.3 e).[2-3, 9, 15, 22, 29, 34]

Also, ^{29}Si NMR showed that at phosphorus loadings above 2 wt.%, silicon species were found in a distorted electronic environment, caused by phosphorus species inside the zeolite channels.[4, 38] However, with increasing phosphorus loadings, the concentration of phosphorus surface species increases faster than those in the bulk and after phosphorus loadings above 5 wt.% mostly excess phosphorus is deposited on the external surface.[8-9, 13-15, 30, 34] Platelets of excess polyphosphates have been observed with scanning electron microscopy (SEM). [8] A schematic drawing of this effect is presented in Figure 2.3 f. SEM images indicate phosphorus modification promotes aggregation as well. [21] The method of phosphorus introduction might play an important role in the distribution of phosphorus. It has been reported that using the hydrothermal dispersion method mentioned in section 2.2, phosphorus was more homogeneously distributed in the micropores, while impregnation lead to a high concentration of phosphorus species on the surface, as was established by N_2-physisorption. [56-57]
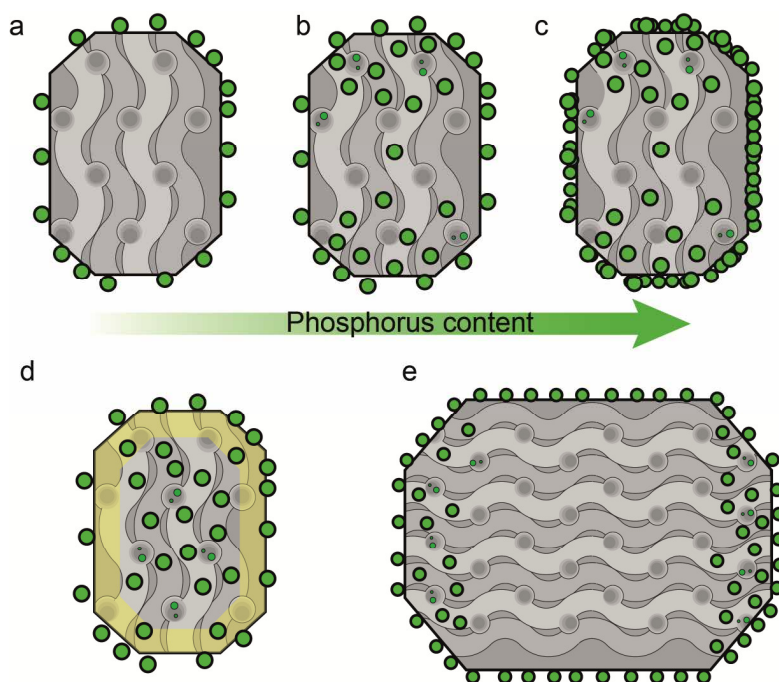
Figure 2.3 Proposed schematic model of phosphorus species location depending on crystal size, aluminum distribution and increasing phosphorus weight loadings. The model is based on XPS data by references [7, 48, 50] ^{129}Xe NMR and ^{1}H NMR tracer desorption by references [13, 15] (a-c) Effect of increasing phosphorus loading. Due to diffusion limitations the location of phosphorus is more dependent on actual P weight loading than P/Al ratio. Crystals are viewed along the [100][001] plane. (d) Effect of aluminum distribution. Yellow is an aluminum-poor region. (e) Effect of crystal size.

2.3.2 Effect of phosphorus on accessibility and porosity

The addition of phosphorus to H-ZSM-5 leads to a decrease in microporous volume and surface area, as was established by N$_2$-physisorption. This decrease is gradually more severe with increasing phosphorus content, as more phosphorus is able to penetrate the zeolite interior. [2-3, 8-9, 12-13, 20-22, 24-26, 28-32, 34-36, 38-39, 43, 57] Commonly, the decrease in micropore volume and surface area is attributed to dealumination, partial blockage of channels by phosphorus species and aggregation of zeolite particles. Chen and co-workers suggested that the presence of phosphorus changed diffusional characteristics by decreasing pore dimensions and openings, leading to longer diffusion pathways for reactants and products.[40, 47, 53] These results have recently been confirmed and it has been reported that phosphorus forms monolayer islands throughout the MFI channel system.[41] Adsorption with the probe molecules cyclohexane and *n*-heptane showed a strong decrease in accessibility for samples with more than 3 wt.% loading of phosphorus species.[20] However, the adsorption of pyridine was not affected by the presence of phosphorus, as all FT-IR visible zeolite bridging hydroxyl groups remained accessible.[1, 3, 8, 10]

The BET surface area and micropore volume of phosphated H-ZSM-5 could be restored to 95% of the parent material after 84% of phosphorus was eluted before thermal treatment. [9] Washing of phosphated H-ZSM-5 after calcination leads to a partial restoration of surface area and micropore volume of about 70% - 85% of the parent material. [9, 39, 41, 43] One of the reasons that after thermal treatment of phosphated H-ZSM-5 the amount of retrievable surface area and micropore volume decrease, is suggested because phosphorus species become condensed and occluded during thermal treatment and have a decreased solubility in water.[21] More reasons will be discussed in the coming sections.

2.3.3 Dealumination induced by phosphorus modification

Dealumination of H-ZSM-5 due to phosphatation without a subsequential thermal treatment does not take place [1, 9, 21] However, not many studies have been performed to study this effect. Nevertheless, dealumination does take place after phosphatation is followed by a thermal treatment and the severity of dealumination does seem to be influenced by P/Al ratios, as we will read in the following sections.

2.3.3.1 *Effect of phosphorus on crystallinity*

The crystallinity of the parent H-ZSM-5 is reduced to a certain extent after introduction of phosphorus and subsequential thermal treatment, but the MFI structure is maintained and no additional phases are observed. The decrease in crystallinity is generally attributed to dealumination. [4, 9, 22, 24, 26, 28-29, 34-38, 56] However, Gao et al. attributed the loss in crystallinity to scattering of X-rays by phosphorus species present in the zeolite pores.[57] Loss in crystallinity was found for samples treated with acidic and non-acidic precursors and with different acidities used in the impregnation solution, excluding acid leaching as the source of crystallinity loss.

In some papers a loss in crystallinity was not detected with XRD. [8, 13, 31, 37, 50] Some of these reports used, e.g. mild synthesis conditions [50] and high Si/Al ratios [31], which could account for a maintained crystallinity. However, other researchers observed a maintained crystallinity, while using similar phosphatation synthesis conditions as discussed above.[8, 13, 37] Furthermore, Song and co-workers observed a decrease in crystallinity for phosphated H-ZSM-5 (Si/Al = 80), but not for phosphated H-ZSM-5 (Si/Al = 30).[37]

2.3.3.2 *Effect of phosphorus on Si-O-Al bonds*

The Si/Al ratio of zeolites can be determined in a number of ways. In the case of chemical analysis all aluminum in the zeolite is detected, which includes extra-framework aluminum. Therefore, when using chemical analysis, after phosphatation the total amount of aluminum in the zeolite usually decreases only slightly, or not at all.[11, 42, 48] If Si/Al ratios are calculated from ^{29}Si MAS NMR spectra only the decrease in framework Si-O-Al bonds is probed.[4, 10, 15, 17, 26, 34-35] We have used these reported values to calculate the decrease in the percentage of Si-O-Al bonds. These values have been plotted against their respective P/Al ratios in Figure 2.4. Four works report framework Si/Al ratios that decrease with increasing phosphorus loading.[4, 15, 17, 35] Seeing a trend that apparently depends on P/Al ratio, it would seem that phosphorus species promote the hydrolysis of Si-O-Al bonds during thermal treatment.

The exception is the work of Blasco et al. where no dealumination is observed. Moreover, careful inspection of the ^{29}Si MAS NMR spectra indicates that the amount framework silicon atoms connected through oxygen bonds with three silicon and one Al atom appear to increase. In the respective work, the post calcination of the sample was mild (500 °C, 1 h), which could have been insufficient for the cleaving of Si-O-Al bonds. However, Göhlich and co-workers state that the framework Si/Al ratio does increase with increasing phosphorus content, based on FT-IR spectra of the T-O bending vibrations, while applying even milder post-calcination conditions (450 °C, 1 h). [9]
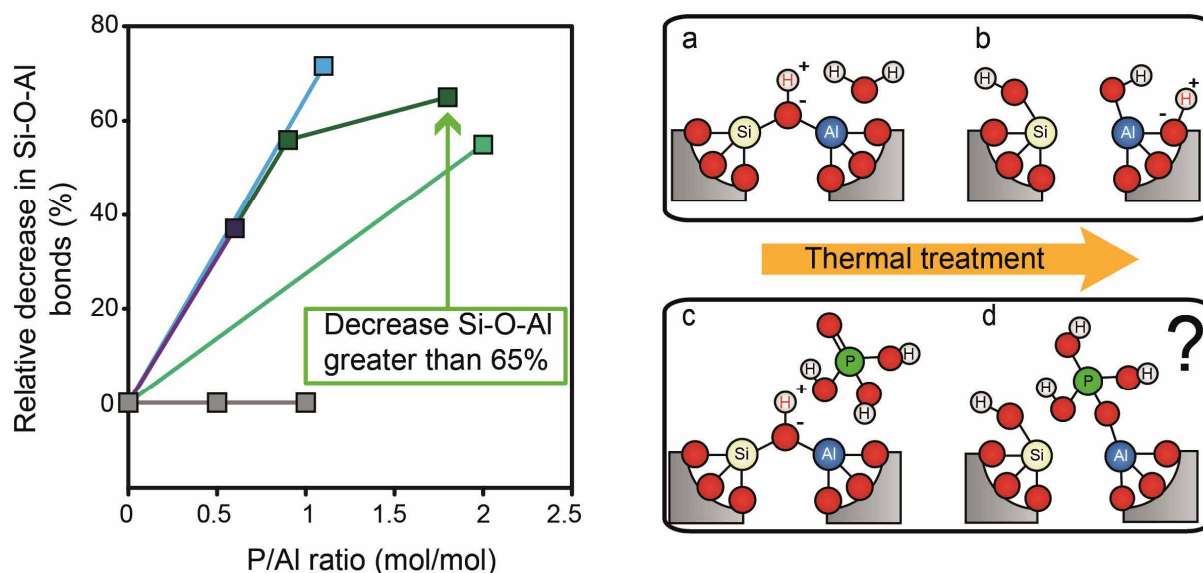
Figure 2.4 The decrease in Si-O-Al bonds vs. P/Al ratio after phosphatation. Values are calculated from reported Si/Al ratios obtained by ^{29}Si MAS NMR. ■ = Caro et al.[15] ■ = Zhuang et al.[4] ■ = Abubakar et al.[17] ■ = Blasco et al.[3] ■ = Li et al.[35] The decrease in TFAl for P/Al ratio 1.8 corresponds to a reported Si/Al ratio greater than 200, so the actual percentage is higher. (a-d) Possible mechanism of Si-O-Al bond hydrolysis during thermal treatment in the presence of H_2O and H_3PO_4.

On a final note, the method of calculating Si/Al ratios from the relative intensities of the Si(nAl) resonances is only precise below a ratios of Si/Al of 10, which are rarely found for H-ZSM-5. [58] So the reported values should be considered with some caution.

2.3.4 Acid sites

2.3.4.1 *Acid site number*

2.3.4.1.1 Acid sites on unmodified H-ZSM-5

A perfect crystalline zeolite H-ZSM-5 has three types of acid sites. The strongest acid sites are formed by the protons present in framework bridging hydroxyl groups (Si-OH-Al) where they act as counter cations for the negatively Al tetrahedra, forming Brønsted acid sites. [59] The remaining acid sites are very weak and comprise of surface terminal silanol and aluminol groups, discussed in Chapter 1. Thermal treatment, applied to convert the ammonium form of H-ZSM-5 into H-ZSM-5, can lead to dealumination.[60] With the breaking of Si-O-Al bonds new acid sites can form. These are silanol groups that form at defect sites and (partial) extra-framework aluminum species.[59, 61-62] Furthermore, framework aluminum species that are only partially connected to the framework can form Lewis or Brønsted acid sites. [63-64]

2.3.4.1.2 Acid sites on phosphorus modified H-ZSM-5

After modification of H-ZSM-5 with phosphorus, FT-IR, TPD of pyridine, ammonia, propylamine and ^{1}H MAS NMR all revealed that bridging hydroxyl groups and silanol groups are found to decrease with increasing phosphorus content. [1, 3-4, 8-13, 15-16, 18-21, 23-24, 26, 28-32, 34-36, 38-39, 41, 43-44, 46, 48-50] Within a single study, as can be seen in Figure 2.5, the relative decrease in Brønsted acid sites correlates quite well with the P/Al ratio. [3] The values reported in other literature works for the decrease in Brønsted acid site number vs. P/Al ratio can be observed in Figure 2.6. The figure shows that, while for all reports the total acid site number decreases with increasing phosphorus content, there seems to be no clear correlation between P/Al ratio and the actual decrease in acid site number. This finding indicates that other parameters are at play as well, such as diffusion of phosphorus into the material due to crystal size, phosphorus loading technique and subsequential thermal treatment, as was discussed in section 2.3.1 and 2.3.3.

In the literature it is reported that with phosphorus weight loadings above 5 wt.% the amount of strong acid sites has almost completely disappeared. [8, 20, 29, 34] The Brønsted/Lewis acid site ratio is found to decrease in phosphorus modified samples, which would indicate that Lewis acid

sites are not as much affected by phosphorus as Brønsted acid sites. [8, 26, 28, 45, 50, 55, 57] It is important to point out that all samples have been thermally treated after phosphatation. In one work the decrease in Brønsted acid sites was determined for phosphated H-ZSM-5 before thermal treatment. [1] The results showed about 30% reversible decrease in Brønsted acid site number for P/Al = 0.5. In Chapter 4, we will present a study on the reversible decrease of acid sites.
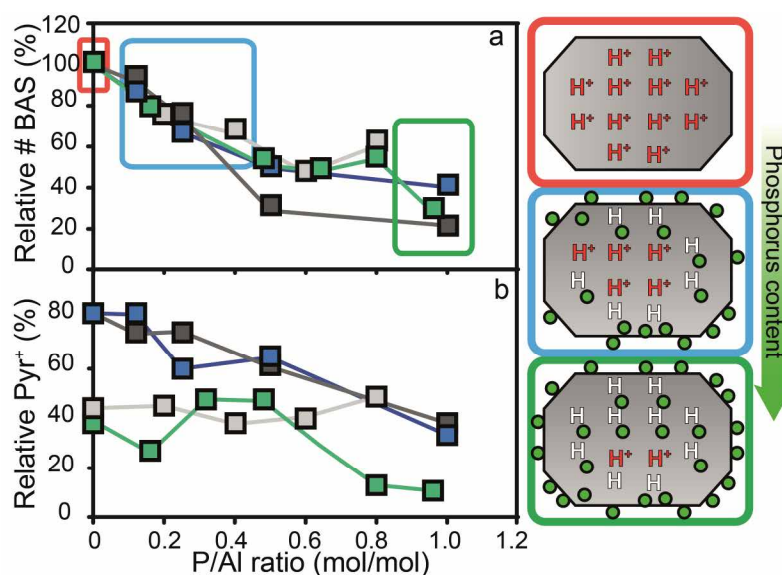

Figure 2.5 (a) Relative amount of Brønsted acid sites vs. P/Al ratio, as determined by pyridine adsorption at 150 °C. The concentration is relative to the parent material. (b) Relative acid site strength of Brønsted acid sites vs. P/Al ratio, as determined by pyridine adsorption at 150 °C and 350 °C. The percentage is the protonated pyridinium ion concentration of a sample at 350 °C, divided by the protonated pyridinium ion concentration of the same sample at 150 °C. ■ = H-ZSM-5 + NH$_4$H$_2$PO$_4$ (Si/Al = 15) ■ = H-ZSM-5 + NH$_4$H$_2$PO$_4$ (Si/Al = 25) ■ = H-ZSM-5 + H$_3$PO$_4$ (Si/Al = 25) ■ = H-ZSM-5 + NH$_4$H$_2$PO$_4$ (Si/Al = 40). Data obtained from the work of Blasco et al. [3]

2.3.4.1.4 *Effect of precursor*

As can be seen in Figure 2.6, there seems to be no correlation between the type of phosphate precursor and decrease in the number of acid sites. [3, 12-13, 28] Modification using phosphine and phosphate precursors like TMP and TMPT lead to a decrease in total acidity as well. [11, 30, 44-45] Lee et al. used TMPT, but found no differences in acid site number decrease when compared to H$_3$PO$_4$ as a precursor. [30] However, Vinek et al. reported that the phosphorus precursor that was used determines the amount of strong and weak acid sites in H-ZSM-5. When H$_3$PO$_4$ was used the decrease in the number of strong acid sites was not as severe as for TMP and TMPT. [44] The probable reason for the apparent similar effects of precursors could be the thermal treatment followed after phosphatation, which renders all precursors into phosphate species. The effect of phosphate precursor before thermal treatment will be shown in Chapter 4.
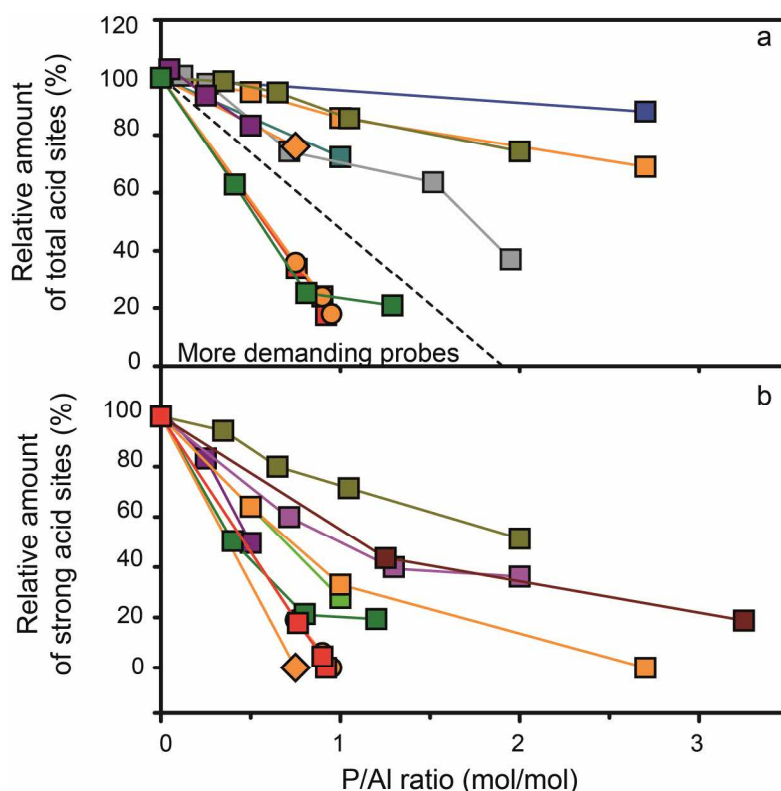
Figure 2.6 a) Relative concentration of total acid sites (%) vs. P/Al ratio. b) Relative concentration of strong acid sites (%) vs. P/Al ratio. ■ = Rumplmayr et al. [45] precursor: TMP, probe: pyridine, ■ = Vinek et al. [44] precursor: □ = H_3PO_4, ○ = TMP ◊ = TMPT, probe: pyridine ■ = Lischke et al. [1] , precursor: H_3PO_4, probe: NH_3 ■ = Tynjala et al. [11] (precursor: TMPT probe: NH_3, ■ = Jiang et al. [28] precursor: $(NH_4)H_2PO_4$, probe: NH_3 ■ = Lee et al. [30] precursor: H_3PO_4, probe: NH_3, ■ = Zhan et al. [36], precursor: H_3PO_4, probe: NH_3 ■ = Göhlich et al. [9], precursor: H_3PO_4, probe: NH_3 ■ = Caeiro et al. [2], precursor: H_3PO_4, probe: *n*-propylamine ■ = Cabral de Menezes et al. [22] (precursor: H_3PO_4, probe: *n*-propylamine ■ = Xue et al. [12] precursor: H_3PO_4, probe: NH_3

2.3.4.1.4 Causes for Brønsted acid site loss

With the exception of trimethylphosphine, which can chemisorb on acid sites, the exact interaction of phosphorus species with the acid sites is not well understood. [65] In Figure 2.7, different suggestions from the literature for acid site loss are shown.

One obvious cause of Brønsted acid site loss is dealumination induced by the thermal treatment that is performed after phosphatation. The breaking of Si-O-Al bonds and the formation of Al-OH groups have been observed after phosphatation and subsequent calcinations. [4, 11, 15, 17, 35, 38, 66] Internal silanol groups at defect sites have been reported to form with phosphorus loadings above 2.5 wt.%. [9, 11, 26] Not surprisingly, some authors therefore attribute the decrease in acid sites solely to dealumination.[1, 4, 15, 17, 35] However, Lischke and co-workers reported that a sample, which had not been calcined after phosphorus introduction showed a decrease of 60% in bridging hydroxyl groups, protonated pyridine and ammonia probe

molecules. After washing the sample retrieved almost all strong acid sites again, without any signs of permanent dealumination.[1]
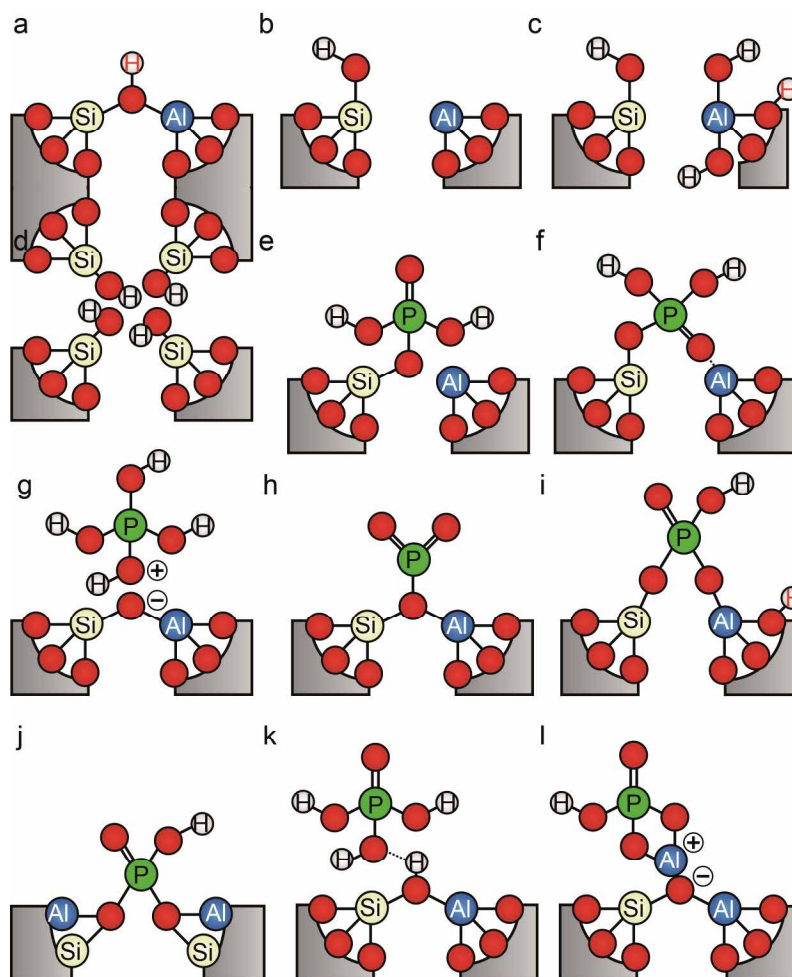

Figure 2.7 Overview of different proposed mechanisms for Brønsted acid site loss and the formation of weak acid sites by different authors. (a) parent bridging hydroxyl group. (b) Brønsted acid site loss by Si-O-Al breaking[1, 4, 10, 15, 17, 35] (c) Brønsted acid site loss by Si-O-Al breaking and formation of weak acid sites [1, 4, 10, 15, 35, 62-63] (d) Formation of weak acid sites. [10] Decrease in acid sites due to phosphorus framework interaction (e) Kaeding and Butter [5] (f) Lercher et al. [8] (g) Blasco et al. [3], (h) Rahman et al. [50] (i) Tynjala et al. [11], (j) Xue et al. [12] (k) Abubakar et al. [17] (l) Romannikov et al. [16]

Furthermore, Blasco et al. did not find indications of dealumination after a mild thermal treatment, while a decrease in the number of acid sites was reported. [3] The group of Lercher calculated that the number of Brønsted acid sites did not correspond to the amount of tetrahedrally coordinated framework aluminum (TFAl) species for phosphate and thermally treated sample. That is, there were 20% more TFAl species present than Brønsted acid sites. When the sample was mixed with alumina, these phosphorus species reacted and the 20% of

Brønsted acid sites were retrieved. [46] Blasco et al., proposed that the reversible interactions are due to the protonation of phosphoric acid into a tetrahydroxyphosphonium ion by a zeolitic Brønsted acid site.[3] However, spectroscopic evidence for these interactions is lacking and a theoretical work pointed at the unlikeliness of these species. [67] Haw and co-workers suggested that the Brønsted acid sites of the Si-OH-Al groups form a hydrogen bond with phosphoric acid.[17] Hydrogen bonded bridging hydroxyl groups after phosphorus modification have been observed with FT-IR spectroscopy and a recent DFT work showed the formation of hydrogen bonds between H_3PO_4 and the zeolite framework. [1, 68] Important to understand from the former results is that phosphorus is not only a dealuminating agent, but can reduce the number of Brønsted acid sites in a reversible way. Therefore, it is unlikely that dealumination is the sole cause of acid site loss.

2.3.4.2 *Acid site strength*

The acid site strength of zeolites is usually determined by TPD of pyridine or ammonia. [1-3, 8-13, 18-21, 25-26, 28-31, 34-39, 41, 48, 57, 66] In a few studies the acid site strength is determined by TPD of *n*-propylamine. [2, 7, 22, 38] Generally, it is reported that the average acid site strength decreases with increasing amounts of phosphorus as can be seen in Figure 2.8 a and b. These observations originate from three effects.

First of all, the maximum temperature where probe molecules are desorbed from the bridging hydroxyl groups shifts to lower temperatures with increasing phosphorus content, which indicates that these sites decrease in acid site strength. [1, 3, 8-12, 25-29, 31, 39, 44-45, 48, 57, 69] Conversely, rates of H/D exchange for propene and adsorption of acetonitrile indicated that remaining acid sites in phosphorus modified H-ZSM-5 were not altered in acid site strength. [17, 43] Second, relative more strong acid sites are affected by phosphatation than weak acid sites. The corresponding increase in weak/strong acid site ratio leads to an overall decrease in average acid site strength. [1, 9, 11, 13, 20, 26-31, 35-36, 39, 45, 69] Third, there have been reports where the amount of weak acid sites actually increases. [1, 8, 10, 12, 34, 38, 44] The formation of these new weak acid sites has been attributed to the formation of P-OH groups, hydrogen bonded Si-OH groups in silanol nests and framework incorporated phosphate species. [1, 8, 10-12]

With phosphorus weight loadings above 2 wt.% P-OH groups have been observed with FT-IR and ^{1}H MAS NMR. [3, 10, 15, 35, 43, 46, 50, 70] However, attribution of P-OH groups by ^{1}H MAS NMR is ambiguous, since different authors attribute the species to different resonances.[4, 15, 35, 43, 46, 70] It has been reported that these P-OH groups are able to protonate pyridine [3, 10] and were

attributed to phosphate anions, which replaced Brønsted acid sites [10] or P-OH groups in extra-framework $AlPO_4$. [3, 10] In contrast, Rahman et al. reported that P-OH groups have no acidic character and attributed the species to excess phosphates. [50-51] Other attributions have been P-OH groups in framework incorporated phosphate species and orthophosphoric acid. [4, 11, 15, 46]
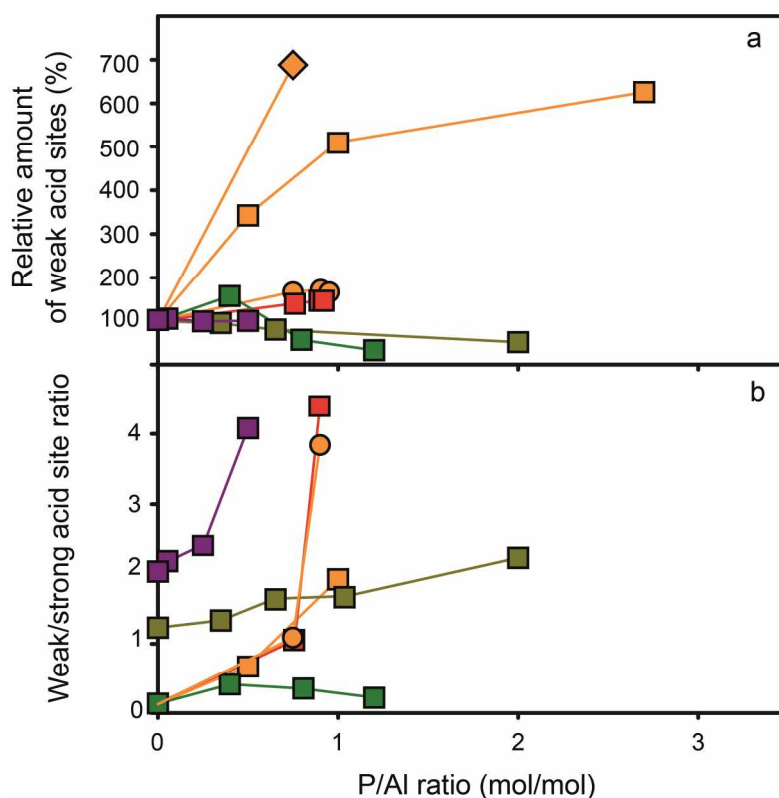

Figure 2.8 (a) Relative concentration of weak acid sites (%) vs. P/Al ratio (b) Strong/weak acid site ratio vs. P/Al ratio. Concentrations are relative to the respective parent H-ZSM-5 material. ■ = Rumplmayr et al. [45] precursor: TMP, probe: pyridine, ■ = Vinek et al. [44] precursor: □ = H_3PO_4, ○ = TMP ◊ = TMPT, probe: pyridine ■ = Jiang et al. [28] precursor: $(NH_4)H_2PO_4$, probe: NH_3 ■ = Lee et al. [30] precursor: H_3PO_4, probe: NH_3, ■ = Caeiro et al. [2], precursor: H_3PO_4, probe: *n*-propylamine

2.3.5 State and coordination of T-atoms and P-atoms

2.3.5.1 *Effect of phosphorus on framework aluminum species*

^{27}Al MAS NMR spectroscopy is the technique of choice to study the state of aluminum atoms in zeolite H-ZSM-5 and has been applied widely to assess the effect of phosphatation on aluminum sites. [1-4, 9, 12-15, 17, 21-22, 29-30, 34-35, 38-39, 46, 52, 71] A perfect zeolite crystal consists of tetrahedrally coordinated framework aluminum (TFAl) species, which have a chemical shift at 55 ppm are shown in Figure 2.9. However, another resonance that is frequently observed in H-ZSM-5 is a sharp but small peak at 0 ppm. This resonance corresponds to octahedrally coordinated Al

(OAl). There is some debate as to whether these are extra-framework Al (EFAl) species, such as $Al(H_2O)_6^{3+}$, or Al species coordinated with three oxygen atoms to the zeolite framework and to three H_2O molecules (Figure 2.9).

When phosphoric acid is introduced to H-ZSM-5 there is a gradual decrease in the TFAl resonance and a gradual increase in resonances corresponding to OAl species with increasing phosphorus content. The chemical shift of the latter shifts and broadens from 0 ppm to -5 ppm and a broad resonance around -10 ppm to -14 ppm appears (which we will refer to as -10 ppm).[1] Seo and co-workers suggested that phosphorus species react with TFAl species, resulting in aluminum species with an octahedral coordination, which appears around -10 ppm. [13] The resonance at -10 ppm can be washed out completely before and partially after thermal treatment. [1, 39] The removal of the -10 ppm peak by washing before thermal treatment leads to an increase of the resonance for TFAl species.[1]
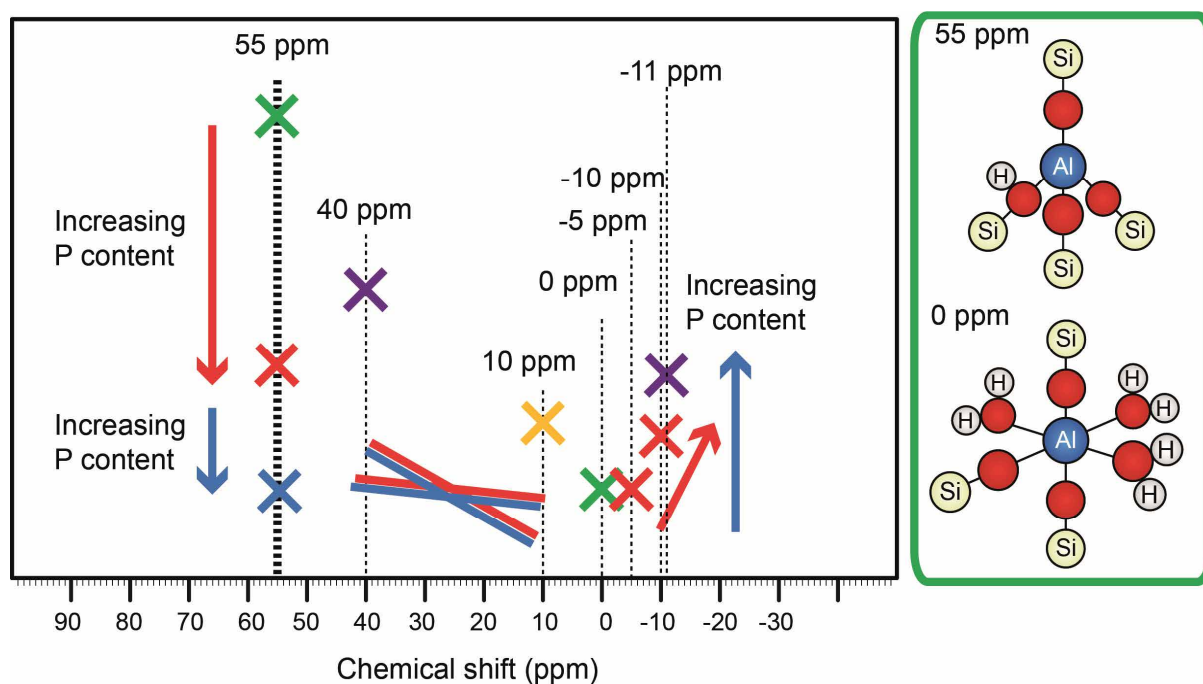
Figure 2.9 Schematic representation of the different ^{27}Al NMR signals found in the phosphated H-ZSM-5 literature: ■ = H-ZSM-5 ■ = P/H-ZSM-5 ■ = P/H-ZSM-5 hydrothermally treated ■ = AlPO₄ ■ = Suggested Al(V) interacting with P. The red arrows describe the increase or decrease in intensity of resonances during phosphatation, the blue arrow describes these effects during hydrothermal treatment.

After phosphatation and subsequential thermal treatment the reported overall effect on the ^{27}Al MAS NMR spectrum of H-ZSM-5 is similar throughout the literature. In Figure 2.9 a schematic representation of the effects is presented. After thermal treatment a broad and

asymmetrical resonance from 40 ppm to 10 ppm appears. [2-4, 12, 21-22, 27, 35, 39, 46] 2-D ^{27}Al MQ MAS NMR spectroscopy has shown that these are TFAl species in a highly distorted electronic environment. [4, 22] This distortion could arise from (i) TFAl species in an electronically distorted environment due to chemical or spatial interaction with phosphorus. [4, 14, 17, 22] Or (ii) to partially dislodged or extra-framework aluminum species formed by dealumination, due to acid treatment or thermal treatment. [72] The 40 ppm - 10 ppm resonance does not disappear after washing with hot water. [39]

With increasing amounts of phosphorus content the TFAl species gradually decrease, while the resonances at 40 ppm - 10 ppm and -10 ppm gradually increase in intensity. [3, 9, 21-22, 35, 46] Göhlich et al. reported a resonance at 10 ppm at P/Al ratio of 1.5. The peak is attributed to penta-coordinated extra-framework aluminum species interacting with phosphorus. At higher loadings the resonance disappears. [9] ^{27}Al - ^{31}P coupling experiments have shown that TFAl species (55 ppm) are not in the vicinity of P, while species found at the 40 ppm - 10 ppm and -10 ppm resonances are. [14] However, direct Al-O-P bonds by *J*-coupling NMR were not detected after thermal treatment. [14]

2.3.5.2 *Effect of phosphorus on silicon atoms*

As mentioned in section 2.3.1, the electronic environment of Si atoms is distorted due to spatial interaction with phosphorus and Si-OH groups have been suggested to interact with phosphorus species in dehydrated conditions. [4, 10-11, 13, 15, 23-25, 38, 46] However, irreversible phosphorus silicon interactions and substitutions as shown in Figure 2.7 are unlikely as the necessary Si-O-P bonds have been found to be unstable. [67, 73-76] However, there is a theoretical study where it is suggested that the substitution of penta-coordinated phosphorus into the framework is possible at high temperatures. [71] Si(1P) (Si-O-P) species for tetrahedrally coordinated Si have been observed with ^{29}Si MAS NMR and reported to be between -110 ppm and -120 ppm in silicon phosphate glasses. [77-78] Unfortunately, these ^{29}Si NMR resonances overlap somewhat with the resonances found for silicon atoms in H-ZSM-5. For [PO$_4$] tetrahedra linked to [SiO$_4$] tetrahedra ^{31}P MAS NMR chemical shifts have been reported between -44 ppm and -54 ppm in ^{31}P NMR. [78-80] However, these type of interactions correspond to phosphates coordinated to octahedral silicon, of which the ^{29}Si MAS NMR signals can be observed at even lower chemical shifts, around -215 ppm. [77, 81] These ^{29}Si resonances, attributed to octahedrally coordinated Si-O-P species have, to our best knowledge, never been reported in the phosphated H-ZSM-5 literature.

Neither have distinct resonances at -44 ppm to -54 ppm for ^{31}P NMR except for the small contribution of a resonance at -46 ppm, which will be discussed in the next section.

In an often cited paper by Xue et al., it was proposed phosphorus is incorporated in vacant framework positions in dealuminated H-ZSM-5 (See Figure 2.7 j).[12] They attributed a single ^{31}P MAS NMR -23 ppm resonance to phosphorus incorporated in the framework. However, a detailed study on phoshosilicate glasses showed that the -23 ppm resonance stems from polyphosphate species that are trapped in a siloxane framework and have no interactions with silicon species through bond.[78] The authors argued that P-OH and Si-OH groups rather self-condense than form cross-links. The only Si-O-P bonds in phosphosilicate glasses that have been unequivocally assigned by means of INEPT MAS NMR have ^{31}P MAS NMR resonances between -44 ppm and -56 ppm and ^{29}Si MAS NMR resonances at -119 ppm and -213 ppm to -215 ppm.[79]

Due to unstable character of Si-O-P bonds compared to the stable character of Al-O-P bonds and the lack of any experimental evidence, it seems very implausible that Si-O-P bonds easily form in phosphated H-ZSM-5.

2.3.5.3 Types of phosphorus species

Throughout the literature ^{31}P MAS NMR spectra published on phosphated H-ZSM-5 are very similar. [1-4, 9, 12-15, 17, 19, 21, 26, 30, 34-35, 39, 41, 46, 52, 66] For samples treated with precursors containing phosphate, PCl$_5$ and TMPT the ^{31}P MAS NMR spectra shows a very broad resonance from 0 ppm to -46 ppm with a few well distinguishable peaks. The most clear are 0 ppm, -6 ppm and -12 ppm. Their assignment is the least controversial as well. The resonance at 0 ppm corresponds to monomeric phosphates. The resonances at -6 ppm and -12 ppm are attributed to terminal phosphates in di- or polyphosphate chains and middle group phosphates in polyphosphate chains respectively. [15] Another peak that is often observed is at -40 ppm. This peak stems most likely from phosphorus pentoxide species formed during dehydration. [17] A resonance at -46 ppm is most often assigned to condensed polyphosphates. Already observed by Caro et al. dehydration of the P/H-ZSM-5 leads to the formation of condensed polyphosphates, while rehydration hydrolyses them into smaller mono-, di-, and small polyphosphate chains. [15, 17] These peaks correspond to species that have no interaction with the zeolite and the resonances 0 ppm and -6 ppm increase when phosphorus loadings are increased, in agreement with the results discussed in section 2.3.1. Lischke and co-workers showed that the peaks corresponding to smaller phosphates could easily be removed by elution with hot water. However, the condensed

polyphosphates that form after thermal treatments proved more difficult to remove by washing with hot water. [1, 14, 21, 39, 41]

Another resonance that is often observed is around -32 ppm. The resonance is generally attributed to phosphorus in (amorphous) $AlPO_4$. [2-3, 9, 15, 26, 35, 39, 46] The assignment seems to correspond with reported NMR results on $AlPO_4$ materials. [82] Moreover, these species cannot be washed out with water, which is expected of $AlPO_4$ crystals, as they are highly insoluble in water. [1, 39] CP ^{27}Al - ^{31}P HETCOR NMR showed that the phosphorus species corresponding to the -32 ppm shift are in the closest vicinity to the aluminum species represented by the broad ^{27}Al resonance at 40 ppm - 10 ppm, discussed in section 2.3.5.1. [14] Due to the highly unsymmetrical environment of aluminum atoms in the 40 ppm – 10 ppm resonance, it is unlikely that the ^{31}P MAS NMR resonance corresponds to crystalline $AlPO_4$ species.

Tetrahedral phosphate present in extra framework crystalline $AlPO_4$ can be recognized by a sharp ^{31}P resonance around -30 ppm, which will be discussed in section 2.3.7. [1, 4, 83] An overview of some of the discussed phosphorus species is presented in Figure 2.10.
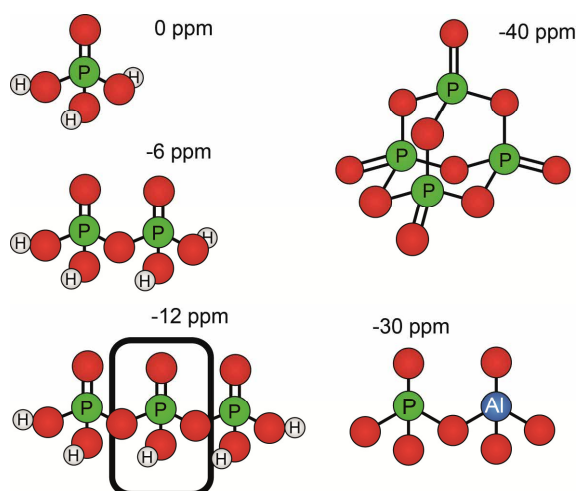
Figure 2.10 Schematic representation of a variety of phosphorus species found with ^{31}P MAS NMR. For the sake of clarity the phosphates have protons as counter cations. Assignments are based on references [4, 14-15, 17, 21].

Chapter 2

2.3.6 Hydrothermal stabilization effect of phosphorus

2.3.6.1 *Acid sites*

   2.3.6.1.1 Acid site number

Hydrothermal treatment of zeolite H-ZSM-5 promotes the expulsion of framework aluminum species from the zeolite framework. The severity of dealumination depends on the conditions of the steam treatment. Increasing steam volume, reaction temperature and steaming time leads to an increase in the amount of TFAl species that are expelled from the framework.[60]

   The removal of TFAl species leads to a loss in active sites. Hydrothermal treatment with temperatures above 750 °C and above 5 h, leads to an almost complete disappearance of the bridging hydroxyl groups in parent H-ZSM-5. [3-4] After hydrothermal treatment of phosphated H-ZSM-5 it is generally found that Brønsted acid sites are (relatively) better retained in phosphorus modified samples than in their non-phosphated counterparts. [1-4, 7, 12, 30, 39] If the steam treatment is mild in temperature or time, the total loss of acid site number is relatively lower in comparison with the non-phosphated samples. However, the absolute number of acid sites is still lower for the phosphated and then steamed samples, than for the parent and steamed samples. [1-2] This effect was also observed at high phosphorus weight loadings above 3.5 wt.% [39] and is because the phosphatation step leads to an initial decrease in acid sites as described in section 2.3.4.1.2.
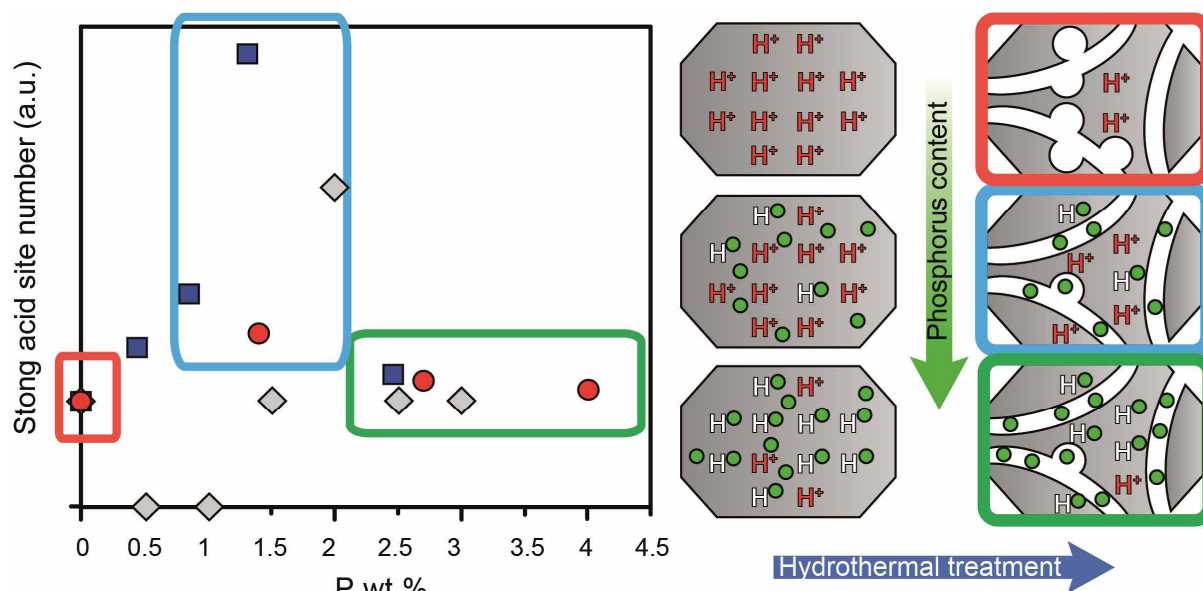
Figure 2.11 Schematic representation of the promoting effect on acid site number after hydrothermal treatment with increasing phosphorus weight loading. The number of strong acid site is normalized to the amount of acid sites for the parent material after hydrothermal treatment. ■ = Caeiro et al. [2] ■ = Lee et al. [30] ■ = Blasco et al. [3]

If the steam treatment is more severe an absolute higher number of acid sites is remaining for phosphated H-ZSM-5. [1-4, 7, 12, 30] The phosphorus content plays a role as increasingly higher loadings lead to an increasingly higher number of acid sites being retained after steaming. [3, 7] However, optimal phosphorus loadings have been reported, which lead to a maximum number of strong acid sites being retained as can be seen in Figure 2.11. [2-3, 30] The reported corresponding P/Al ratios are different, i.e. 0.5, 0.65 and 1. However, the weight loadings are somewhat more similar, i.e. 1.3 wt.%, [30] 1.4 wt.%, [2] and 2 wt.%. [3] The reason for an optimum in retained strong acid site number most likely stems from the two effects of phosphorus on H-ZSM-5, i.e. the progressed decrease in acid sites with increasing phosphorus loading on the one hand and the increase of hydrothermal stability on the other. [2] This effect is schematically drawn in Figure 2.11.

2.3.6.1.2 Acid site strength

Generally, the weak acid site number is not as much affected by steam treatment as the strong acid site number. [1-2, 7, 12, 26-27, 30] This phenomenon leads to an even stronger shift towards weaker average acid site strength. Furthermore, Lischke and co-workers showed the formation of a new weak acid site type by following the decomposition of ammonium for steamed NH_4^+ exchanged P/NH_4-H-ZSM-5 samples. Washing with hot water did not remove this new weak type of Brønsted acid site, but washing with HNO_3 could. The authors attributed the newly formed weak acid type to surface bonded phosphoric acid species, which cannot be removed by hot water washing. [1] This type of weak acid sites were confirmed in another work and also attributed to (pyro) phosphoric acid. [2]

2.3.6.1.3 Reversible decrease in acid site number after steaming

Hydrothermal treatment of H-ZSM-5 and P/H-ZSM-5 reduced strong acid sites for both samples. However, it has been found that elution of phosphorus after hydrothermal treatment leads to a recovery of strong acid sites. When a sample was phosphated and then post-steam treated at 700 °C for 0.5 h, the amount of phosphorus that could be removed from the sample by washing was 60%.[1] Before elution of P/H-ZSM-5 the number of acid sites that remained was only 13% of the parent material as was determined by NH_3 TPD. After elution the concentration of acid sites increased to 42% of the parent material. Steamed and washed P/H-ZSM-5 had 114% more strong acid sites than steamed H-ZSM-5. Other experiments on the elution of phosphorus from hydrothermally treated P/H-ZSM-5 confirmed these results. [3, 39]

Acid sites of steamed non-phosphated materials could not be retrieved after washing with NH$_4$F. [19] The retrieval of acid site number by washing is shown in Figure 2.11. In addition, Liu and co-workers found a small quantity of a new type of strong Brønsted acid site to be formed after a steam and washing step. [39] They reported that a consecutive steam treatment removed the acid site, while a following washing step caused it to reappear again.

Although the latter findings are not quite understood at the moment, an important consequence of the recovery of strong acid site number after washing is that the hydrothermal stabilization effect of phosphorus does not seem to require irreversible phosphorus aluminum interactions.

2.3.6.2 *Porosity*

When zeolite H-ZSM-5 is steam-treated, the microporous volume and surface area decrease due to dealumination. [2-3, 12, 30, 39] It is been reported that the external surface area increases after hydrothermal treatment of the parent material. [39] The (relative) decrease in micropore volume and surface area after steaming is less for phosphorus-modified samples when compared to their non-phosphated counterpart. [2-3, 30, 57] This is in line with the reducing effect that phosphorus appear to have on dealumination, as it was shown by ^{29}Si MAS NMR that less Si-O-Al bonds were broken for phosphated and steamed H-ZSM-5 than for non-phosphated samples.[4] There are reports for phosphated H-ZSM-5 with phosphorus content above 1 wt.% where the micropore volume and area increase after post-steam treatment. [3, 12, 27, 30] After hydrothermal treatment of phosphated H-ZSM-5, 94% of phosphorus could be eluted by washing with NH$_4$F. However, the amount of surface area and micropore volume only increased with below 6% [19] and no increase in surface area and micropore volume was retrieved after washing with hot water. [39] Therefore, it seems unlikely that phosphorus species are blocking pores or reducing accessibility for N$_2$ after a hydrothermal treatment.

2.3.6.3 *Effect of hydrothermal treatment on phosphorus species*

XPS measurements showed a 55% increase of phosphorus species on the surface of 2 wt.% phosphated H-ZSM-5 after steam-treatment. This would indicate that phosphorus migrates to the surface during steaming. [7] Chemical analysis has shown that 5-10% of phosphorus species disappear after hydrothermal treatment.[12] With increasing phosphorus content, the P$_{Surface}$/P$_{Bulk}$

ratio decreased for hydrothermally treated samples, i.e. with increasing phosphorus weight loadings more phosphorus was found in the bulk. [7] Unfortunately the $P_{Surface}/P_{Bulk}$ ratios before steaming were not given in the work.

After post-steam treatment the amount of smaller phosphate species decreases and the amount of more condensed polyphosphate species increases. [1-4, 12, 14, 26, 30, 39] Liu et al. observed a resonance with ^{31}P MAS NMR at -39 ppm after hydrothermal treatment. [31] This peak was reduced in intensity after a washing step, which would indicate either that the condensed species are washed out, or hydrolyzed into smaller species. [1, 17] Furthermore, during hydrothermal treatment the resonances between -30 ppm and -32 ppm mentioned in section 2.3.5.3 increase and are often the dominating peaks in the post-steamed ^{31}P MAS NMR spectra. [1-4, 12, 14, 26, 30, 39] The latter resonances are especially dominant for samples with P/Al ratios above 0.6. [1-4, 12, 14, 26, 30, 39]

2.3.6.4 *Stabilization of framework aluminum species*

During dealumination of H-ZSM-5 the removal of aluminum from the framework leads to formation of extra-framework aluminum (EFAl). [1-4, 22, 30, 39] The EFAl species migrate to the surface of the zeolite as was found by XPS. [7] It seems that after 2 h of steaming, formation of EFAl reaches a maximum and does not increase with increasing steaming time anymore. [4]

For phosphated H-ZSM-5 the decrease in the number of Si-O-Al bonds during steaming is reduced, further confirming that phosphorus stabilizes TFAl species. [1, 3-4, 27, 30] In two reports, the reduced decrease in the number of TFAl species during steam treatment for phosphated H-ZSM-5 was only relative when compared to non-phosphated H-ZSM-5 and the absolute number of TFAl species after steam treatment remained higher for the non-phosphated samples. This holds even for samples that were steamed under severe conditions. [2, 22] It was found that aluminum does not migrate to the zeolite surface during steaming with increasing amounts of phosphorus loading. [7] This indicates that phosphorus either prohibits the migration of aluminum species, or prevents dealumination.

Similar to the retrieval of acid sites, after hydrothermal treatment, the amount of TFAl species that can be recovered by elution of phosphorus is much lower than before steaming. [1] Still, a considerable amount of aluminum species can be retrieved as TFAl species. That is, after steaming P/H-ZSM-5 at mild conditions, 30% of the original amount of TFAl species remained. After washing 70% of the original amount of TFAl species could be obtained. With increasing severity of the hydrothermal treatment conditions, this amount decreases, i.e. from 15% of the

original amount of TFAl species after steaming, to 30% of the original amount of TFAl species after washing, as is shown in Figure 2.12. [1] Similar results have recently been confirmed in another work. [39]
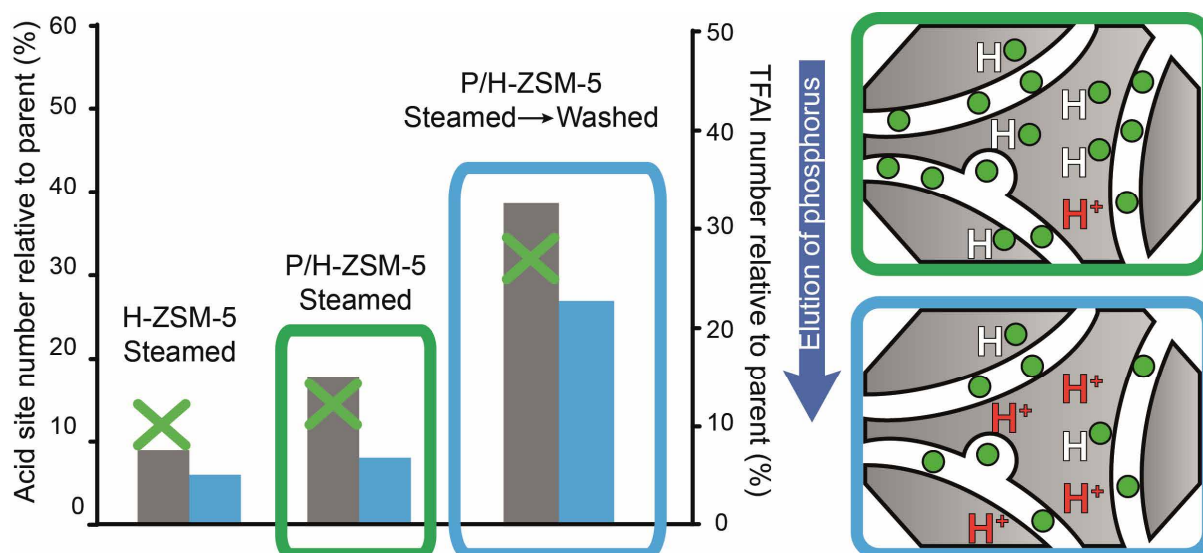

Figure 2.12 Schematic representation of the retrieval of acid site number and TFAl species by washing after hydrothermal treatment. The acid site number is a relative to the respective parent materials. Left axis (bars): Acid site number was determined using pyridine adsorption. ■ = Lischke et al. [1] (Steamed at 700 °C for 30 min. Washed using hot water) ■ = Blasco et al. [3] (Steamed at 750 °C for 5 h. Washed using NH₄F) Right axis (cross): TFAl number was determined using ^{27}Al MAS NMR. ■ = Lischke et al. (Steamed at 700 °C for 30 min. Washed using hot water) [1]

2.3.6.5 *Correlation between TFAl atoms and acid sites*

In principle the amount of strong acid sites in fully proton exchanged H-ZSM-5 should correspond directly to the amount of TFAl atoms. However, a discrepancy was reported between the number of strong acid sites observed with *n*-propylamine and the amount of TFAl species determined with ^{27}Al MAS NMR before and after steam treatment, i.e. more strong acid sites were found than one would expect from the amount of TFAl sites. [2] This would indicate that there is either another type of acid site, or the presence of acidic framework aluminum species that have a different chemical shift in ^{27}Al MAS NMR. In contrast, as was already mentioned in section 2.3.4.1.4, in other works more TFAl species were found to be present than Brønsted acid site number. [21, 46] These results were obtained before any steam treatment and showed that only after a washing step the amount of TFAl species and Brønsted acid site number correlated. [21, 46] Furthermore, it has also been reported that the amount of strong acid

sites and TFAl sites correlated quite well for P/H-ZSM-5 before hydrothermal treatment and after hydrothermal treatment.[1, 22] Therefore, it would seem that using correlations between ^{27}Al MAS NMR and probe adsorption data is not the most reliable method to make any claims about the (non-) existence of new acid sites.

2.3.6.6 *Phosphorus-framework interactions after hydrothermal treatment*

After hydrothermal treatment of phosphated H-ZSM-5 the general trend in the ^{27}Al MAS NMR is as follows: (i) tetrahedrally coordinated framework aluminum (TFAl) species (55 ppm) decrease, (ii) octahedrally aluminum (OAl) species interacting with phosphorus (-10 ppm) increases and broadens, (iii) the broad resonance of distorted framework aluminum (40 ppm to 10 ppm) is unaffected, as is illustrated in Figure 2.9. With increasing amounts of phosphorus content the resonance corresponding to distorted framework aluminum species and OAl species interacting with phosphorus become dominant, while the TFAl peak disappears. [1-4, 12, 22, 26-27, 30, 39] At phosphorus loadings above 7 wt.% a resonance at 15 ppm is reported that appears after steaming. [22] The peak position is similar to the resonance discussed in section 2.3.5.1, found by Göhlich et al. and is similarly attributed to penta-coordinated aluminum (Al_V) species interacting with phosphorus.[9] Although both groups used different P/Al ratios (3.25 and 1.95) the P loading was around 7 wt.% in both works. ^{27}Al MQ MAS NMR showed that the 15 ppm signal comes from a single species seemingly in a symmetrical environment.[22] It is not sure if these are the same species, as Göhlich and co-workers did not apply a steam treatment.

^{27}Al - ^{31}P INEPT-HETCOR NMR experiments revealed that the [27]Al MAS resonances from 40 ppm - 10 ppm, the 15 ppm, and the -10 ppm were all connected to phosphorus as Al-O-P. [14] The authors proposed that phosphorus binds with partially dislodged TFAl and OAl species that form during steam-treatment, leading to the formation of framework Si-Al-O-P bonds. This hypothesis was previously suggested by Zhuang and co-workers, based on ^{27}Al MQ MAS NMR results. [4]

2.3.7 Extra-framework aluminum-phosphate species

As mentioned in the previous section, the broad ^{27}Al MAS NMR 40 ppm - 10 ppm resonance was not as strongly affected during short steam treatments. However, for steam treatments at elevated temperatures and prolonged times this resonance disappears and the formation of a symmetrical resonance at 40 ppm appeared, attributed to an extra-framework crystalline $AlPO_4$

phase. [4, 39] Crystalline $AlPO_4$ is only formed during severe steaming conditions, as $AlPO_4$ is not observed after steaming P/H-ZSM-5 at temperatures below 760 °C for less than 2 h. [4, 14, 22] Therefore, the formation of $AlPO_4$ is gradual during steam treatment. In the case of Caeiro and co-workers, an $AlPO_4$ phase was not observed even after 20 hours of steaming phosphated H-ZSM-5 at 800 °C. [2]

The formation of an $AlPO_4$ phase also takes place when a supply of extra-framework aluminum is already present in zeolite H-ZSM-5 before phosphatation. FT-IR, ^{1}H MAS NMR and ^{27}Al MAS NMR spectroscopy has shown that EFAl species disappear when phosphorus is introduced to H-ZSM-5. [1, 3, 16, 26, 46] It has been established that extra-framework aluminum (EFAl) species that are present before phosphatation react with phosphorus and form an extra-framework $AlPO_4$ phase. [1, 3, 46] Extra-framework crystalline $AlPO_4$ has a [27]Al chemical shift of 40 ppm and amorphous aluminum orthophosphates display a broad resonance at -11 ppm, which are shown in Figure 2.9. [1, 83]

2.4 Catalysis with phosphated H-ZSM-5

In the previous sections we have shown that phosphorus affects the acidity, porosity and hydrothermal stability of H-ZSM-5. While this has a profound effect on the catalytic properties of H-ZSM-5 in a variety of catalytic processes, it is not as straightforward to directly link physicochemical effects to performance, as can be read in the following sections.

Furthermore, since catalytic conditions and materials differ in most of the literature, direct comparisons concerning performance are almost impossible to make. Therefore, all comparisons and figures in the following section are only meant to show rough trends and the reader should keep in mind that differences between e.g. reaction temperature, Si/Al ratio, crystal size and space velocity have not been taken into account.

2.4.1 Alkylation of aromatics

In early reports, phosphated H-ZSM-5 was often utilized as a Friedel-Crafts catalyst in the alkylation of aromatics. It was found that the alkylation of toluene with methanol to xylene over phosphated H-ZSM-5 was very stereo-selective for *p*-xylene. The overall conversion of toluene was 21% after phosphatation. The selectivity for *p*-xylene increased from 23% to 97%.[40] Other

works report a similar trend, where it was shown that the conversion of toluene decreased, while the selectivity for *p*-xylene increased, as can be seen in Figure 2.13 [16, 41, 44, 49, 53] This effect was also observed in the disproportionation of toluene [47] In general, the increase in selectivity was attributed to the effective reduction in pore size for channels, channel intersections and in pore openings. [40, 49, 53] The bulkier *o*- and *m*-xylenes diffuse slower out of the pores and the rapid decrease in concentration of *p*-xylenes promotes the isomerization of the former two isomers into the latter.

However, Vinek et al. suggested that the increased *para*-selectivity, besides steric constraints, could be induced by the decrease in strong acid sites in the pores, which are catalytically active in xylene isomerisation. [44] Selectivity changes induced by a decreased number of strong acid sites was also considered by other authors. [16, 20] However, a recent work reported that while the washing of phosphated H-ZSM-5 lead to a recovery of strong acid sites and increased activity, the selectivity towards *p*-xylene stayed at 95%.[41]

For the alkylation of benzene with ethanol it was found that modification with 5 wt.% phosphorus lead to a 100% selectivity towards ethylbenzene and diethylbenzene. [20] This was due to the fact that the formation of xylenes and C_9 aromatics was suppressed. It was suggested that the removal of strong acid sites, together with decreased effective pore size, reduced the secondary cracking reactions that lead to the formation of xylenes and ethyltoluenes. [20]
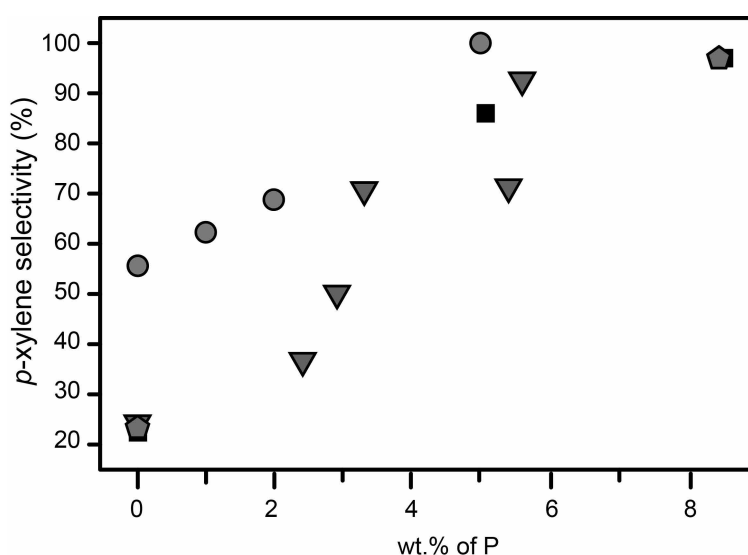
Figure 2.13 Effect of phosphorus weight loading on *p*-xylene selectivity during toluene alkylation with methanol. Pentagon = Chen et al. [7] Triangle = Young et al. [11] Square = Kaeding et al. [53] Circle = Vinek et al. [44] Differences between reaction temperature, Si/Al ratio, crystal size and space velocity have not been taken into account.

Romannikov et al. found that for H-ZSM-5 samples with strong acid sites concentrations higher than 20 μmol/g, the conversion of toluene and benzene was ruled by diffusion limitations. For lower concentrations the conversion is related to the amount of strong acid sites. [16] The selectivity for alkylation reactions in phosphorus modified H-ZSM-5 was attributed to the decrease in the number strong Brønsted acid sites, thereby reducing the isomerisation activity. However, the fact that ortho-selectivity was reduced in phosphated samples with high acid site number would indicate that steric constraints play a role as well.

2.4.2 Methanol-To-Olefins

Phosphated H-ZSM-5 has a reduced concentration of strong acid sites. When P/H-ZSM-5 was used as a catalyst in the methanol-to-olefins (MTO) process it was found that the conversion of methanol decreased. However, with increased reaction temperatures a 100% conversion could be obtained. The selectivity towards light olefins increased dramatically from 20% to 70% as the formation of aromatics was suppressed. [5] Other works reported similar results and especially the selectivity towards propylene is increased, with selectivity up to 55%, for phosphated H-ZSM-5 (Si/Al = 220). [17, 21, 31, 35, 48, 50-51] Liu et al. reported a decrease in coke formation for P/H-ZSM-5 as well. [31] As can be seen in Figure 2.14 a, the relative increase of propylene selectivity seems to increase with increasing phosphorus weight loadings. However, in Figure 2.14 b it can be observed that in case of phosphorus weight loading there appears to be an optimum in selectivity towards C_2-C_4 olefins.[43] In the work of Dyballa and co-workers it was shown that for phosphorus weight loadings above 1.5 wt.% the absolute C_2-C_4 olefins selectivity starts to decrease in comparison to samples with lower wt.% of P, accompanied with a decrease in conversion.[43] Nevertheless, the differences in reaction conditions and starting materials make it hard to find clear trends concerning phosphorus content and selectivity between the different works as can be seen in Figure 2.14.

The question arises which factors determine the performance of phosphated H-ZSM-5 in MTO, (i) the reduced acid site number, (ii) the reduced acid site strength, or (iii) the physical presence of phosphorus species, acting as a sterical impediment. The increased selectivity towards light olefins and decrease in coke formation was attributed to the decrease in strong acid site number, reducing hydride transfer and cyclisation reactions of products during diffusion.[31] Most authors attribute the increase in selectivity towards light olefins to a decrease in strong acid site number. [21, 31, 35, 48, 50-51] This was shown in the works where an increase in Si/Al ratio, and

therefore a decrease in acid site number, already lead to a significant increase in propylene selectivity. [17,31]

However, Haw and co-workers suggested that besides lower acid site number, steric factors are also a cause for the increased selectivity. It was found that propylene oligomerisation was suppressed and the authors stated that phosphorus species, under wet conditions, are an impediment to sterically demanding reactions.[17] The same was recently suggested by Dyballa et al. [43] They found a reversible increase in light olefin selectivity, which could be reverted after hot water washing and suggested phosphorus species block MFI channel intersections, hindering the formation of bulky molecules. However, from the previous sections we have learned that acid sites can also be retrieved after hot water washing, which could also be observed for this work. [43]As was mentioned in section 2.3.4.2, Haw et al. measured H/D exchange rates in propylene formation for phosphorus modified and unmodified samples, which is an indication of acid site strength, and found them to be indistinguishable. [17] Dyballa and co-workers could not observe a decrease in acid site strength using the adsorption of acetonitrile. [43] In a recent study no significant effect of acid site strength was found for the product distribution in the MTO reaction for materials with a chabazite framework. [84]
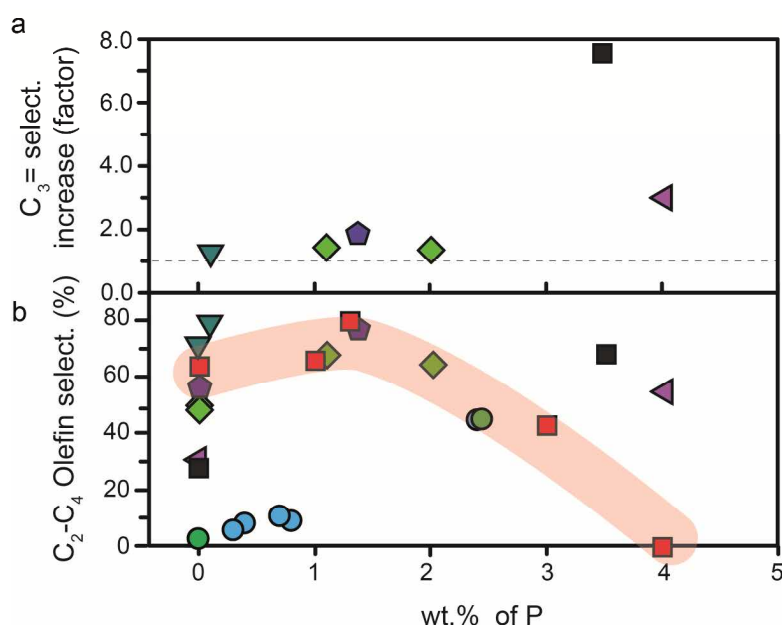
Figure 2.14 (a) Effect of phosphorus weight loading on propylene selectivity increase during the methanol-to-olefins process. The increase in propylene selectivity is relative to that of the respective parent material. (b) Actual C_2-C_4 selectivity vs. phosphorus weight loading. ■ = Kaeding et al. [5] ■ = Rahman et al. [50] ■ = Rahman et al. [51] ■ = Vedrine et al. [48] ■ = Abubakar et al. [17] ■ = Liu et al. [31] ■ = Li et al. [35] ■ = Dyballa et al. [43] The red highlight focusses on a trend on an optimum phosphorus loading reported in reference 43. Reaction temperatures are between 400 °C and 460 °C. Differences between Si/Al ratio, crystal size and space velocity have not been taken into account.

Taking the former arguments into consideration the acid site number seems to have a clear effect on the product distribution during the MTO reaction, while the role of acid site strength is less clear. Steric factors are most likely also of influence. For more information on the effect of topology on the MTH reaction we refer to a recently published review by Olsbye and co-workers. [85]
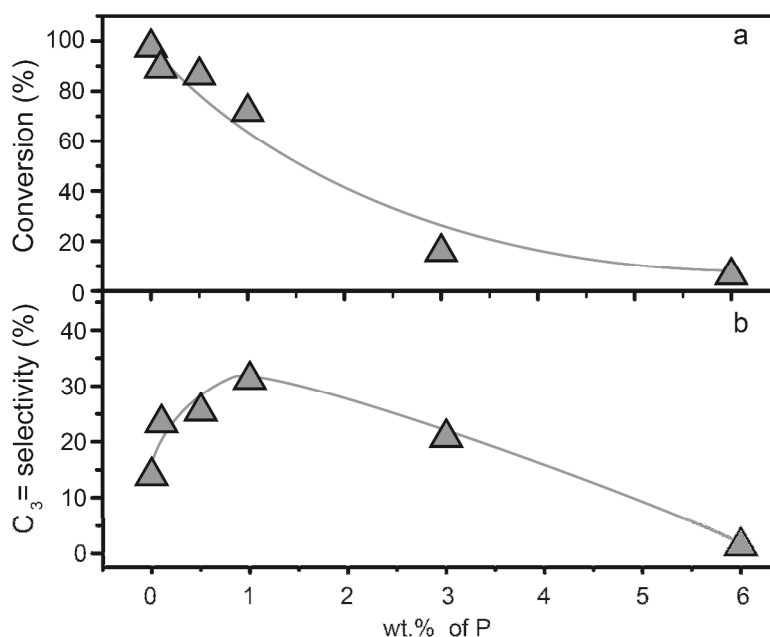

Figure 2.15 Effect of phosphorus weight loading on C_4-paraffin cracking. Effect on (a) conversion of reactant. (b) Propylene selectivity. From Jiang et al. [28] Si/Al ratio is 12.5, reaction temperature is 600 °C. Lines are not fits and meant to guide to eye.

2.4.3 Catalytic cracking reactions

2.4.3.1 *Catalytic cracking of paraffins*

Catalytic cracking of C_{4+} aliphatics requires strong acid sites. Therefore, a decrease in cracking activity for phosphated H-ZSM-5 is expected, due the reduction of the number of strong acid sites. For the catalytic cracking of paraffins, i.e. C_4-alkanes and *n*-pentane, a gradual decrease in product conversion with increasing phosphorus loadings was found. With increasing phosphorus loadings the selectivity towards C_2-C_4 olefins increased for the phosphated samples, as can be seen in Figure 2.15. [28, 51] It was suggested that the suppression of secondary reactions, due to reduced acid site number, acid site strength and the formation of basic sites, lead to the increased selectivity towards light olefins. [28]

In the case of *n*-hexane and naphta cracking, phosphatation lead to a decrease in cracking activity, accompanied by decrease in the number of strong acid sites.[2, 39, 44, 54] It was found that phosphorus modified H-ZSM-5 samples, which had no strong Brønsted acid sites, all had similar decreased conversions compared to the parent H-ZSM-5 and it was established that there was a linear correlation between strong Brønsted acid site number and cracking activity. [2, 44] Although the weak Brønsted acid sites were also found to be active in catalytic cracking, they had turn-over frequencies that were three orders of magnitude smaller than those found for strong Brønsted acid sites. [44] In the case of *n*-decane cracking, results are very similar to cracking of shorter chain hydrocarbons. Increased amounts of phosphorus content decrease the number of strong acid sites and therefore the cracking activity. [3]

Reschetilowski reported that while the strong acid site number did decrease after phosphatation, a maximum was reached with increasing amounts of phosphorus. However, the conversion of *n*-hexane did decrease gradually with increasing phosphorus content. According to these authors, this observation indicated that the acid site strength of all sites is weakened with increasing amounts of phosphorus. [54] However, Lercher and co-authors could not confirm these results. [44] Therefore, diffusion limitations caused by excess phosphorus could also play a role, as Chandawar and co-workers found a decrease in the amount of *n*-hexane that could be adsorbed with increasing phosphorus content. [20]

The direct link between a decrease in strong acid sites and a decrease in cracking activity is not as straightforward after hydrothermal treatment. Samples with high phosphorus weight loadings and a higher strong acid site number determined by pyridine adsorption after hydrothermal treatment, were not as active in the cracking of *n*-decane than samples with lower phosphorus weight loadings and lower or equal acid site number. [3] Furthermore, it was found that steamed parent H-ZSM-5 had a higher number of Brønsted acid sites, while steamed phosphated H-ZSM-5 had a lower amount. However, the cracking activity for the latter sample was higher. [2] As the authors explained it, other factors such as acid site distribution, accessibility and limitations in coke formation would play a role. The authors also observed hexane cracking activity for a severely steamed sample with a high loading of phosphorus. It was suggested that despite the lack of TFAl species there is still cracking activity and therefore other Al sites must be responsible. However, from their ^{27}Al MAS NMR spectra it can be observed that a small amount of TFAl species is still present. Consequently, the cracking activity for the reported sample was very low. [18]
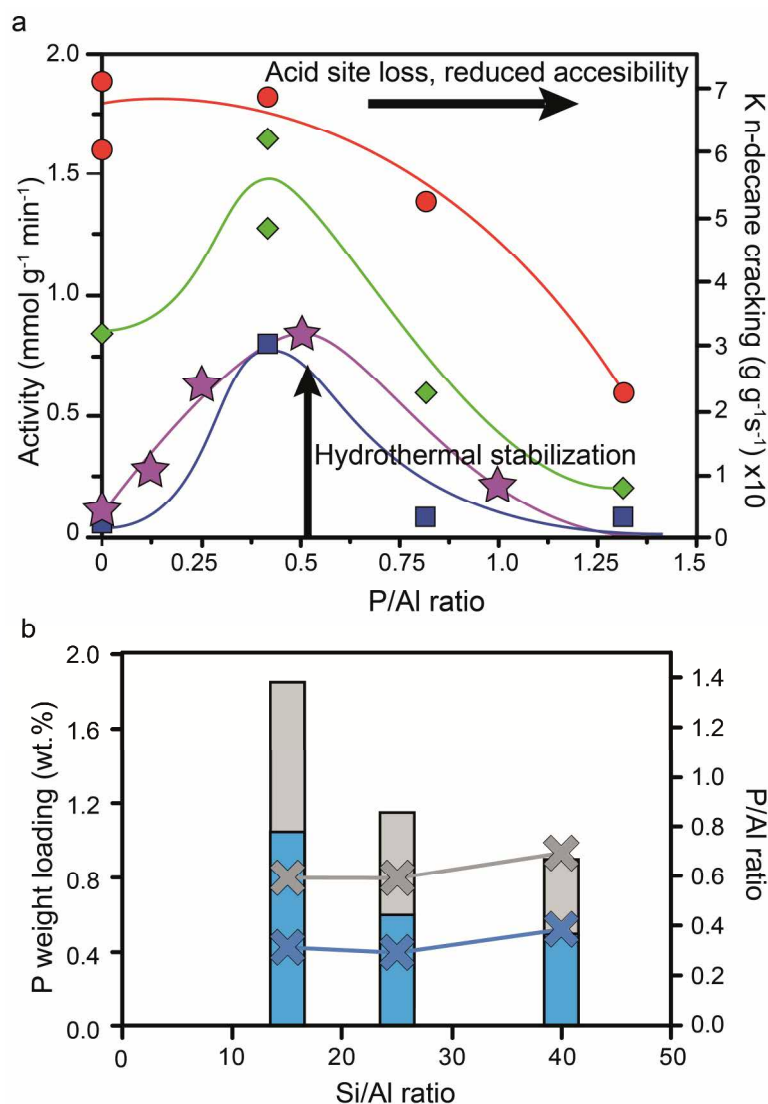
Figure 2.16 (a) Effect of phosphorus and post steam treatment on the cracking of *n*-hexane [2] (left axis) and *n*-decane [3] (right axis) by H-ZSM-5. Adapted from reference 2. Activity is plotted against phosphorus weight loading (H$_3$PO$_4$ precursor). Left axis [2]: ■ = H-ZSM-5 (Si/Al = 13). ■ = H-ZSM-5 steamed at 800 °C for 5 h. ■ = H-ZSM-5 steamed at 800 °C for 20 h. Reaction temperature is 500 °C. Right axis [3]: ■ = H-ZSM-5 (Si/Al = 25) steamed at 750 °C for 5 h. Reaction temperature is 500 °C. Lines are not fits and meant to guide to eye. (b) ■ = Optimal average cumulative catalytic conversion during naphta cracking with additional H$_2$O in the feed at 650 °C after 1 h for H-ZSM-5 with different Si/Al ratios vs P weight loadings and P/Al ratios (NH$_4$H$_2$PO$_4$ precursor) .[42] ■ = Optimal first order kinetic rate constants in *n*-decane cracking of H-ZSM-5 steamed at 750 °C for 5 h. [3] Left axis in bars: Phosphorus weight loading. Right axis as crosses with lines: P/Al ratio

After hydrothermal treatment, phosphorus modified samples with a reported optimum for P/Al ratios of 0.4-0.7 had higher paraffin cracking activity, as is shown in Figure 2.16 a and b. [2-3, 42] Similar to the MTO reaction, samples that were eluted of phosphorus regained strong acid sites and consequently the cracking activity increased. [3, 39] When *n*-hexane cracking was performed under hydrothermal conditions, phosphated H-ZSM-5 with P/Al ratio of 1.1 retained the highest activity with time-on-stream.[19] The authors found furthermore that elevated

calcination temperatures after phosphatation lead to improved stability, as the activity with time-on-stream was better retained with increasing calcination temperatures up to 750 °C. [19]

It was found that selectivity towards light olefins decreased for hydrothermally treated phosphorus modified samples. [3] However, with prolonged steam treatments (20 h), phosphated samples produced a higher yield of light olefins than non-phosphated samples.[2] Furthermore it was established that six-coordinated aluminum species bonded to phosphorus (Al6-O-P) were not active in cracking during the FCC process.[14]

The observed optimum in phosphorus weight loading vs. cracking activity for hydrothermally treated phosphated H-ZSM-5 zeolites has been explained as follows: Phosphatation of H-ZSM-5 leads to pore-blockage, reduced accessibility and acid site number, which is amplified with increasing phosphorus loadings. Therefore, a decrease in cracking activity is expected with increasing phosphorus content. However, after steaming the promotion of hydrothermal stability by phosphorus comes into effect. Therefore, when comparing a steamed H-ZSM-5 sample with a steamed phosphated H-ZSM-5 sample, the latter performs better in cracking, especially after more severe steaming conditions have been applied. This effect is surpassed when the phosphorus loading become very high, as then the negative effects of acid site loss and reduced accessibility starts to dominate again. [2]

Corma and co-workers have reported that the optimum of phosphorus weight loading differed for H-ZSM-5 with different Si/Al ratios during naphta and *n*-decane cracking and therefore depended on P/Al ratio. [3, 42] The optimization effect of phosphorus loading is increasing with longer steaming times or longer time-on-stream. [2, 42]

2.4.3.2 *Catalytic cracking of olefins*

Experiments on the catalytic cracking of C_4-olefins have also been performed. [12, 18, 26, 32, 57] It was found that with increasing phosphorus content the cracking conversion decreased and the selectivity towards propylene increased, as can be seen in Figure 2.17. [12, 17, 26, 32] As with paraffin cracking, most authors suggested that the reduced acid site number and strength, lead to the suppression of secondary reactions, which increased selectivity towards propylene. [12, 32, 57] As can be seen in Figure 2.17 b, the selectivity towards propylene decrease after phosphorus weight loadings above 2 wt.%. Lin et al. proposed that the reduction in average acid site strength plays an important role, as strong acid sites favor another reaction pathway than weak acid sites, leading to higher propylene yields. [17]
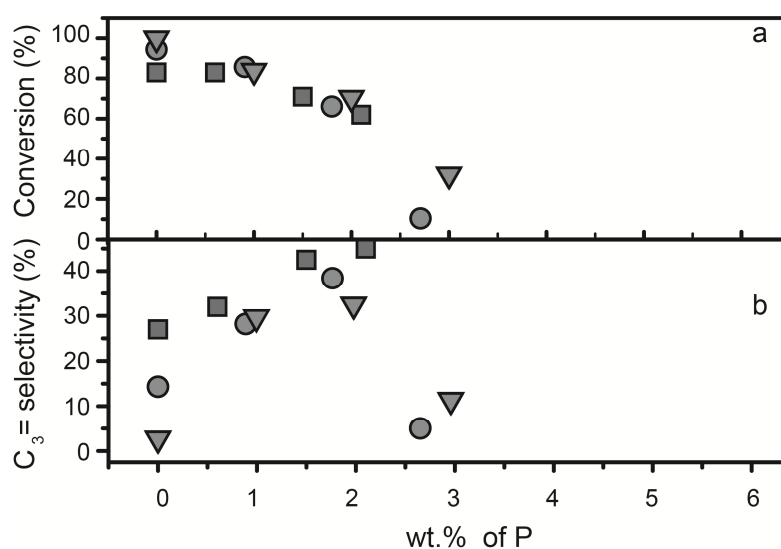
Figure 2.17 Effect of phosphorus weight loading before hydrothermal treatment on (a) conversion of reactant. (b) Propylene selectivity during the C₄-olefin cracking. Square = Zhao et al. [26] Circle = Xue et al. [12] Triangle = Xue et al. [32] Differences between reaction temperature, Si/Al ratio, crystal size and space velocity have not been taken into account.

An exception was the work by Gao and co-workers, who did observe a decrease in strong acid sites, a higher selectivity towards propylene, but also an increased conversion for phosphated samples. A possible reason for these contradicting results could be the hydrothermal dispersion method applied by the authors to introduce phosphorus. [57]

After hydrothermal treatment phosphated samples had increased or maintained conversions, while conversions for non-phosphated samples decreased. [12, 26, 32] E.g. the cracking activity increased from 10.4% before to 53.1% after steaming for a sample with 2.2 wt.% of phosphorus. [12] This result would indicate that the accessibility of the zeolite improves after steam treatment. The propylene selectivity also improved after hydrothermal treatment. [12, 32] As with paraffin cracking, optimal phosphorus loadings have been reported for the highest conversion (0.7-1.0 wt.% P) [12, 57] and propylene selectivity, which were 1 wt.% [32] and 1.68 wt.% [12] after hydrothermal treatment. Most likely, the continued reduction in acid site number and acid site strength after hydrothermal treatment, as discussed in section 2.3.6.1, is the cause for the increased selectivity towards propylene.

It was found that phosphated samples had a higher stability with longer time-on-stream as coking was reduced and dealumination was prevented. [26] This was attributed to the reduced average acid site strength of the phosphated samples and the stabilizing effect that phosphorus

has on TFAl species. Since the sustained catalytic activity of P/H-ZSM-5 coincided with the formation of partially dislodged aluminum sites, the authors suggested that these species are still active in the cracking of C_4-olefins. [26] Xue and co-workers attributed the remaining activity during cracking after thermal treatment also to newly formed acid sites, due to phosphorus framework interactions. [12] However, more conclusive evidence for such statements is required.

2.4.4 Dehydration of ethanol and ethanol to propylene

By using phosphorus, H-ZSM-5 can be optimized to produce either (i) ethylene or (ii) propylene. [29, 34, 36-38, 86] The selectivity towards one of the two products depends on phosphorus loading and the reaction temperature. After phosphatation of H-ZSM-5 the conversion of ethanol into ethylene by dehydration decreases at lower temperatures. [29, 34, 36, 38] The selectivity towards ethylene increases with increasing phosphorus content and reaction temperature, as shown in Figure 2.18. [29, 34, 36-38, 86] If all strong acid sites are removed, at weight loadings above 3 wt.% the selectivity towards ethylene reaches 99.4% as only dehydration takes place. [29, 34, 36-38]

If the catalyst still contains a small amount of strong Brønsted acid sites, higher hydrocarbons are also detected. At weight loadings of 1.3-1.9 wt.% P the selectivity towards propylene has been reported to obtain a maximum and can reach up to 33% at temperatures between 400 °C and 500 °C. [34, 37-38, 86] Propylene selectivity is maintained with time-on-stream, while parent H-ZSM-5 gradually loses selectivity.[37]
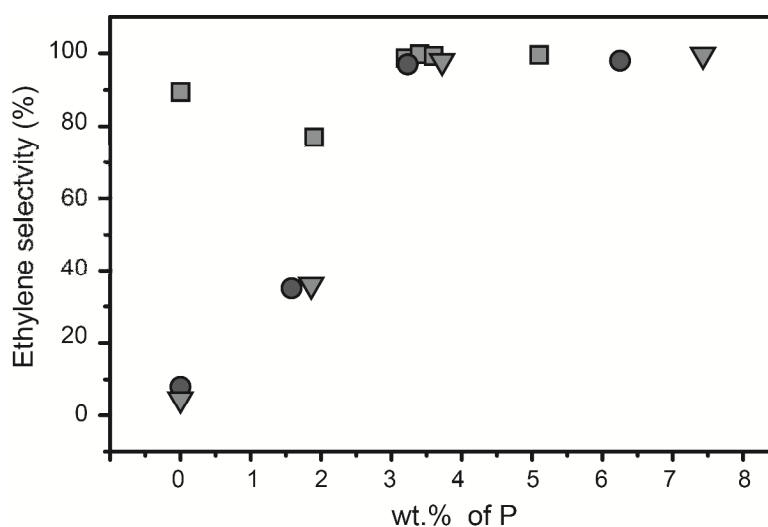
Figure 2.18 Effect of phosphorus weight loading on ethylene selectivity at temperatures above 400 °C Square = Zhang et al.[29] Circle =Ramesh et al.[34] Triangle = Ramesh et al.[38] Differences between reaction temperature, Si/Al ratio, crystal size and space velocity have not been taken into account.

Besides hydrothermal stabilization, the formation of coke is reduced as well. [29, 34, 37-38] This is attributed to the weak acid sites that are formed after phosphatation. The weak acid sites are unable to catalyze the formation of higher hydrocarbons. [29, 34, 38]

2.5 Conclusions

The study and comparison of the existing literature on phosphorus modification of H-ZSM-5 has revealed many universal physicochemical effects that take place. One of the most important realizations should be that most structural changes induced by phosphorus, which influence the catalytic performance of H-ZSM-5, are at least partially reversible.

During the phosphatation process of zeolite H-ZSM-5, phosphorus species deposit on the external surface before entering the zeolite channels. Phosphorus enters the zeolite channels with increasing loadings, but diffusion limitations lead to a distribution gradient, with a higher concentration of phosphorus at the outer surface. With weight loadings above 5 wt.% of phosphorus, the formation of large polyphosphates on or near the external surface are observed. Phosphorus species do not cause severe pore blockage at average phosphorus loadings (P above 2 wt%). However, treatment with phosphorus always leads to decreased surface area and micropore volume. This decrease is amplified with increasing phosphorus content.

Excess phosphorus is present as ortho,- pyro,- and polyphosphates. With increasing phosphorus content the amount of excess phosphorus increases. Excess phosphorus dehydrates at high temperatures forming condensed polyphosphates. This effect is reversible. Rehydration leads to the formation of smaller phosphate species. Phosphorus species that are not interacting with the zeolite framework can be easily eluted by hot water washing.

Introduction of phosphorus leads to the reduction of strong acid sites. This reduction increases with increasing amounts of phosphorus. The reduction in acid sites has three origins. Before thermal treatment the reduction of acid sites is caused by (i) fully reversible phosphorus-framework interactions. After thermal treatment there is an irreversible loss of acid sites, which is caused by (ii) dealumination and possibly by (iii) irreversible interaction of phosphorus with framework aluminum. The choice of phosphorus precursor does not have a strong influence on the final modification effects after thermal treatment.

Besides a reduction in the number of acid sites, there is also a decreases in the average acid site strength after phosphatation. Increasing phosphorus content leads to a further decrease in

average acid site strength. There are three causes for the observed decrease in average site strength. (i) A decrease in the acid site strength of bridging hydroxyl groups. (ii) Relative more strong acid sites are decreased by phosphatation than weak acid sites. (iii) An actual increase in the number of weak acid sites. Possible candidates for these new weak acid sites are silanol nests, extra-framework aluminum species and P-OH groups. The question how the average acid site strength is reduced and what the source of new weak acid sites is, is not understood at this moment.

Phosphorus has a promoting effect on the hydrothermal stability of H-ZSM-5. During hydrothermal treatment (i) less Si-O-Al bonds are broken, (ii) more micropore volume is retained (iii) relatively or absolutely more strong acid sites are retained and (iv) the amount of tetrahedrally coordinated framework (TFAl) atoms that are expelled from the framework are either relatively or absolutely less than in non-phosphated samples. The exact origin of this effect is unknown and requires further investigation. However, studies have shown that an irreversible phosphorus-aluminum interaction is not required for acid site and TFAl stabilization. After washing with hot water, more acid sites and TFAl species can be retrieved. Prolonged hydrothermal treatment of phosphated H-ZSM-5 eventually leads to formation of an extra-framework $AlPO_4$ phase.

The decrease in strong Brønsted acid site number and the increase in weak Brønsted acid sites or weak/strong acid site ratio have most often been attributed as the origin for most performance changes in catalytic reactions such as hydrocarbon cracking, methanol-to-olefins, dehydration of ethanol and alkylation of aromatics. Reactions that demand strong acid sites show a reduced conversion with increasing amounts of phosphorus content. Often, applying higher reaction temperatures increases the overall catalytic conversion. The decrease in acid site number and average acid site strength, leads to a reduction of secondary reactions, such as hydride transfer, cracking and cyclization reactions. This prevents oligomerization of light olefins, coke formation as well as the cracking of products. Besides chemical alterations, the introduction of phosphorus into the zeolite channel leads to decreased pore dimensions and reduced accessibility, which in turn lead to longer diffusion pathways for reactants and products. Therefore, there is an increased selectivity towards products that diffuse fast out of the zeolite. Phosphorus species deposited in the pores act as steric impediments and are expected to hinder the formation of bulky (intermediate) products. All these physicochemical effects change the activity and selectivity of phosphated H-ZSM-5. Consequently, phosphorus-modified samples have a higher selectivity towards light olefins and retain higher activities with time-on-stream

compared to their non-phosphated counterparts, due to reduced coke formation and improved hydrothermal stability.

We can conclude this Chapter with the notion that after more than 30 years of research on phosphated H-ZSM-5, it is still not completely understood if and how phosphorus interacts with the framework. Nevertheless, it is clear that there is an attraction between phosphorus and aluminum and that the formation of stable Si-O-P bonds is very unlikely. The role of phosphorus on acid site loss and the possible formation of newly formed weak acid sites is not elucidated, while the actual origin of the promoting effect of phosphorus on the hydrothermal stability is even more elusive. In the following Chapters of this dissertation we will study these intriguing phenomena.

References

[1]   G. Lischke, R. Eckelt, H. G. Jerschkewitz, B. Parlitz, E. Schreier, W. Storek, B. Zibrowius and G. Öhlmann, *J. Catal.* **1991**, *132*, 229-243.

[2]   G. Caeiro, P. Magnoux, J. M. Lopes, F. R. Ribeiro, S. M. C. Menezes, A. F. Costa and H. S. Cerqueira, *Appl. Catal. A-Gen* **2006**, *314*, 160-171.

[3]   T. Blasco, A. Corma and J. Martínez-Triguero, *J. Catal.* **2006**, *237*, 267-277.

[4]   J. Zhuang, D. Ma, G. Yang, Z. Yan, X. Liu, X. Liu, X. Han, X. Bao, P. Xie and Z. Liu, *J. Catal.* **2004**, *228*, 234-242.

[5]   W. W. Kaeding and S. A. Butter, *J. Catal.* **1980**, *61*, 155-164.

[6]   G. Yang, J. Zhuang, Y. Wang, D. Zhou, M. Yang, X. Liu, X. Han and X. Bao, *J. Mol. Struc.* **2005**, *737*, 271-276.

[7]   M. J. B. Cardoso, D. D. O. Rosas and L. Y. Lau, *Adsorption* **2005**, *11*, 577-580.

[8]   J. A. Lercher and G. Rumplmayr, *Appl. Catal.* **1986**, *25*, 215-222.

[9]   M. Göhlich, W. Reschetilowski and S. Paasch, *Micropor. Mesopor. Mater.* **2011**, *142*, 178-183.

[10]   A. Jentys, G. Rumplmayr and J. A. Lercher, *Appl. Catal.* **1989**, *53*, 299-312.

[11]   P. Tynjälä, T. T. Pakkanen and S. Mustamaki, *J. Phys. Chem. B* **1998**, *102*, 5280-5286.

[12]   N. Xue, X. Chen, L. Nie, X. Guo, W. Ding, Y. Chen, M. Gu and Z. Xie, *J. Catal.* **2007**, *248*, 20-28.

[13]   G. Seo and R. Ryoo, *J. Catal.* **1990**, *124*, 224-230.

[14]   K. Damodaran, J. W. Wiench, S. M. Cabral de Menezes, Y. L. Lam, J. Trebosc, J. P. Amoureux and M. Pruski, *Micropor. Mesopor. Mater.* **2006**, *95*, 296-305.

[15]   J. Caro, M. Bülow, M. Derewinski, J. Haber, M. Hunger, J. Kärger, H. Pfeifer, W. Storek and B. Zibrowius, *J. Catal.* **1990**, *124*, 367-375.

[16]   V. N. Romannikov, A. J. Tissler and R. Thome, *React. Kinet. Catal. Lett.* **1993**, *51*, 125-134.

[17]   S. M. Abubakar, D. M. Marcus, J. C. Lee, J. O. Ehresmann, C. Y. Chen, P. W. Kletnieks, D. R. Guenther, M. J. Hayman, M. Pavlova, J. B. Nicholas and J. F. Haw, *Langmuir* **2006**, *22*, 4846-4852.

[18]   L. Lin, C. Qiu, Z. Zhuo, D. Zhang, S. Zhao, H. Wu, Y. Liu and M. He, *J. Catal.* **2014**, *309*, 136-145.

[19]   A. Yamaguchi, D. Jin, T. Ikeda, K. Sato, N. Hiyoshi, T. Hanaoka, F. Mizukami and M. Shirai, *Catal. Lett.* **2014**, *144*, 44-49.

[20]   K. H. Chandawar, S. B. Kulkarni and P. Ratnasamy, *Appl. Catal.* **1982**, *4*, 287-295.

[21]   M. Derewinski, P. Sarv, X. Sun, S. Müller, A. C. van Veen and J. A. Lercher, *J. Phys. Chem. C* **2014**, *118*, 6122-6131.

[22]   S. M. Cabral de Menezes, Y. L. Lam, K. Damodaran and M. Pruski, *Micropor. Mesopor. Mater.* **2006**, *95*, 286-295.

[23]   M. Ghiaci, A. Abbaspur, M. Arshadi and B. Aghabarari, *Appl. Catal. A-Gen* **2007**, *316*, 32-46.

[24]   M. Ghiaci, A. Abbaspur and R. J. Kalbasi, *Appl. Catal. A-Gen* **2006**, *298*, 32-39.

[25]   R. J. Kalbasi, M. Ghiaci and A. R. Massah, *Appl. Catal. A-Gen* **2009**, *353*, 1-8.

[26]   G. Zhao, J. Teng, Z. Xie, W. Jin, W. Yang, Q. Chen and Y. Tang, *J. Catal.* **2007**, *248*, 29-37.

[27]   R. Lü, Z. Cao and X. Liu, *J. Nat. Gas Chem.* **2008**, *17*, 142-148.

[28]   G. Jiang, L. Zhang, Z. Zhao, X. Zhou, A. Duan, C. Xu and J. Gao, *Appl. Catal. A-Gen* **2008**, *340*, 176-182.

[29]   D. Zhang, R. Wang and X. Yang, *Catal. Lett.* **2008**, *124*, 384-391.

[30]   Y.-J. Lee, J. M. Kim, J. W. Bae, C.-H. Shin and K.-W. Jun, *Fuel* **2009**, *88*, 1915-1921.

[31]   J. Liu, C. Zhang, Z. Shen, W. Hua, Y. Tang, W. Shen, Y. Yue and H. Xu, *Catal. Commun.* **2009**, *10*, 1506-1509.

[32]   N. Xue, L. Nie, D. Fang, X. Guo, J. Shen, W. Ding and Y. Chen, *Appl. Catal. A-Gen* **2009**, *352*, 87-94.

[33]   Z. Wang, G. Jiang, Z. Zhao, X. Feng, A. Duan, J. Liu, C. Xu and J. Gao, *Energ. Fuel* **2009**, *24*, 758-763.

[34]   K. Ramesh, L. M. Hui, Y.-F. Han and A. Borgna, *Catal. Commun.* **2009**, *10*, 567-571.

[35]   P. Li, W. Zhang, X. Han and X. Bao, *Catal. Lett.* **2010**, *134*, 124-130.

[36]   N. Zhan, Y. Hu, H. Li, D. Yu, Y. Han and H. Huang, *Catal. Commun.* **2010**, *11*, 633-637.

[37]   Z. Song, A. Takahashi, I. Nakamura and T. Fujitani, *Appl. Catal. A-Gen* **2010**, *384*, 201-205.

[38]   K. Ramesh, C. Jie, Y.-F. Han and A. Borgna, *Ind. Eng. Chem. Res.* **2011**, *49*, 4080-4090.

[39]   D. Liu, W. C. Choi, C. W. Lee, N. Y. Kang, Y. J. Lee, C.-H. Shin and Y. K. Park, *Catal. Today* **2011**, *164*, 154-157.

[40]   N. Y. Chen, W. W. Kaeding and F. G. Dwyer, *J. Am. Chem. Soc.* **1979**, *101*, 6783-6784.

[41]   H. L. Janardhan, G. V. Shanbhag and A. B. Halgeri, *Appl. Catal. A-Gen* **2014**, *471*, 12-18.

[42]   A. Corma, J. Mengual and P. J. Miguel, *Appl. Catal. A-Gen* **2012**, *421*, 121-134.

[43]   M. Dyballa, E. Klemm, J. Weitkamp and M. Hunger, *Chem. Ing. Tech.* **2013**, *85*, 1719-1725.

[44]   H. Vinek, G. Rumplmayr and J. A. Lercher, *J. Catal.* **1989**, *115*, 291-300.

[45]   G. Rumplmayr and J. A. Lercher, *Zeolites* **1990**, *10*, 283-287.

[46]   N. Xue, R. Olindo and J. A. Lercher, *J. Phys. Chem. C* **2010**, *114*, 15763-15770.

[47]   W. W. Kaeding, C. Chu, L. B. Young and S. A. Butter, *J. Catal.* **1981**, *69*, 392-398.

[48]   J. C. Védrine, A. Auroux, P. Dejaifve, V. Ducarme, H. Hoser and S. Zhou, *J. Catal.* **1982**, *73*, 147-160.

[49]   J. Nunan, J. Cronin and J. Cunningham, *J. Catal.* **1984**, *87*, 77-85.

[50]   A. Rahman, G. Lemay, A. Adnot and S. Kaliaguine, *J. Catal.* **1988**, *112*, 453-463.

[51]   A. Rahman, A. Adnot, G. Lemay, S. Kaliaguine and G. Jean, *Appl. Catal.* **1989**, *50*, 131-147.

[52]   M. Kojima, F. Lefebvre and Y. Ben Taârit, *Zeolites* **1992**, *12*, 724-727.

[53]   W. W. Kaeding, C. Chu, L. B. Young, B. Weinstein and S. A. Butter, *J. Catal.* **1981**, *67*, 159-174.

[54]   W. Reschetilowski, B. Meier, M. Hunger, B. Unger and K. P. Wendlandt, *Angew. Chem. Int. Ed.* **1991**, *30*, 686-687.

[55]   B. Viswanathan and A. C. Pulikottil, *Catal. Lett.* **1993**, *22*, 373-379.

[56]   X. Gao, Z. Tang, D. Ji and H. Zhang, *Catal. Commun.* **2009**, *10*, 1787-1790.

[57]   X. Gao, Z. Tang, H. Zhang, C. Liu, Z. Zhang, G. Lu and D. Ji, *Kor. J. Chem. Eng.* **2010**, *27*, 812-815.

[58]   J. Klinowski, *Prog. Nucl. Mag. Res. Sp.* **1984**, *16*, 237-309.

[59]   M. Hunger in *Catalytically active sites: generation and characterization*, *Vol. 2* Wiley-VCH: Weinheim, **2010**, pp. 493-546.

[60]   S. M. Campbell, D. M. Bibby, J. M. Coddington, R. F. Howe and R. H. Meinhold, *J. Catal.* **1996**, *161*, 338-349.

[61]   S. Malola, S. Svelle, F. L. Bleken and O. Swang, *Angew. Chem. Int. Ed.* **2012**, *51*, 652-655.

[62]   T. Fjermestad, S. Svelle and O. Swang, *J. Phys. Chem. C* **2013**, *117*, 13442-13451.

[63]   E. Loeffler, U. Lohse, C. Peuker, G. Oehlmann, L. M. Kustov, V. L. Zholobenko and V. B. Kazansky, *Zeolites* **1990**, *10*, 266-271.

[64]   J. A. van Bokhoven, A. M. J. van der Eerden and D. C. Koningsberger, *J. Am. Chem. Soc.* **2003**, *125*, 7435-7442.

[65]   W. P. Rothwell, W. X. Shen and J. H. Lunsford, *J. Am. Chem. Soc.* **1984**, *106*, 2452-2453.

[66]   B. Zhao, H. Pan and J. H. Lunsford, *Langmuir* **1999**, *15*, 2761-2765.

[67]   R. Lü, Z. Cao and S. Wang, *J. Mol. Struc.-THEOCHEM* **2008**, *865*, 1-7.

[68]   Y. Huang, X. Dong, M. Li, M. Zhang and Y. Yu, *R. Soc. Chem. Adv.* **2014**, *4*, 14573-14581.

[69]   Z. Song, A. Takahashi, I. Nakamura and T. Fujitani, *Appl. Catal. A-Gen* **2011**, *384*, 201-205.

[70]   P. Tynjälä and T. T. Pakkanen, *Micropor. Mesopor. Mater.* **1998**, *20*, 363-369.

[71]   Z. Liu, Z.-X. Chen, W. Ding, G.-J. Kang and Z. Li, *J. Mol. Struc.-THEOCHEM* **2010**, *948*, 99-101.

[72]   A. Samoson, E. Lippmaa, G. Engelhardt, U. Lohse and H. G. Jerschkewitz, *Chem. Phys. Lett.* **1987**, *134*, 589-592.

[73]   G. Sastre, D. W. Lewis and C. R. A. Catlow, *J. Phys. Chem.* **1996**, *100*, 6722-6730.

[74]   D. Barthomeuf, *Zeolites* **1994**, *14*, 394-401.

[75]   J. Tan, Z. Liu, X. Bao, X. Liu, X. Han, C. He and R. Zhai, *Micropor. Mesopor. Mater.* **2002**, *53*, 97-108.

[76]   S. L. Suib, A. M. Winiecki and A. Kostapapas, *Langmuir* **1987**, *3*, 483-488.

[77]   S. P. Szu, L. C. Klein and M. Greenblatt, *J. Non-Cryst. Solids* **1992**, *143*, 21-30.

[78]   N. J. Clayden, S. Esposito, P. Pernice and A. Aronne, *J. Mater. Chem.* **2001**, *11*, 936-943.

[79]   C. Coelho, T. Azaïs, L. Bonhomme-Coury, G. Laurent and C. Bonhomme, *Inorg. Chem.* **2007**, *46*, 1379-1387.

[80]   I. L. Mudrakovskii, V. M. Mastikhin, V. P. Shmachkova and N. S. Kotsarenko, *Chem. Phys. Lett.* **1985**, *120*, 424-426.

[81]   T. L. Weeding, B. H. W. S. de Jong, W. S. Veeman and B. G. Aitken, *Nature* **1985**, *318*, 352-353.

[82]   E. C. de Oliveira Lima, J. M. Moita Neto, F. Y. Fujiwara and F. Galembeck, *J. Colloid Interface Sci.* **1995**, *176*, 388-396.

[83]   A. Corma, V. Fornes, W. Kolodziejski and L. J. Martineztriguero, *J. Catal.* **1994**, *145*, 27-36.

[84]   F. Bleken, M. Bjørgen, L. Palumbo, S. Bordiga, S. Svelle, K.-P. Lillerud and U. Olsbye, *Top. Catal.* **2009**, *52*, 218-228.

[85]   U. Olsbye, S. Svelle, M. Bjørgen, P. Beato, T. V. W. Janssens, F. Joensen, S. Bordiga and K. P. Lillerud, *Angew. Chem. Int. Ed.* **2012**, *51*, 5810-5831.

[86]   A. Takahashi, W. Xia, I. Nakamura, H. Shimada and T. Fujitani, *Appl. Catal. A-Gen* **2012**, *423*, 162-167.

Phosphatation of Zeolite H-ZSM-5: A Combined Microscopy and Spectroscopy Study

A variety of phosphated zeolite H-ZSM-5 samples are investigated with a combination of FT-IR spectroscopy, single pulse ^{27}Al, ^{29}Si, ^{31}P, ^{1}H-^{31}P CP, ^{27}Al-^{31}P CP, and ^{27}Al 3Q MAS NMR spectroscopy, STXM and N$_2$ physisorption. This approach leads to insights into the physicochemical processes that take place during phosphatation. Direct phosphatation of H-ZSM-5 promotes zeolite aggregation, as phosphorus does not penetrate deep into the zeolite material and is found at higher concentrations on and close to the outer surface of the zeolite, acting as a kind of glue.

Phosphatation of pre-steamed H-ZSM-5 gives rise to the formation of a crystalline tridymite AlPO$_4$ phase, which appears to be in the mesopores of dealuminated H-ZSM-5. Framework aluminum species interacting with phosphorus are not affected by hydrothermal treatment. Dealuminated H-ZSM-5, containing AlPO$_4$, retains more framework Al atoms and acid sites after hydrothermal treatment than directly phosphated H-ZSM-5.
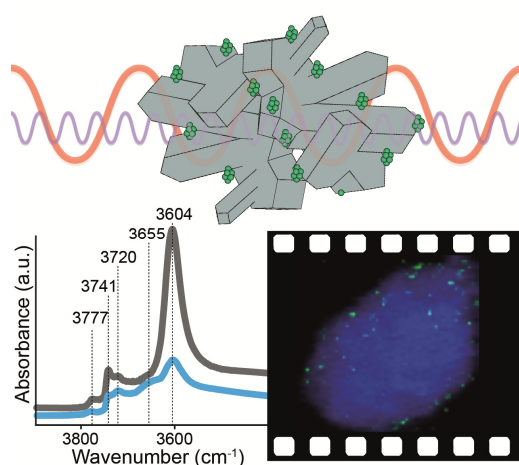
Chapter 3

3.1 Introduction

As was discussed in Chapter 1, hydrothermal conditions promote the dealumination of aluminosilicate materials, such as H-ZSM-5, and the loss of aluminum from zeolites leads to a decrease in catalytically active acid sites.[1] Lischke et al.[2] reported that impregnation of H-ZSM-5 with H_3PO_4 improved the hydrothermal stability of the H-ZSM-5 zeolite, while Védrine et al.[3] and Chandawar et al.[4] published works that revealed a decrease in strong Brønsted acid site number after phosphatation. This decrease in strong-acid-site number, and the increased hydrothermal stability, are the most distinctive effects of post-modification of H-ZSM-5 with phosphorus. [2, 5-21]

However, the exact nature of the two phenomena is not thoroughly understood, since the precise phosphorus-zeolite interactions have always been a point of discussion. As was discussed in Chapter 2, many different theories have been postulated over the years, ranging from direct framework incorporation, formation of tetrahydroxyphosphonium ions, to no phosphorus-framework interactions at all. [2, 5, 7, 13, 15, 22-31] What has been demonstrated is that phosphorus can react with extra-framework aluminum (EFAl) species, which are generated during hydrothermal treatment, to form crystalline and amorphous $AlPO_4$. [2, 5, 32] Furthermore, magic angle spinning nuclear magnetic resonance (MAS NMR) spectroscopy and *J*-coupling 2-D heteronuclear ^{27}Al-^{31}P correlation studies have given indications that phosphorus binds to partially dislodged framework Al species. [5, 8, 23]

Therefore, in this Chapter we attempt to shed new light on the physicochemical processes that take place during the phosphatation of H-ZSM-5, by applying scanning transmission X-ray microscopy (STXM) to a series of phosphated H-ZSM-5 samples for the first time. Two routes of phosphorus modification are followed: (1) direct phosphatation of H-
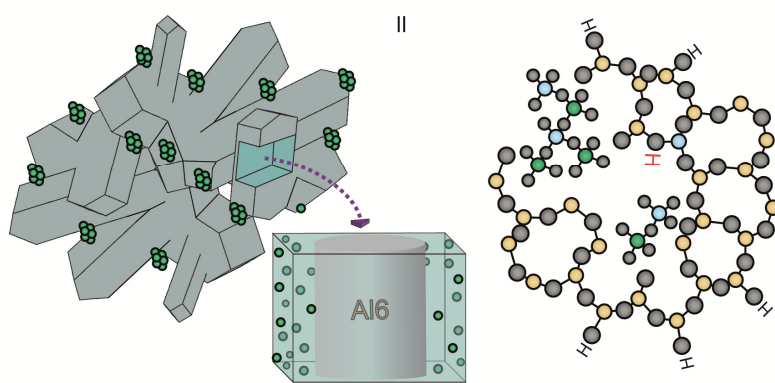
Scheme 3.1 Schematic representation of the two main phosphatation effects (I) Direct phosphatation of H-ZSM-5 gives rise to aggregation and external phosphorus deposits. Phosphorus that is interacting with tetrahedrally coordinated framework species is not affected by steam. As these interacting species are dominantly sited on or close to the zeolitic surface, higher concentrations of six coordinated Al (Al6) are formed deeper in the interior of the zeolite, during a steam-treatment. (II) Pre-steamed H-ZSM-5 contains extra-framework Al (EFAl) species, which readily react with phosphoric acid to form extra framework crystalline tridymite $AlPO_4$. ■ = Si, ■ = P, ■ = Al, ■ = O

ZSM-5 and (2) phosphatation of H-ZSM-5 preceded by a pre-steam treatment, see Scheme 1. It is expected that these two phosphatation routes will provide the spectroscopic signatures that will allow us to make the distinction between phosphorus interactions with *framework* aluminum and phosphorus interactions with *extra-framework* aluminum. This Chapter can be considered as an exploration study acting as a stepping stone for the following more in-depth Chapters.

Besides STXM, also more established bulk techniques are employed, which are ^{1}H-^{31}P cross-polarization (CP), ^{27}Al-^{31}P CP, 1D ^{27}Al and ^{31}P MAS NMR spectroscopy, triple quantum (3Q) MAS NMR spectroscopy, Fourier transform infrared (FT-IR) spectroscopy, and N_2 physisorption studies to add a solid foundation to the STXM results. By combining nanoscale chemical imaging and bulk information we provide novel insights into the genesis of phosphated H-ZSM-5 materials.

3.2 Experimental methods

3.2.1 Sample preparation

Commercially available Zeolyst CBV 2314 NH_4-ZSM-5 (Si/Al ratio = 11.5) was calcined in flowing air at 550 °C for 6 h. The obtained HZSM-5 material is referred to as [Z]. Phosphatation was performed as described by Xue et al. [20] 1 g of [Z] was mixed with an appropriate amount H_3PO_4 in 100 ml H_2O (2 wt.% P and P/Al ratio = 0.5). The mixture was kept under reflux conditions for 2 h. Afterwards, the solvent was removed by rotary evaporation. Subsequently, the sample was dried

Scheme 3.2 Overview and abbreviations of the samples under study. TT= thermal treatment, HT = hydrothermal, treatment, ST = steam treated, P = phosphated.

overnight at 120 °C and then calcined at 600 °C for 5 h. This sample is referred to as [Z]$_{2P}$. Sample [Z] was also calcined at 600 °C for 5 h, without phosphorus, this sample is denoted [Z]$_{TT}$

A pre-steam treatment was performed on [Z], similar to Lischke et al. [2] The sample was treated with 80 vol.% steam using N_2 as a carrier gas. Hydrothermal conditions were kept at 500 °C for 4 h. This sample is referred to as [ST]. Phosphatation of the pre-steamed sample was

identical to the procedure described for [Z]. This sample is referred to as $[ST]_{2P}$. Both $[Z]_{2P}$ and $[ST]_{2P}$ were hydrothermally treated at 600 °C for 2 h. These samples are referred to as $[Z]_{2P-ST}$ and $[ST]_{2P-ST}$.

3.2.3 Scanning transmission X-ray microscopy

Scanning transmission X-ray microscopy (STXM) experiments were performed at the Canadian Light Source (CLS) Beamline 10ID-1. Samples were dispersed in H_2O and a droplet was placed on a silicon nitride window. After drying in air the sample was placed in the STXM chamber,
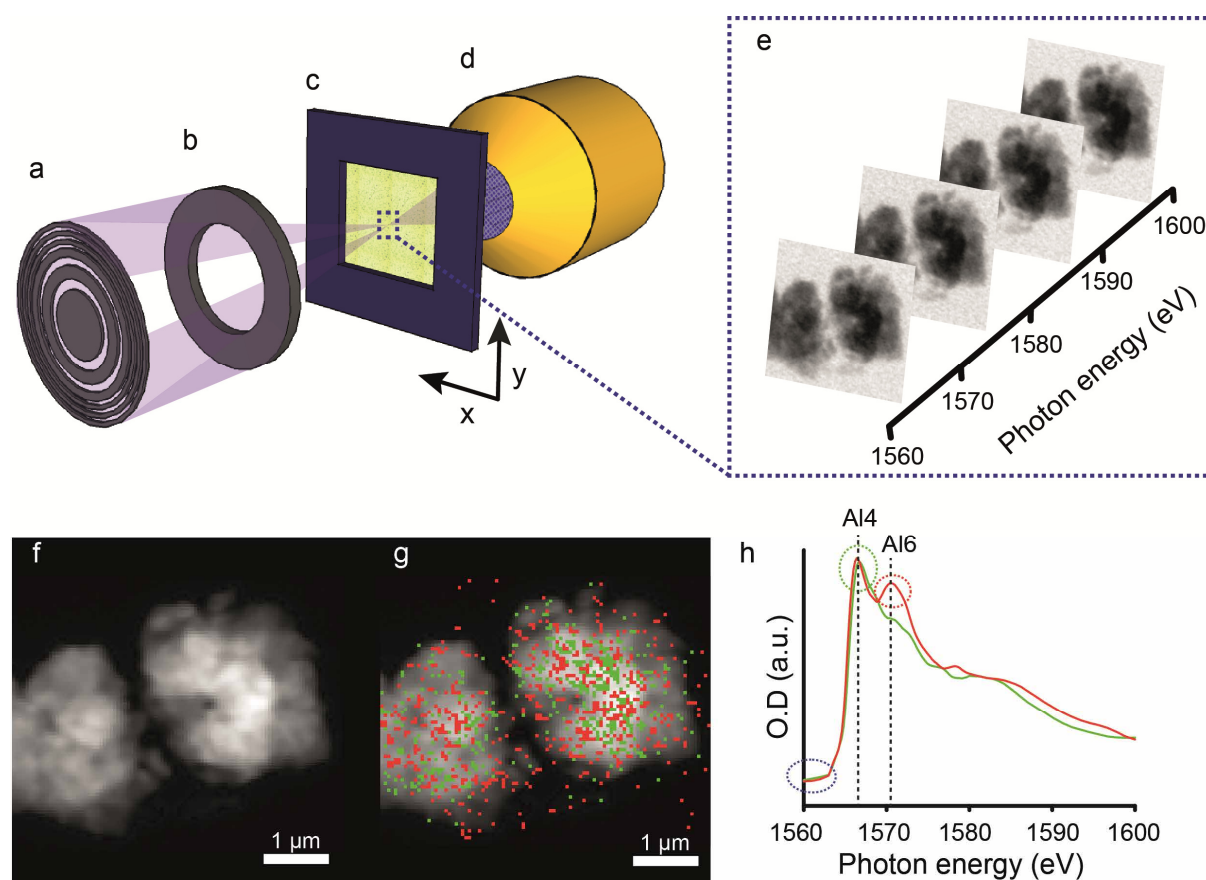
Figure 3.1 Schematic representation of the Scanning Transmission X-ray Microscopy (STXM) setup. (a) the zone plate focusses monochromatic X-rays to nanometer resolution (b) the order sorting aperture allowing only first order light to pass (c) the silicon nitride window on which the sample is dispersed. The window is mounted on a piezo sample stage that allows scanning of the sample in the x and y dimension with nanometer precission. (d) X-ray detector. The different components are not scaled with respect to each other. (e) X-ray absorption maps are collected at specific energies. They are normalized to optical density and stacked together. (f) Average stack-map of sample [ST], constructed from the X-ray absorption maps in (e). Every pixel contains an Al K-edge XANES. Scale bar is 1 μm (g) Two masks overlaid on the same stack map. (f) XANES that correspond to the masks. The green spectrum is an average of the spectra from each green highlighted pixel on (g). The red spectrum is an average of the spectra from each red highlighted pixel on (g). It can be seen that the red pixels highlight areas with high concentrations of six-coordinated aluminum (Al6), while the green pixels highlight areas with a low concentration of Al6. Furthermore, the dotted circles indicate how elemental maps can be constructed, by subtracting the average maps corresponding to the whiteline with the average maps corresponding to energies before the edge-jump.

which was subsequently evacuated to 10^{-1} mbar. A polarized X-ray beam was obtained using a 1.5 m long, 75 mm period Apple II undulator. The X-ray beam was focused to ~30 nm on the sample plane using a Fresnel zone plate (ZP). The beam from the ZP passed through a molybdenum-based order-sorting aperture (OSA), with a 50 μm pinhole. The OSA allowed only first-order ZP diffracted light to pass. Spectral image sequences (stacks) are measured by recording images over a range of photon energies. After aligning the image sequence, spectra of the whole or a subregion were extracted for comparison. In addition, stacks were fit to reference spectra of the components using linear regression. [33] All STXM data analysis was performed using aXis2000. A schematic representation of the STXM setup and data analysis is presented in Figure 3.1.

3.2.2 Solid-state nuclear magnetic resonance spectroscopy

The solid state nuclear magnetic resonance (NMR) spectroscopy experiments were performed at 11.7 T using a Bruker Avance III spectrometer equipped with a 3.2 mm triple resonance (Magic Angle Spinning) MAS probehead at room temperature. The MAS rate was 20 kHz for all experiments. The ^{27}Al NMR spectra were obtained using π/12 pulses at a rf-field of 94 kHz, 10000 scans and a recycle delay of 0.5s. The ^{27}Al 3QMAS experiments were carried out with a three pulse z-filtering sequence. [34] The spectra were acquired with 4800 scans for each of the 60 experiments in the indirect dimension. The recycle delay was 0.8s. The ^{29}Si spectra were obtained using 1000 scans with a recycle delay of 60 s and the ^{31}P spectra were obtained with 120 scans also with a recycle delay of 60 s. ^{1}H-^{31}P cross polarization (CP) spectra were acquired with 400 scan, a recycle delay of 5 seconds and a contact time of 500 micro seconds. The ^{27}Al-^{31}P CP experiments were acquired with 100000 scans, a recycle delay of 2s, and with a contact time of 5000 micro-seconds. The chemical shifts of ^{27}Al, ^{29}Si, and ^{31}P were externally referenced to 1M $Al(NO_3)_3$(aq), DSS (2,2-dimethyl-2-silapentane-5-sulfonic acid), and 85% H_3PO_4(aq), respectively.

3.2.4 Fourier transform infrared spectroscopy

Fourier Transform Infrared (FT-IR) spectroscopy measurements were performed on self-supporting zeolite wafers. 15 mg of sample was pressed with 3 tons for 10 s into a thin disk. The sample was evacuated to 10^{-6} bar and heated with 3 K/min to 673 K and kept at that temperature for 1 h. IR spectra were taken with a Bruker FT-IR instrument with an optical resolution of 4 cm^{-1} and 32 accumulations with wavenumbers ranging from 4000 cm^{-1} to 1000 cm^{-1}. Spectra

were baseline corrected and normalized using the bands corresponding to zeolitic framework vibrations found at 1967 cm^{-1}, 1873 cm^{-1}, and 1637 cm^{-1}.

3.2.5 N$_2$-physisorption

N$_2$-physisorption isotherms were recorded using a Micromeritics Tristar 3000 setup operating at -196 °C. Prior to physisorption measurements, all samples were dried overnight at 500 °C under a N$_2$ flow. In order to obtain the external surface area of the samples the *t*-Plot method was applied to the obtained physisorption isotherms.

3.3 Results

In the following sections we will present the physicochemical effects observed during the two routes of phosphorus modification. The first route being a direct phosphatation of H-ZSM-5 and the second being identical but preceded by a steam treatment. First, we will start by presenting the structural changes that occur upon phosphorus modification of the two H-ZSM-5 samples as
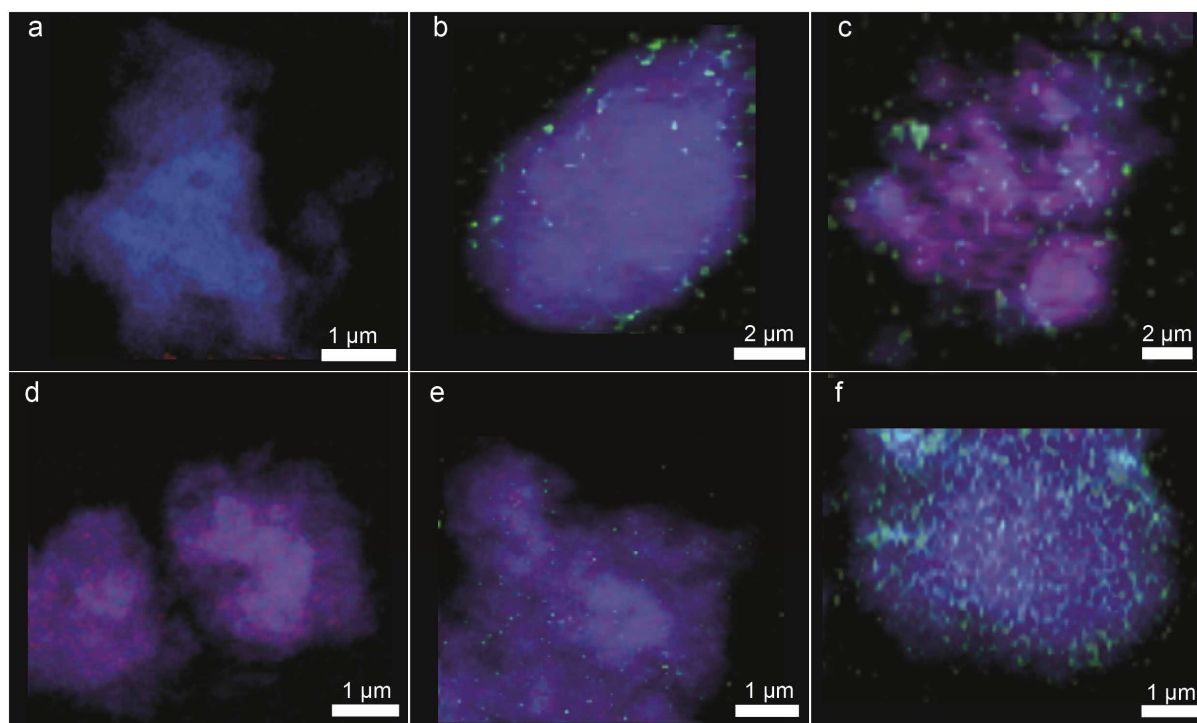
Figure 3.2 Chemical maps of zeolite clusters at different stages of phosphatation, constructed from Al and P K-edge stacks using linear regression analysis. ■ = Al4, ■ = Al4$_{dis}$ and Al6 ■ = P . (a) [Z], pixel size is 60x60 nm². (b) [Z]$_{2P}$, pixel size is 150x150 nm². (c) [Z]$_{2P-ST}$, pixel size is 230x230 nm². (d) [ST], pixel size is 60x60 nm². (e) [ST]$_{2P,,}$ pixel size is 60x60 nm² (f) [ST]$_{2P-ST}$, pixel size is 60x60 nm². Information on the construction of these maps can be found Figures 1 and 3

determined by spatio-chemical imaging. In a second part we will link these observations to the results obtained by more established bulk techniques and third, we will present the changes in acidity that occur upon phosphatation. Fourth, the effect of a hydrothermal treatment on both samples is shown by means of all previously mentioned techniques. We will end with a discussion and interpretation of the results, ultimately comparing the differences between the two phosphatation routes. Scheme 3.1 shows the most important concepts presented in this work.

3.3.1 Phosphatation of H-ZSM-5

3.3.1.1 *Spatio-chemical imaging of phosphated H-ZSM-5*

The ZSM-5 zeolites under study do not represent uniformly shaped crystals, but form a variety of intergrown clusters. They can be considered spherical, or at least spheroid and are on average 1 μm in size. [33] Figure 3.2a shows that the parent H-ZSM-5 ([Z]) has a homogeneous distribution of four-coordinated Al species (Al4) and, following the values in the Table 3.1, a 15% contribution of six-coordinated Al species (Al6). The contributions of Al4 and Al6 species have
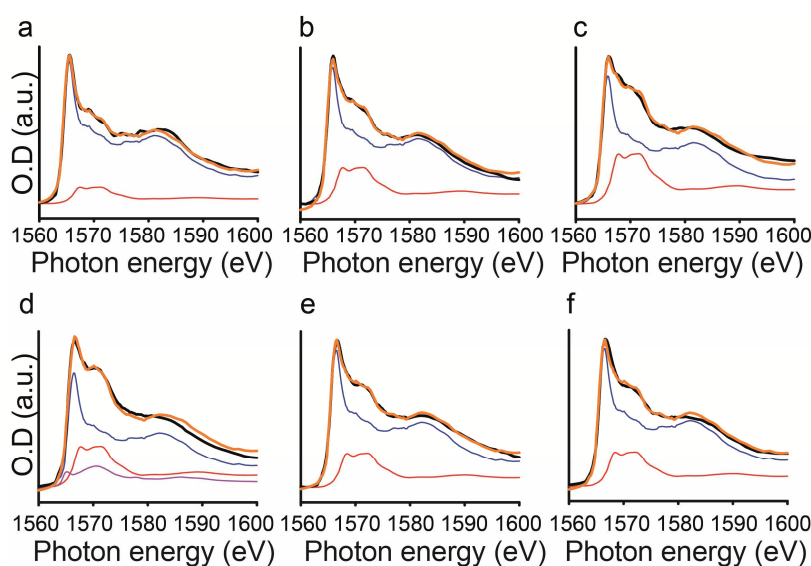
Figure 3.3 Explanation as to how Figure 3.2 was constructed. a = [Z], b = [Z]$_{2P}$, c = [Z]$_{2P-ST}$, d = [ST], e = [ST]$_{2P}$, and f = [ST]$_{2P-ST}$. For each sample the corresponding Al K-edge stack was fitted using linear regression with two reference spectra. These reference materials are NH$_4$-ZSM-5 (Zeolyst CBV 2314, Si/Al = 11.5) and boehmite. The references have been chosen as NH$_4$-ZSM-5 contains exclusively four coordinated Al species and acts as a reference for a more or less 'perfect' parent H-ZSM-5 material. Boehmite has Al in 6 coordination and acts as a reference for extra-framework species. For sample [ST] an additional andalusite reference has been used. In the figure we can see the fit results for the average spectra corresponding to a whole cluster of zeolites. ■ = Sample, ■ = Sample fit result ■ = Boehmite, ■ = NH$_4$-ZSM-5, ■ = Andalusite   In the image every pixel is fitted in an identical manner and the contribution of each reference spectra is resembled in pixel intensity (■ = boehmite and ■ = NH$_4$-ZSM-5) . For the spectral map of sample [ST] the contributions of andalusite and boehmite are combined. Phosphorus maps have been constructed as described in Figure 3.1 and Figure A3.1 and combined with the Al maps.

been quantified using the reference materials zeolite NH_4-ZSM-5 and boehmite, respectively, as is explained in Figure 3.3. When $[Z]_{2P}$ is prepared by phosphatation of sample $[Z]$, an increase in Al6 species to 27% of the total Al atoms is observed, as can be found in Figure 3.2b and Table 3.1. Figure 3.2b and Figure 3.4 further reveal that the majority of the phosphorus species is present at the outer surface of the zeolite. N_2-physisorption data presented in Figure 3.5 shows that phosphatation promotes a decrease in external surface area, which would indicate zeolite aggregation. The micropore volume decreases, indicating that phosphorus moves into the zeolite to a certain extent, but signs for of mesopore formation are not observed.

Table 3.1. Contributions of reference spectra used in linear regression fits.

Sample	NH_4-ZSM-5	boehmite
[Z]	0.85	0.15
$[Z]_{2P}$	0.71	0.29
$[Z]_{2P-ST}$	0.62	0.38
[ST]	0.61	0.39[a]
$[ST]_{2P}$	0.72	0.28
$[ST]_{2P-ST}$	0.72	0.28

[a] Combined contribution of boehmite = 0.26 and andalusite = 0.13 [33]

When zeolite [Z] is subjected to a pre-steam treatment, we obtain sample [ST]. Figure 3.2d clearly shows that the dealumination after steam treatment occurs homogenously throughout the zeolite crystals, with 39% of the Al in five-, and six-coordination, which is further shown in Table 3.1. These results are in good agreement with 3-D tomography performed by our group on a steamed H-ZSM-5 crystal, revealing randomly distributed patches of Al6 species.[35] The formation of a hysteresis cycle at high relative pressures in the N_2-physisorption adsorption/desorption isotherms shown in Figure 3.5, is indicative of the formation of mesopores. [36] An increase in the external surface area is observed as well. The formation of a low pressure hysteresis cycle, which is typically found for MFI topologies with high framework
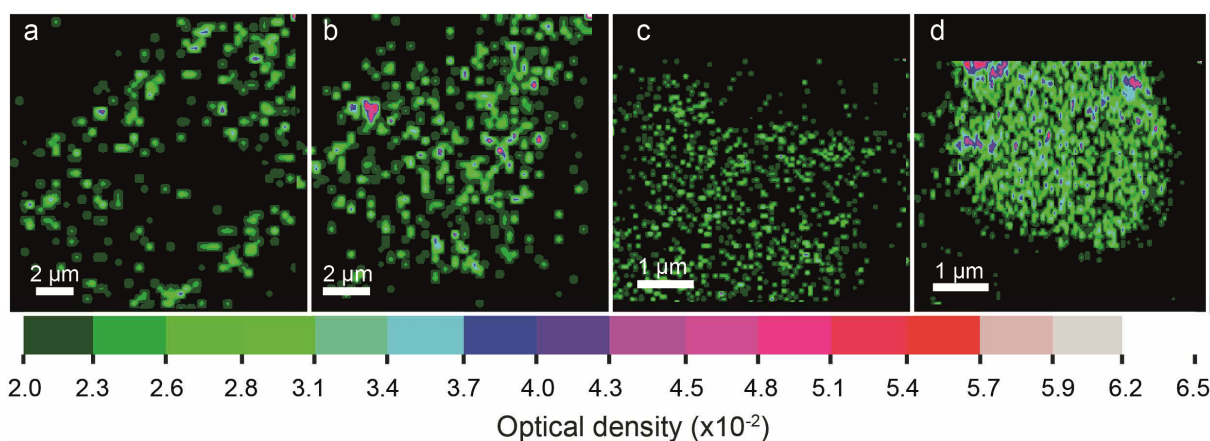

Figure 3.4 Phosphorus distribution and optical density maps derived from P K-edge stacks as explained in Figure 3.1. Samples correspond to those presented in Figure 3.2. (a) $[Z]_{2P}$, (b) $[Z]_{2P-ST}$, (c) $[ST]_{2P}$, (d) $[ST]_{2P-ST}$.

Si/Al ratios, is not visible. [37] After the phosphatation of sample [ST], producing [ST]$_{2P}$, the distribution of phosphorus species is not random, as there is a higher concentration in the thinner parts of the zeolite as presented in Figure A3.3. However, phosphorus is better distributed throughout the zeolite for the [ST]$_{2P}$ samples than for [Z]$_{2P}$ samples, as can be seen in Figures 3.2d and 3.4, suggesting that phosphorus moieties can more easily penetrate a pre-steamed zeolite. This is confirmed by N$_2$-physisorption data that indicates a decrease of mesopores in sample [ST]$_{2P}$. Signs for particle aggregation are not observed from the N$_2$-physisorption data as there is no strong decrease in external surface area. Table 3.1 shows that the amount of Al6 species decreases from 39 % for sample [ST] to 28 % for sample [ST]$_{2P}$.

3.3.1.2 *T-atoms, P-atoms and Phosphorus-Zeolite Interaction*

Figure 3.6 is an overview of the state of T-atoms, P-atoms and interactions between them for the different stages of direct phosphatation. The parent sample [Z] is a typical highly ordered crystalline microporous zeolite. The ^{29}Si NMR spectrum shows two distinct resonances at -112 and -106 ppm. The first corresponds to framework silicon bonded through oxygen with four silicon atoms (Si(0Al)), while the second resonance stems from framework silicon connected through oxygen bonds with three silicon and one Al atom (Si(1Al)).[38] The corresponding framework Al(OSi)$_4$ species are resembled in the ^{27}Al MAS NMR spectra and Al K-edge XANES seen in Figures 3.6b and 3.6d, respectively, by intense resonance at 54 ppm in ^{27}Al MAS NMR and the strong single-edge maximum at 1565.6 eV seen in the Al K-edge XANES. [33, 38-39] As previously shown by our group the peaks observed at energies above the rising edge are typically found for tetrahedral aluminosilicates, with a small contribution of Al6
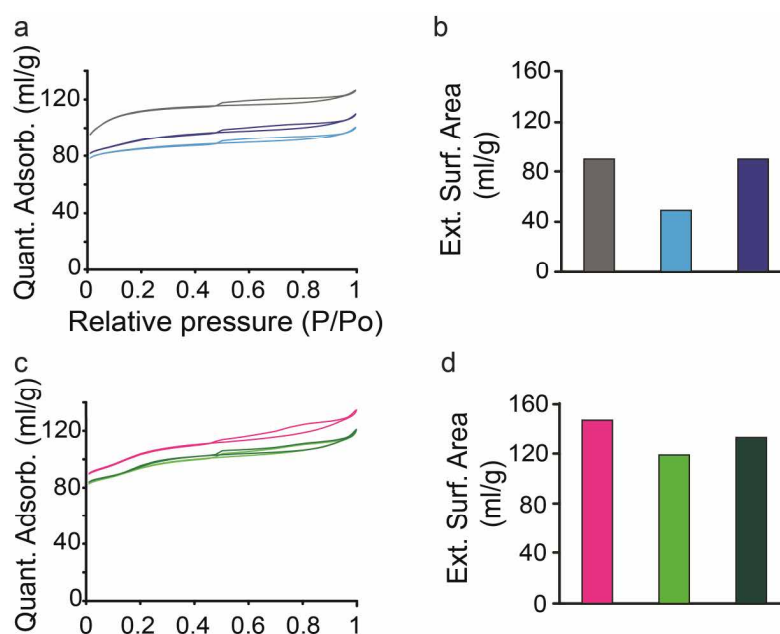
Figure 3.5 (a and c) Nitrogen physisorption adsorption/desorption isotherms, and (b and) external surface area of the samples of samples ■= [Z] ■= [Z]$_{2P}$ ■ = [Z]$_{2P-ST}$ ■ = [ST] ■ = [ST]$_{2P}$ ■ = [ST]$_{2P-ST}$.

species as seen in Figure 3.3. [33, 39] Besides tetrahedrally coordinated Al (TFAl) species there is another type of Al species found for sample [Z]. The sharp resonance observed with ^{27}Al MAS NMR at 0 ppm stems from octahedrally coordinated Al species (OFAl), which are connected to the framework with three Si-O-Al bonds and physically bonding with three H_2O ligands. [40-41]

After phosphatation and calcination to obtain sample [Z]$_{2P}$, the amount of Si(1Al) species decrease, while the amount of Si(0Al) species increases as can be seen in Figure 3.6a. This points to the breaking of Si-O-Al bonds, as silicon loses aluminum neighbors. However, a sample presented in Figure 3.7

Figure 3.6 Structural investigation of the T-atoms and P-atoms in three different H-ZSM-5 samples. ■ = [Z] ■ = [Z]$_{2P}$ ■ = [Z]$_{2P-ST}$ (a) ^{29}Si MAS NMR. (b) ^{27}Al MAS NMR. (c) 2-D ^{27}Al 3Q MAS NMR. d) XANES of Al K-edge of samples. (e) and (f) ^{31}P MAS NMR spectra of [Z]$_{2P}$ (e) and [Z]$_{2P-ST}$ (f). Included are ^{1}H-^{31}P (brown) and ^{27}Al-^{31}P (grey) cross-polarization spectra.

that received the same thermal treatment as sample [Z]$_{2P}$ without phosphorus addition showed a similar decrease in Si-O-Al bonds, indicating that part of the Si-O-Al bonds are broken by the thermal treatment. Figure 3.6a further shows a shift of the -112 ppm resonance to -113 ppm after phosphatation, which could be explained by the presence of phosphorus in the zeolite pores. The breaking of Si-O-Al bonds is also observed in the ^{27}Al MAS NMR and ^{27}Al 3Q MAS

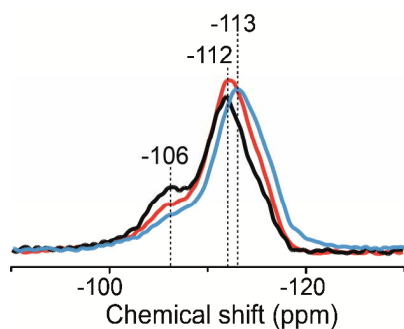**Figure 3.7** ^{29}Si MAS NMR of ■ = [Z], ■ = [Z]$_{2P}$ and ■ = Thermally Treated (TT) [Z] (600 C, 5 h). The thermal treatment identical for [Z]$_{TT}$ and [Z]$_{2P}$.

NMR spectra, presented in Figure 3.6b and 3.6c. The signal from TFAl species decreases sharply, while another broad resonance at 40 ppm - 10 ppm appears. The 2-D ^{27}Al 3Q MAS NMR spectrum in Figure 3.6c shows that the isotropic shift of this resonance 2 is similar to the resonance 1 attributed to TFAl. This indicates that these species are TFAl atoms with a larger quadrupolar coupling due to a highly distorted electronic environment.[5, 8] The broad resonance can therefore be attributed to TFAl species in a less symmetrical environment (TFAl$_{dis}$) due to the presence of phosphorus. Phosphatation gives rise to an increase in Al6 species. It can be observed that a new broad resonance at -4.5 ppm appears, while resonance 3 at 0 ppm decreases in intensity. This indicates that OFAl species are distorted by the presence of phosphorus and subsequent thermal treatment. Al K-edge XANES show a small increase in the peak around 1570.1 eV, which indicates some Al species to be in a different coordination environment. This effect is not observed in all measured [Z]$_{2P}$ clusters, which leads to some doubt as to whether there is a real change in the Al K-edge spectra after phosphatation.

When considering the nature of the phosphorus species, it is found that the ^{31}P MAS NMR spectra of sample [Z]$_{2P}$, as seen in Figure 3.6e, shows a broad resonance composed of several superimposed signals. The clearest positions are at -6.1 ppm, -14.7 ppm, -23.3 ppm, -32.1 ppm, and -39.6 ppm. The first two peaks are often found in phosphated H-ZSM-5 and correspond to terminal phosphate groups and middle phosphate groups in polyphosphate chains. [2, 30] As these species have terminal hydroxyl groups the ^{1}H-^{31}P cross polarization spectra support this interpretation. The resonance at -39.6 ppm can be attributed to P$_4$O$_{10}$ species.[42] The peaks at -31.1 ppm and -23.3 ppm have been attributed to Al-O-P and Si-O-P respectively. [2, 23, 29] In this study the formation of Si-O-P bonds were not evident from ^{29}Si MAS NMR. A ^{29}Si resonance at 119 ppm would be expected for tetrahedrally coordinated silicophosphate species, and ^{31}P resonance are expected at -43 ppm. [43] Both resonances are not visible in the spectra. On the other hand, the ^{27}Al-^{31}P CP experiment indicates some interaction through space between Al and P in the -32 ppm to -39 ppm region, i.e. that phosphate species in this region are in close vicinity to Al.

Figure 3.8a demonstrates that hydrothermal treatment of sample [Z] is followed by an almost complete loss of Si(1Al) species. The peak at -115 ppm comes from Si atoms in crystallographic inequivalent sites indicating that the zeolite framework was damaged. [38] A sharp decrease in the

resonance at 54 ppm is observed with ^{27}Al MAS NMR and the signal at 0 ppm attributed to OFAl species becomes broader (Figure 3.8b). Another new broad signal appears around 31.7 ppm, which has been assigned to extra-framework aluminum (EFAl) five-coordinated aluminum (Al5) or Al4 species.[44-46] Broadening of the signals is caused by second neighbor effects and indicates a poor structure ordering of atoms. Resonance 5 shown by ^{27}Al 3Q MAS NMR in Figure 3.8c proves the presence of EFAl Al5/Al4 species.[8] Furthermore, a new Al4 type species is visible (resonance 6). This Al4 species are attributed to four-coordinated EFAl species. XANES at the Al K-edge of [ST] confirms the formation of Al6 species as can be seen in Figure 3.8 by the increase of the peak at 1569.8 eV, reported recently by our group. [33, 39]
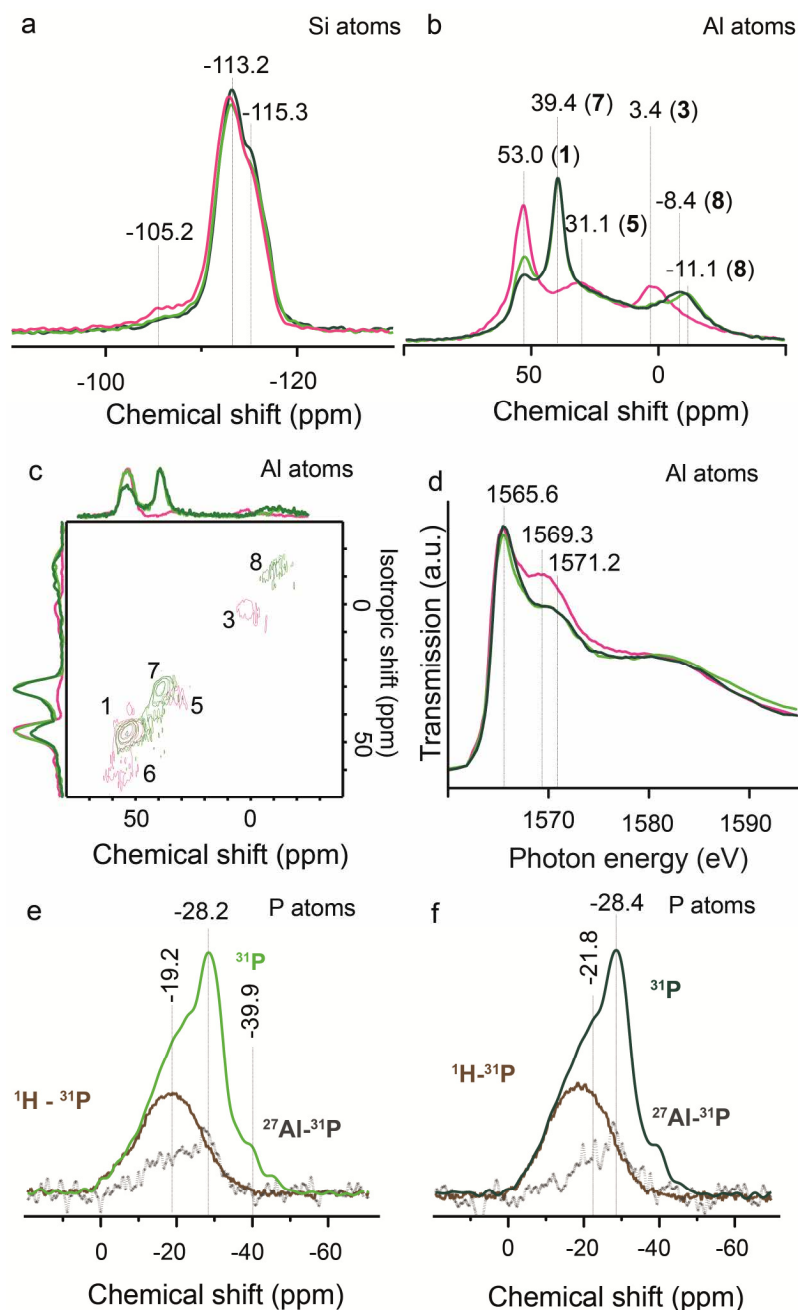
Figure 3.8 Structural investigation of the T-atoms and P-atoms in phosphated H-ZSM-5. ■ = [ST] ■ = [ST]$_{2P}$ ■ = [ST]$_{2P-ST}$ (a) ^{29}Si MAS NMR. (b) ^{27}Al MAS NMR. (c) 2-D ^{27}Al 3Q MAS NMR. d) XANES of Al K-edge of samples. (e) and (f) ^{31}P MAS NMR spectra of [ST]$_{2P}$ (e) and [ST]$_{2P-ST}$ (f). Included are ^{1}H-^{31}P (brown) and ^{27}Al-^{31}P (grey) cross-polarization spectra.

As seen in Figure 3.8b, when sample [ST] is phosphated there is a decrease for the ^{27}Al MAS NMR resonance at 53 ppm and resonance at 3.4 ppm, while a broad signal at -11 ppm appears. This resonance has been previously ascribed to Al6 in extra-framework $Al(H_2O)_3(PO_4)_3$ or framework Al(6)-O-P type species. [2, 23, 27] Another sharp signal appears at 39.4 ppm, seemingly

at the cost of the signal at 31.1 ppm. [27]Al 3Q MAS data show that two signals in [ST] marked 5 and 6 for Al5 and distorted Al4 respectively, disappear and that a new signal, marked 7, appears in sample [ST]$_{2P}$. This well-defined new resonance has been attributed to Al4 in crystalline AlPO$_4$. [2, 5, 32] The ^{27}Al 3Q MAS NMR spectrum of sample [ST]$_{2P}$ indicates that the resonances at 53 ppm and 39.4 ppm comprise of more than two Al species and that a distribution of chemical shifts of these units exists. Following these observations, we conclude that H$_3$PO$_4$ preferentially reacts with four-, five-, and six-coordinated EFAl and partially dislodged Al species and forms AlPO$_4$. The Al K-edge XANES fully agree with the previous conclusion, as the Al6 peak of EFAl species decreases after phosphatation. The ^{31}P MAS NMR spectrum shows a broad resonance with a maximum at -28 ppm. The overall shape of the spectrum correlates well with that of AlPO$_4$ materials. [2, 5, 32, 47] However, the broad distribution of chemical shifts from 0 pm to -40 ppm indicates that there are still phosphate groups present in polyphosphate chains or more condensed polyphosphate chains.

3.3.1.3 *Acid Sites and OH-groups*

The state of acid sites of the samples has been studied with FT-IR. Infrared spectra of the OH-stretch region are shown in Figure 3.9. Sample [Z] has a very strong band at 3604 cm^{-1} and a smaller peak at 3736 cm^{-1}. These bands are attributed to bridging hydroxyl groups (Si-OH-Al) and external silanol groups respectively. [48] Two less distinct bands are observed at 3620 cm^{-1}, which stem from internal silanol groups and at 3780 cm^{-1}, which correspond to external Al-OH groups.[48] After phosphatation ([Z]$_{2P}$) there is a sharp decrease in the amount of bridging hydroxyl groups. The 3600 cm^{-1} band and corresponding Brønsted acid site number decreases with 80%, as was determined by
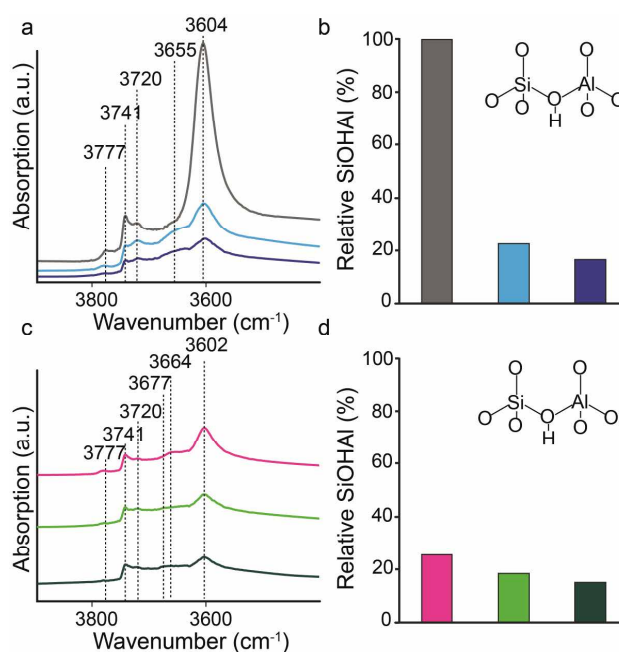

Figure 3.9 FT-IR spectra of the OH-stretch region of samples ■ = [Z] ■ = [Z]$_{2P}$ ■ = [Z]$_{2P-ST}$ ■ = [ST] ■ = [ST]$_{2P}$ ■ = [ST]$_{2P-ST}$. Right: The bands in the spectra have been deconvoluted to determine the area of the band at 3604 cm^{-1} corresponding to Si-OH-Al and Brønsted acid site number. The values are relative to sample [Z]. Further information on the deconvolution process can be found in Figure A3.4 and Table A3.1.

deconvolution, which can be found in the appendix section in Table A3.1. A new peak appears at 3650 cm^{-1}, which can be attributed to the hydroxyl groups of (partially) dealuminated species. [48-49] The bands for external silanol and Al-OH groups decrease in intensity and the peak for the internal silanol groups becomes more pronounced.

The extracted TFAl species from the framework in sample [ST], coincide with a loss of bridging hydroxyl groups. A new band appears at 3660 cm^{-1} corresponding to EFAl species.[48] The intensity of all other peaks decreases. After phosphatation ([ST]$_{2P}$) the band corresponding to bridging hydroxyl groups decreases slightly in intensity. The peak for EFAl species decreases, while a new band at around 3675 cm^{-1} appears. This peak is attributed to P-OH groups found in AlPO$_4$.[7, 20, 49] There was a minor decrease in the intensity of the band at 3736 cm^{-1} corresponding to external silanol groups.

3.3.1 Effect of hydrothermal treatment

In order to assess the effect of hydrothermal treatment on samples [Z]$_{2P}$ and [ST]$_{2P}$ a post-steam treatment was performed. After hydrothermal treatment Figure 3.2e and 3.4 of sample [Z]$_{2P-ST}$ shows that the elemental distribution of phosphorus is more homogenous, indicating that some of the phosphorus has migrated further into the interior of the zeolite. The fraction of Al6 species decreases from 27% in sample [Z]$_{2P}$ to 38% in sample [Z]$_{2P-ST}$. N$_2$-physisorption showed an increase in external surface area, can be seen in Figure 3.5. The near-linear uptake of nitrogen in the 0 to 0.3 P/P$_0$ region in sample [Z]$_{2P-ST}$ is indicative of the formation of small mesopores. [59]

^{29}Si MAS NMR presented in Figure 3.6a, demonstrates that sample [Z]$_{2P-ST}$ loses more Si-O-Al bonds, with a corresponding increase in Si(0Al) species. TFAl sites decrease while the TFAl$_{dis}$ species remain largely unaffected. However, as can be seen from the ^{27}Al MAS NMR and 2-D ^{27}Al 3QMAS spectra in Figure 3.6b and c, there is a slight shift of the resonance at 40 ppm - 10 ppm. Insensitive Nuclei Enhanced by Polarization Transfer (INEPT) hetero-correlation (HETCOR) NMR has shown that the resonances at 40 ppm - 10 ppm and -6 ppm are Al species forming Al-O-P type bonds with phosphorus. [23] An increase in the amount of Al6 interacting with phosphorus is also observed, leading to conclude that these species are formed at the cost of expelled TFAl species that normally form during an identical steam treatment as shown in
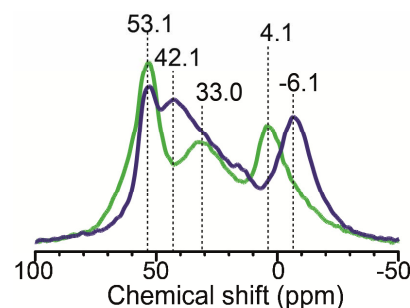

Figure 3.10 ^{27}Al MAS NMR of ■ = [Z] ST 600 °C, 2 h, ■ = [Z]$_{2P-ST}$. Both samples have been steamed at 600 °C for 2 h. Steamed sample [Z] does not contain any P.

Figure 3.10. It can be observed that no additional $Al4_{dis}$ species are formed. The formation of Al6 species is confirmed by the XANES of the Al K-edge, which shows an increase of the 1570 eV peak.[33, 39]

The ^{31}P MAS NMR spectra in Figure 3.6f, shows that most condensed phosphorus species in the -32 ppm to -39 ppm region, or those interacting with Al, are reduced in size by the hydrothermal treatment. The resonances corresponding to smaller polyphosphate chains increase in intensity around -14 ppm. An explanation could be the rehydration that occurs after steam treatment, as P_4O_{10} species in phosphated zeolites are known to revert into ortho,- pyro,- and small polyphosphates during rehydration.[30, 42] Steaming has a severe effect on Brønsted site number as is shown in Figure 3.9 and by deconvolution of FT-IR spectra in Table A3.2. Of the original number of Brønsted acid sites for [Z] only 15% are left in sample $[Z]_{2P\text{-}ST}$. For the other
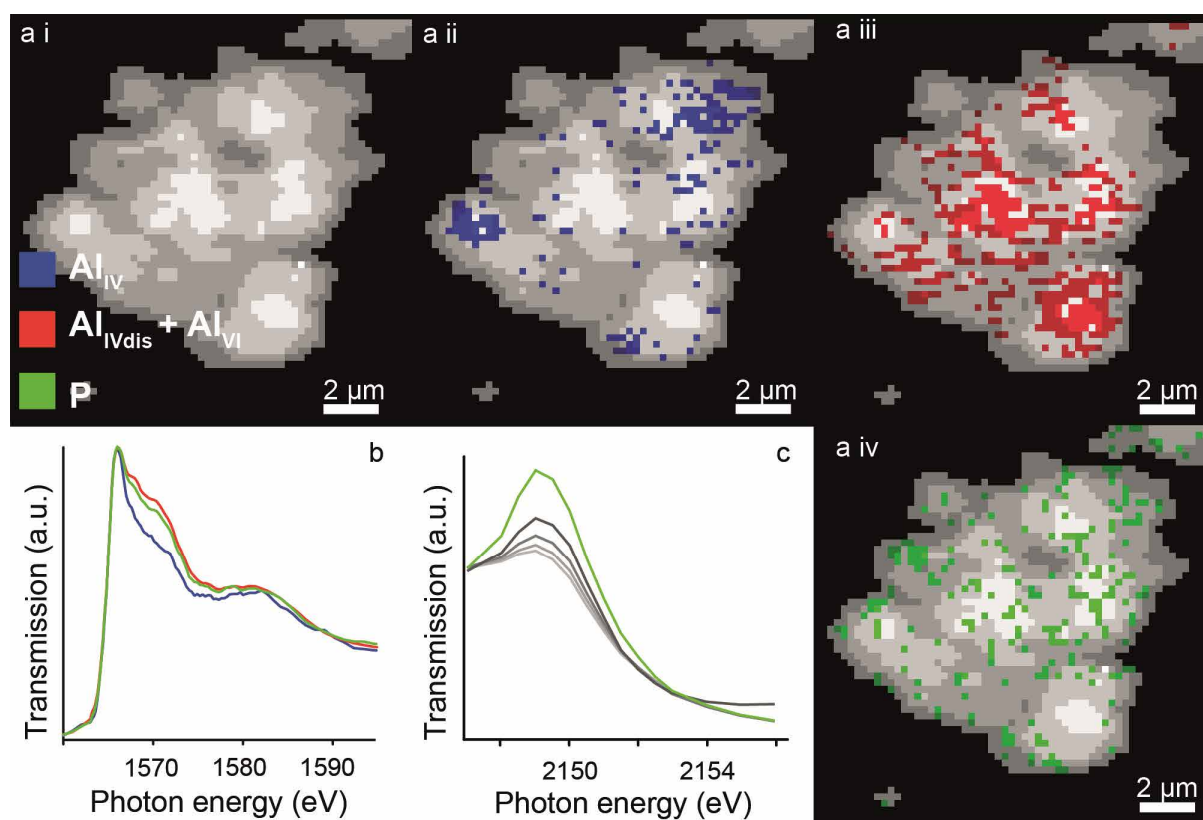
Figure 3.11 Distribution of phosphorus and different Al species on sample $[Z]_{2P\text{-}ST}$. Pixel size is 230x230 nm². (a i) Average of Al K-edge X-ray absorption maps, divided in four different optical density regions. Bright regions have a larger optical density. (a ii, a iii and a iv) Distribution of ■ = Al4, ■ = $Al4_{dis}$ and Al6 ■ = P The corresponding XANES of these regions can be seen in Figure 3.5 b. Linear fitting of the different spectra with reference compounds NH_4-ZSM-5 and boehmite have been performed to determine Al4 and Al6 contributions, as explained in Figure 3.1. (c) Phosphorus K-edge spectra as found in different optical densities in the cluster. It can be observed that phosphorus concentration is relatively higher in thinner regions. Phosphorus concentration is the highest in the green regions.
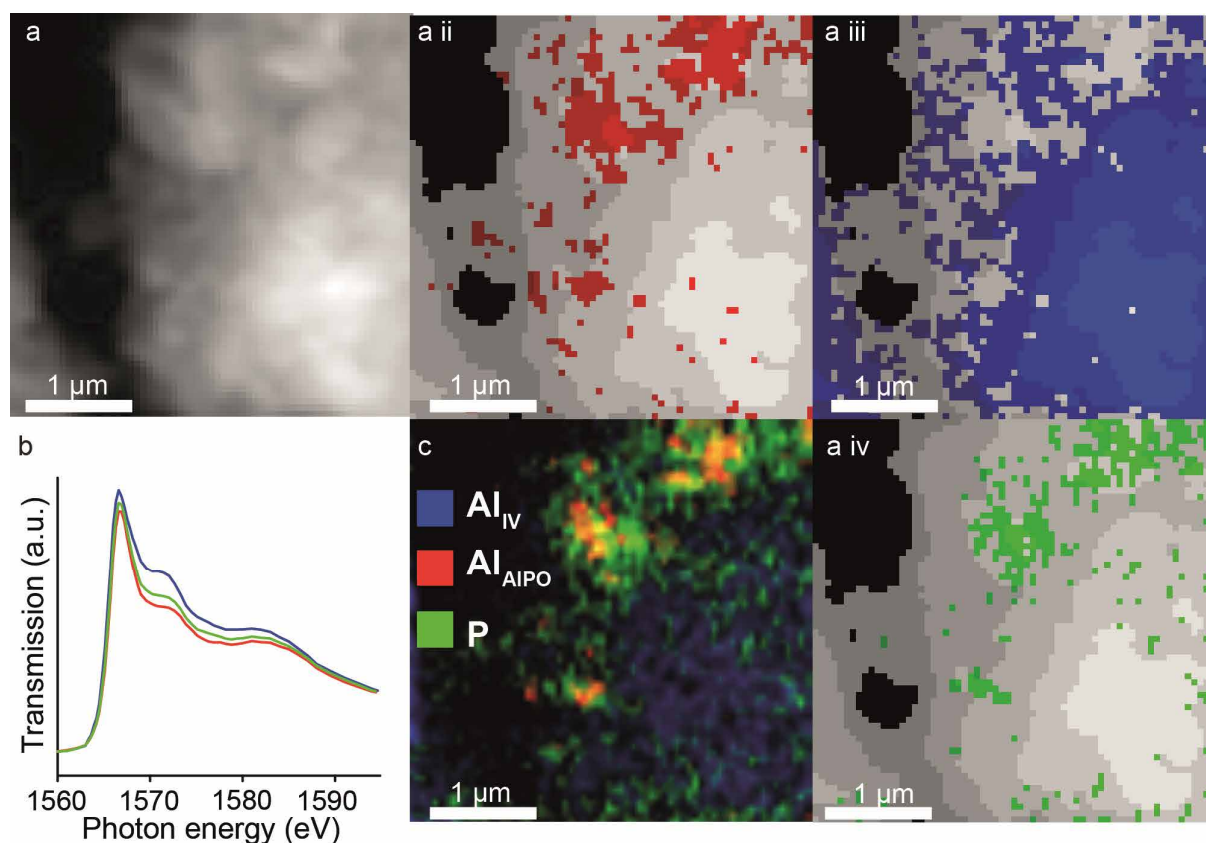
Figure 3.12 Distribution of phosphorus and different Al species on sample [ST]$_{2P\text{-}ST}$. Pixel size is 60x60 nm². (a i) Average of Al K-edge X-ray absorption maps. (a ii) Distribution of ■ = Al$_{AlPO4}$.=. (a iii) Distribution of ■ = Al4. (a iv) Distribution of ■ = P Bright regions have a higher optical density. The correspondingly colored XANES of these regions can be seen in Figure 6b. (c) Recombined images of the P K-edge and the Al K-edge stacks revealing the presence of AlPO$_4$ islands.

bands it seems that the overall absorbance decreases in intensity.

As the Al K-edge XANES obtained by STXM are confirmed by the bulk measurements, they can be used for a detailed spatially resolved investigation of the samples under study. Figure 3.11 presents the Al K-edge XANES analysis of sample [Z]$_{2P\text{-}ST}$. The individual contributions of the coordination states of Al are different in the various regions of the cluster, especially at the thinner regions on the sides. While most of the regions in the cluster contain about 38% of Al6 species formed by dealumination, the outer sides of the cluster contain 13% less Al6 species. Especially in certain hotspots marked blue in Figure 3.11a ii, the concentration of Al6 species is only 25%. At first glance there does not seem to be a clear correlation between the location of these regions and the presence of phosphorus However, careful analysis of the stacks presented in Figure 3.11 and Figure A3.2 shows that at the thinner, outer regions of the zeolite higher concentrations of phosphorus are present, while more Al6 species are found at the thicker, inner phosphorus-poorer regions.

For the pre-steam treated sample [ST]$_{2P-ST}$ the T-atoms are not strongly affected by the post-steam treatment. In Figure 3.8b it can be seen that the ^{27}Al MAS NMR signal at 53 ppm is decreased slightly, while a signal at -8.4 ppm appears. The signal at -115.3 ppm in ^{29}Si MAS NMR that we attributed to Si in crystalline defect sites is increased slightly. From both techniques it can be concluded that there is mild dealumination. The Al K-edge XANES do not change, nor is the ^{31}P MAS NMR spectra affected by the hydrothermal treatment. The FT-IR spectrum of sample [ST]$_{2P-ST}$ is quite similar to that of [ST]$_{2P}$. This is in line with the slight dealumination that was also observed using ^{27}Al MAS NMR.

Although the various spectra for sample [ST]$_{2P-ST}$ appeared very similar to sample [ST]$_{2P}$ using the applied spectroscopic bulk techniques, an interesting zeolite cluster of the former is presented in Figure 3.2f. One can see that phosphorus is quite homogeneously distributed, but that there are a few hot spots. In Figure 3.12, we focus on these hot spots. Sample [ST]$_{2P-ST}$ has various regions with different Al K-edge spectra. The region marked with red comprises a high concentration of phosphorus and an Al K-edge spectrum that has a feature that is found for AlPO$_4$ with a tridymite structure.[50] The blue region in Figure 3.12a iii has a XANES that appears to have features of the AlPO$_4$ peak as well, but also has a contribution coming from Al6 species. These AlPO$_4$ 'islands' are around 1 μm in size and are found at the edges of the zeolite cluster. It is uncertain if these islands are pure AlPO$_4$ phase or if they are present in zeolites that contain high amounts of AlPO$_4$ in the micro-, meso-, and macropores. As can be seen in Figures 3.12 and A3.3 the thickest part of the cluster has the lowest amount of phosphorus, indicating that phosphorus/AlPO$_4$ does not penetrate completely into the zeolite.

3.4 Discussion

By employing a combined spectroscopic approach it is established that with phosphatation of H-ZSM-5, followed by a thermal treatment, phosphorus enters the outer shell of the zeolite and promotes aggregation of individual zeolite clusters. Assuming there is interaction between phosphorus and aluminum, this could be explained by using simple geometry. If one considers that in a spherical object, the volume of the first outer 25% of the spheres radius makes up for 60% of the total volume and, since the P/Al ratio, the chance of finding P close to the surface is quite high. In Chapter 2 we discussed this effect, however diffusion limitations will also play a role. Previous studies showed that with low loadings, phosphorus is found dominantly at or close to the surface. [3, 13, 24, 51-53] Thermal treatment promotes the annealing of phosphate groups

on the zeolite external surface with the external phosphate groups on other zeolite clusters, leading to aggregation.

The presence of phosphorus in the zeolite pores leads to a decrease in micropore volume. Furthermore, the presence of phosphorus distorts the electronic environment of TFAl and tetrahedrally coordinated silicon (TFSi) species. This indicates that phosphorus is not exclusively on the surface, but also in the micropores close to the outer surface. No strong dealumination is induced by phosphorus, as EFAl species are not formed. Si-O-Al bonds are broken, which can be mainly attributed to thermal treatment. However, as was discussed in Chapter 2, more Si-O-Al bonds disappear in the presence of phosphorus. Distorted TFAl species lose their Brønsted acidity. Although the decrease in external silanol groups observed with FT-IR can tentatively be attributed due to silanol bonding with phosphates, it is highly unlikely that these species can exist outside a water-free environment. [54-55] However, there have been reports on the formation of Si-O-PO(OH)$_2$ surface groups on silica and zeolites in hydrous conditions. [56-57] Nevertheless, the fact that phosphorus interacts with almost all FT-IR visible external surface Si-OH and Al-OH groups, does agree with the external phosphorus distribution found with STXM.

If the phosphatation step is preceded by a steam treatment a different type of material is obtained. The pre-steam treatment leads to the dealumination of sample [Z]. Si-O-Al bonds are broken, TFAl species are expelled and Brønsted acid sites are lost. The zeolitic framework is partially damaged and mesopores are formed. Four-, five-, and six-coordinated EFAl aluminum species are present in the zeolite. Phosphoric acid preferentially reacts with the EFAl species and forms tridymite AlPO$_4$ (Scheme 1). This crystalline extra-framework AlPO$_4$ phase forms clusters and fills part of the mesopores. More TFAl sites are removed from the framework during phosphatation and the amount of Brønsted acid sites decreases further.

During hydrothermal treatment of the phosphated zeolite [Z]$_{2P}$, steam penetrates deep into the zeolite micropores, creating small mesopores. Phosphorus species are hydrolyzed to smaller phosphates that migrate further into the zeolite. Dealumination takes place and Si-O-Al bonds are broken. TFAl species that are not interacting with phosphorus are (partially) expelled from the framework and form Al6-O-P species (Scheme 3.1). The decrease in TFAl species leads to a further decrease in Brønsted acid site number. As phosphorus is present in higher concentrations close to the surface, the outer shell of the zeolite is better protected against dealumination during steam treatment. As such, distorted TFAl species due to phosphorus interaction do not seem to be affected by steam. Steaming has a minimal effect on sample [ST]$_{2P}$. There is a limited amount of dealumination and limited loss of Brønsted acid site number. The

$AlPO_4$ phase is not influenced by the hydrothermal treatment. To state that the $AlPO_4$ phase has a similar promoting effect on H-ZSM-5 as phosphorus is speculative at the moment, but hydrothermal stabilization effects have been reported for $AlPO_4$ bound H-ZSM-5 extrudates.[58]

When comparing the ^{27}Al MAS NMR data of $[Z]_{2P}$ and $[ST]_{2P}$, it is apparent that material $[Z]_{2P}$ has more TFAl species than $[ST]_{2P}$ following from ^{27}Al MAS NMR. This is in line with FT-IR data showing a larger amount of Brønsted acid sites in $[Z]_{2P}$. However, the differences are quite small and sample $[Z]_{2P}$ loses relatively more active sites than sample $[ST]_{2P}$ during steaming. When comparing the ^{29}Si NMR spectra of samples $[Z]_{2P}$ and $[ST]_{2P}$ one can observe that sample $[Z]_{2P}$ has much more Si-O-Al bonds than sample $[ST]_{2P}$. This can be explained by the fact that sample $[Z]_{2P}$ has no EFAl species and the decrease in active sites can be attributed to distorted Al species, which are still connected to the framework with at least one Si-O-Al bond. Sample $[ST]_{2P}$ has EFAl species present in the $AlPO_4$ phase, hence almost no Si-O-Al bonds. $[ST]_{2P}$ has a slightly smaller micropore volume, but a much broader distribution of pore sizes ranging from micropores to mesopores, possibly making the material better accessible for molecules.

Sample $[Z]_{2P}$ has a significant broader range of various phosphates, while for sample $[ST]_{2P}$ most phosphorus species are present in the $AlPO_4$ phase. Whereas the phosphates of sample $[Z]_{2P}$ are found on the zeolite exterior, phosphorus is more randomly distributed throughout sample $[ST]_{2P}$, with the exception of the $AlPO_4$ islands found for sample $[ST]_{2P}$. The more homogeneous distribution of phosphorus in $[ST]_{2P}$ could explain why no signs of aggregation are observed, while phosphorus in the form of surface phosphate deposits promotes aggregation in sample $[Z]_{2P}$.

Hydrothermal treatment of the samples leads to some dealumination in both materials. For sample $[Z]_{2P-ST}$ the loss of TFAl and Brønsted acid sites is relatively high. We attribute this to the apparent observation that phosphorus is not interacting to any particular extent with TFAl atoms located deeper in the interior of sample $[Z]_{2P}$. This would explain why these species are dislodged and to a certain amount expelled from the framework during hydrothermal conditions, i.e. the inner regions of sample $[Z]_{2P}$ are prone to the regular effects of steam. There is no formation of crystalline $AlPO_4$ in sample $[Z]_{2P-ST}$, but the formation of a small fraction of Al6 in AlPO species is observed with ^{27}Al MAS NMR. It is suggested that these species are still partly attached to the framework. Zhuang et al. have shown that for a prolonged steam treatments of phosphated H-ZSM-5 crystalline $AlPO_4$ will form eventually.[5] For sample $[ST]_{2P-ST}$ the loss of active sites from step $[ST]_{2P}$ to $[ST]_{2P-ST}$ is quite minimal. Both samples have a similar amount of

TFAl sites and Brønsted acidity after hydrothermal treatment. While the micropore volume is almost the same for both samples, the total pore volume of $[ST]_{2P\text{-}ST}$ is larger than that of $[Z]_{2P\text{-}ST}$.

Most importantly, this Chapter shows that are to be two different types of phosphorus-aluminum interactions, i.e. phosphorus interacting with framework aluminum and phosphorus interacting with extra-framework aluminum. By combining ^{27}Al (MQ) MAS NMR, ^{31}P MAS NMR spectroscopy, and Al K-edge and P K-edge XANES micro-spectroscopy we are able to distinguish between these interaction types. Motivated by the obtained insights the combined spectroscopy approach will be applied in the following Chapters as well.

3.5 Conclusions

Depending on the starting material, the phosphatation of zeolite H-ZSM-5 follows two different pathways. When zeolite H-ZSM-5 is directly phosphated, phosphorus species penetrate only partially into the zeolite. The highest concentration of phosphorus moieties are located close or at the zeolite external surface, where they promote particle aggregation. Where phosphorus enters the zeolite pores it interacts with Al, although it is not clear what the nature of the interaction exactly is. No real dealumination takes place, as extra-framework aluminum (EFAl) species are not observed. However, due to the thermal treatment that is used to stabilize phosphorus, many tetrahedrally coordinated framework aluminum (TFAl) species are partially dislodged from the framework. Both interaction of P with Al and the consecutive thermal treatment lead to a decrease in Brønsted acid sites number.

When H-ZSM-5 is pre-steam treated, a mesoporous, dealuminated material is formed, containing an extra-framework alumina phase. When this material is phosphated, phosphoric acid readily reacts with EFAl species and forms an extra-framework crystalline tridymite $AlPO_4$ phase. This phase appears to be predominantly located in the zeolite mesopores, which were formed during steaming. There are specific regions where large concentrations of $AlPO_4$ are found. It is uncertain if $AlPO_4$ is present in the zeolite micropores.

Hydrothermal treatment of the phosphated samples leads to a certain extent to progressed dealumination of the materials. However, the relative dealumination of the directly phosphated material is more severe than it is for the pre-steam treated counterpart, especially deeper into the zeolitic interior, where less phosphorus is located. Aluminum species that are distorted by the presence of phosphorus are not affected by steam treatment. However, dealumination leads for

both samples to a minor formation of Al6-O-P species. Both pathways end up with materials containing a similar amount of active sites and micropore volume. However, pre-steamed H-ZSM-5 has larger pore volume and a broad distribution of pore sizes, expectedly leading to a material with a more accessible interior.

Acknowledgements

References

[1]   C. S. Triantafillidis, A. G. Vlessidis, L. Nalbandian and N. P. Evmiridis, *Micropor. Mesopor. Mater.* **2001**, *47*, 369-388.

[2]   G. Lischke, R. Eckelt, H. G. Jerschkewitz, B. Parlitz, E. Schreier, W. Storek, B. Zibrowius and G. Öhlmann, *J. Catal.* **1991**, *132*, 229-243.

[3]   J. C. Védrine, A. Auroux, P. Dejaifve, V. Ducarme, H. Hoser and S. Zhou, *J. Catal.* **1982**, *73*, 147-160.

[4]   K. H. Chandawar, S. B. Kulkarni and P. Ratnasamy, *Appl. Catal.* **1982**, *4*, 287-295.

[5]   J. Zhuang, D. Ma, G. Yang, Z. Yan, X. Liu, X. Liu, X. Han, X. Bao, P. Xie and Z. Liu, *J. Catal.* **2004**, *228*, 234-242.

[6]   S. Yang, J. N. Kondo and K. Domen, *Catal. Today* **2002**, *73*, 113-125.

[7]   T. Blasco, A. Corma and J. Martínez-Triguero, *J. Catal.* **2006**, *237*, 267-277.

[8]   S. M. Cabral de Menezes, Y. L. Lam, K. Damodaran and M. Pruski, *Micropor. Mesopor. Mater.* **2006**, *95*, 286-295.

[9]   G. Caeiro, P. Magnoux, J. M. Lopes, F. R. Ribeiro, S. M. C. Menezes, A. F. Costa and H. S. Cerqueira, *Appl. Catal. A-Gen* **2006**, *314*, 160-171.

[10]   Y.-J. Lee, J. M. Kim, J. W. Bae, C.-H. Shin and K.-W. Jun, *Fuel* **2009**, *88*, 1915-1921.

[11]   B. Viswanathan and A. C. Pulikottil, *Catal. Lett.* **1993**, *22*, 373-379.

[12]   G. Zhao, J. Teng, Z. Xie, W. Jin, W. Yang, Q. Chen and Y. Tang, *J. Catal.* **2007**, *248*, 29-37.

[13]   M. J. B. Cardoso, D. D. O. Rosas and L. Y. Lau, *Adsorption* **2005**, *11*, 577-580.

[14]   X. Gao, Z. Tang, H. Zhang, C. Liu, Z. Zhang, G. Lu and D. Ji, *Kor. J. Chem. Eng.* **2010**, *27*, 812-815.

[15]   M. Göhlich, W. Reschetilowski and S. Paasch, *Micropor. Mesopor. Mater.* **2011**, *142*, 178-183.

[16]   K. Ramesh, C. Jie, Y.-F. Han and A. Borgna, *Ind. Eng. Chem. Res.* **2011**, *49*, 4080-4090.

[17]   G. Rumplmayr and J. A. Lercher, *Zeolites* **1990**, *10*, 283-287.

[18]   Z. Song, A. Takahashi, I. Nakamura and T. Fujitani, *Appl. Catal. A-Gen* **2011**, *384*, 201-205.

[19]   H. Vinek, G. Rumplmayr and J. A. Lercher, *J. Catal.* **1989**, *115*, 291-300.

[20]   N. Xue, R. Olindo and J. A. Lercher, *J. Phys. Chem. C* **2010**, *114*, 15763-15770.

[21]   N. Zhan, Y. Hu, H. Li, D. Yu, Y. Han and H. Huang, *Catal. Commun.* **2010**, *11*, 633-637.

[22]   G. Yang, J. Zhuang, Y. Wang, D. Zhou, M. Yang, X. Liu, X. Han and X. Bao, *J. Mol. Struc.* **2005**, *737*, 271-276.

[23]   K. Damodaran, J. W. Wiench, S. M. Cabral de Menezes, Y. L. Lam, J. Trebosc, J. P. Amoureux and M. Pruski, *Micropor. Mesopor. Mater.* **2006**, *95*, 296-305.

[24]   A. Jentys, G. Rumplmayr and J. A. Lercher, *Appl. Catal.* **1989**, *53*, 299-312.

[25]   W. W. Kaeding and S. A. Butter, *J. Catal.* **1980**, *61*, 155-164.

[26]   J. A. Lercher and G. Rumplmayr, *Appl. Catal.* **1986**, *25*, 215-222.

[27]   G. Seo and R. Ryoo, *J. Catal.* **1990**, *124*, 224-230.

[28]   P. Tynjälä and T. T. Pakkanen, *Micropor. Mesopor. Mater.* **1998**, *20*, 363-369.

[29]   N. Xue, X. Chen, L. Nie, X. Guo, W. Ding, Y. Chen, M. Gu and Z. Xie, *J. Catal.* **2007**, *248*, 20-28.

[30]   J. Caro, M. Bülow, M. Derewinski, J. Haber, M. Hunger, J. Kärger, H. Pfeifer, W. Storek and B. Zibrowius, *J. Catal.* **1990**, *124*, 367-375.

[31]   R. Lü, Z. Cao and S. Wang, *J. Mol. Struc.-THEOCHEM* **2008**, *865*, 1-7.

[32]   A. Corma, V. Fornes, W. Kolodziejski and L. J. Martinez-Triguero, *J. Catal.* **1994**, *145*, 27-36.

[33]   L. R. Aramburo, E. de Smit, B. Arstad, M. M. van Schooneveld, L. Sommer, A. Juhin, T. Yokosawa, H. W. Zandbergen, U. Olsbye, F. M. F. de Groot and B. M. Weckhuysen, *Angew. Chem. Int. Ed.* **2012**, *51*, 3616-3619.

[34]   J. P. Amoureux, C. Fernandez and S. Steuernagel, *J. Magn. Reson. Ser. A* **1996**, *123*, 116-118.

[35]   L. R. Aramburo, Y. Liu, T. Tyliszczak, F. M. F. de Groot, J. C. Andrews and B. M. Weckhuysen, *ChemPhysChem* **2013**, *14*, 496-499.

[36]   J. Rouquerol, F. Rouquerol, P. Llewellyn, G. Maurin and K. S. Sing, *Adsorption by powders and porous solids: principles, methodology and applications*, Academic press London, **1999,** pp. 389-396.

[37]   P. L. Llewellyn, Y. Grillet, J. Patarin and A. C. Faust, *Micropor. Mater.* **1993**, *1*, 247-256.

[38]   J. Klinowski, *Prog. Nucl. Mag. Res. Sp.* **1984**, *16*, 237-309.

[39]   P. Ildefonse, D. Cabaret, P. Sainctavit, G. Calas, A. M. Flank and P. Lagarde, *Phys. Chem. Miner.* **1998**, *25*, 112-121.

[40]   G. L. Woolery, G. H. Kuehl, H. C. Timken, A. W. Chester and J. C. Vartuli, *Zeolites* **1997**, *19*, 288-296.

[41]   J. A. van Bokhoven, D. C. Koningsberger, P. Kunkeler, H. van Bekkum and A. P. M. Kentgens, *J. Am. Chem. Soc.* **2000**, *122*, 12842-12847.

[42]   S. M. Abubakar, D. M. Marcus, J. C. Lee, J. O. Ehresmann, C. Y. Chen, P. W. Kletnieks, D. R. Guenther, M. J. Hayman, M. Pavlova, J. B. Nicholas and J. F. Haw, *Langmuir* **2006**, *22*, 4846-4852.

[43]   C. Coelho, T. Azaïs, L. Bonhomme-Coury, G. Laurent and C. Bonhomme, *Inorg. Chem.* **2007**, *46*, 1379-1387.

[44]   J.-P. Gilson, G. C. Edwards, A. W. Peters, K. Rajagopalan, R. F. Wormsbecher, T. G. Roberie and M. P. Shatlock, *J. Chem. Soc. Chem. Comm.* **1987**, 91-92.

[45]   J. Sanz, V. Fornés and A. Corma, *J. Chem. Soc. Faraday Trans.* **1988**, *84*, 3113-3119.

[46]   E. Brunner, H. Ernst, D. Freude, T. Fröhlich, M. Hunger and H. Pfeifer, *J. Catal.* **1991**, *127*, 34-41.

[47]   M. P. Peeters, J. W. de Haan, L. J. van de Ven and J. H. van Hooff, *J. Phys. Chem.* **1993**, *97*, 5363-5369.

[48]   M. Hunger in *Catalytically active sites: generation and characterization*, *Vol. 2* Wiley-VCH: Weinheim, **2010**, pp. 493-546.

[49]   H. Pastore, S. Coluccia and L. Marchese, *Annu. Rev. Mater. Res.* **2005**, *35*, 351-395.

[50]   S. Daviero, A. Ibanez, C. Avinens, A. Flank and E. Philippot, *Thin Solid Films* **1993**, *226*, 207-214.

[51]   M. Ghiaci, A. Abbaspur, M. Arshadi and B. Aghabarari, *Appl. Catal. A-Gen* **2007**, *316*, 32-46.

[52]   M. Ghiaci, A. Abbaspur and R. J. Kalbasi, *Appl. Catal. A-Gen* **2006**, *298*, 32-39.

[53]   R. J. Kalbasi, M. Ghiaci and A. R. Massah, *Appl. Catal. A-Gen* **2009**, *353*, 1-8.

[54]   I. Lukes, M. Borbaruah and L. D. Quin, *J. Am. Chem. Soc.* **1994**, *116*, 1737-1741.

[55]   M. Low and P. Ramamurthy, *J. Phys. Chem.* **1968**, *72*, 3161-3167.

[56]   I. Hannus, I. Kiricsi, P. Fejes, A. Fonseca, J. B.Nagy, W. O. Parker Jr and Z. Szendi, *Zeolites* **1996**, *16*, 142-148.

[57]   T. Kovalchuk, H. Sfihi, A. Korchev, A. Kovalenko, V. Il'in, V. Zaitsev and J. Fraissard, *J. Phys. Chem. B* **2005**, *109*, 13948-13956.

[58]   Y.-J. Lee, Y.-W. Kim, N. Viswanadham, K.-W. Jun and J. W. Bae, *Appl. Catal. A-Gen* **2010**, *374*, 18-25.

[59]   H. Wang and T. J. Pinnavaia, *Angew. Chem. Int. Ed.* **2006**, *45*, 7603-7606.
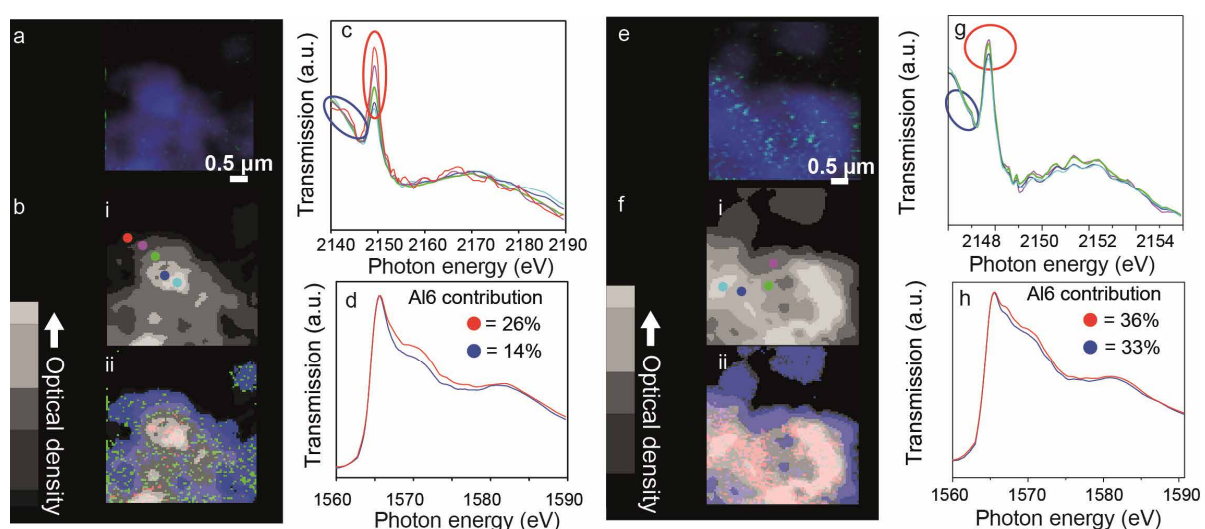
3.6 Appendix
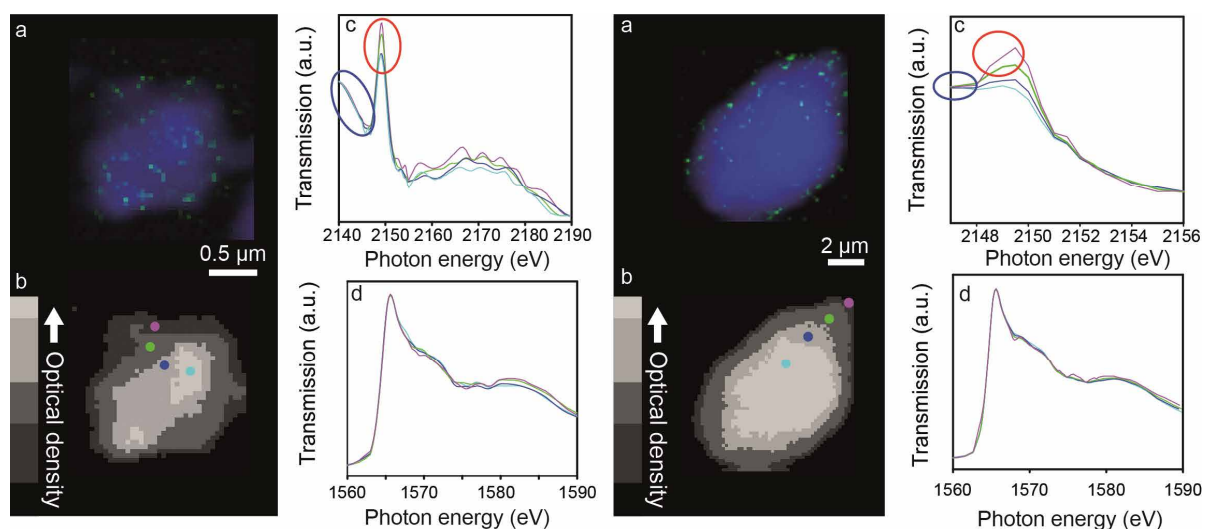
Figure A3.1 Two [Z]$_{2P}$ clusters measured with STXM showing the distribution of phosphorus. (a and e) Phosphorus distribution (green) on particle (blue). The particle map is constructed from the average of the P pre-edge maps (blue circle in spectra (c), the phosphorus distribution is constructed by subtracting the average maps of the P K-edge from with the P pre-edge (red and blue circles in spectra (c). (b and f) Optical density masks overlaid on the Al K-edge and P K-edge stacks. Each mask probes exclusively the pixels on which it is overlaid. The bar on the left indicates the ratio of the optical density probed. Full bar represents 1.00 and the brightest grey part, the top 0.15 dense pixels etc. The colored circles function as an indicator for the respective P K-edge and Al K-edge XANES that correspond to the masks in which they are placed. (c and g) P K-edge XANES of the corresponding optical density. The spectra are normalized at the transmission intensity at 2140 eV and 2190 eV (c) and 2147 eV and 2156 eV (g). (d and h) Al K-edge spectra of the corresponding optical density. It can be observed that relative more phosphorus is present in the thin regions of the particles, while Al is homogeneously distributed throughout the crystal.

Figure A3.2 Two [Z]$_{2P\text{-}ST}$ clusters measured with STXM showing the distribution of phosphorus. (a and e) Phosphorus distribution (green) on particle (blue). The particle map is constructed from the average of the P pre-edge maps (blue circle in spectra (c), the phosphorus distribution is constructed by subtracting the average maps of the P K-edge from with the P pre-edge (red and blue circles in spectra (c). (b i and f i) Optical density masks overlaid on the P K-edge stack. Each mask probes exclusively the pixels on which it is overlaid. The bar on the left indicates the ratio of the optical density probed. Full bar represents 1.00 and the brightest grey the top 0.15 dense pixels etc. The colored circles function as an indicator for the respective P K-edge spectra that correspond to the

masks in which they are placed. (b ii and f ii) Masks overlaid on the Al K-edge stack to probe different states of Al. The blue and red Al K-edge XANES in (d) correspond to the red and blue masks. The green mask shows the distribution of phosphorus. (c and g) P K-edge XANES of the corresponding optical density. The spectra are normalized at the transmission intensity at 2140 eV and 2190 eV (c) and 2147 eV and 2155 eV (g). (d and h) Al K-edge spectra of the corresponding to the red and blue masks in (b ii). It can be observed that more phosphorus is present in the thin regions of the particles, while Al contains more Al6 species in the thicker regions. Contributions of boehmite and NH_4-ZSM-5 have been used as references to determine the fractions of Al4 and Al6 species as is explained in Figure 3.3.
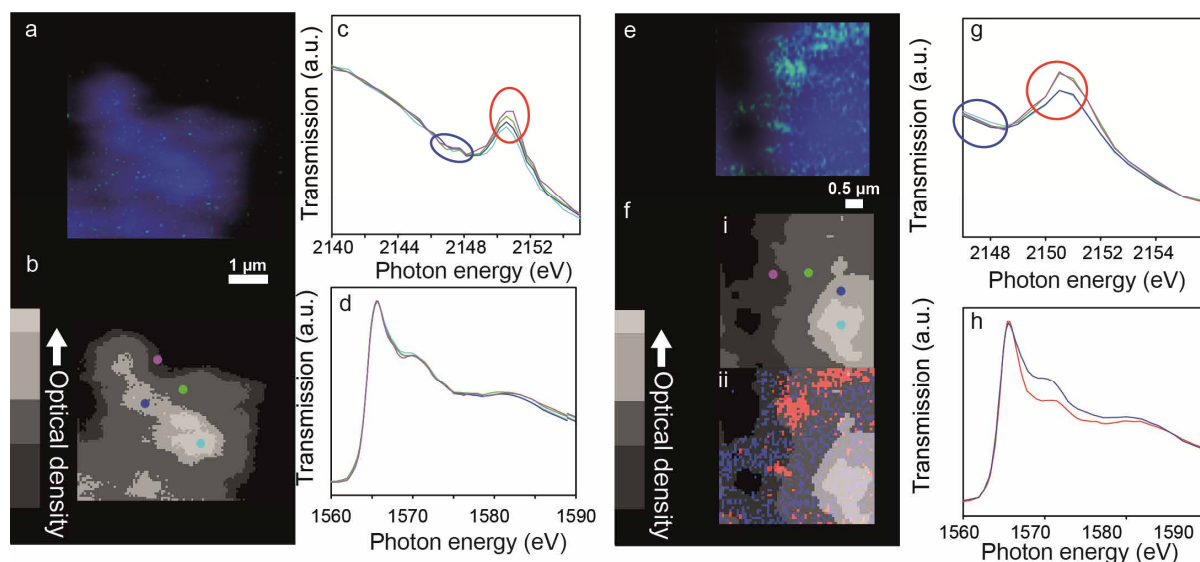
Figure A3.3 Left $[ST]_{2P}$ cluster and right $[ST]_{2P-ST}$ cluster, measured with STXM showing the distribution of phosphorus. a and e) Phosphorus distribution (green) on particle (blue). The particle map is constructed from the average of the P pre-edge maps (blue circle in spectra (c and g), the phosphorus distribution is constructed by subtracting the average maps of the P K-edge from with the P pre-edge (red and blue circles in spectra (c and g). (b and f i) Optical density masks overlaid on the Al K-edge and P K-edge stacks. Each mask probes exclusively the pixels on which it is overlaid. The bar on the left indicates the raTtio of the optical density probed. Full bar represents 1.00 and the brightest grey the top 0.15 dense pixels etc. The colored circles function as an indicator for the respective P K-edge and (Al K-edge only for b) XANES that correspond to the masks in which they are placed. (c and g) P K-edge XANES of the corresponding optical density. The spectra are normalized at the transmission intensity at 2140 eV and 2155 eV (c) and 2147 eV and 2155 eV. (d) Al K-edge XANES of the corresponding optical density. (f ii) Masks overlaid on the Al K-edge stack to probe different states of Al. The blue and red Al K-edge XANES in h) correspond to the red and blue masks. h) Al K-edge spectra corresponding to the red and blue masks in (f ii).
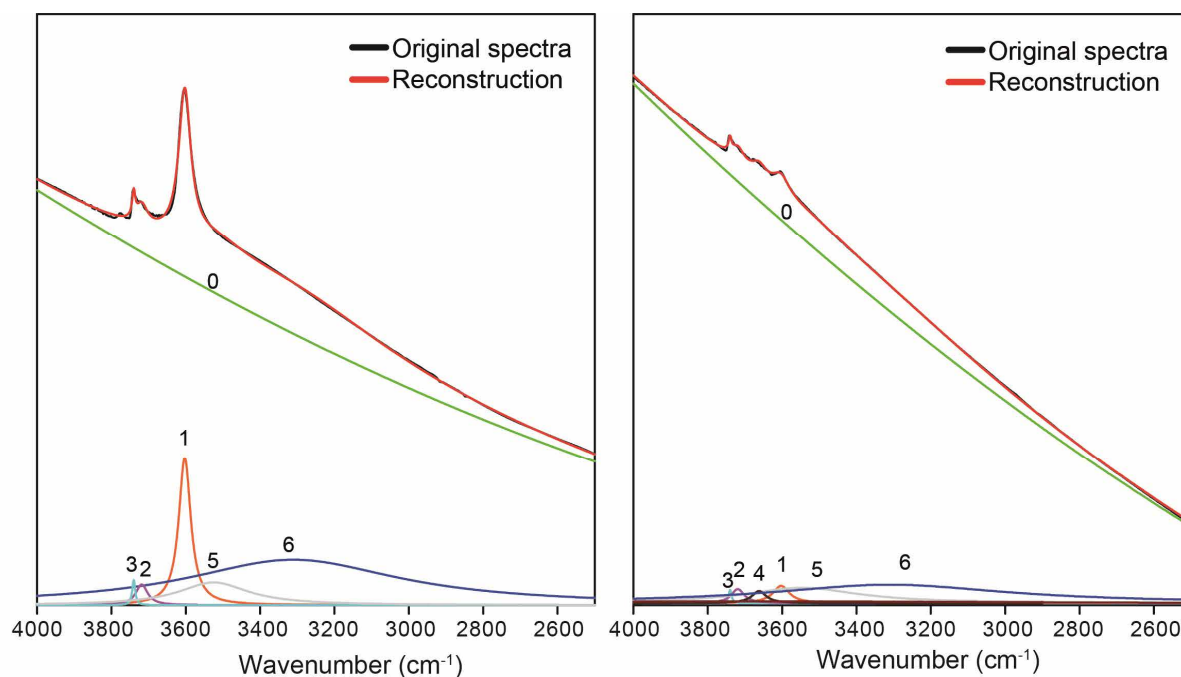
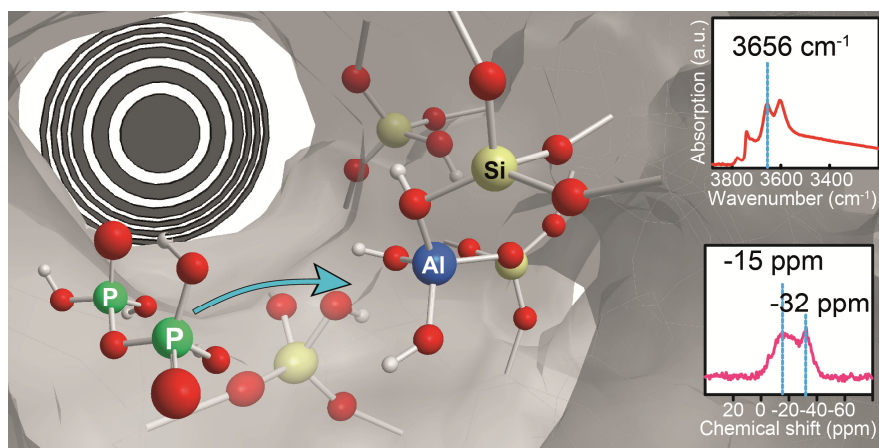**Figure A3.4** Examples of the deconvolution of the FT-IR spectra. Left) Sample [Z]. Right) Sample [ST]$_{2P-ST}$.

Table A3.1 Parameters used for FT-IR spectra deconvolution

Type	Center	Height	FWHM	Type
0 Quadratic	-	-	-	
1 Lorentzian	3603[a], 3602[b], 3601[c], 3602[d], 3602[e], 3603[f]	0.25[a], 0.08[b], 0.04[c], 0.08[d], 0.04[e], 0.03[f]	39.11[a], 39.11[b], 41.83[c], 39.62[d], 42.69[e], 42.91[f]	Si-OH-Al
2 Lorentzian	3719[a], 3720[b], 3720[c], 3720[d], 3720[e], 3719[f]	0.03[a], 0.04[b], 0.02[c], 0.03[d], 0.03[e], 0.03[f]	38.31[a], 27.96[b], 33.34[c], 42.82[d], 59.01[e], 53.30[f]	Si-OH (internal)
3 Lorentzian	3740[a], 3740[b], 3741[c], 3741[d], 3741[e], 3740[f]	0.04[a], 0.03[b], 0.02[c], 0.03[d], 0.02[e], 0.02[f]	9.63[a], 7.98[b], 7.89[c], 9.71[d], 7.23[e], 9.77[f]	Si-OH (external)
4 Lorentzian	3653[b], 3657[c], 3662[d], 3662[e], 3662[f]	0.05[b], 0.03[c], 0.03[d], 0.02[e], 0.02[f]	86.35[b], 80.89[c], 55.95[d], 55.95[e], 55.95[f]	Al-OH
5 Lorentzian	3673[e], 3677[f]	0.003[e], 0.003[f]	4.15[e], 9.19[f]	P-OH
6 Lorentzian	3311[a], 3311[b], 3311[c], 3311[d], 3311[e], 3311[f]	0.08[a], 0.07[b], 0.05[c], 0.05[d], 0.04[e], 0.03[f]	705.98[a], 705.98[b], , 705.98[c], 705.98[d], 705.98[e], , 705.98[f]	unknown
7 Lorentzian	3525[a], 3525[b], 3546[c], 3546[d], 3546[e], 3546[f]	0.04[a], 0.05[b], 0.03[c], 0.04[d], 0.03[e], 0.03[f]	227.05[a], 227.05[b], 227.05[c], 227.05[d], 227.05[e], 227.05[f]	unknown

[a] [Z] [b] [Z]$_{2P}$ [c] [Z]$_{2P-ST}$ [d] [ST] [e] [ST]$_{2P}$ [f] [ST]$_{2P-ST}$

Local Silico-Aluminophosphate Interfaces within Phosphated H-ZSM-5 Zeolites

I n order to elucidate phosphorus-zeolite H-ZSM-5 interactions, a variety of phosphorus-modified zeolite H-ZSM-5 materials were studied with a multi-pronged spectroscopic approach. By deploying single pulse ^{27}Al, ^{31}P MAS NMR, 2-D ^{27}Al-^{31}P HETCOR, ^{27}Al MQ MAS NMR spectroscopy, TPD of pyridine monitored by FT-IR spectroscopy, and STXM, the interplay and influence of acidity, thermal treatment and phosphorus on the structure and acidity of H-ZSM-5 were established. It was found that while acid treatment did not affect the zeolite structure, thermal treatment leads to the breaking of Si-OH-Al bonds, a decrease in strong acid site number and the formation of terminal Al-OH groups. No extra-framework aluminum species were observed. Phosphorus precursors interact with the zeolitic framework through hydrogen bonds and physical coordination, as phosphorus species can be simply washed out with hot water. After phosphatation and thermal treatment two effects occur simultaneously, namely (i) Phosphorus species transform into water insoluble condensed poly-phosphoric acid and (ii) Phosphoric acid binds irreversibly with the terminal Al-OH groups of partially dislodged four-coordinated framework aluminum, forming local silico-aluminophosphate interfaces. These interfaces are potentially the origin of increased hydrothermal stability in phosphated zeolite H-ZSM-5.

Chapter 4

4.1 Introduction

As has already been discussed in length in Chapters 1-3 hydrothermal stabilization of H-ZSM-5 is an important issue in both the fluid-catalytic-cracking (FCC) process as the methanol-to-hydrocarbon-process. Water that forms during the regeneration of coke or during the methylation of methanol, slowly leads to permanent deactivation, due to dealumination of the zeolite. Addition of phosphorus to the zeolite stabilizes the framework aluminum atoms during hydrothermal conditions. Furthermore, it has been found that phosphation of H-ZSM-5 leads to improved selectivity towards propylene in hydrocarbon cracking and the methanol-to-olefins reaction, which is often attributed to a decrease in acid site number and strength (Chapters 1.5 and 2.4) While it needs no further explanation that improved propylene selectivity is beneficial, the reasons behind the decrease in acid-site strength is hotly debated, as the exact nature of phosphorus-zeolite interactions are not yet understood. [1-8]

These disagreements on zeolite-phosphorus interaction have led to much confusion with regard to the interpretation of data and spectra, as different authors attribute similar peaks to different species, e.g. in ^{27}Al magic angle spinning nuclear magnetic resonance (MAS NMR) spectroscopy and especially ^{31}P MAS NMR.[1-2, 8-9] A specific example, was discussed in Chapter 3: the ^{27}Al MAS NMR resonance that was suggested to stem from interactions of phosphorus with distorted four-coordinated framework aluminum is not undisputed. Another complicating factor is the synthesis conditions used during phosphatation, which vary for the different research reports in the open literature.

There are three parameters that can affect the structure of the zeolite material, namely (i) acid leaching of aluminum by the acidic precursor H_3PO_4, which is often used, (ii) thermal treatment that is customarily performed after phosphorus introduction, and (iii) the actual presence of phosphorus species. Especially the effect of thermal treatment has never been investigated in detail, as it is nearly always performed after phosphorus introduction directly. Thermal treatment leads to the hydrolysis of Si-O-Al bonds and condensation of phosphates, and therefore have a strong effect on the coordination environment of framework aluminum atoms and phosphorus species. In order to observe to sole effect of phosphorus on the zeolitic framework, it is important to study the phosphorus zeolite interactions before thermal treatment.
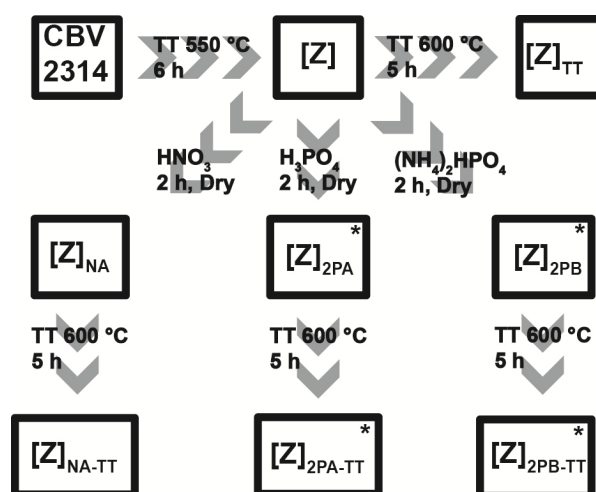
In this Chapter we aim to provide a better understanding of the physicochemical processes that take place during phosphatation and obtain qualitative insight into phosphorus-zeolite interactions. A set of samples, representing different steps in the phosphatation process, was

prepared of which an overview is presented in Scheme 4.1. These samples have been studied using a multi-pronged spectroscopic approach, consisting of Fourier transform infrared spectroscopy (FT-IR), single pulse ^{27}Al, ^{31}P MAS NMR, 2-D heteronuclear ^{27}Al-^{31}P correlation (HETCOR), ^{27}Al MQ MAS NMR spectroscopy, temperature programmed desorption (TPD) of pyridine, as monitored with FT-IR, and scanning transmission X-ray microscopy (STXM). Using this combination of characterization techniques we have elucidated several physicochemical phenomena, i.e. the state, location and interaction of aluminum and phosphorus species, the number, type and strength of acid sites and the effects of the phosphate precursor, acid- and thermal treatment. Spectroscopic signatures for surface and bulk species will be presented to facilitate interpretation of past and future results. Finally, a synthesis route is proposed to obtain local silico-aluminophosphate (SAPO) interfaces within H-ZSM-5 materials, which are considered to be the potential inorganic phases that lead to an increased hydrothermal stability.

4.2 Experimental methods

4.2.1 Sample preparation

Commercially available Zeolyst CBV 2314 NH$_4$-ZSM-5 (Si/Al ratio = 11.5) was calcined in flowing dry air at 550°C for 6 h. The obtained H-ZSM-5 material is referred to as [Z]. From the parent sample [Z] all other samples have been made. An overview of sample preparation is shown in Scheme 4.1. Sample [Z]$_{NA}$ was prepared by suspending 1.2 g of [Z] in a 200 ml aqueous solution of nitric acid (pH = 2.7) and 200 ml hot water (70°C), where it was stirred for 2 h. Afterwards the sample was retrieved by filtration and dried at 150°C. Phosphatation

Scheme 4.1 Preparation scheme of the samples under study: TT = Thermal treatment, HT = Hydrothermal treatment, and * = Sample contains an eluted variety.
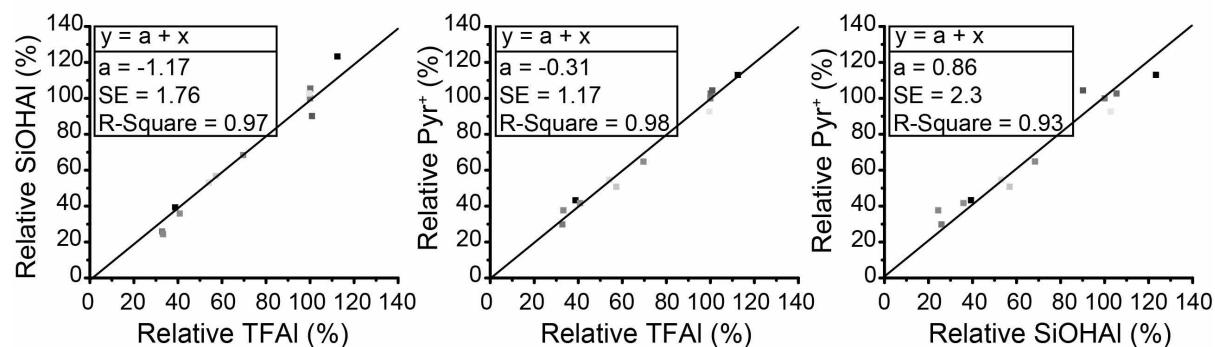
was performed as described by Xue et al. [10] Sample [Z]$_{2PA}$ was prepared by suspending 2.4 g of [Z] in an aqueous solution of an appropriate amount of H$_3$PO$_4$ in 200 ml H$_2$O (P/Al ratio = 0.5, pH = 2.7), where it was stirred for 2 h. Afterwards, the solvent was removed by rotary evaporation.

Figure 4.2 Relation between SiOHAl groups, tetrahedrally coordinated framework aluminum (TFAl) species and Brønsted acid sites. Values of SiOHAl correspond to the area of the deconvoluted 3600 cm^{-1} band of each sample, relative to the area of the deconvoluted 3600 cm^{-1} band of [Z]. Details of the deconvolution procedure can be found in Table A1. Values for TFAl correspond to the relative contribution of the deconvoluted 55 ppm peak of each sample relative to the relative contribution of the deconvoluted 55 ppm peak of [Z]. Details of the deconvolution procedure can be found in Table A2. Values for the pyridinium ions correspond to the baseline corrected area of the 1540 cm^{-1} pyridinium ion N-H stretch band of each sample, relative to area of the 1540 cm^{-1} band for sample [Z] at 200 °C.

Subsequently, the sample was dried overnight at 150°C. Sample [Z]$_{2PA-e}$ was prepared by suspending 0.6 g of sample [Z]$_{2PA}$ in 200 ml hot water (70°C), where it was stirred for 2 h and subsequently filtered. [Z]$_{2PB}$ was prepared by suspending 2.4 g of [Z] in an aqueous solution of an appropriate amount of (NH$_4$)$_2$HPO$_4$ in 200 ml H$_2$O (P/Al ratio = 0.5, pH = 7.8), where it was stirred for 2 h. Afterwards, the solvent was removed by rotary evaporation. Subsequently, the sample was dried overnight at 150°C. Sample [Z]$_{2PB-e}$ was prepared by suspending 0.6 g of sample [Z]$_{2PB}$ in 200 ml hot water (70°C), where it was stirred for 2 h. Afterwards, the sample was retrieved by filtration and dried at 150°C. Samples [Z]$_{TT}$, [Z]$_{NA-TT}$, [Z]$_{2PA-TT}$, and [Z]$_{2PB-TT}$ were prepared by calcination of sample [Z], [Z]$_{NA}$, [Z]$_{2PA}$ and [Z]$_{2PB}$ respectively in static air at 600°C, for 5 h. Samples [Z]$_{2PA-TT}$ e, and [Z]$_{2PB-TT-e}$ were prepared by suspending 0.6 g of sample [Z]$_{2PA-TT}$ and [Z]$_{2PB-TT}$ respectively in 200 ml hot water (70°C), where they were stirred for 2 h filtered.

Table 4.1 ICP results for phosphorus-containing samples.

Sample	P-content (wt%)	Remaining[a] (%)	Sample	P-content (wt%)	Remaining[a] (%)
[Z]$_{2PA}$	2.26	-	[Z]$_{2PB-e}$	1.01	43
[Z]$_{2PA-e}$	0.56	25	[Z]$_{2PB-TT}$	2.30	98
[Z]$_{2PA-TT}$	2.18	96	[Z]$_{2PB-TT-e}$	1.73	75
[Z]$_{2PA-TT-e}$	1.59	73	[Z]$_{TT-2PA}$	2.19	-
[Z]$_{2PB}$	2.35	-	[Z]$_{TT-2PA-e}$	0.82	37

[a] Relative to the parent material of the sample.

Sample $[Z]_{TT}$ was resynthesized using identical conditions. 0.6 g of sample $[Z]_{TT}$ remade was suspended in a 200 ml aqueous solution of 0.06 M HNO_3 (pH below 0.89) where it was stirred overnight at 70 °C and subsequently filtered and dried. This acid leached (L) sample is deemed $[Z]_{TT-L}$. Next, 1.2 g of sample $[Z]_{TT}$ remade was phosphated with H_3PO_4 using identical conditions as sample $[Z]_{2PA}$ this sample is deemed $[Z]_{TT-2PA}$. Sample $[Z]_{TT-2PA-e}$ was by prepared starting from $[Z]_{TT-2PA}$ and applying an identical procedure as for sample $[Z]_{2PA-e}$. Phosphorus loadings were determined by ICP analysis.

4.2.2 Solid-state nuclear magnetic resonance

With the exception of samples $[Z]_{TT}$ remade, $[Z]_{TT-L}$ $[Z]_{TT-2PA}$, and $[Z]_{TT-2PA-e}$ all MAS NMR experiments were performed at 18.8 T on a Bruker Avance 800 MHz spectrometer using a 3.2 mm HX low gamma MAS probe at room temperature. The MAS rate was 20 kHz for all experiments. The ^{27}Al NMR spectra were obtained using a pulse length of 1 µs, 1000 scans and a recycling delay of 2 s. The ^{27}Al 3Q-MAS were performed with a three-pulse sequence. The spectra were obtained using 540 scans and a recycling delay of 1 s. The ^{31}P spectra were obtained using a pulse length of 1.8 µs, 64 scans and with a recycle delay of 60 s. The ^{27}Al-^{31}P CP experiments were acquired with 1600 scans, a recycle delay of 1 s, and with a contact time of 8000 µs. The chemical shifts of ^{27}Al, and ^{31}P were externally referenced to 1M $Al(NO_3)_3$(aq), and 85% H_3PO_4(aq), respectively. All curve fittings were performed using the Dmfit software.[11]

The NMR experiments for the samples $[Z]_{TT}$ remade, $[Z]_{TT}$ A.L., $[Z]_{TT-2PA}$, and $[Z]_{TT-2PA-e}$, were performed at 11.7 T on a Bruker Avance III 500 MHz spectrometer using a 4 mm MAS probe at room temperature. The MAS rate was 15 kHz for all experiments. The 27Al NMR spectra were obtained using $\pi/12$ pulses, 1000 scans and a recycling delay of 0.5 s at a rf-field of 94 kHz. The 31P spectra were obtained using a pulse length of 1.8 µs, 64 scans and

Table 4.2 Relative amounts of SiOHAl groups, TFAl atoms and pyridinium ions.

Sample	SiOHAl (%)[a]	TFAl (%)[a]	Pyr$^+$ (%)[a]
[Z]	100	100	100
$[Z]_{TT}$	57	57	51
$[Z]_{NA}$	105	100	103
$[Z]_{NA-TT}$	53	53	55
$[Z]_{2PA}$	68	70	65
$[Z]_{2PA-e}$	103	100	93
$[Z]_{2PA-TT}$	26	33	30
$[Z]_{2PA-TT-e}$	39	39	43
$[Z]_{2PB}$	90	101	104
$[Z]_{2PB-e}$	123	112	113
$[Z]_{2PB-TT}$	24	33	38
$[Z]_{2PB-TT-e}$	36	41	42

[a] Relative to sample [Z].

with a recycle delay of 60 s. The chemical shifts of ^{27}Al, and ^{31}P were externally referenced to 1M Al(NO$_3$)$_{3(aq)}$, and 85% H$_3$PO$_{4(aq)}$, respectively.

Table 4.3 ^{27}Al 1D MAS NMR contributions of deconvoluted resonances.

Sample	TFAl (%)	TFAl$_{dis}$ (%)	Al5 (%)	OFAl (%)	Al6$_{new}$ (%)	Resonance[a]	Al4[b]/Al6[c]
[Z]	85	-	-	15	-	-	5.5
[Z]$_{TT}$	49	22	1	3	9	17	5.8
[Z]$_{NA}$	85	-	-	15	-	-	5.6
[Z]$_{NA-TT}$	46	22	2	4	10	16	4.8
[Z]$_{2PA}$	59	8	-	2	33	-	2.0
[Z]$_{2PA-e}$	84	-	-	7	9	-	16
[Z]$_{2PA-TT}$	28	38	4	2	29	-	2.2
[Z]$_{2PA-TT-e}$	33	29	-	7	13	18	3.1
[Z]$_{2PB}$	85	1	-	-	14	-	6.2
[Z]$_{2PB-e}$	95	-	-	-	5	-	19.0
[Z]$_{2PB-TT}$	28	39	4	2	28	-	2.2
[Z]$_{2PB-TT-e}$	35	29	-	4	17	15	3.0

[a] Broad underlying Gaussian at 20 ppm [b] Al4 = TFAl + TFAl$_{dis}$ [c] Al6 = OFAl + Al6$_{new}$.

4.2.3 Scanning transmission X-ray microscopy

Scanning transmission X-ray microscopy (STXM) experiments were performed at the Canadian Light Source Beamline 10ID-1. Samples were dispersed in H$_2$O and a droplet was placed on a silicon nitride window. After drying in air the sample was placed in the STXM chamber, which was subsequently evacuated to 10^{-1} mbar. A polarized X-ray beam was obtained using a 1.5 m long, 75 mm period Apple II undulator. The X-ray beam was focused to ~30 nm on the sample plane using a Fresnel zone plate (ZP). The beam from the ZP passed through a molybdenum-based order-sorting aperture (OSA), with a 50 μm pinhole. The OSA allowed only first-order ZP diffracted light to pass. Spectral image sequences (stacks) are measured by recording images over a range of photon energies. After aligning the image sequence, spectra of the whole or a subregion were extracted for comparison. All STXM data analysis was performed using aXis2000.
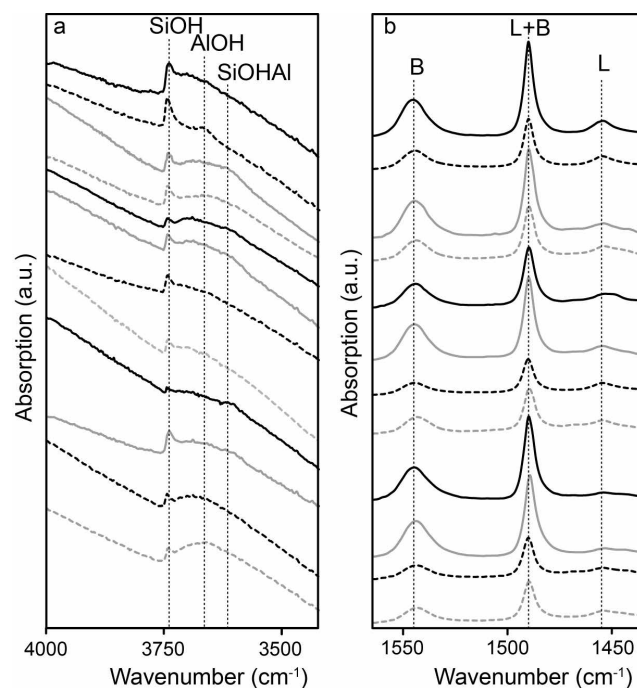
Figure 4.3 FT-IR spectra of pyridine TPD at 200°C for (a) the O-H stretch region and (b) the N-H stretch region of the following samples: From top to bottom [Z], [Z]TT, [Z]NA, [Z]NA-TT, [Z]2PA, [Z]2PA-e, [Z]2PB, and [Z]2PB-e [Z]2PA-TT, [Z]2PA-TT-e, [Z]2PB-TT, [Z]2PB-TT-e.

4.2.4 Fourier transform infrared spectroscopy

Fourier transform infrared (FT-IR) spectroscopy measurements were performed on self-supporting zeolite wafers. 15 mg of sample was pressed with 3 tons for 10 s into a thin disk. The sample was evacuated to 10^{-2} bar and heated with 7 °C/min to 600 °C and immediately cooled with steps of 25 K to 50 °C taking a spectrum at every interval. Pyridine was introduced in the vapour phase for 15 min and physisorbed pyridine was removed by outgassing at 50 °C and 10^{-2} bar for 30 min. TPD was performed by increasing the temperature in steps of 25°C to 600°C. For each step FT-IR spectra were taken with a Perkin-Elmer FT-IR instrument with an optical resolution of 4 cm^{-1} and 12 accumulations with wavenumbers ranging from 4000 cm^{-1} to 1000 cm^{-1}. Spectra were baseline corrected and normalized using the bands corresponding to zeolitic framework vibrations found at 1967 cm^{-1}, 1873 cm^{-1}, and 1637 cm^{-1}. To construct the pyridine temperature programmed desorption (TPD) profiles, the normalized areas of the 1540 cm^{-1} peak were calculated from T= 200 °C to 600°C. All values were a percentage relative to the area of the 1540 cm^{-1} band for sample [Z] at T = 200 °C.

4.3 Results

4.3.1 Effect of thermal and acid treatment

The zeolite H-ZSM-5 parent material [Z] under investigation has an ordered crystalline structure, which is confirmed by the data presented in Figure 4.4. The ^{27}Al MAS NMR spectrum shows an intense and sharp signal at 54 ppm, which stems from Al atoms located at four-coordinated T-atom positions in the framework (TFAl species).[12] The O-H stretch vibrations of charge compensating protons that are found at these positions can be observed in the FT-IR spectra at around 3605 cm^{-1}.[13] Another resonance signal in the ^{27}Al MAS NMR spectra is found at 0 ppm, which is known to originate from octahedral framework Al (OFAl).[14-15] Three other vibrational bands, located at 3721 cm^{-1}, 3742 cm^{-1}, and 3780 cm^{-1}, can be found in the FT-IR spectra. These bands correspond to internal silanol groups, external silanol groups and external Al-OH groups, respectively. [13] The FT-IR spectrum of adsorbed pyridine, presented in Figure 4.3, indicates that the sample contains both Brønsted acid sites and Lewis acid sites. Figure 4.5a shows that pyridine desorption reaches a maximum at around 525°C. The corresponding sites to this release are typically attributed to the Brønsted acid sites stemming from TFAl species.[16] The aluminum K-edge XANES of the parent sample presented in Figure 4.6 resembles those recorded for zeolite H-ZSM-5, with a white-line at 1566 eV and two features at +3 eV and a broad feature
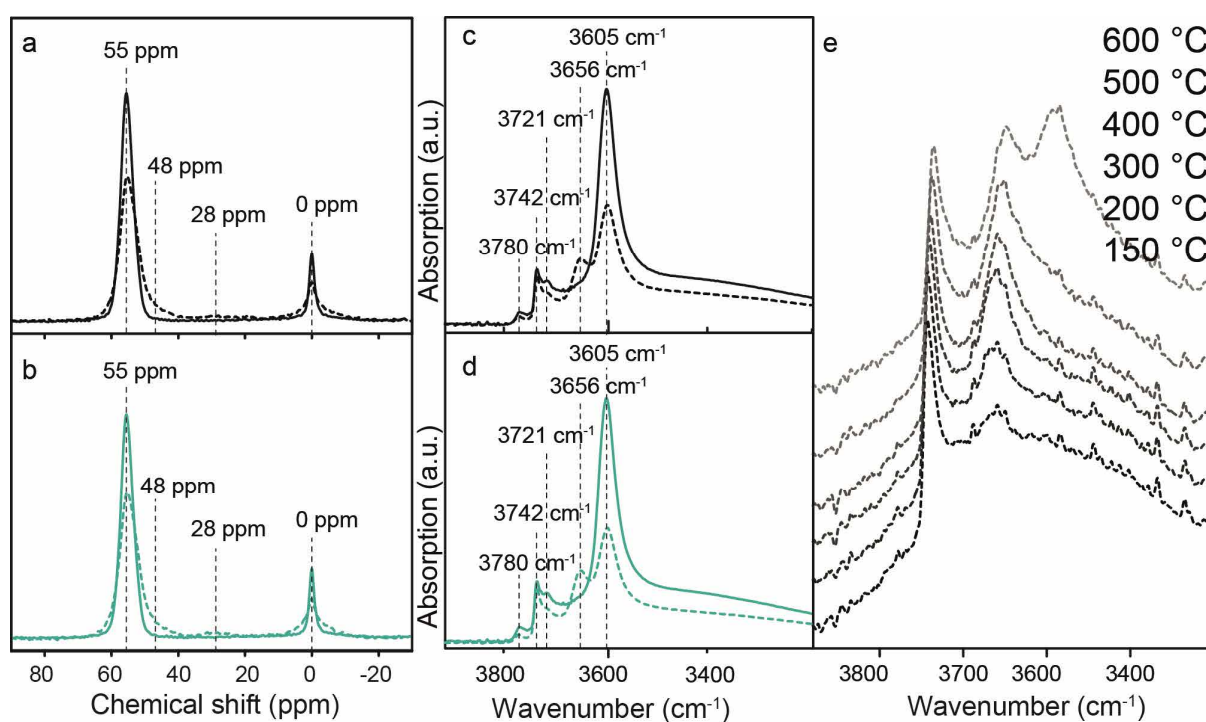

Figure 4.4 (a-b) ^{27}Al MAS NMR spectra and (c-d) FT-IR spectra, highlighting the OH region of the following samples: ■ = [Z], ■ dashed = [Z]$_{TT}$, ■ = [Z]$_{NA}$, and dashed = [Z]$_{NA-TT}$. (e) FT-IR OH-stretch spectra of sample [Z]$_{TT}$ during pyridine temperature programmed desorption.
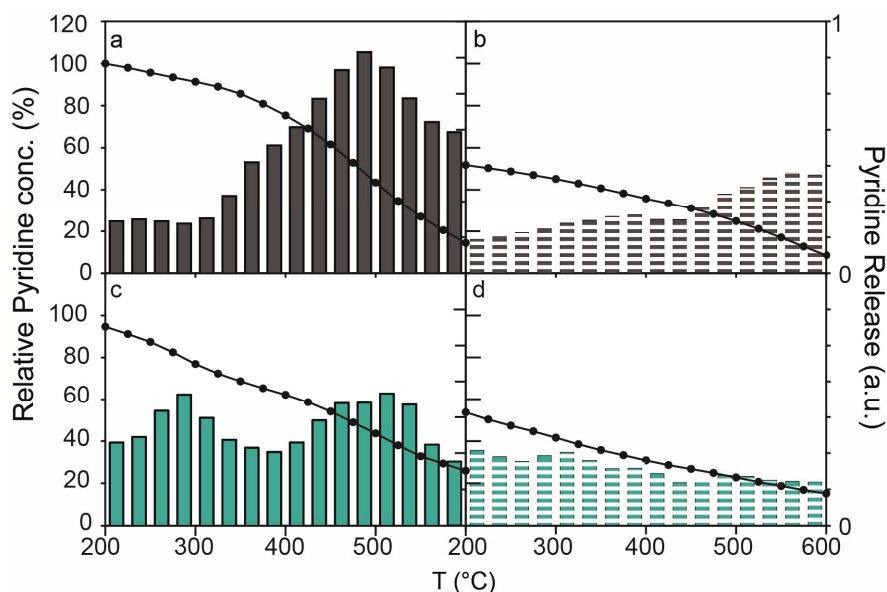
Figure 4.5 Profiles obtained during the temperature programmed desorption of adsorbed pyridine on different samples. Left y-axis shows a plotted line, which is the pyridine concentration relative to sample [Z] at 200 °C. Right y-axis shows the release of pyridine in between two temperature points as bars. The units are arbitrary but are normalized for each sample. (a) ■ = [Z], (b) ■ dashed = [Z]$_{TT}$, (c) ■ = [Z]$_{NA}$, and (d) ■ dashed = [Z]$_{NA-TT}$.

around + 15 eV from this position. This spectrum is typical for four-coordinated aluminum in aluminum-silicates. [17-18]

The effect of acid treatment on the zeolite structure is minimal. After treating sample [Z] in an aqueous nitric acid (NA) solution (pH = 2.7), we obtain sample [Z]$_{NA}$. As shown in Figure 4.4b and 4.4d, no changes in the ^{27}Al MAS NMR and FT-IR spectra are observed. Dissolution of TFAl and OFAl is therefore unlikely, which is accordingly not expected at a pH of 3. [19] Unexpectedly, the acidity profile of acid-treated [Z]$_{NA}$ changes. There is a loss of strong acid sites and a slight increase in the number of weak acid sites.

After thermal treatment, both [Z]$_{TT}$ and [Z]$_{NA-TT}$ experience a decrease in the number of TFAl sites, as shown in Figure 4.4a and 4.4b. The decrease in the number of TFAl sites leads to a loss of the number of Si-OH-Al groups and a decrease in the number of Brønsted acid sites of approximately 45%. This is presented in Figures 4.4c, 4.4d, 4.5 and Table 4.2. A good correlation was found between the relative decrease in the number of TFAl species and the number of SiOHAl groups (Figure 4.1). Nevertheless, these values have been obtained by deconvolution of NMR and FT-IR spectra and one should take into account that the quantification of NMR and FT-IR spectra is to a certain extend arbitrary. Therefore, these values should only be considered as a numerical approximation of essentially qualitative data.
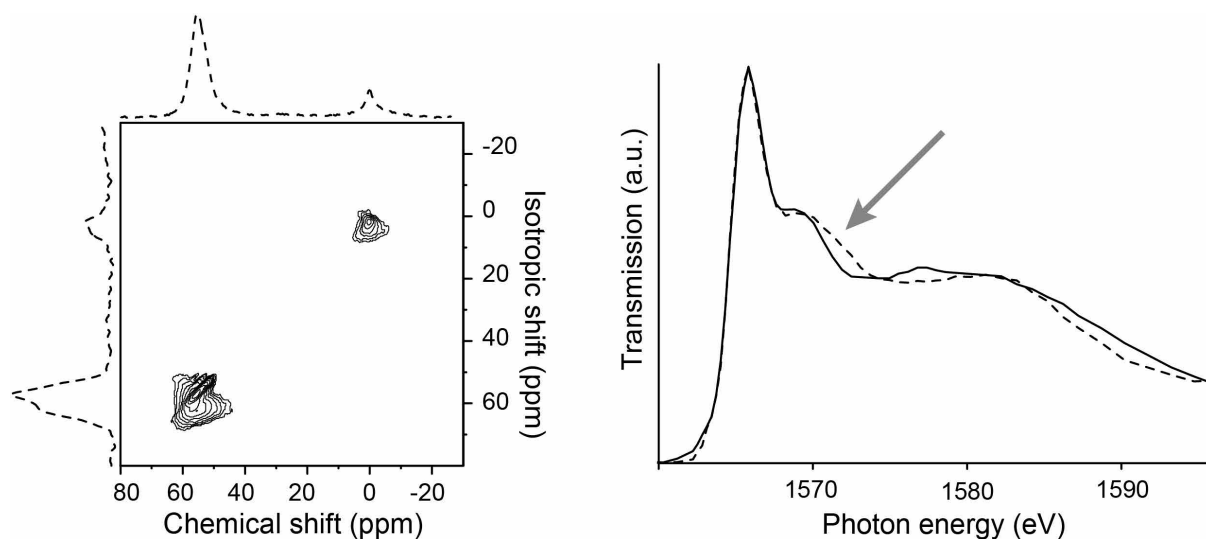
Figure 4.6 (a) ^{27}Al MQ MAS NMR spectra of sample [Z]$_{TT}$. (b) Aluminum K-edge XANES of samples: ■ = [Z], ■ dashed = [Z]$_{TT}$. The broadening of the post-edge feature marked by the arrow indicates the formation of partially dislodged aluminum species

Simultaneously with the decrease in TFAl and acid sites, a new type of distorted framework Al (TFAl$_{dis}$) is formed in samples [Z]$_{TT}$ and [Z]$_{NA-TT}$. This type of site can be seen in Figure 4a-d with the ^{27}Al NMR technique as a distorted signal coming from TFAl located at 48 ppm and with the FT-IR technique as a vibrational band located at 3656 cm^{-1}. ^{27}Al MQ MAS NMR of sample [Z]$_{TT}$ is in Figure 4.6, shows that the resonance has a different isotropic shift than the TFAl resonance, indicating a different kind of species is formed. This resonance has a higher quadrupolar coupling than TFAl, representative of an asymmetrical environment. Al K-edge XANES shows a change in the post-edge features as a contribution at + 6 eV appears and the broad peak at +15 eV decreases in intensity. Van Bokhoven et al. reported similar effects for a steamed H-beta zeolite and attributed these to an increase in octahedral aluminum and decrease in local ordering around tetrahedral aluminum. The authors showed furthermore that the observed changes in aluminum coordination could be partly reverted by treatment with ammonia. [18] Based on ^{27}Al MQ MAS NMR, we attribute the changes in Al K-edge XANES to a loss of ordering and the formation of distorted framework aluminum species. The acidic character of TFAl$_{dis}$ can be observed in Figure 4.4e.

^{27}Al MAS NMR shows also a broadening of the resonance at 0 ppm indicating a decrease in crystallinity and the formation of a broad resonance at 28 ppm, which is often attributed to the presence of Al5 species.[20] Interestingly, as can be seen in Figure 4.4b and 4.4d, sample [Z]$_{TT}$ contains more strong acid sites, while sample [Z]$_{NA-TT}$ has more weak acid sites. This follows from the pyridine temperature programmed desorption (TPD) profiles of their respective parent materials.

4.3.2 Effect of phosphorus

After the introduction of phosphoric acid (PA) and ammonium hydrogen phosphate (PB) samples $[Z]_{2PA}$ and $[Z]_{2PB}$ are obtained. When H_3PO_4 is used as a precursor one can observe a decrease of about 30% in the number of TFAl species and SiOHAl groups, as shown in Figures 4.1, 4.7 and Table 4.2. Figure 4.7c shows there is a decrease in the number of external silanol groups and external aluminol groups as well as the formation of a small band at 3670 cm^{-1} and a new broad band between 3520 and 3200 cm^{-1}. The latter two vibrational bands can be attributed to respectively P-OH groups and bridging hydroxyl groups interacting with oxygen.[10, 21] All these effects can be observed in the spectra of a similar sample in the work of Lischke and co-workers. [1] Unfortunately, the authors did not mention nor comment on these spectral changes.

Four new resonances appear in the ^{27}Al MAS NMR spectra of sample $[Z]_{2PA}$, seen in Figure 4.7a. Figure 4.8 shows the ^{27}Al MQ MAS NMR spectrum of sample $[Z]_{2PA}$, which provides more evidence for the presence of these new species. The isotropic shift of resonance 3 is similar to the resonance attributed to TFAl. This indicates that these species are TFAl atoms with a larger quadrupolar coupling due to a highly distorted electronic environment. The three new six-coordinated aluminum species corresponding to Signals 4, 5, and 6 lie along the anisotropic axis and are in a more symmetric environment. The ratio between the contribution of Al4 species and Al6 species decreases, as shown in Table 4.3, which would indicate that Al4 species are
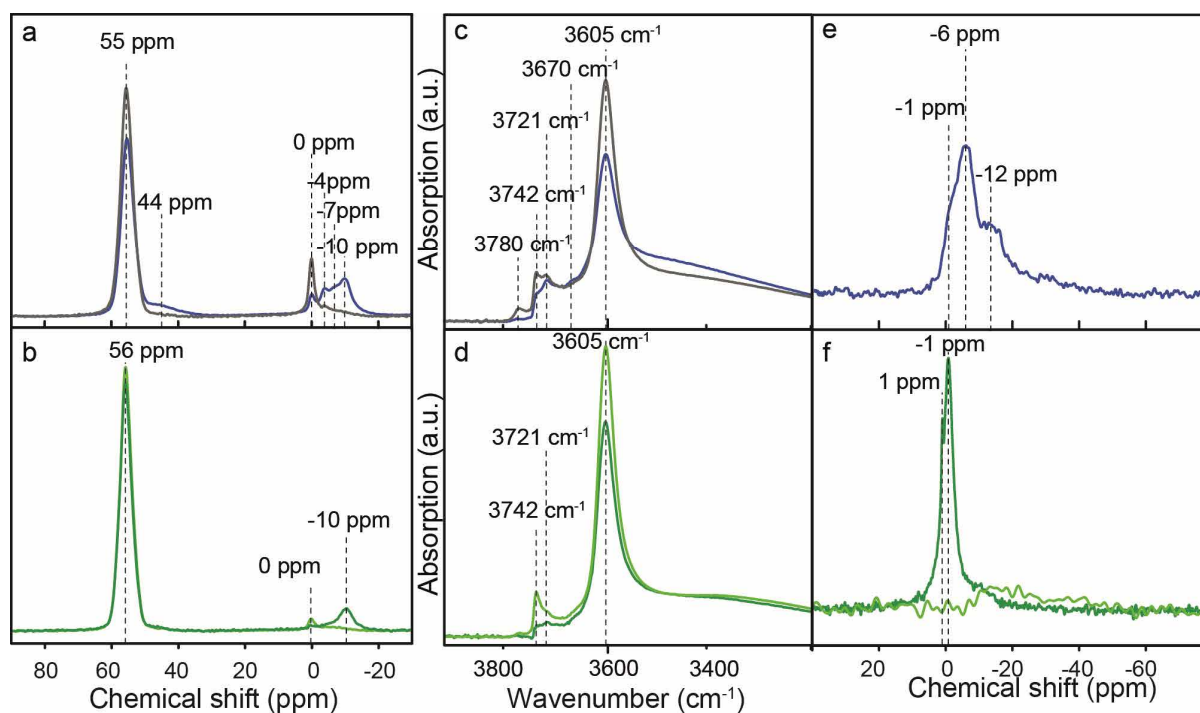

Figure 4.7 (a-b) ^{27}Al MAS NMR spectra and (c-d) FT-IR spectra, highlighting the OH-stretch region, and (e-f) ^{31}P MAS NMR spectra of the following samples: ■ = $[Z]_{2PA}$, ■ = $[Z]_{2PA-e}$, ■ = $[Z]_{2PB}$, and ■ = $[Z]_{2PB-e}$.
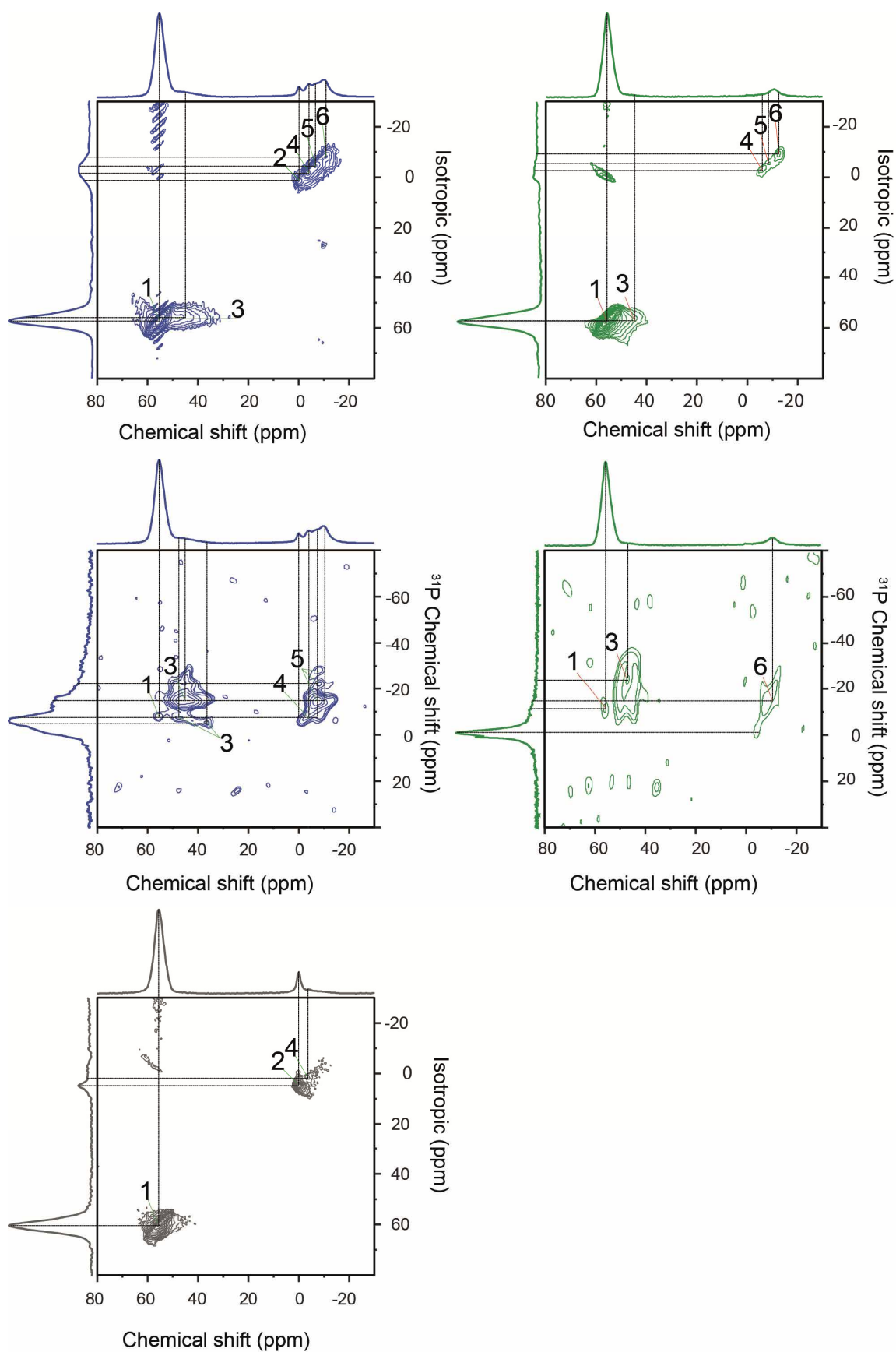
Figure 4.8 ^{27}Al MQ MAS NMR and ^{27}Al-^{31}P CP HETCOR NMR spectra of the following samples: ■ =[Z]$_{2PA}$, ■ = [Z]$_{2PA\text{-}e}$, and ■ = [Z]$_{2PB}$.
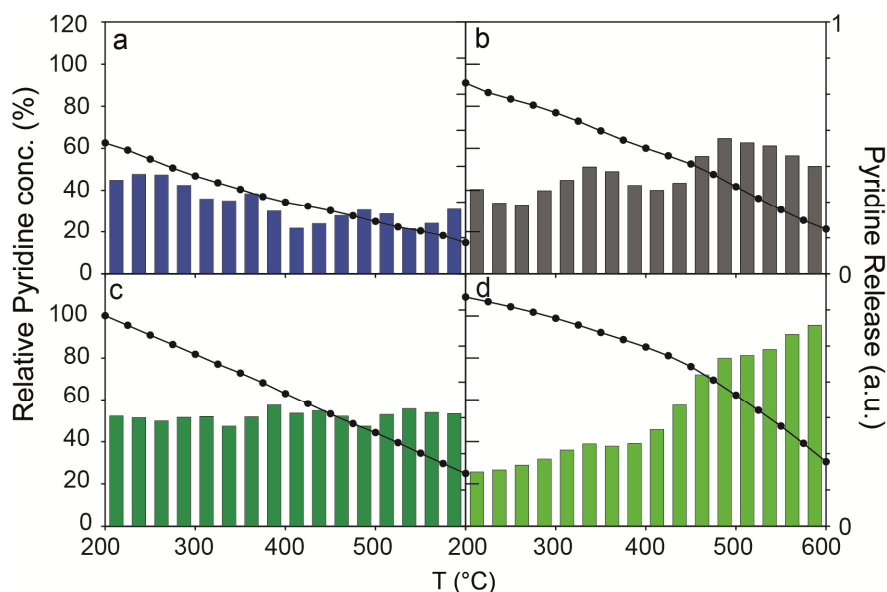
Figure 4.9 Profiles obtained during the temperature programmed desorption of adsorbed pyridine on different samples. Left y-axis shows a plotted line, which is the pyridine concentration relative to sample [Z] at 200 °C. Right y-axis shows the release of pyridine in between two temperature points in bars. The units are arbitrary but are normalized for each sample: a-d) samples ■ = $[Z]_{2PA}$, ■ = $[Z]_{2PA-e}$, ■ = $[Z]_{2PB}$, and ■ = $[Z]_{2PB-e}$.

formed at the cost of Al4 species.

2D ^{27}Al-^{31}P hetero-correlation (HETCOR) NMR spectra in Figure 4.8 reveal that all the new aluminum species are in close proximity to phosphorus. The phosphorus species are dominantly found at -6 ppm, which can be attributed to pyrophosphates or terminal phosphate groups in polyphosphate chains. [8] The signal at -12 ppm is often attributed to middle chain phosphate groups. [8] The strongest Al-P interactions through space are found for the -15 ppm signal. Resonance 5 interacts with a variety of ^{31}P resonances.

The formation new NMR resonances is accompanied with changes in both the number and strength of the acid site (Figure 4.9). As reported before, there is a decrease in the number of strong acid sites and an increase in the number of weak acid sites, giving rise to a weaker average site strength distribution.[1] In order to check the reversibility of the phosphorus interaction, samples were washed with hot water. Table 4.1 shows that after washing 75% of the phosphorus is removed and it is apparent from Figures 4.3 and 4.7 that the interaction of phosphorus is fully reversible as the ^{27}Al NMR and FT-IR spectra of sample $[Z]_{2PA-e}$ are similar to the parent material [Z]. When phosphorus is eluted, the pyridine desorption profile of sample $[Z]_{2PA-e}$ shown in Figure 4.9 resembles that of the acid washed sample $[Z]_{NA}$ shown in Figure 4.5.

When ammonium hydrogen phosphate is used as a precursor, the absorption intensity of the SiOHAl band does not decrease as can be seen in Figure 4.7d. The intensity of the 55 ppm peak, corresponding to TFAl species, is higher than for the parent [Z] sample. Furthermore, Figure

A4.2 (Appendix) shows that the spinning side bands of the 55 ppm resonance increase in intensity, indicating a more symmetric environment for the TFAl species in sample $[Z]_{2PB}$. In agreement with these findings are the limited Al-P interactions, as observed with the ^{27}Al MQ MAS and ^{27}Al-^{31}P HETCOR NMR techniques shown in Figure 4.8.

The type of phosphorus-framework interactions are similar to that of $[Z]_{2PA}$, although minor in intensity as shown in Figure 4.8. The ^{31}P NMR spectra of $[Z]_{2PB}$ in Figure 4.7f reveal that most of the phosphorus is represented by the 0 ppm resonances, corresponding to ammonium hydrogen phosphate.[22] ^{31}P resonances of sample $[Z]_{2PB}$ at -15 ppm interact with the newly formed Al species at -10 ppm, as depicted in Figure 4.8. There is a strong decrease in the number of external Si-OH groups and internal Si-OH groups as can be seen in Figure 4.7d. The acid site strength is heterogeneous in nature, with an equal and continuous distribution of weak and strong acid sites as shown in Figure 4.9c.

After elution the contribution of four-coordinated aluminum increases even further as can be observed in Figure 4.7 and Table 4.3 The treatment with ammonium hydrogen phosphate followed by washing, leads to a decrease in the 0 ppm resonance (OFAl species) and an increase in the 55 ppm resonance (TFAl species). The number of SiOHAl species is 10% higher than parent sample $[Z]$, and the Al4/Al6 ratio is 19 for sample $[Z]_{2PB-e}$, while 5.5 for sample $[Z]$, as follows from Tables 4.2 and 4.3. There is a strong decrease in the number of internal Si-OH and Al-OH species, though the band for external Si-OH species reappears, as seen in Figure 4.7d. The total acid site number and average acid site strength increase as sample $[Z]_{2PB-e}$ is able to retain more pyridine at higher temperatures as compared to parent sample $[Z]$, as shown in Figure 4.9d.

4.3.3 Effect of thermal treatment on phosphated samples

Although the choice of phosphate precursor leads to a difference in structure and acidity of the H-ZSM-5 material, a subsequent thermal treatment nullifies these differences. As can be witnessed from the aluminum K-edge, ^{27}Al, ^{31}P (MQ) MAS NMR, ^{27}Al-^{31}P CP HETCOR, FT-IR spectra and the pyridine TPD profiles in Figures 4.10-4.13, the samples $[Z]_{2PA-TT}$ and $[Z]_{2PB-TT}$ are close to identical. In Figure 4.10 and Table 4.2 it can be seen that the thermal treatment of $[Z]_{2PA}$ and $[Z]_{2PB}$ leads to a 80% decrease in the number of TFAl species and SiOHAl groups. As mentioned for samples $[Z]_{NA-TT}$ and $[Z]_{TT}$ the decrease caused by the thermal treatment was 45%, so 35% of the total decrease can be attributed to the presence of phosphorus.

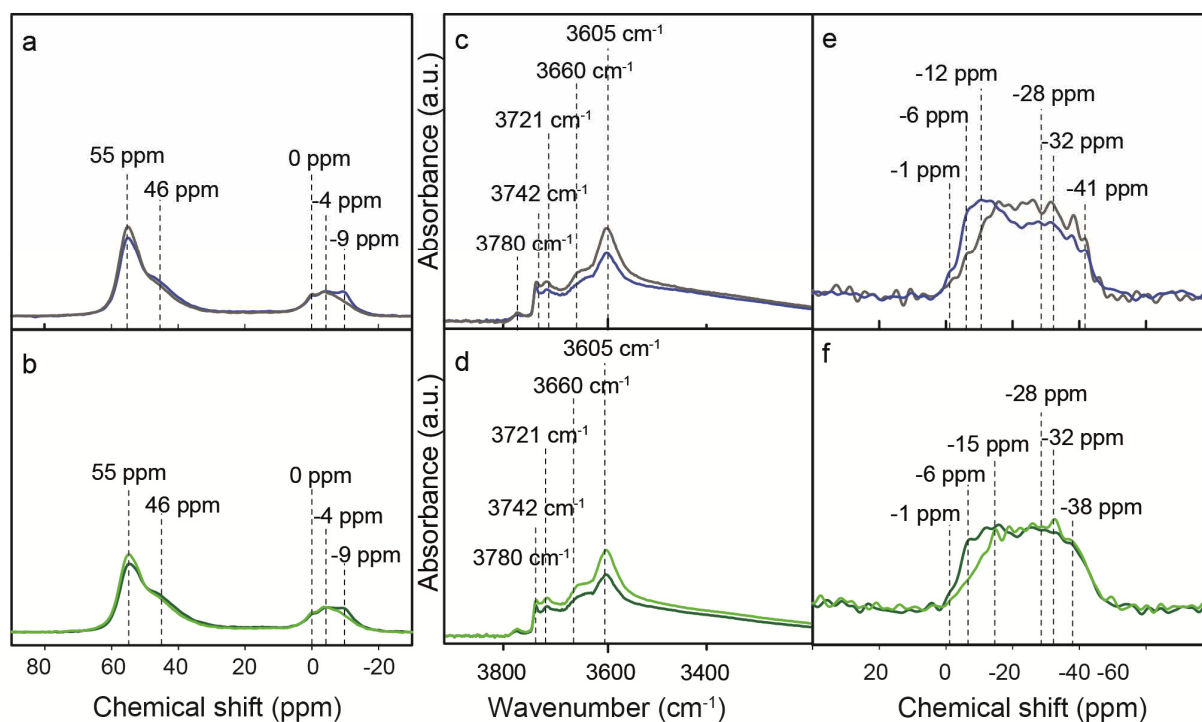The ^{27}Al MQ MAS NMR spectra in Figure 4.13 shows that resonances 3, 4, 5 and 6 have

Figure 4.10 (a-b) ^{27}Al MAS NMR, (c-d) FT-IR OH-stretch region spectra, and (e-f) ^{31}P MAS NMR of samples ■ dashed = [Z]$_{2PA-TT}$, ■ dashed = [Z]$_{2PA-TT-e}$, ■ dashed = [Z]$_{2PB-TT}$, and ■ dashed = [Z]$_{2PB-TT-e}$.

increased in intensity and broadened, indicating a larger distribution of these species in sample [Z]$_{2PA-TT}$ and [Z]$_{2PB-TT}$. There is a shoulder on the isotropic axis at 57 ppm, indicating a new type of species, similar to the one found for sample [Z]$_{TT}$. ^{31}P MAS NMR spectra presented in Figure 4.10e and 4.10f, reveal that thermal treatment leads to a wide variety of phosphates, of which the majority is in close vicinity to aluminum. There are many P-Al correlations found, shown Figure 4.13 and phosphorus species with a resonance at -15 ppm interact with most of the OFAl species, while most of the
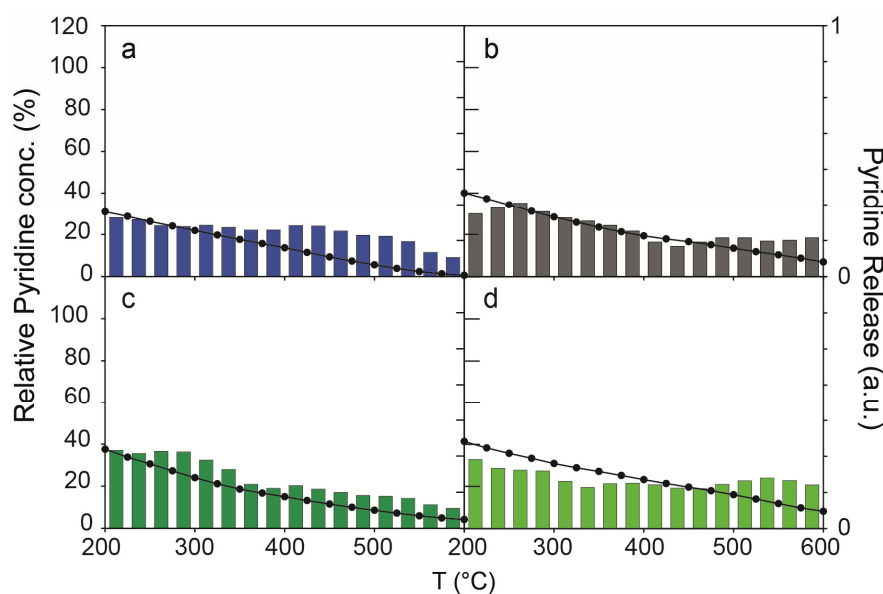

Figure 4.11 Profiles obtained during the temperature programmed desorption of adsorbed pyridine on different samples. Left y-axis shows a plotted line, which is the pyridine concentration relative to sample [Z] at 200 °C. Right y-axis shows the release of pyridine in between two temperature points in bars. The units are arbitrary but are normalized for each sample: (a-d) samples ■ = [Z]$_{2PA}$, ■ = [Z]$_{2PA-e}$, ■ = [Z]$_{2PB}$, and ■ = [Z]$_{2PB-e}$.
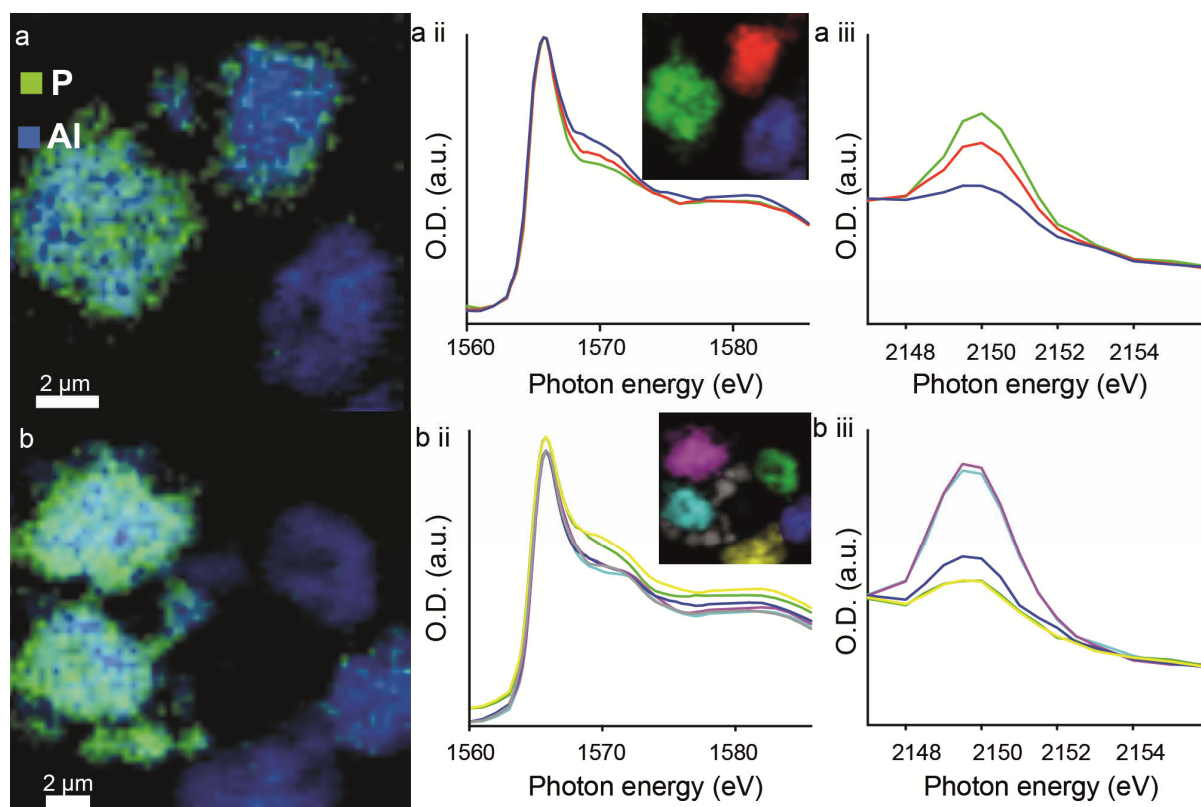
Figure 4.12 Chemical maps of zeolite clusters, constructed from Aluminum K-edge spectra and Phosphorus K-edge spectra stacks, displaying samples $[Z]_{2PA-TT}$ (a) and $[Z]_{2PB-TT}$ (b). ■ = Al ■ = P Resolution is 60 x 60 nm². (a ii and b ii) Aluminum K-edge XANES, each spectra is colored according to the corresponding cluster in the inset. a iii and b iii) Phosphorus K-edge XANES, each spectra is colored according to the corresponding cluster in the inset

TFAl$_{dis}$ species interact with phosphorus at a broad number of resonances centered around -28 ppm. For sample $[Z]_{2PA-TT}$ there is an interaction between ^{31}P at -15 ppm and ^{27}Al at 26 ppm, which could correspond to Al5 species. The average acid strength distributions for samples $[Z]_{2PB-TT}$ and $[Z]_{2PA-TT}$ shift to weaker average acidities, as shown in Figure 4.11a and 4.11c which is in accordance to literature.[1-2, 9, 23-24]

STXM data presented in Figure 4.12 reveals both inter-, and intra-particle heterogeneities in the distribution of phosphorus. As was mentioned in Chapter 3, there is a gradient in the phosphorus distribution, revealing a higher concentration of phosphorus closer to the external surface of the H-ZSM-5 particle. Furthermore, the phosphorus-modification method leads to an inhomogeneous distribution of phosphorus between different aggregates. Zeolite aggregates that do not contain high loadings of phosphorus have a broadened post-edge feature around +6 eV similar to that described for sample $[Z]_{TT}$. However, samples containing high phosphorus content have a decreased post-edge feature, indicating a change in the neighboring atoms of aluminum. The latter finding indicates that with higher loadings of phosphorus, more phosphorus can penetrate into the zeolite and more aluminum atoms are expected to be affected by the presence of phosphorus.
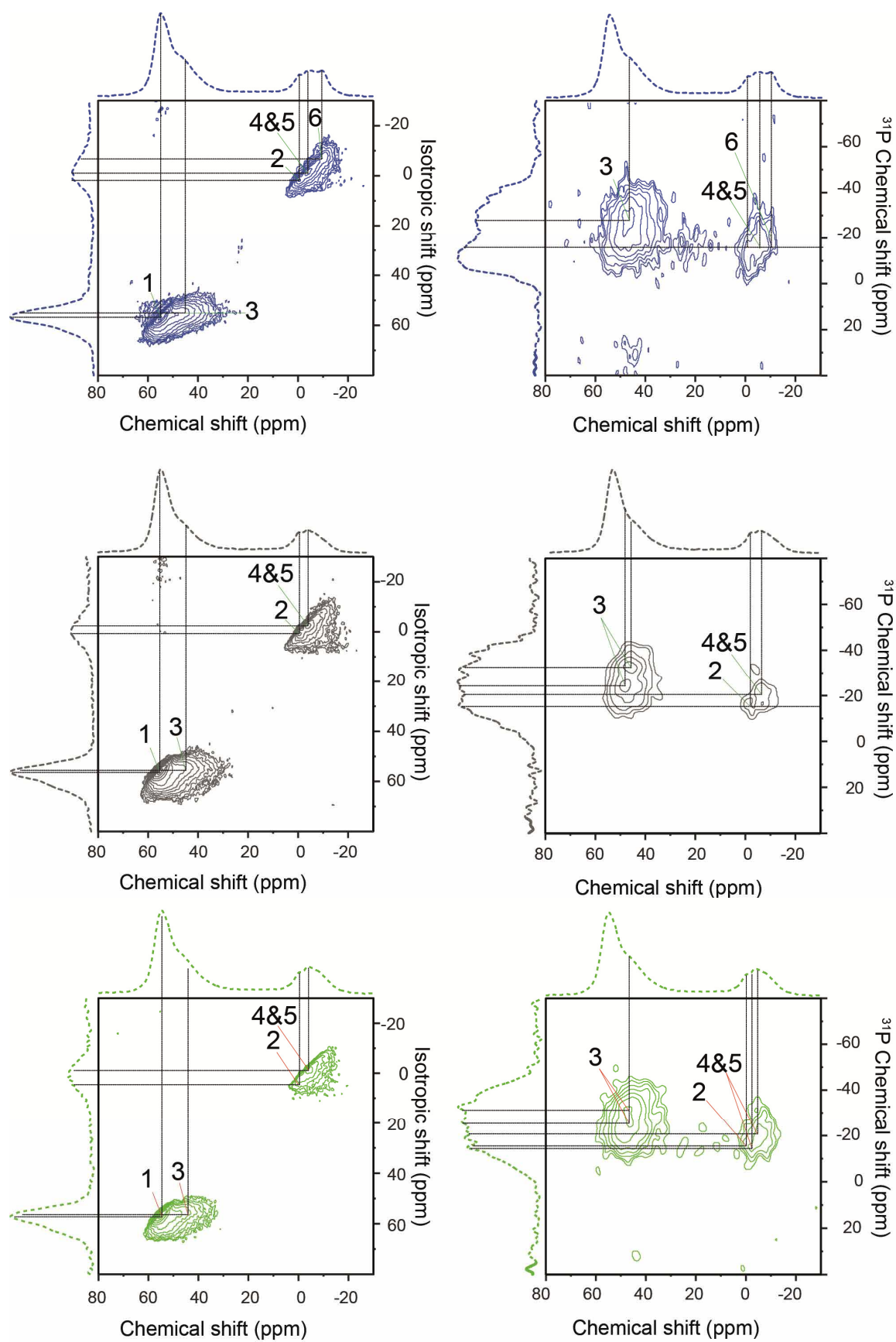
Figure 4.13 ^{27}Al MQ MAS NMR and ^{27}Al-^{31}P CP HETCOR NMR for the samples: ■ dashed = [Z]$_{2PA-TT}$, ■ dashed = [Z]$_{2PA-TT-e}$, and ■ dashed = [Z]$_{2PB-TT-e}$.

Washing results only in the elution of a fraction of phosphorus, with still 75% of the original phosphorus content remaining (Table 4.1). This could be explained by the formation of water insoluble condensed polyphosphoric acid that is formed after thermal treatment[25], which was found to form when we performed an identical thermal treatment on phosphoric acid. However, from Figure 4.13 it becomes clear that the phosphorus that is in close vicinity to aluminum is not washed out either. Figure 4.10e and 4.10f show that the ^{31}P resonances around -6 ppm to -12 ppm, which have no strong correlation with aluminum, are sharply decreased after washing. Figure 4.13 shows that for both samples $[Z]_{2PB-TT-e}$ and $[Z]_{2PA-TT-e}$ Al-P correlations disappear, including ^{27}Al resonance 6 with ^{31}P resonance -15 ppm and ^{27}Al resonances 20 ppm to 25 ppm with ^{31}P resonance -19 ppm. After washing, two types of phosphorus with resonances at -24 ppm and -32 ppm interact with aluminum in resonance 3. The two types of species stem from the same ^{27}Al NMR resonance, so it is more likely that these are two types of phosphorus interacting with one type of aluminum than *vice versa*. Phosphorus resonances at higher chemical shifts, i.e., -19 ppm and -15 ppm, interact with the OFAl species. The washing results in a 20% increase in the number of TFAl species and SiOHAl sites (Table 4.2). Unaffected TFAl species are not in close vicinity with phosphorus. Although the average acid site strength distribution does not change significantly, the number of protonated pyridinium ions increase with approximately 10% as shown in Table 4.2 and Figure 4.11b and 4.11d.

4.3.4 Effect of thermal treatment preceding phosphatation

From the results described above it can be deduced that either, (i) Al-O-P bonds do not exist in hydrated samples and the only interactions between the two atoms are through space. Additionally, the formation of water insoluble phosphorus species after thermal treatment prevents phosphorus to be eluted, or (ii) Aluminum species that are formed during thermal treatment react irreversibly with phosphates. This would lead to framework Si-O-Al-O-P bonds and the formation of local silico-aluminophosphate (SAPO) interfaces. To test these two hypotheses sample $[Z]_{TT}$ has been resynthesized and subsequently phosphated.

First the sample was suspended in an aqueous HNO_3 solution to test if the $TFAl_{dis}$ species that form after thermal treatment could be leached from the zeolite and would therefore be extra-framework. As can be seen in Figure 4.14a and 4.14c, this was not possible and it is therefore unlikely that the $TFAl_{dis}$ species are extra-framework. After phosphatation of $[Z]_{TT}$ with H_3PO_4, we obtain sample $[Z]_{TT-2PA}$ and both the ^{27}Al, ^{31}P MAS NMR and FT-IR spectra shown in Figure 4.14b and 4.14d resemble sample $[Z]_{2PA-TT}$. The broad asymmetric resonance at 40 ppm
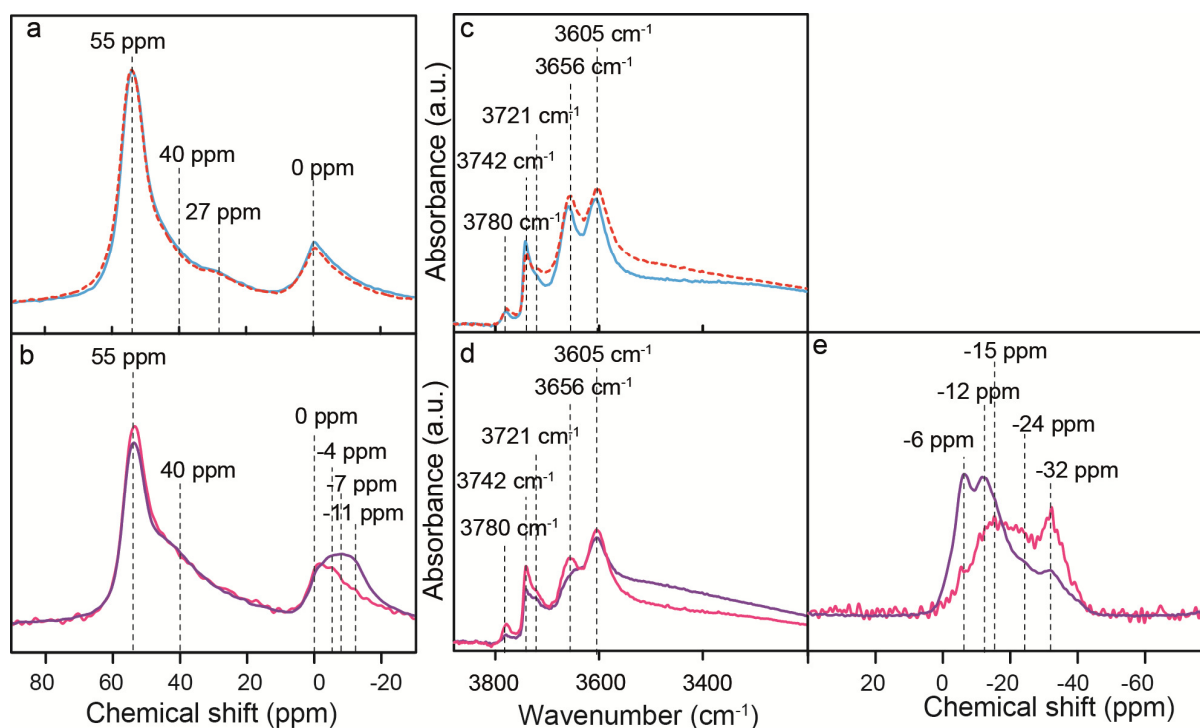
Figure 4.14 (a-b) ^{27}Al MAS NMR spectra, (c-d) FT-IR spectra, highlighting the OH-stretch region, and (e-f) ^{31}P MAS NMR spectra of the following samples: ■ dashed = [Z]$_{TT}$ remade, ■ = [Z]$_{TT-L}$, ■ = [Z]$_{TT-2PA}$, and ■ = [Z]$_{TT-2PA-e}$.

and the resonances at -4 ppm, -7 ppm and -11 ppm are present in the ^{27}Al MAS NMR spectra. There is a strong decrease in intensity for the band at 3650 cm^{-1} attributed to TFAl$_{dis}$ species observable with FT-IR. It is encouraging to see that the ^{31}P MAS NMR resonances at -32 ppm and -24 ppm are present, indicating that these species are not formed due to thermal treatment after phosphatation.

After elution with hot water, it can be observed that the ^{27}Al MAS NMR resonances of sample [Z]$_{TT-2PA-e}$ at 40 ppm, -4 ppm, and -7 ppm remain, while only a fraction of the 3650 cm^{-1} band is retrieved. Although the remaining amount of phosphorus content of 40% is similar to that of [Z]$_{2PB-e}$, the ^{31}P MAS NMR spectrum is quite different and resemble that of the samples [Z]$_{2PB-TT-e}$ and [Z]$_{2PA-TT-e}$. The resonance at around -32 ppm has remained, as do the broad resonances around -23 ppm and -15 ppm. We can therefore attribute these resonances to the presence of phosphate species exclusively and irreversibly interacting with TFAl$_{dis}$ and OFAl$_{dis}$ species.

4.4 Discussion

By precisely following the different steps in the phosphorus post-modification process with an array of spectroscopic methods we have established the type of Al species present in H-ZSM-5 and as well as the phosphorus interactions with these Al species. An overview of the species and their spectroscopic signatures is given in Table 4.4.

4.4.1 Formation of partially dislodged TFAl species

The parent zeolite H-ZSM-5 has an ordered crystalline structure comprising two types of framework aluminum. Namely tetrahedrally coordinated framework aluminum species (TFAl) and octahedrally coordinated framework aluminum species (OFAl), both are schematically drawn in Figure 4.15a and 4.15b respectively. The latter is connected with three bonds to the framework and possesses an octahedral coordination in hydrated form with three framework oxygen atoms and three oxygen atoms in H_2O (OFAl). [14-15] In dehydrated form these aluminum
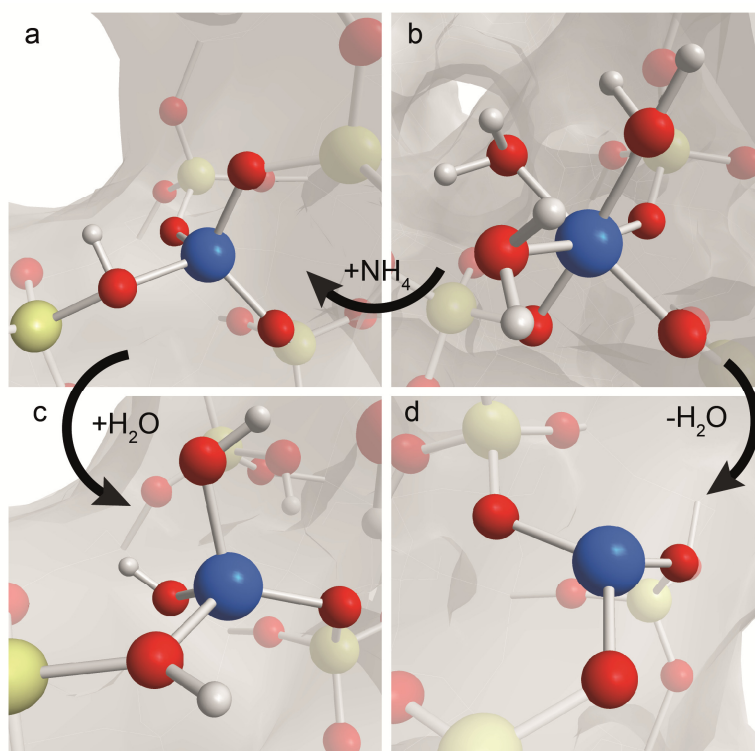

Figure 4.15 Schematic representation of four different aluminum species found in the H-ZSM-5 framework, located at the straight and sinusoidal channel intersection. (a) Tetrahedrally coordinated framework aluminum (TFAl) forming a bridging hydroxyl group with neighboring Si. (b,d) Octahedrally coordinated framework aluminum (OFAl) interacting with three water molecules in hydrated form. In dehydrated form it forms three-coordinated aluminum. (c) Distorted tetrahedrally coordinated framework aluminum (TFAl$_{dis}$), only attached with one or two bonds to the zeolitic framework. Three protons compensate the negative charge on the $(SiO)_2AlO_2^{3-}$ unit. ■ = Si, ■ = Al, ■ = O, □ = H

Table 4.4 Type of species found in phosphorus-modified H-ZSM-5 materials

Type of species	Description	Spectroscopic signature	Acid type
TFAl	Tetrahedrally coordinated framework Al and corresponding bridging hydroxyl groups	3604[a] , 55[b] (1)[c]	Brønsted
OFAl	Octahedrally coordinated triple-bound framework Al physically coordinated to three H_2O molecules	Partial 3780[a], 0[b] (2)[c]	Lewis
TFAl$_{dis}$	Partially dislodged tetrahedrally coordinated double-bound framework Al with two hydroxyl groups	3656[a], 48 and (28)[b]	Brønsted
Si-OH ext	External Si-OH	3742[a]	Brønsted
Si-OH int	Internal Si-OH located next to OFAl species	3721[a]	Brønsted
TFAl + H_3PO_4 (a)	Bridging hydroxyl groups hydrogen bonded with H_3PO_4	3500 – 3200[a], 44[b], (3)[c]	Uncertain
TFAl + H_3PO_4 (b)	Octahedrally coordinated framework Al physically coordinated with two H_3PO_4 or $(NH_4)_2HPO_4$ molecules.	-10[b] 6[c], -15[d]	Uncertain
OFAl + H_3PO_4	Octahedrally coordinated triple-bound framework Al physically coordinated to one or two H_2O molecules	-4, and -7[b] (4,5)[c], -15[d]	Uncertain
TFAl$_{dis}$-O-P	Partially dislodged tetrahedrally coordinated double-, or triple-bound framework Al bonded to one or two phosphate monodentate or bidentate species.	40 ppm to 10 ppm[b]*, (3)[c], -24[d], -32[d]	Uncertain

[a] Wavenumber (cm^1), [b] ^{27}Al Chemical shift (ppm), [c] ^{27}Al MQ MAS Resonance, and [d] ^{31}P Chemical shift (ppm) * Depends on magnetic field strength

species transform into three-fold coordination with the three framework oxygen atoms, as can be seen in Figure 15d. [46,47] As the samples have been dehydrated for FT-IR measurements no OH

groups connected to these species can be seen in the spectra, except for external terminal Al-OH groups. Brønsted acidity comes from Si-OH-Al bridging hydroxyl groups at TFAl sites and the Lewis acidity comes from the dehydrated three-coordinated aluminum sites.[14, 18]

The effect of acid treatment during phosphatation on the structure and acid site number of H-ZSM-5 is negligible. Still, it is found that acid treatment does shift the acid site strength distribution, as there is a decrease in the number of strong acid sites and increase the number of weaker acid sites. Thermal treatment, on the other hand, has an altering effect on the structure and acidity of H-ZSM-5. High temperatures and the presence of water in the air and the zeolites lead to partial dealumination. We use the word partial to describe the breaking of Si-O-Al bonds and the formation of partially dislodged aluminum species. Based on literature we attribute these species to tetrahedrally coordinated aluminum that is connected with only three or two bonds to the framework (TFAl$_{dis}$). [26] One or two terminal Al-OH groups are formed and one proton compensates for the negative charge on the framework, as can be seen in Figure 4.15c. The acidic bridging SiOHAl group of this species is responsible for the 3656 cm^{-1} FT-IR band. Density Functional Theory (DFT) calculations performed by other groups predicted these species to form in early stages of dealumination as stable intermediates.[27-29] It was suggested that in the hydrated form they can be penta-coordinated, with aluminum binding with one extra water molecule, which would explain the small amount of Al5 species observed with ^{27}Al MAS NMR.[27] These species do still possess Brønsted acidity as they are able to protonate pyridine. Acid leaching does not remove these species, implying that they are not extra-framework. [26]

4.4.2 Reversible phosphorus-framework interactions

Phosphatation with H_3PO_4 does not lead to a noticeable dealumination of the material, as H_3PO_4 can be easily removed from the zeolite by hot water washing, returning the zeolite to its former state. This indicates that the interaction of phosphorus with the zeolite is not through covalent bonds. However, there is an interaction of phosphorus with framework aluminum.

Phosphorus in close vicinity to TFAl has a distorting effect on its symmetric surrounding, as shown by ^{27}Al MQ MAS NMR. We would like to follow the suggestion of Haw and co-workers, that these distortions arise from a hydrogen bond between the bridging hydroxyl group and an phosphate oxygen atom as is shown in Figure 4.16a. [30] The appearance of the broad band in FT-IR between 3520 cm^{-1} and 3200 cm^{-1}, which indicate intramolecular bonds between framework protons and oxygen, support this.[21]
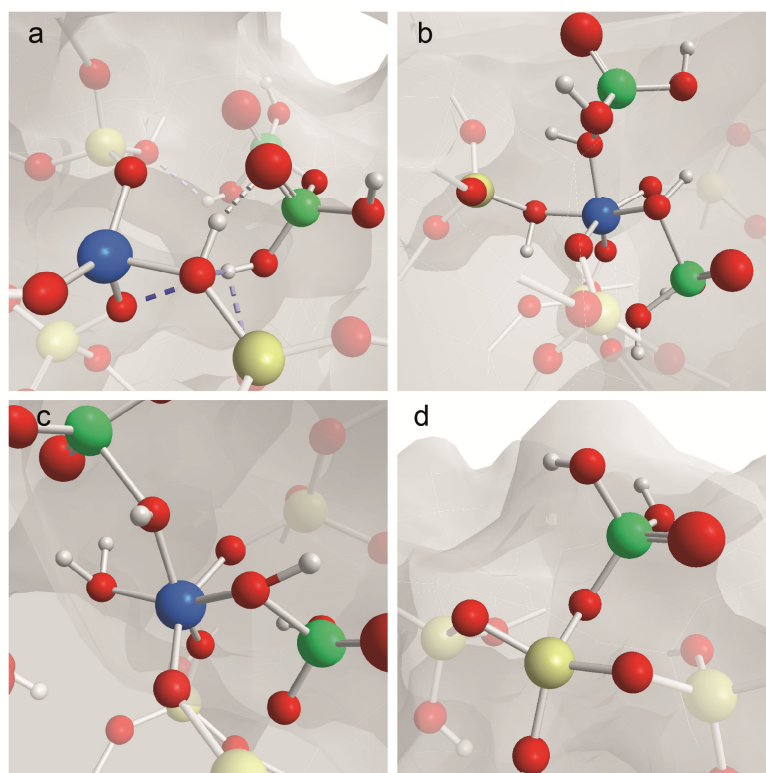
Figure 4.16 Schematic representation of simplified reversible phosphorus-framework interactions (a) TFAl interacting with phosphoric acid through hydrogen bonds, (b) TFAl physically coordinated with two phosphoric acid molecules, adopting six-coordination (c) OFAl species physically coordinated by two phosphoric acid molecules and one water molecule (d) Condensation reaction between silanol groups and phosphoric acid, induced by dehydration. ▪ = Si, ▪ = Al, ▪ = O, □ = H, ▪ = P

Furthermore, OFAl species that can coordinate with three water molecules, appear to be able to coordinate with phosphorus as well. Since three new resonances are found for OFAl species, it is tempting to attribute these to $(SiO)_3Al(H_2O)_{3-x}(H_3PO_4)_x$ (x = 1, 2, or 3), which is depicted in Figure 4.16c. [7] However, the length of polyphosphoric chains that interact could also have an effect on the chemical shift. Especially resonance 5 is interacting with different types of phosphorus species. Finally, the fact that Al4/Al6 ratios decrease significantly after H_3PO_4 introduction, indicates that TFAl species can also physically coordinate with phosphoric acid, adopting a reversible octahedral coordination. This has been suggested in the literature, where an ^{27}Al chemical shift and ^{31}P chemical shift at -10 ppm and -12 ppm were reported respectively. [1, 31] This species is shown in Figure 4.16b.

It is uncertain if phosphorus species that are close to aluminum actually affect the acidity of H-ZSM-5 in its hydrated form. Nevertheless, we do observe a reversible decrease in the number of T-OH groups and bridging hydroxyl groups by FT-IR spectroscopy. The decrease in observable Si-OH-Al groups observed by FT-IR can be partly attributed to the hydrogen bonds that bridging hydroxyl groups form with nearby phosphorus, leading to a shift of the band from

3605 cm^{-1} to 3520-3200 cm^{-1} and TFAl species that adopt six-fold coordination. The decrease in protonated pyridine molecules could then stem from steric hindering caused by nearby phosphate species.

Although Si-O-P bonds formed by silanol with phosphorus interaction have been shown to be unstable in hydrous conditions, they have been found to be stable in a water-free environment.[32-33] One should consider that FT-IR experiments, and for that matter many other characterization techniques to probe acid sites (including ^{1}H NMR), are performed in the absence of water. Therefore, dehydroxylation is promoted and consequently, although unstable, P-O-Si bonds are proposed to form, as shown in Figure 4.16d. It is important to realize that the decrease in acid site number and strength does not necessarily require permanent phosphorus-framework interactions. After washing there is a redistribution of the acid site strength towards weaker average site strength. As this result is very similar to washing with a nitric acid solution with the same pH, we attribute the effect to acid treatment.

4.4.3 Ammonium hydrogen phosphate as precursor

Ammonium hydrogen phosphate does not interact as strongly with H-ZSM-5 as orthophosphoric acid. It is mostly present as ammonium hydrogen phosphate. The minimal interaction that is observed with aluminum is similar to orthophosphoric acid interaction, as shown with ^{27}Al MQ MAS NMR. However, the type of phosphorus species interacting is different, as FT-IR spectroscopy does not show a decrease in the amount of SiOHAl species and only a decrease in the number of external Si-OH groups. We propose that due to the ion-exchange of Brønsted acid site protons with NH$_4^+$ ions, the affinity between framework aluminum and phosphate species is reduced.

Ion exchange with NH$_4^+$ ions present in the ammonium hydrogen phosphate, lead to the repair of formerly broken Al-O-Si bonds and an increase in the amount of TFAl species. This effect has been described previously by Woolery and co-workers and was attributed to the healing of three-coordinated framework Al (OFAl) species to four-coordinated species under the influence of NH$_4^+$.[14, 18] The effect has also been observed for zeolite Beta treated with K and Na cations.[54] Van Bokhoven et al. suggested that counter cationic protons induce strong electric fields on the framework and subsequently water molecules are attracted, which delocalize the cationic charge and part of the framework converts to octahedral aluminum.[15]

The conversion of Lewis acid OFAl species into Brønsted acid TFAl species by ammonia is followed by a decrease in the absorption intensity for coordinately bound pyridine (1454 cm^{-1})

and an increase in the absorption intensity for protonated pyridinium ions (1540 cm^{-1}). This effect is especially clear when the ammonium hydrogen phosphate is washed out and an increase in the amount of TFAl species, SiOHAl groups and Brønsted acid sites, plus a decrease in the number of OFAl species and Lewis acid sites is observed. A decrease in the number of internal Si-OH groups indicates that these species are positioned next to three-coordinated aluminum sites and share a previously broken oxygen bond. A decrease in the number of surface Al-OH groups indicate that these species can form TFAl species as well and are the only OFAl species that stay visible in FT-IR after dehydration. Following this reasoning and assuming that in sample [Z]$_{2PB}$ all OFAl species are transformed into TFAl species, one can observe that for sample [Z]$_{2PB}$ the only six-fold coordinated species is resonance 6. Consequently, this resonance is attributed to TFAl species reversibly adopting octahedral coordination after coordinating with phosphate species.

4.4.4 Permanent phosphorus-framework interactions

Thermal treatment of [Z]$_{2PA}$ and [Z]$_{2PB}$ leads to two similar materials. There is an 80% decrease of TFAl species and SiOHAl groups. ^{27}Al MAS NMR resonances found for Al-P interaction are similar to those for [Z]$_{2PA}$, but have a higher distortion and an increased intensity. The resonances of phosphorus shift to lower chemical shifts, which indicate a different type of interaction. The interaction of phosphorus with distorted framework aluminum seen as resonance 3 in ^{27}Al MQ MAS NMR in Figure 4.13 is a broad resonance with a higher quadrupolar coupling than TFAl, not dissimilar to those found for the SAPO interfaces in SAPO materials, such as SAPO-34 and SAPO-11. [34-35] Furthermore, in the literature reported J-coupling experiments have shown a direct Al-O-P bond for resonance 3 and the -32 ppm resonance observed in ^{31}P MAS NMR.[7] The change in the aluminum K-edge XANES post-edge feature for samples with high phosphorus loadings, indicates a change in neighboring atoms.

Whether a thermal treatment follows or proceeds phosphorus introduction, the type of interactions found with ^{27}Al and ^{31}P MAS NMR are similar and washing with hot water does not remove all of these newly formed species.

4.4.5 Formation of local SAPO interfaces

Considering the results, we feel comfortable to propose a model for P-O-Al framework interaction, which elaborates on a previous model proposed by Zhuang et al. and Damodaran

and co-workers.[7, 36-37] Thermal treatment leads to the formation of $TFAl_{dis}$ and $OFAl_{dis}$ species. Consequently, the free Al-OH groups can react with phosphoric acid to form monodentate and bidentate $(SiO)_3Al(OP(OR))$, $(SiO)_2Al(O_2P(OR)_2)$ or $(SiO)_2Al(O_2P_2O_2(OR)_3)$ species where R = H or (poly)phosphoric acid, giving rise to local SAPO interfaces. An example of these species is presented in Figure 4.17.

It was found that for porous alumina surface Al-OH groups readily reacted with H_3PO_4 to form surface Al-O-P groups.[38] We need to stress that irreversible phosphorus interaction with Al-OH species does not occur for terminal triple-bound framework Al-OH groups observed with FT-IR, as these species react reversibly with phosphorus. ^{31}P MAS NMR indicates that at least two well distinguished types of phosphorus species bind with $TFAl_{dis}$ species at -32 ppm and -24 ppm. The former has been ascribed to an aluminum-bound mono,- or bidentate middle chain phosphate species.[7, 39] The latter at -24 ppm has been ascribed to either aluminum-bound middle chain phosphate species, extra-framework $AlPO_4$ or condensed polyphosphates. [7, 39] Since the formation of EFAl was not observed we would not expect the formation of extra-framework $AlPO_4$ species and condensed polyphosphates only form after thermal treatment. Therefore we attribute the -24 ppm species to aluminum-bound middle chain phosphate species. The resonance at -15 ppm is also observed after hot water washing in Figure 4.13. Therefore, this resonance cannot be exclusively attributed to reversibly interacting phosphate species, but also to phosphorus forming Al-O-P bonds with octahedrally coordinated aluminum atoms, as was previously shown by Damadoran and co-workers.[7] As the ^{31}P MAS NMR spectra show
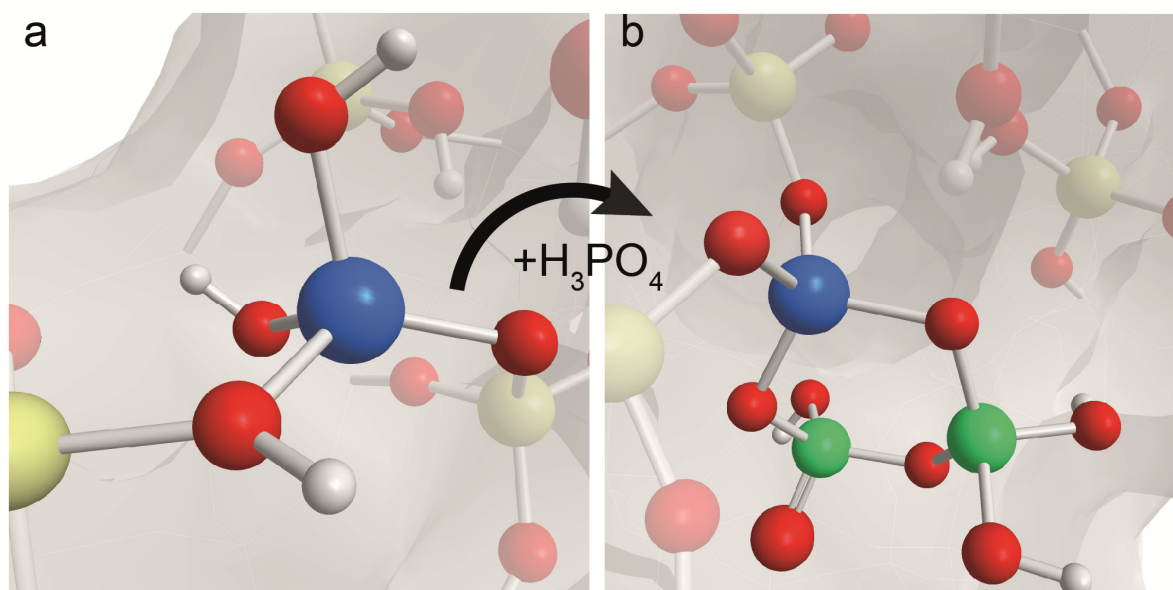

Figure 4.17 Schematic representation of (a) $TFAl_{dis}$ (b) proposed result of $TFAl_{dis}$ after reaction with phosphoric acid. ■ = Si, ■ = Al, ■ = O, □ = H, ■ = P

quite a broad distribution, it is likely that multiple Si-Al-O-P type phosphate species exist.

Local SAPO interfaces, together with thermal treatment explain the decrease in strong Brønsted acid site number, as $[AlO_4]^-$ connected to framework $[SiO_4]$ and one $[PO_4]^+$ group does not require counter cations. Whether the local SAPO interfaces form a new type of weak acid site, that has often been described in the literature, remains uncertain. From our results it follows that an acid treatment followed by a thermal treatment already leads to a decrease in the average acid site strength. Interestingly, it was reported that the formation of surface $Al-O-PO(OH)_3$ groups in porous alumina, was followed by a decrease in the number of strong acid sites and in the concomitant increase in the number of weak acid sites. [38] This phenomenon was attributed to the decrease in the number of Al-OH groups and the increase in the number of P-OH groups.

4.5 Conclusions

By modifying zeolite H-ZSM-5 using a phosphate precursor, a large variety of aluminum and phosphorus species are formed. In this work several of these species have been identified by spectroscopic means, leading to new insights into phosphorus-framework interactions and its effect on zeolite acidity. Most importantly, by impregnating zeolite H-ZSM-5 that contains partially dislodged tetrahedrally coordinated framework aluminum ($TFAl_{dis}$) species using a phosphate precursor, it is possible to introduce local silico-aluminophosphate (SAPO) interfaces, proving that permanent phosphorus-framework interactions can exist.

The formation of $TFAl_{dis}$ species occurs during thermal treatment, when elevated temperatures and water present in the atmosphere hydrolyze Si-O-Al bonds, giving rise to a distorted four-coordinated acidic framework Al species. This $TFAl_{dis}$ species is connected with three or two bonds to the framework. One or two terminal Al-OH groups are formed and one proton compensates for the negative charge on the framework. When phosphorus is present it readily reacts with the Al-OH groups of the dislodged species, forming a framework-$(SiO)_{3-x}$-Al-$(PO)_x$ type species. Introducing the phosphate precursor before or after a thermal treatment leads to seemingly structurally similar materials, with the exception of water insoluble condensed poly-phosphoric acid, which only forms during thermal treatment.

After thermal treatment of phosphated H-ZSM-5 materials there is, irrespective of the phosphate precursor, a strong decrease in the number of acid sites as well as a shift towards

weaker average acid site strength. A large part of this decrease can be attributed to partial dealumination induced by thermal treatment. However, a significant other part is caused by the presence of phosphorus. Due to charge compensation it is unlikely that the local SAPO interfaces have a Brønsted acid site similar to microporous SAPO materials, such as H-SAPO-34 or H-SAPO-11. Possibly the terminal P-OH groups of the interfaces are responsible for the formation of weak acid sites.

If a thermal treatment is not performed, the interaction of the phosphate precursors is fully reversible. Phosphate precursors physically coordinate with, (i) octahedrally coordinated framework Al (OFAl) species and (ii) tetrahedrally coordinated framework (TFAl), which adopts a six-fold coordination. Furthermore, the bridged hydroxyl protons found at TFAl species form an intramolecular bond with nearby phosphate oxygen groups present in (poly)-phosphoric acid. These interactions lead to an observed reduction in the number of strong acid sites and an increase in the number of weak acid sites. After washing, the acid number and strength increases again. Therefore, it can be concluded that the observed decrease in acid site number and strength does not require permanent or stable phosphorus-framework interactions.

Performing a pre-thermal treatment before phosphorus introduction, followed by hot water washing, provides a material where phosphorus is almost exclusively situated in local SAPO interfaces. With the nature of phosphorus-framework interactions being elucidated, we will investigate in Chapter 5 if these species are indeed responsible for the improved hydrothermal stability, as often described for phosphated H-ZSM-5.

Acknowledgements

References

[1]   G. Lischke, R. Eckelt, H. G. Jerschkewitz, B. Parlitz, E. Schreier, W. Storek, B. Zibrowius and G. Öhlmann, *J. Catal.* **1991**, *132*, 229-243.

[2]   T. Blasco, A. Corma and J. Martínez-Triguero, *J. Catal.* **2006**, *237*, 267-277.

[3]   M. J. B. Cardoso, D. D. O. Rosas and L. Y. Lau, *Adsorption* **2005**, *11*, 577-580.

[4]   W. W. Kaeding and S. A. Butter, *J. Catal.* **1980**, *61*, 155-164.

[5]   M. Göhlich, W. Reschetilowski and S. Paasch, *Micropor. Mesopor. Mater.* **2011**, *142*, 178-183.

[6]   A. Jentys, G. Rumplmayr and J. A. Lercher, *Appl. Catal.* **1989**, *53*, 299-312.

[7]   K. Damodaran, J. W. Wiench, S. M. Cabral de Menezes, Y. L. Lam, J. Trebosc, J. P. Amoureux and M. Pruski, *Micropor. Mesopor. Mater.* **2006**, *95*, 296-305.

[8]   J. Caro, M. Bülow, M. Derewinski, J. Haber, M. Hunger, J. Kärger, H. Pfeifer, W. Storek and B. Zibrowius, *J. Catal.* **1990**, *124*, 367-375.

[9]   G. Caeiro, P. Magnoux, J. M. Lopes, F. R. Ribeiro, S. M. C. Menezes, A. F. Costa and H. S. Cerqueira, *Appl. Catal. A-Gen* **2006**, *314*, 160-171.

[10]   N. Xue, R. Olindo and J. A. Lercher, *J. Phys. Chem. C* **2010**, *114*, 15763-15770.

[11]   D. Massiot, F. Fayon, M. Capron, I. King, S. Le Calvé, B. Alonso, J.-O. Durand, B. Bujoli, Z. Gan and G. Hoatson, *Magn. Res. Chem.* **2002**, *40*, 70-76.

[12]   J. Klinowski, *Prog. Nucl. Mag. Res. Sp.* **1984**, *16*, 237-309.

[13]   M. Hunger in *Catalytically active sites: generation and characterization, Vol. 2* Wiley-VCH: Weinheim, **2010**, pp. 493-546.

[14]   G. L. Woolery, G. H. Kuehl, H. C. Timken, A. W. Chester and J. C. Vartuli, *Zeolites* **1997**, *19*, 288-296.

[15]   J. A. van Bokhoven, D. C. Koningsberger, P. Kunkeler, H. van Bekkum and A. P. M. Kentgens, *J. Am. Chem. Soc.* **2000**, *122*, 12842-12847.

[16]   N.-Y. Topsöe, K. Pedersen and E. G. Derouane, *J. Catal.* **1981**, *70*, 41-52.

[17]   P. Ildefonse, D. Cabaret, P. Sainctavit, G. Calas, A. M. Flank and P. Lagarde, *Phys. Chem. Miner.* **1998**, *25*, 112-121.

[18]   J. A. van Bokhoven, D. C. Koningsberger, P. Kunkeler and H. van Bekkum, *J. Catal.* **2002**, *211*, 540-547.

[19]   X. Lin, Y. Fan, Z. Liu, G. Shi, H. Liu and X. Bao, *Catal. Today* **2007**, *125*, 185-191.

[20]   J.-P. Gilson, G. C. Edwards, A. W. Peters, K. Rajagopalan, R. F. Wormsbecher, T. G. Roberie and M. P. Shatlock, *J. Chem. Soc. Chem. Comm.* **1987**, 91-92.

[21]   V. L. Zholobenko, L. M. Kustov, V. Y. Borovkov and V. B. Kazansky, *Zeolites* **1988**, *8*, 175-178.

[22]   K. Eichele and R. E. Wasylishen, *J. Phys. Chem.* **1994**, *98*, 3108-3113.

[23]   J. C. Védrine, A. Auroux, P. Dejaifve, V. Ducarme, H. Hoser and S. Zhou, *J. Catal.* **1982**, *73*, 147-160.

[24]   J. A. Lercher and G. Rumplmayr, *Appl. Catal.* **1986**, *25*, 215-222.

[25]   M. Derewinski, P. Sarv, X. Sun, S. Müller, A. C. van Veen and J. A. Lercher, *J. Phys. Chem. C* **2014**, *118*, 6122-6131.

[26]   E. Loeffler, U. Lohse, C. Peuker, G. Oehlmann, L. M. Kustov, V. L. Zholobenko and V. B. Kazansky, *Zeolites* **1990**, *10*, 266-271.

[27]   O. Lisboa, M. Sánchez and F. Ruette, *J. Mol. Catal. A-Chem,* **2008**, *294*, 93-101.

[28]   S. Malola, S. Svelle, F. L. Bleken and O. Swang, *Angew. Chem. Int. Ed.* **2012**, *51*, 652-655.

[29]   T. Fjermestad, S. Svelle and O. Swang, *J. Phys. Chem. C* **2013**, *117*, 13442-13451.

[30]   S. M. Abubakar, D. M. Marcus, J. C. Lee, J. O. Ehresmann, C. Y. Chen, P. W. Kletnieks, D. R. Guenther, M. J. Hayman, M. Pavlova, J. B. Nicholas and J. F. Haw, *Langmuir* **2006**, *22*, 4846-4852.

[31]   G. Seo and R. Ryoo, *J. Catal.* **1990**, *124*, 224-230.

[32]   I. Lukes, M. Borbaruah and L. D. Quin, *J. Am. Chem. Soc.* **1994**, *116*, 1737-1741.

[33]   E. Bourgeat-Lami, P. Massiani, F. Di Renzo, P. Espiau, F. Fajula and T. Des Courières, *Appl. Catal.* **1991**, *72*, 139-152.

[34]   T.-H. Chen, K. Houthoofd and P. J. Grobet, *Micropor. Mesopor. Mater.* **2005**, *86*, 31-37.

[35]   Z. M. Yan, J. Q. Zhuang, L. Xu, X. W. Han, Z. M. Liu and X. H. Bao, *Chin. Chem. Lett.* **2003**, *14*, 87-90.

[36]   J. Zhuang, D. Ma, G. Yang, Z. Yan, X. Liu, X. Liu, X. Han, X. Bao, P. Xie and Z. Liu, *J. Catal.* **2004**, *228*, 234-242.

[37]   S. M. Cabral de Menezes, Y. L. Lam, K. Damodaran and M. Pruski, *Micropor. Mesopor. Mater.* **2006**, *95*, 286-295.

[38]   A. Stanislaus, M. Absi-Halabi and K. Al-Doloma, *Appl. Catal.* **1988**, *39*, 239-253.

[39]   E. C. de Oliveira Lima, J. M. Moita Neto, F. Y. Fujiwara and F. Galembeck, *J. Colloid Interface Sci.* **1995**, *176*, 388-396.

4.6 Appendix

Table A4.1 Parameters used for the deconvolution of the FT-IR spectra.

Type	Center	Height	FWHM	Type
0 Quadratic	-	-	-	
1 Lorentzian	3603[a], 3603[b], 3605[c], 3603[d], 3605[e], 3603[f], 3602[g], 3602[h], 3603[i], 3603[j], 3604[k], 3604[l]	0.25[a], 0.17[b], 0.32[c], 0.19[d], 0.20[e], 0.37[f], 0.06[g], 0.13[h], 0.19[i], 0.55[j], 0.05[k], 0.09[l]	38.14[a], 43.70[b], 37.62[c], 44.43[d], 44.36[e], 37.79[f], 41.31[g], 46.70[h], 34.76[i], 34.45[j], 43.21[k], 47.40[l]	Si-OH-Al
2 Lorentzian	3718[a], 3724[b], 3718[c], 3723[d], 3719[e], 3718[f], 3720[g], 3720[h], 0[i], 3726[j], 3718[k], 3719[l]	0.03[a], 0.03[b], 0.05[c], 0.05[d], 0.04[e], 0.05[f], 0.03[g], 0.06[h], 0.00[i], 0.03[j], 0.03[k], 0.04[l]	35.03[a], 24.13[b], 38.42[c], 25.20[d], 20.39[e], 36.61[f], 31.24[g], 33.45[h], 0.00[i], 16.75[j], 27.44[k], 27.38[l]	Si-OH (internal)
3 Lorentzian	3740[a], 3741[b], 3740[c], 3741[d], 3737[e], 3739[f], 3741[g], 3740[h], 0[i], 3740[j], 3741[k], 3740[l]	0.04[a], 0.06[b], 0.06[c], 0.09[d], 0.02[e], 0.05[f], 0.03[g], 0.05[h], 0.00[i], 0.07[j], 0.03[k], 0.03[l]	9.65[a], 8.57[b], 9.45[c], 9.41[d], 8.25[e], 10.34[f], 7.51[g], 8.66[h], 0.00[i], 8.64[j], 7.04[k], 8.25[l]	Si-OH (external)
4 Lorentzian	0[a], 3658[b], 0[c], 3658[d], 3685[e], 0[fe], 3653[g], 3659[h], 0[i], 0[j], 3656[k], 3659[l]	0.00[a], 0.07[b], 0.00[c], 0.10[d], 0.02[e], 0.00[f], 0.03[g], 0.06[h], 0.00[i], 0.00[j], 0.04[k], 0.04[l]	0.00[a], 32.40[b], 0.00[c], 35.53[d], 38.63[e], 0.00[f], 78.30[g], 64.23[h], 0.00[i], 0.00[j], 62.71[k], 54.72[l]	Al-OH
5 Lorentzian	3355[a], 3355[b], 3355[c], 3355[d], 3355[e], 3355[f], 3355[g], 3355[h], 3355[i], 3355[j], 3355[k], 3355[l]	0.05[a], 0.05[b], 0.07[c], 0.06[d], 0.07[e], 0.07[f], 0.03[g], 0.07[h], 0.04[i], 0.09[j], 0.02[k], 0.03[l]	436.85[a], 436.85[b], 436.85[c], 436.85[d], 436.85[e], 436.85[f], 436.85[g], 436.85[h], 436.85[i], 436.85[j], 436.85[k], 436.85[l]	unknown
6 Lorentzian	3544[a], 3544[b], 3544[c], 3544[d], 3544[e], 3544[f], 3544[g], 3544[h], 3544[i], 3544[j], 3544[k], 3544[l]	0.03[a], 0.03[b], 0.04[c], 0.04[d], 0.05[e], 0.05[f], 0.04[g], 0.06[h], 0.02[i], 0.04[j], 0.03[k], 0.04[l]	153.26[a], 153.26[b], 153.26[c], 153.26[d], 153.26[e], 153.26[f], 153.26[g], 153.26[h], 153.26[i], 153.26[j], 153.26[k], 153.26[l]	unknown

[a] [Z] [b] [Z]$_{TT}$ [c] [Z]$_{NA}$ [d] [Z]$_{NA-TT}$ [e] [Z]$_{2PA}$ [f] [Z]$_{2PA-e}$ [g] [Z]$_{2PA-TT}$ [h] [Z]$_{2PA-TT}$ e [i] [Z]$_{2PB}$ [j] [Z]$_{2PB-e}$ [k] [Z]$_{2PB-TT}$ [l] [Z]$_{2PB-TT-e}$.

Table A4.2 Isotropic chemical shifts and second-order quadrupolar effect parameters (SOQE) estimated from the analysis of ^{27}Al MQ MAS spectra.

Sample	[Z]$_{TT}$		[Z]$_{2PA}$		[Z]$_{2PA-e}$		[Z]$_{2PA-TT}$		[Z]$_{2PA-TT-e}$		[Z]$_{2PB}$		[Z]$_{2PB-TT-e}$	
	δ_{iso} (ppm)	SOQE (MHz)	δ_{iso} (ppm)	SOQE (MHz)	δ_{iso} (ppm)	SOQE (MHz)	δ_{iso} (ppm)	SOQE (MHz)	δ_{iso} (ppm)	SOQE (MHz)	δ_{iso} (ppm)	SOQE (MHz)	δ_{iso} (ppm)	SOQE (MHz)
1	56.6	2.6	56.6	2.6	58.7	4.6	56.6	3.1	55.8	2.1	56.8	2.6	56.5	2.8
2	1.27	2.8	0.9	2.5	3.1	4.7	1.1	3.0	0.3	2.4	-	-	0.9	3.6
3	-	-	51.7	6.6	58.9	7.7	51.7	6.5	51.6	6.6	55.8	6.7	52.0	6.7
4	-	-	-2.6	2.6	-0.3	5.1	-2.45	3.2	-3.0	2.7	-4.2	3.6	-2.1	3.8
5	-	-	-5.1	3.4	-2.9	4.8	-5.12	3.4	-5.1	2.9	-7.1	3.6	-5.0	3.8
6	-	-	-9.1	3.6	-	-	-9.0	3.6	-9.7	2.9	-10	3.7	-8.9	3.6
7	58.5	6.5	-	-	-	-	-	-	-	-	-	-	-	-

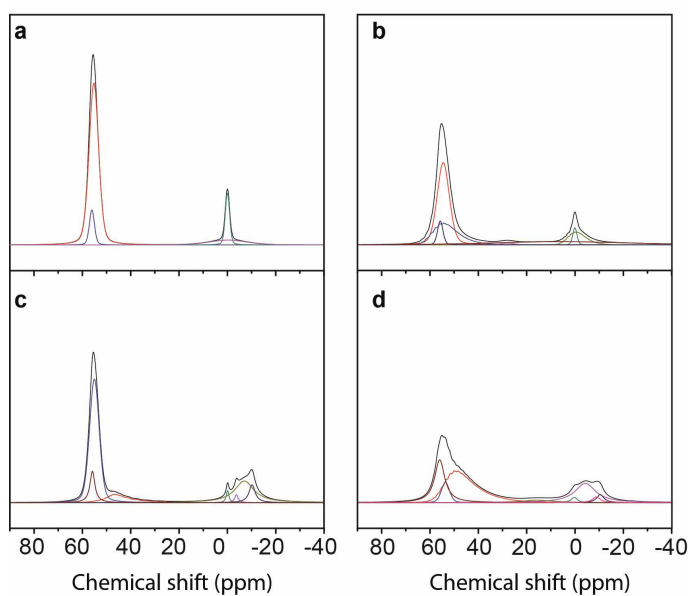**Figure A4.1** Examples of ^{27}Al 1D MAS NMR spectra and corresponding deconvolution for the following samples: (a) [Z]], (b) [Z]$_{TT}$, (c) [Z]$_{2PA}$, and (d) [Z]$_{2PA-TT}$
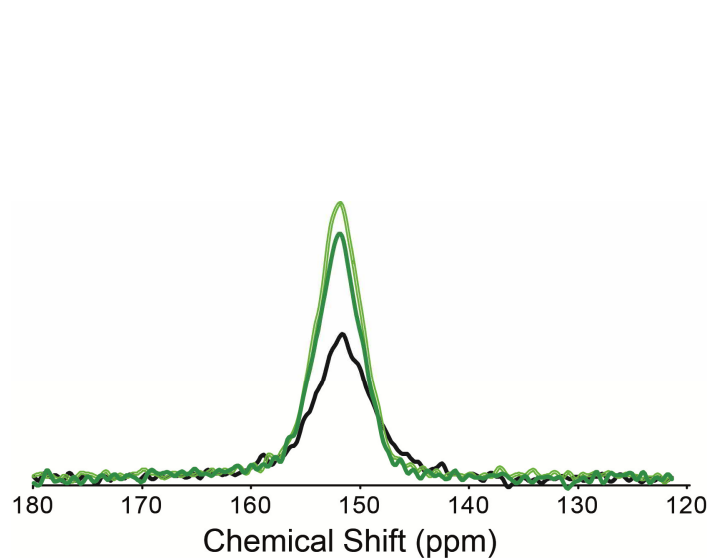
Figure A4.2 ^{27}Al MQ MAS NMR spinning sideband of the 55 ppm resonance of the following samples: ■ = [Z] ■ =[Z]$_{2PB}$, and ■ = [Z]$_{2PB-e}$

Hexane Cracking over Steamed Phosphated Zeolite H-ZSM-5: Promotional Effect on Catalyst Performance and Stability

The nature behind the promotional effect of phosphorus on the catalytic performance and hydrothermal stability of zeolite H-ZSM-5 has been studied using a combination of ^{27}Al and ^{31}P MAS NMR spectroscopy, soft X-ray absorption tomography and *n*-hexane catalytic cracking, complemented with NH$_3$ TPD and N$_2$ physisorption. Phosphated H-ZSM-5 retains more acid sites and catalytic cracking activity after steam treatment than its non-phosphated counterpart, while the selectivity towards propylene is improved. It was established that the stabilization effect is two-fold. First, the local framework SAPO interfaces - that form after phosphatation - are not affected by steam and hold aluminum atoms fixed in the zeolite lattice, preserving the pore structure of zeolite H-ZSM-5. Second, four-coordinated framework aluminum can be forced into a reversible six-fold coordination by phosphate. These species remain stationary in the framework under hydrothermal conditions as well. Removal of physical-coordinated phosphate after steam-treatment leads to an increase in the number of strong acid sites and increased catalytic activity. We propose that the improved selectivity towards propylene during catalytic cracking can be attributed to local SAPO interfaces located at channel intersections, where they act as impediments in the formation of bulky carbenium ions and therefore suppress the bimolecular cracking mechanism.
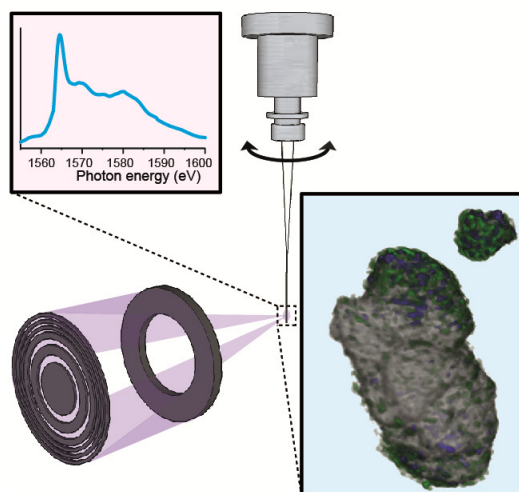
Chapter 5

5.1 Introduction

As was mentioned in the previous Chapters, the dealumination of zeolites under hydrothermal conditions poses a challenge in the industrial application of zeolites as acid catalysts. For example, in the fluid catalytic cracking (FCC) process, a regeneration step of the zeolites is performed at high temperatures and in the presence of steam. While this step is effective in the removal of coke deposits, it also promotes dealumination, leading to gradual permanent deactivation of the catalyst.[1-2] This catalytic deactivation of zeolites may also take place in high temperature reactions where H_2O forms as a reaction byproduct, examples being the methanol-to-hydrocarbons (MTH) process and the dehydration of alcohols. Therefore, hydrothermal stabilization is paramount for the industrial application of zeolites.

We have read in Chapters 1 and 2 that phosphorus modification is a well-known method to increase hydrothermal stability in zeolite H-ZSM-5.[3-6] H-ZSM-5 materials that contain phosphorus have more Brønsted acid sites, more tetrahedrally coordinated framework aluminum (TFAl) atoms, less extra-framework aluminum (EFAl) species and most importantly, better catalytic activity after hydrothermal treatment than their non-phosphated counterparts.[7-10] Besides an improved hydrothermal stability, phosphorus-modified H-ZSM-5 has been found to show an improved selectivity toward propylene during catalytic cracking and the MTH reaction, which is usually attributed to a change in acid site number and strength. [11-24] Although the benefits of phosphorus addition to H-ZSM-5 are obvious, the exact role it plays in stabilization is not quite understood, as there is no clear consensus if and how phosphorus-framework interactions occur. [8, 22, 25-37]

In the last ten years, a series of reversible and irreversible phosphorus interactions with framework aluminum have been proposed.[11, 27, 35, 38] Both Zhuang et al. and Damodaran and co-workers have suggested that phosphate forms aluminum-phosphate-like structures with partially dislodged framework aluminum species and stabilizes these species during hydrothermal treatment. [27, 35, 38] In Chapter 4, we found more evidence for these species and identified them as local silico-aluminophosphate (SAPO) interfaces, still connected to the zeolitic framework.

In this Chapter we have used a combination of micro-spectroscopy, spectroscopy and catalytic testing methods in order to link these interactions to the promotional effect of phosphorus on the performance and stability of steamed zeolite H-ZSM-5. One of the techniques that has been applied in this Chapter is 3-D scanning transmission X-ray microscopy (STXM),
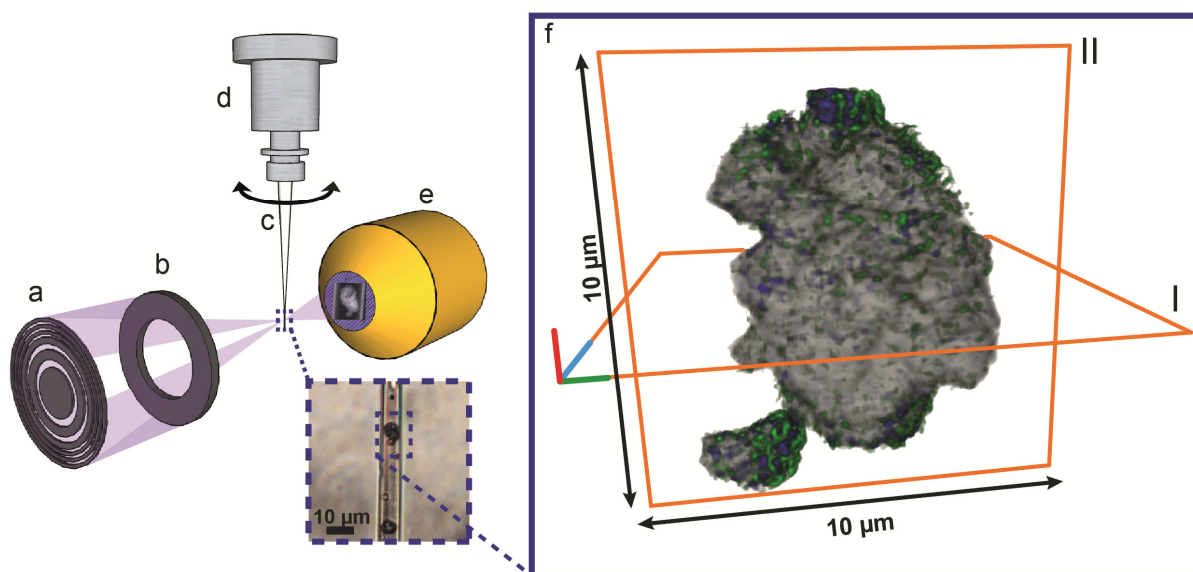
Figure 5.1 Left hand side, soft X-ray tomography setup. Monochromatic X-rays are focused by a (a) zone plate, while all but first-order light is blocked by (b) an order sorting aperture. The X-rays are focused to ~30 nm spot size, which pass through a zeolite aggregate of about 8 μm in diameter. The aggregate is positioned in a (c) borosilicate capillary tip of 10 μm, with wall thickness of approximately 1 μm. The capillary is placed in a (d) tomography stage and can freely rotate 360°. X-rays that passed through the sample are collected by an (e) X-ray detector. Right hand side, (f) 3-D reconstruction of a phosphated (4 wt.% P), and steamed (800 °C, 2 h) zeolite H-ZSM-5 aggregate ($[Z]_{4P-ST}$), based on X-ray tomography images. Voxel size = 69x69x69 nm³. ■ = particle density (Figure 5.2 b i), ■ = aluminum (Figure 5.2 b iv), ■ = phosphorus (Figure 5.2 d iii). Different cross-sections of the particle are indicated by I and II, which are shown in Figure 5.4 and 5.8 The positions of the cross sections are marked in orange. More information on 3-D reconstruction is shown in Figure 5.2.

presented in Figure 5.1, which has recently been employed by our group to obtain 3-D nanoscale chemical images of aluminum in zeolite H-ZSM-5.[39]

By extending this approach to the phosphorus K-edge, we have been able to simultaneously record the 3-D distribution of phosphorus and aluminum species in H-ZSM-5 for the first time. Soft X-ray tomography, in combination with the bulk techniques ^{27}Al and ^{31}P magic angle spinning (MAS) NMR spectroscopy, NH_3 temperature programmed desorption (TPD), N_2 physisorption, and *n*-hexane cracking, provided us with fundamental insights in the stabilization phenomena. It will be shown that hydrothermal stabilization indeed stems from phosphorus interactions with framework aluminum and that the stabilization has two major origins: The first resulting from irreversible phosphorus-framework interactions, which also promote propylene selectivity. The second from reversible interactions of phosphorus with framework aluminum, which can be removed after steam treatment, leading to improved cracking activity.

Chapter 5

5.2 Experimental methods

5.2.1 Sample preparation
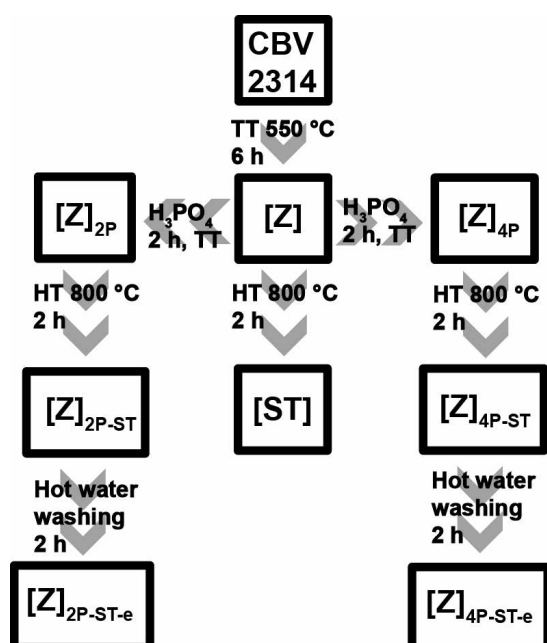
Scheme 5.1 Overview of the zeolite samples used in this study and prepared using different treatments. TT = thermal treatment, HT = hydrothermal treatment. Number (2 or 4) indicates target phosphorus weight loading, P = phosphated, ST = Steam-treated, e = (phosphorus has been) eluted.

Commercially available Zeolyst CBV 2314 NH_4-ZSM-5 (Si/Al ratio = 11.5) was calcined in a 100 ml/min O_2 stream at 550 °C for 6 h. The obtained H-ZSM-5 material is referred to as [Z]. Phosphatation was performed as described by Xue et al., 3 g of [Z] was mixed with an appropriate amount H_3PO_4 in 200 ml H_2O (P/Al ratio = 0.5 or P/Al ratio = 1). [40] The mixture was kept at 80° C and stirred for 2 h. Afterwards, the solvent was removed by rotary evaporation. Subsequently, the sample was dried overnight at 120 °C and then calcined at 600 °C for 5 h. The sample is referred to as $[Z]_{2P}$ for P/Al = 0.5 and $[Z]_{4P}$ for P/Al = 1. A steam treatment was performed on the samples [Z], $[Z]_{2P}$ and $[Z]_{4P}$ similar to Zhuang et al.[27] The samples were treated with 80 vol.% steam using N_2 as a carrier gas. Hydrothermal conditions were kept at 800 °C for 2 h. Afterwards, samples [ST], $[Z]_{2P-ST}$ and $[Z]_{4P-ST}$ were obtained. Samples $[Z]_{2P-ST-e}$, and $[Z]_{4P-ST-e}$ were prepared by suspending 0.6 g of samples $[Z]_{2P-ST}$ and $[Z]_{4P-ST}$ respectively in 200 ml hot water (80°C), where they were stirred for 2 h and filtered. Afterwards, water was removed from both samples by filtration over a millipore filter and samples were dried at 120 °C overnight.

5.2.2 Catalytic cracking of *n*-hexane

50 mg of sample in the form of 400-200 μm grains was placed in a packed bed reactor that consisted of a cylindrical quartz tube, with a squared section containing optical grade windows, on a quartz grit. The reactor tube was placed inside an oven that contained a hole, in which a Avantes UV-Vis probe was aligned through the optical grade windows on the sample. The UV-Vis light source was a Micropack DH-2000-BAL. Reflected UV-Vis light was collected by an Avantes Avaspec 2048 Spectrometer. The sample was heated with 10 K/min to 550° C in a flow of 10 ml/min O_2 and kept at this flow and temperature for 1h. After that the sample was cooled

to 100 °C. The UV-Vis background was collected on the calcined sample. A 14 ml/min flow of He was guided through a saturator filled with *n*-hexane (99+% pure Acros) that was cooled to -7.2 °C. The outgoing flow was diluted with a 13 ml/min flow of He to a total flow of 27.54 ml/min, of which approximately 1.9 vol% was *n*-hexane (WHSV = 2.2 h^{-1}). The sample was kept at 100° C in this flow of *n*-hexane for 7 min, after which the temperature program was started. The sample was heated to 600° C with a rate of 2 K/min. Every 60 s a UV-Vis spectrum was collected and every 320 s the effluent was injected into a Global Analyser Solutions Compact GC. The GC had three channels (i) an Alumina 10 m column + FID detector, (ii) an RTX-1 15 m 0.25 µm column + FID detector and (iii) an RT-Q-BOND 3 m column + TCD detector.

5.2.3 Ammonia temperature programmed desorption

Ammonia temperature programmed desorption (NH$_3$ - TPD) experiments were performed on a Micromeretics Autochem II. Samples were dried in a He flow at 600° C for 15 min and cooled to 100° C, after which ammonia was introduced in loops. Once the sample was saturated the temperature program was started. Under a flow of He the sample was heated with 5 K/min to 600° C. The outgoing NH$_3$ was detected by a TCD detector.

5.2.4 N$_2$-physisorption

Adsorption-desorption isotherms were recorded using a Micromeritics Tristar 3000 setup operating at -196 °C. Prior to physisorption measurements, all samples were dried overnight at 500 °C under a N$_2$ flow.

5.2.5 Scanning transmission X-ray microscopy

Scanning transmission X-ray microscopy (STXM) experiments were performed at the Beamline 10ID-1 of the Canadian Light Source (CLS). The samples were dispersed in H$_2$O and a droplet was placed on a silicon nitride window. After drying in air the sample was placed in the STXM chamber, which was subsequently evacuated to 10^{-1} mbar. A polarized X-ray beam was obtained using a 1.5 m long, 75 mm period Apple II undulator. The X-ray beam was focused to ~30 nm on the sample plane using a Fresnel zone plate (ZP). The beam from the ZP passed through a molybdenum-based order-sorting aperture (OSA), with a 50 µm pinhole. The OSA allowed only first-order ZP diffracted light to pass. Spectral image sequences (stacks) are measured by recording images over a range of photon energies, corresponding to an absorption edge. After
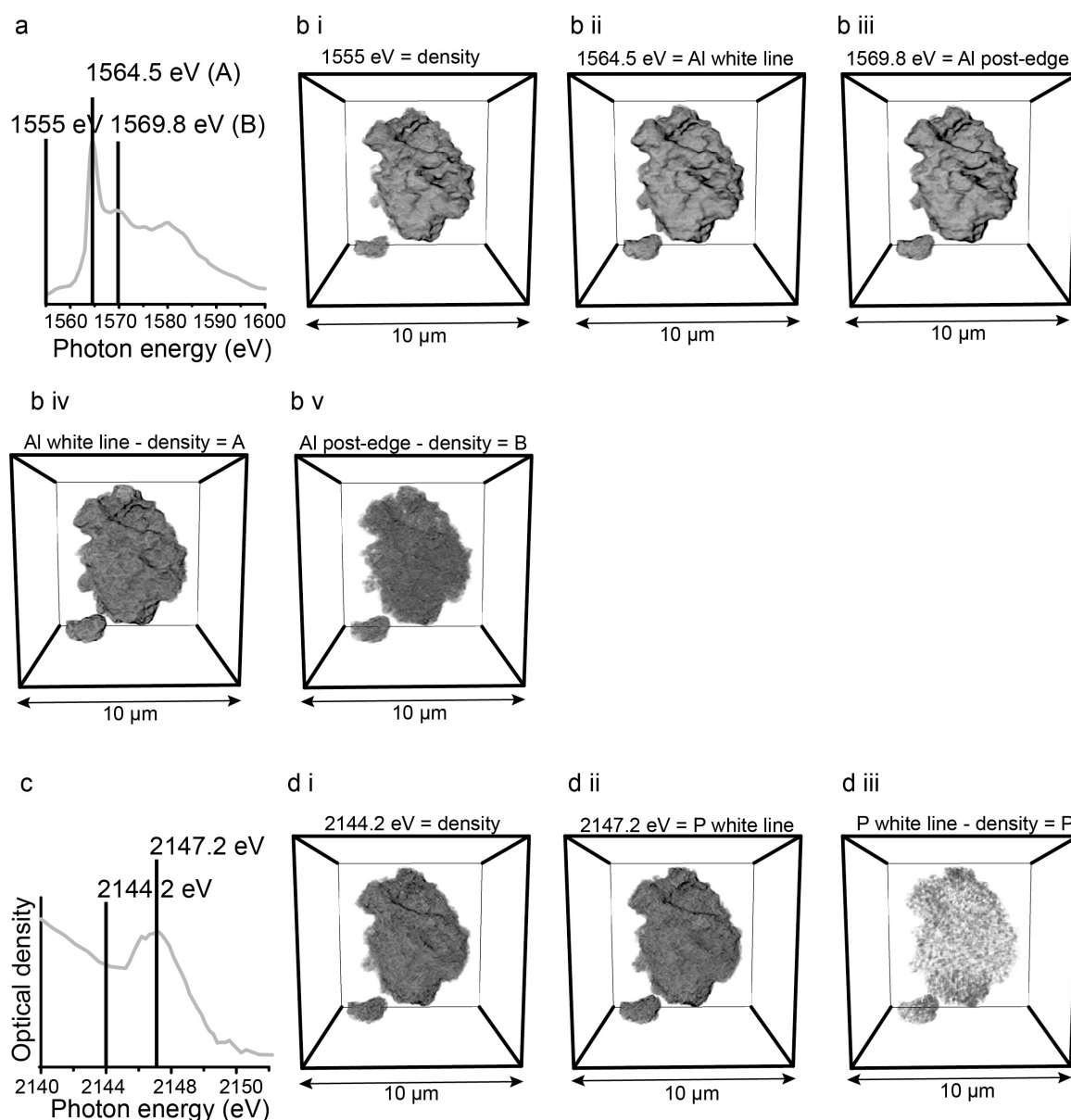
Figure 5.2 Additional information on the tomography experiment. (a) Al K-edge XANES of the whole particle, obtained by 2-D STXM. Black lines indicate which energies have been measured for the tomography experiment. (b) 3-D reconstructions of the X-ray absorption tomography data of the three measured energies at the Al K-edge. (b i) 1555 eV, corresponds to particle density. (b ii) 1565 eV, the Al white line. (b iii) 1569 eV, post-edge feature. (b iv) Volume of 1565 eV subtracted by the volume of 1555 eV = A. (b v) Volume of 1569 eV, subtracted by the volume of 1555 eV = B. (c) P K-edge XANES of the particle measured in tomography, obtained by 2-D STXM. (d i-ii) 3-D reconstructions of the X-ray absorption tomography data of the two measured energies at the P K-edge. (d iii) Volume of 2147 eV subtracted by the volume of 2144 eV, corresponds to the phosphorus concentration (P).

aligning the image sequence, spectra of the whole or a subregion were extracted for comparison.

All STXM data analysis was performed using aXis2000 and MATLAB. As shown in Figure 5.1, tomography experiments were performed by mounting sample $[Z]_{4P-ST}$ in a borosilicate capillary. The capillary had a 1 mm external diameter and was heated and pulled by a micropipette puller. The sample was present in a part of the capillary where the capillary had an

external diameter of 10 microns and a wall thickness of approximately 1 micron. The capillary was placed in a tomography sample stage. For the measurement, the sample was rotated 180° in 36 steps, with a 5° step size. At each step three energies were measured, i.e. 1555 eV, 1564.5 eV and 1569.8 eV. After the sample was rotated the full 180°, the sample was rotated back to 0° in 36 steps with a 5° step size. At each step two energies were measured, i.e. 2144 eV and 2147 eV. Sinograms and binslices were constructed and reconstructed using the TXM-Wizard software using the iterative Algebraic Reconstruction Technique (iART) algorithm. The 3-dimensional data was analyzed using Avizo and MATLAB. More information on how the data was treated is shown in Figure 5.2.

5.2.6 Solid-State nuclear magnetic resonance spectroscopy

The solid-state nuclear magnetic resonance (NMR) experiments were performed at 11.7 T on a Bruker Avance III 500 MHz spectrometer using a 4 mm magic angle spinning (MAS) probe at room temperature. The MAS rate was 15 kHz for all experiments. The ^{27}Al NMR spectra were obtained using $\pi/12$ pulses, 1000 scans and a recycling delay of 0.5 s at a rf-field of 94 kHz. The ^{31}P spectra were obtained using a pulse length of 1.8 µs, 64 scans and with a recycle delay of 60 s. The chemical shifts of ^{27}Al, and ^{31}P were externally referenced to 1M $Al(NO_3)_{3(aq)}$, and 85% $H_3PO_{4(aq)}$, respectively.

5.2.7 Chemical analysis

Chemical analysis of the zeolite samples was performed by inductively coupled plasma-optical emission spectrometry (ICP-OES) on a Perkin-Elmer 3300DV instrument.

5.3 Results and Discussion

In order to determine the promotional effect of phosphorus on the catalytic performance and hydrothermal stability of H-ZSM-5, three sets of samples have been prepared. One family of materials did not contain any phosphorus, while the two other sets of samples contained 2 wt.% and 4 wt.% of phosphorus, respectively. All materials have been subjected to a hydrothermal treatment at 800 °C for 2 h. A detailed overview of the sample preparation routes applied and abbreviation definitions, can be found in Scheme 5.1.
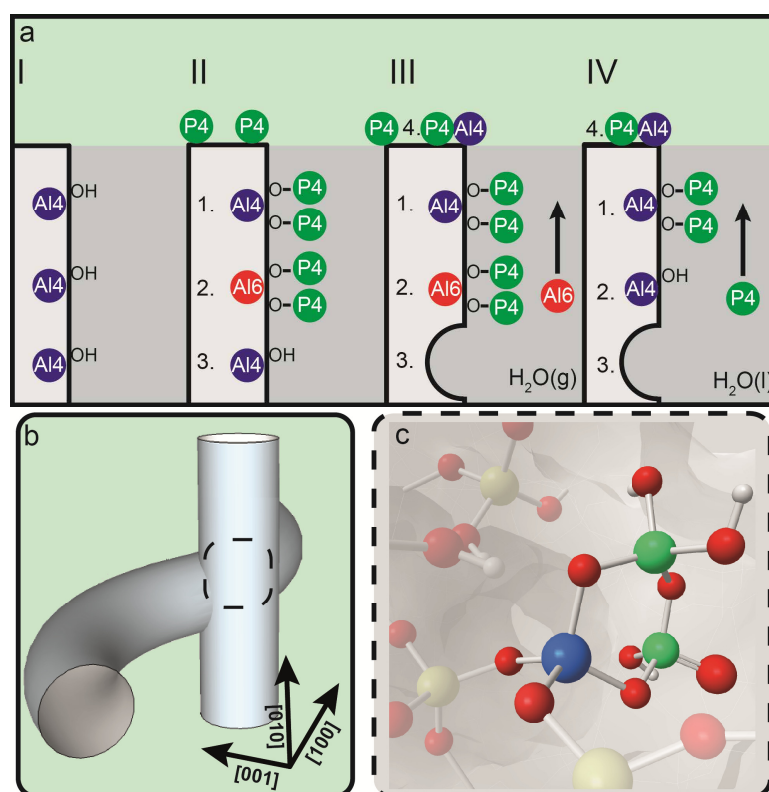
Scheme 5.2 Schematic overview of the results presented in this work. (a) Stabilization effect of phosphorus on the framework of zeolite H-ZSM-5. (I) Unmodified H-ZSM-5 with three schematically drawn tetrahedrally coordinated framework aluminum (TFAl) atoms. (II) Phosphated and calcined H-ZSM-5, showing (1) local silicon-aluminophosphate (SAPO) interfaces, (2) phosphates that induce a six-fold coordination on TFAl and (3) non-interacting TFAl. More details on these species can be found in Scheme 5.3. (III) During steam treatment (3) non-interacting TFAl is expelled from the framework and migrates to the surface where it (4) reacts with phosphates to form $AlPO_4$. (1) Local SAPO interfaces (2) and physically coordinated phosphate aluminum are less affected, keeping aluminum fixed in the framework. (IV) Washing with hot water removes (2) the physically coordinated phosphorus, returning six-coordinated aluminum back into its original form as TFAl atoms, leading to acid site retrieval. (b) Part of the three-dimensional channel system of H-ZSM-5 showing a straight and sinusoidal pore and their intersection. While the straight and sinusoidal channel dimensions fit species up to ~ 5.0 Å in diameter, the channel intersections allow species up to ~ 6.6 Å in diameter.[41] (c) Local SAPO interface located at channel intersections decrease the allowed dimensions of adsorbed species, effectively inhibiting the formation of carbenium ions that form during n-hexane catalytic cracking. As these species are the intermediates in the bimolecular cracking mechanism, this pathway is anticipated to be suppressed.[42]

For the sake of clarity, the focus in the main text is only on the non-phosphated family and the materials containing 4 wt.% of phosphorus. However, we will make one exception and present soft X-ray absorption results of a hydrothermally treated H-ZSM-5 with 2 wt.% of phosphorus sample, as these results clearly exemplify the promotional effect of phosphorus on the hydrothermal stability. All other characterization results of the samples containing 2 wt.% of phosphorus can be found in the Appendix of this Chapter, and illustrate that similar findings can be obtained with a lower phosphorus loading. Any differences that arose from the use of different phosphorus weight loadings are discussed in the Appendix as well.

In the following, we discuss the results obtained along the following sections; first, a structural and catalytic comparison between a steamed phosphated, and a steamed non-phosphated material is made. Second, we present the effect that *irreversible* phosphorus-aluminum interactions have on the hydrothermal stability of H-ZSM-5. In a third part, evidence for the formation of extra-framework aluminum-phosphate during steam treatment is presented, while in a fourth part the effect of *reversible* phosphorus-aluminum interactions on the hydrothermal stability of H-ZSM-5 is discussed. Finally, we discuss the promotional effect of phosphorus on the propylene selectivity during the catalytic cracking of *n*-hexane over H-ZSM-5. Scheme 5.2 presents a schematic overview of the major findings reported in this Chapter and can be used as a visual guideline for the concepts described in the text.

5.3.1 3-D nanoscale chemical imaging

Steam treatment (ST) of the H-ZSM-5 parent sample [Z] at 800 °C for 2 h, leads to the formation of a sample, which we have labeled [ST]. Figures 5.3b and A5.2-A5.5 show that sample [ST] has lost almost all activity as an *n*-hexane cracking catalyst. The deactivation can be attributed to the alteration of the pore structure and the loss of 96% of all strong acid sites, as can be seen in Figures 5.3 and A5.1. N_2-physisorption presented in Figure 5.3a shows the formation of two hysteresis cycles after steam-treatment. The hysteresis cycle at high relative pressures indicates the formation of mesopores, while the low pressure hysteresis is typical for MFI structures and has been proposed to arise from strong vapor-liquid interactions. [43-44] The latter hysteresis cycle is more pronounced with increasing framework Si/Al ratios, indicating that framework aluminum has been expelled from the framework and possibly replaced by silicon. [45, 65]

In contrast, the 4 wt.% phosphorus-containing H-ZSM-5 sample, which we have labeled as $[Z]_{4P-ST}$ and received an identical steam-treatment as sample [ST], yields a factor 8.6 more of C_1-C_5 products during *n*-hexane cracking, as can be observed in Figures 5.3b and A5.2-A5.5. In
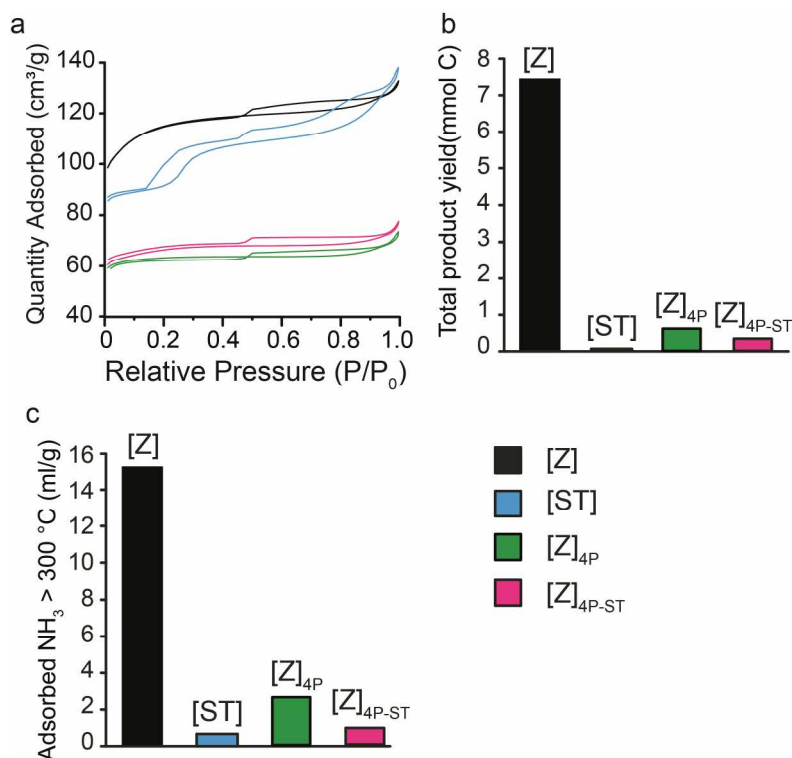
Figure 5.3 (a) N_2 physisorption data. (b) Total product yield of C_1-C_5 species in mmol of carbon atoms that were produced during the temperature programmed reaction (TPR) of n-hexane. (c) Amount of adsorbed ammonia above 300 °C. Samples ■ = [Z] ■ = [ST], ■ = $[Z]_{4P}$ and ■ = $[Z]_{4P-ST}$.

agreement with the latter observation is the higher number of remaining strong acid sites, as sample $[Z]_{4P-ST}$ retains a factor 1.6 more ammonia at temperatures above 300°C than sample [ST] (Figures 5.3b and A5.1). Furthermore, N_2-physisorption presented in Figure 5.3a shows that the pore structure of sample $[Z]_{4P-ST}$ is better retained after steam treatment, as the formation of the low and high pressure hysteresis cycles is not observed, which indicates that mesopores do not form and the framework Si/Al ratio does not change significantly. The initial decrease in pore volume for sample $[Z]_{4P}$, is due to phosphorus species that have migrated into the micropores, as will be discussed below.

Recently, our group performed the first 3-D nanoscale chemical imaging study on the effects of hydrothermal treatment on H-ZSM-5.[39] It was found that for a single H-ZSM-5 catalyst particle steamed at similar conditions as sample $[Z]_{4P-ST}$ (700 °C, 3 h) about 65% of the aluminum species obtained a five- or six-coordination due to hydrolysis of framework Al-O-Si bonds.[39, 46] These (partial) extra-framework aluminum species were heterogeneously distributed throughout the studied zeolite aggregate in patches of nanometer size.
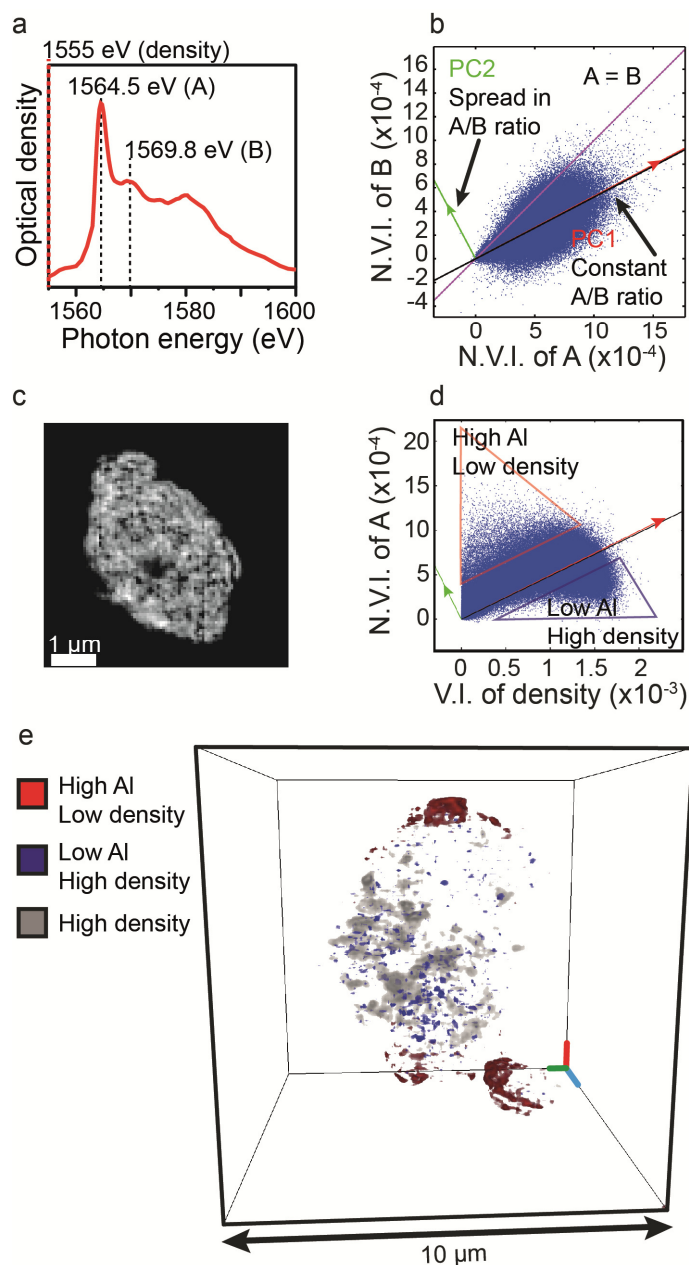
Figure 5.4 (a) The Al K-edge XANES of the whole particle measured with soft X-ray tomography, obtained by 2-D STXM, showing peak A and peak B. (b) Correlation plot of the normalized voxel intensities (N.V.I.) of peak A (x-axis) vs. peak B (y-axis) per voxel of the particle shown in Figure 5.1. The magenta line indicates A = B. The black line is the linear regression fit of the scatterplot. The red vector indicates the positive direction of the first principal component (PC1) and the green vector the positive direction of the second principal component (PC2). Voxels that lie along PC1 behave uniformly, which in this case means that the A/B ratio does not change and the intensity of the peaks increases with increasing optical densities. Any deviations from PC1 run along the axis of PC2. The histogram along PC2 is shown in Figure A5.6 d and shows that these deviations are minimal in terms of participating voxels. (c) Cross-section of the particle indicated by I in Figure 5.1. This is the first Eigenimage (PC1) shown in correlation plot (b), and corresponds directly to the aluminum concentration. (d) Correlation plot of the voxel intensities corresponding to particle density and peak A, which indicate how Al and particle density correlate. The black line is the linear regression fit of the scatterplot. The red vector points in the positive direction of PC1 and the green vector to that of PC2. The red triangle indicates voxels with high Al intensity and low particle density, while the blue triangle indicates voxels with low Al intensity and high particle density. (e) 3-D reconstruction of the PC2 Eigenvolume, indicating volumes corresponding to the voxels in the triangles (d). The grey voxels correspond to high particle density and act as a frame of reference for the particle shape. In summary, Figure 5.4 shows that there is one dominant type of Al K-edge XANES. Aluminum is distributed homogeneously throughout the particle, except at very low and very high particle densities.

Interestingly, when the X-ray tomography approach is applied to hydrothermally treated H-ZSM-5 that contains 4 wt.% of phosphorus, no five- or six-coordinated aluminum species can be observed from the Al K-edge XANES, shown in Figure 5.4 a. The shape of the Al K-edge XANES can be attributed to four-coordinated aluminum (Figure A5.6). [46-47] Furthermore, the Al K-edge XANES can be assumed to be quite uniform throughout the particle under study, as the ratios between the energies at 1564.5 eV (A) and 1569.8 eV (B) do not change significantly. This follows from the correlation plot presented in Figure 5.4 b. Here it can be seen that the average A/B ratio has a higher contribution of A, which follows from the Al K-edge XANES shown in Figure 5.4 a. The shape and density of distribution of the scatterplot indicates that the A/B ratio remains constant with increasing optical density. From these results it can be concluded that in this particle there is one dominant type of Al K-edge XANES for the largest fraction of Al containing voxels. More information can be found in the Appendix, Figure A5.6.

Figure 5.4 c shows cross section I of the particle presented in Figure 5.1. It can be observed that aluminum is found throughout the whole zeolite crystal. However, as is shown in Figure 5.4 d and e, there are high intensities of aluminum at low particle densities, corresponding to specific
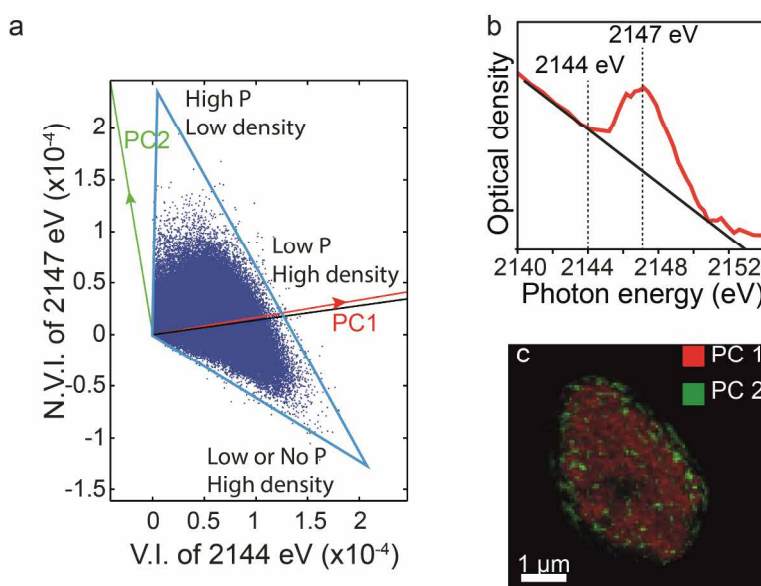

Figure 5.5 (a) Correlation plot of the voxel intensities (V.I.) of 2144 eV (particle density) (x-axis, Figure 5.2 d i) vs. the normalized voxel intensities (N.V.I.) of 2147 eV (P) (y-axis, Figure 5.2 d iii) of each voxel in the 3-dimensional reconstructed particle shown in Figure 5.1. The black line is the linear regression fit of the scatterplot. The red vector indicates the positive direction of the first principle component (PC1) and the green vector that of the second principle component (PC2). The blue triangle was added guide the eye. (b) P K-edge XANES of the particle under study, showing the peak for particle density (2144 eV) and P (2147 eV). Negative intensity values for P in (a) stem from the behavior of the baseline indicated in black. (c) Cross-section of the particle indicated as I in Figure 5.1. Red is the first Eigenimage (PC1) indicated in (a), high red intensity means high optical density and low or no phosphorus concentration. Green is the second Eigenimage (PC2). High green intensity means low optical density and high phosphorus concentration. The image shows that phosphorus is located everywhere in the particle at low concentrations. However, high concentrations of phosphorus are found at low particle densities (on the external surface) and at high particle densities the concentration of phosphorus decreases.

aluminum enriched regions on the particle surface. Furthermore, the correlation plot in Figure 5.4 d shows a negative correlation between the aluminum concentration and the optical density at high optical densities. This indicates that there is less aluminum present in the thicker/deeper regions of the particle, shown in Figure 5.4 e.

The distribution of phosphorus presented in Figures 5.1 and 5.5 show that there is a higher concentration of phosphorus on the zeolitic outer surface, which was also found in Chapters 3 and 4, which was attributed to non-interacting excess (poly)phosphate species.[15, 28, 30] A schematic representation of these excess surface species is shown in Scheme 5.2a. From the positive correlation between optical density and phosphorus concentration presented in Figure 5.5 a, it follows that phosphorus is present in the zeolitic interior as well, albeit in lower concentrations. This is in agreement with the N_2-physisorption results shown in Figure 5.3a and A5.2, which show that the micropore volume decreases after phosphorus modification. At higher optical densities, there is a decrease in phosphorus concentration, similar to the distribution of aluminum.

Figure 5.6 shows the protecting effect of phosphorus quite clearly. As mentioned, we present these results by example of a hydrothermally treated 2 wt.% phosphorus H-ZSM-5 sample. The X-ray absorption maps of sample $[Z]_{2P-ST}$ (Figure 5.6a and b), show that the presence of phosphorus determines the extent to which dealumination takes place. It was established in Chapter 4 that the applied method of phosphorus modification can lead to interparticle heterogeneities in phosphorous distribution. This can be observed in Figure 5.6a and b, where the zeolite aggregate with green contours contains a higher amount of phosphorus than the zeolite aggregate with orange contours. Consequently, the corresponding Al K-edge XANES in
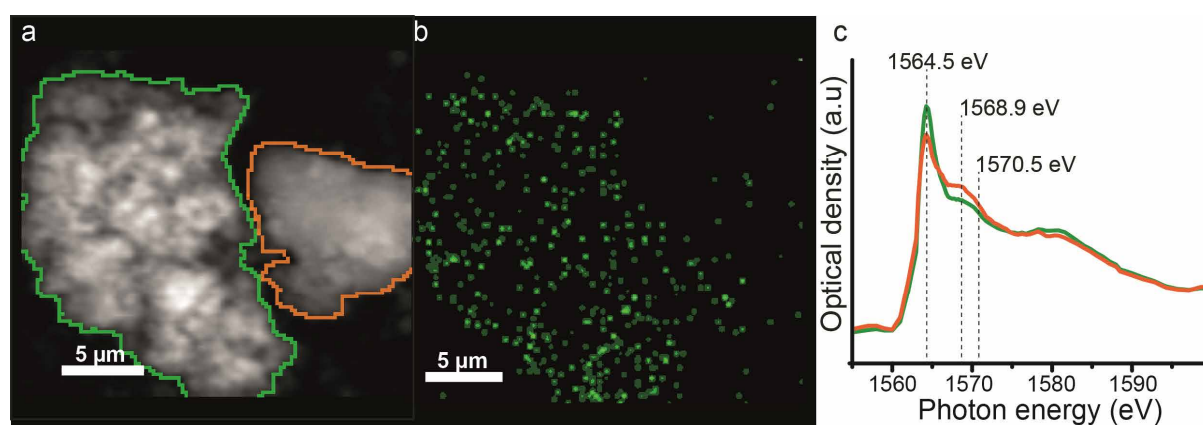
Figure 5.6 (a) X-ray absorption map of sample $[Z]_{2P-ST}$ at 1555 eV. (b) Distribution of phosphorus species in sample $[Z]_{2P-ST}$. Maps have been reconstructed using P K-edge stacks, similar as was performed in Chapter 3 . (c) Al K-edge XANES of sample $[Z]_{2P}ST$. ■ corresponds to the full area of the green contoured zeolite aggregate and ■ corresponds to the full area of the orange contoured zeolite aggregate in Figure 5.6a. Si and Al K-edge map are shown in Figure A5.6.

Figure 5.6c show that the aggregate low on phosphorus has a lower contribution of the peak at 1564.5 eV corresponding four-coordinated framework aluminum (TFAl) atoms, and an increase of a peak at 1568.9 eV, corresponding to five-, and six-coordinated extra-framework aluminum species.[46] Therefore, in absence of phosphorus dealumination of H-ZSM-5 aggregates takes place under hydrothermal conditions.

5.3.2 Combined micro-spectroscopy and bulk spectroscopy

So far we have seen that: (i) the presence of phosphorus prevents the formation of the spectroscopic signatures that correspond to five-, and six-coordinated aluminum during steam treatment, (ii) one dominant type of four-coordinated Al K-edge XANES is found throughout the whole zeolite, with lower concentrations of aluminum in the deeper parts, (iii) there is no indication of mesopore formation or change in framework Si/Al ratio as determined by N_2-physisorption, (iv) enrichments of aluminum and phosphorus are found on the external zeolitic surface and most importantly (v) phosphated H-ZSM-5 retains a higher acid site number and *n*-hexane cracking activity after steaming than its non-phosphated counterpart.

As the Al K-edge XANES, shown in Figures 5.2, 5.4 and 5.6, is not sufficient in elucidating what type of four-coordinated aluminum is present in phosphated H-ZSM-5, bulk ^{27}Al MAS
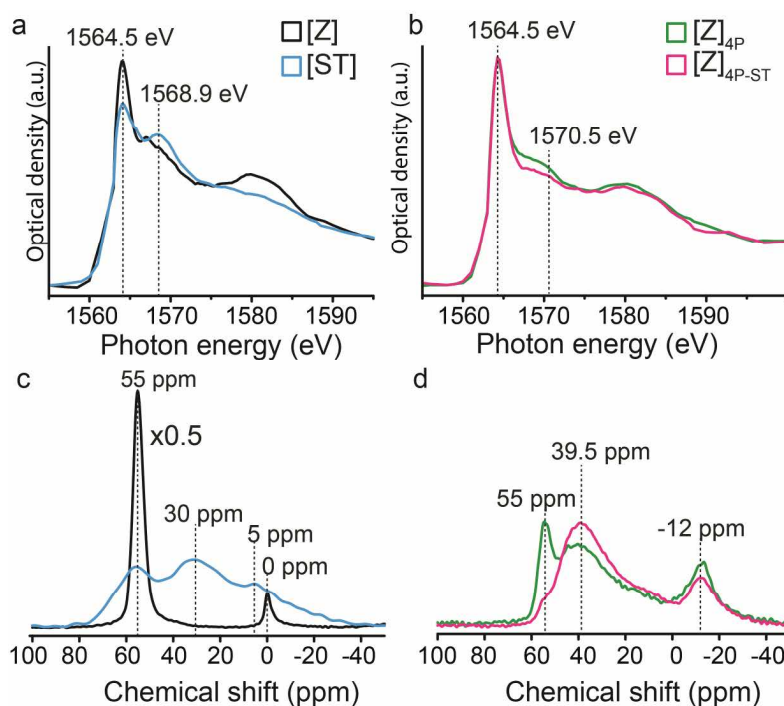

Figure 5.7 (a-b) Al K-edge XANES. (c-d) ^{27}Al MAS NMR. ■ = [Z] ■ = [ST] ■ = [Z]$_{4P}$ and ■ = [Z]$_{4P-ST}$

NMR spectroscopy has been applied to complement the XANES. For the starting H-ZSM-5 sample, denoted as [Z], and its hydrothermally treated descendant [ST], both the ^{27}Al MAS NMR spectra and the Al K-edge XANES, presented in Figure 5.7, are in agreement with previously reported findings.[2, 39, 46] The Al K-edge XANES of parent sample [Z], shown in Figure 5.7a, reveals a white-line at 1564.5 eV, attributed to aluminum in a four-fold coordination. [46-47] This is in accordance with the dominant 55 ppm resonance, observed in the ^{27}Al MAS NMR spectrum of sample [Z], shown in Figure 5.7c, which corresponds to four-coordinated aluminum at framework T-sites (TFAl).[48] These species are schematically presented in Scheme 5.2a. The resonance at 0 ppm corresponds to six-coordinated framework aluminum atoms often found in hydrated H-ZSM-5 (OFAl) .[49-50]

After hydrothermal treatment, the Al K-edge XANES of sample [ST] shows a decrease in intensity of the white-line at 1564.5 eV and the appearance of a new peak at 1568.9 eV, which is attributed to five-, and six-coordinated extra-framework aluminum.[46-47] The formation of extra-framework aluminum (EFAl) species and the decrease of TFAl species is also observed by ^{27}Al MAS NMR spectroscopy, as in Figure 5.7c the formation of a broad resonance at 30 ppm can be observed, corresponding to five-coordinated or four-coordinated extra-framework aluminum. [51-53] Furthermore, the intensity of the 55 ppm resonance decreases sharply after hydrothermal treatment.

The ^{27}Al MAS NMR spectra shown in Figures 5.7d and A5.8-A5.9, are typical for phosphated H-ZSM-5 materials, as we have seen in Chapters 2-4.[27, 38] After phosphatation and prior to steam-treatment, it can be seen in Figure 5.7d that for sample [Z]$_{4P}$ the intensity of the resonance at 55 ppm (TFAl atoms) decreases in comparison to the parent sample [Z]. A broad resonance between 40 ppm - 10 ppm appears, which can be assigned to a variety of local silico-aluminophosphate (SAPO) interfaces. As was mentioned in Chapter 4, these interfaces form when phosphoric acid binds with partially dislodged TFAl species that form during the thermal treatment performed after phosphorus introduction.[27, 35] Schemes 5.2a and 5.3 present schematic drawings of these species. Furthermore, there is a broad resonance around -12 ppm after phosphatation, which was partly attributed to OFAl species interacting with phosphorus and partly to TFAl atoms that are forced into a six-fold coordination by physically coordinated phosphate species in Chapter 4. These species are presented in Schemes 5.2a and 5.3v. [35] Another possible assignment for the -12 ppm resonance is six-coordinated aluminum in amorphous aluminum-phosphate $Al(PO_4) \cdot 2\ H_2O$.[25, 54]
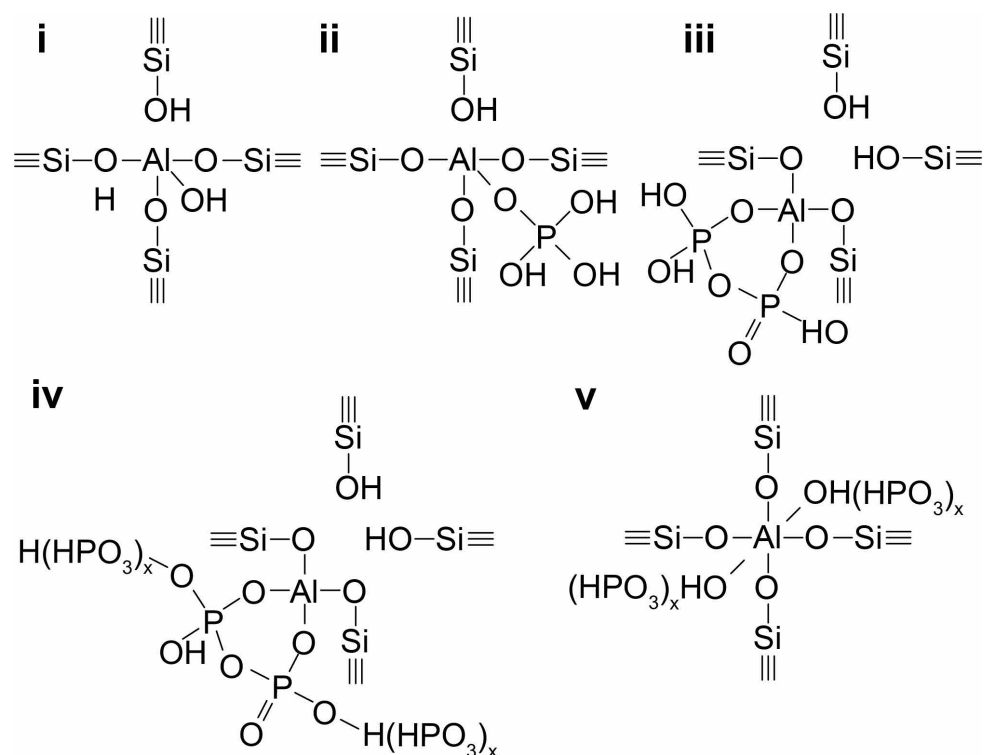
Scheme 5.3 Suggestions of different TFAl species found in phosphated and thermally treated H-ZSM-5. (i) Partially dislodged framework Al species. (ii) Local SAPO interface (iii) Local SAPO interface with phosphorus bidentate (iv) Local SAPO interface with multiple condensed phosphate species, (v) TFAl forced into a six-fold coordination by physically bonded phosphate species.

As was mentioned in the previous section of this Chapter, the formation of EFAl species is not observed for phosphated H-ZSM-5 after steam treatment, as can be seen from the Al K-edge XANES of sample $[Z]_{4P-ST}$ in Figure 5.7b. After steam treatment it can be observed in Figure 5.7d and A5.9 that the classic TFAl species with a resonance at 55 ppm, which have no interaction with phosphorus [35], decrease after steam treatment. As we have already seen in Chapter 3, the resonances for local SAPO interfaces between 40 ppm - 10 ppm are not strongly affected by the steam treatment, which is also in accordance with previous literature reports.[27, 38] Even more, for sample $[Z]_{4P-ST}$ there is an increase in the resonance intensity around -39.5 ppm, indicating this resonance forms at the cost of the decreased 55 ppm resonance. From the ^{27}Al MAS NMR spectra in Figure 5.7d and A5.9 it can be observed that after steaming the majority of the aluminum atoms in phosphated H-ZSM-5 are present as the broad resonance from 40 ppm - 10 ppm. This was previously observed and quantified by Cabral de Menezes et al.[38] However, it cannot be excluded that resonances corresponding to (partially) extra-framework aluminum species in this region are superimposed by the 40 ppm - 10 ppm resonance.

If we apply the following reasoning; that for phosphated and subsequently hydrothermally treated H-ZSM-5 (i) the majority of the aluminum observed in the ^{27}Al MAS NMR spectra is present as the resonance corresponding to local SAPO interfaces and (ii) the corresponding Al

K-edge XANES shows one type of aluminum in a four-coordinated state, we can conclude that at least a majority of the aluminum observed by X-ray tomography can be attributed to four-coordinated aluminum present in local SAPO interfaces, shown in Scheme 5.3. In addition, both the Al K-edge XANES and ^{27}Al MAS NMR spectra show that hydrothermal treatment has a limited effect on the spectroscopic signatures assigned to SAPO interfaces. Furthermore, 3-D X-ray microscopy shows that the local SAPO interfaces are distributed throughout the whole crystal (Figures 5.2 and 5.4)

Thus, we propose that the local framework SAPO interfaces in zeolite H-ZSM-5 stabilize partially dislodged framework aluminum species and hold these fixed in the zeolite lattice, as shown in Scheme 5.2a. Consequently, the pore structure is better retained in comparison to non-phosphated H-ZSM-5, as follows from the N_2-physisorption data shown in Figure 5.3 and A5.2. Nevertheless, it has been shown that with prolonged steam treatments, i.e. at 750 °C for 10 h or more, most aluminum in phosphated H-ZSM-5 forms extra-framework crystalline $AlPO_4$.[10, 27] This indicates that the formation of local SAPO interfaces will not prevent dealumination altogether, but it reduces the speed of the dealumination process.

5.3.3 Extra-framework aluminum-phosphate deposits

The ^{27}Al MAS NMR spectrum of sample $[Z]_{4P-ST}$ in Figure 5.7d shows that there is an increase in the ^{27}Al MAS NMR resonance at 39.5 ppm, after steam treatment. This could point towards two effects, being that (i) local SAPO interfaces adopt a more AlPO-like character, i.e. more Al-O-P bonds replace Si-O-Al bonds (Scheme 5.3iii and iv), as was suggested by Zhuang et al.[27], or (ii) extra-framework $AlPO_4$ is formed, as the ^{27}Al MAS NMR spectrum of four-coordinated aluminum in crystalline $AlPO_4$ is characterized by a sharp resonance around 40 ppm.[25] The latter suggestion is not confirmed by literature reports, as samples steamed at similar conditions (800 °C for 2 h) did not yet show detectable signals of extra-framework $AlPO_4$ by means of 2-D ^{27}Al multiple quantum MAS NMR [27, 38]

However, in support of the $AlPO_4$ formation hypothesis, certain regions on the external surface of the aggregate in Figure 5.1 show an enrichment of aluminum and phosphorus. Figure 5.8 presents the results obtained from a correlation plot between the intensities of phosphorus and aluminum per voxel. From Figure 5.8 b and c, it can be observed that aluminum and phosphorus enriched deposits form on the external surface. This latter finding would indicate that extra-framework $AlPO_4$ is formed during hydrothermal treatment, as has been suggested previously. [25, 27-28, 35-36] As mentioned ^{27}Al MAS NMR in Figure 5.7 shows that framework
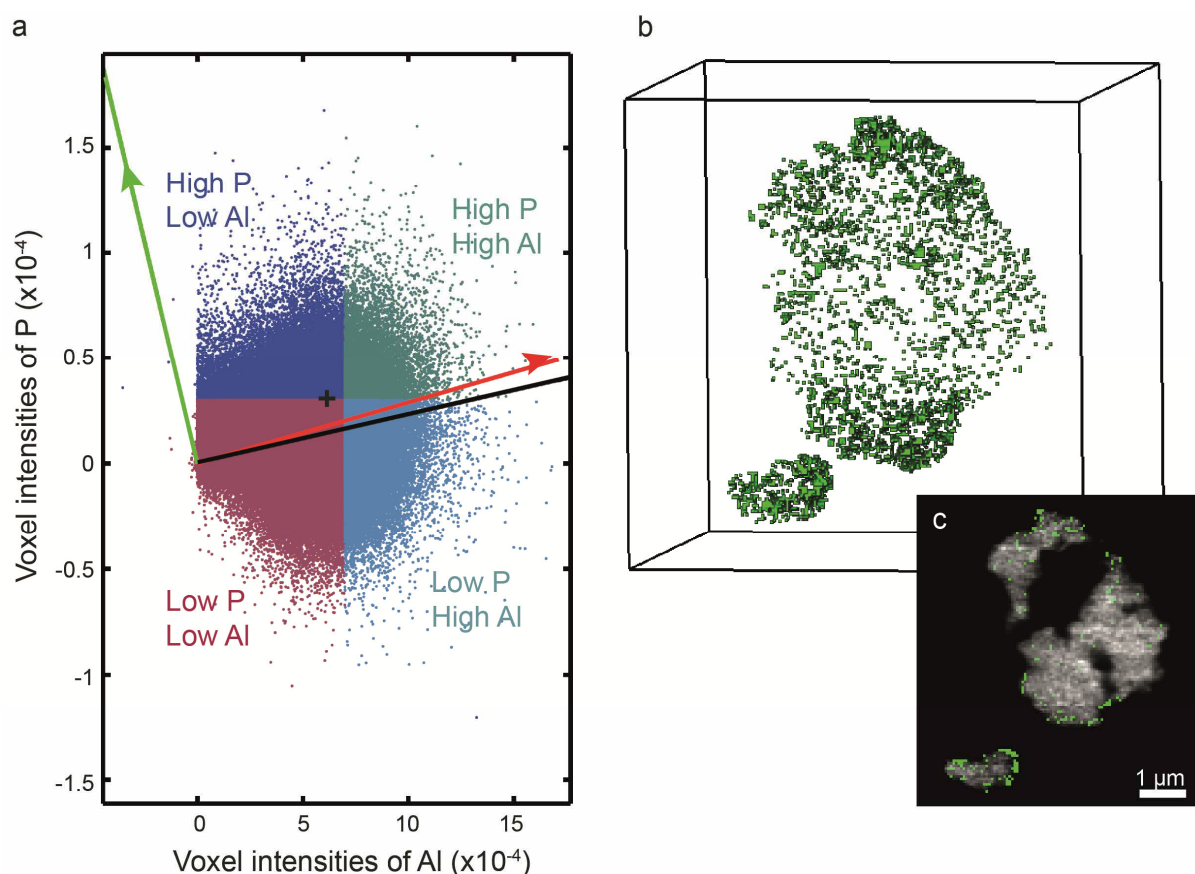
Figure 5.8 (a) Correlation plot of the voxel intensities (V.I.) of Aluminum (x-axis, Figure 5.2 b iv) vs. Phosphorus (y-axis, Figure 5.2 d iii) of each voxel of the volume . The black line is the linear regression fit of the scatterplot. The red vector indicates the positive direction of the first principle component (PC1) and the green vector that of the second principle component (PC2). The correlation plot is divided into four segments Red = low P and low Al, Cyan = low P and high Al, Blue = high P and low Al, Green = high P and high Al (b) Volume rendering of the voxels corresponding to the high P and high Al regime. (c) Cross-section of the particle indicated by II in Figure 5.1, showing the distribution of High P and High Al voxels in respect to the optical density. Figure 5.8 shows that there is an enrichment of phosphorus and aluminum on the external surface of the particle.

aluminum (55 ppm) that is not in the presence of phosphorus disappears during steam treatment. Furthermore, phosphorus was found to be in lower concentrations in the denser parts of the aggregate. Thus, it is suggested that the TFAl atoms located deep in the crystal interior and in the absence phosphorus, are hydrolyzed under steaming conditions and migrate to the surface.[28, 39, 55]

This proposed migration is in agreement with the lower concentrations of aluminum found in the denser parts of the aggregate. Subsequently, migrated aluminum reacts with excess phosphate species present on the zeolitic surface to from crystalline $AlPO_4$ deposits. This process is presented in Scheme 5.2 a. As mentioned, it was difficult to determine if $AlPO_4$ formation took place from the ^{27}Al MAS NMR spectra. Therefore, soft X-ray microscopy is a good choice to indirectly detect these subtle physicochemical effects.
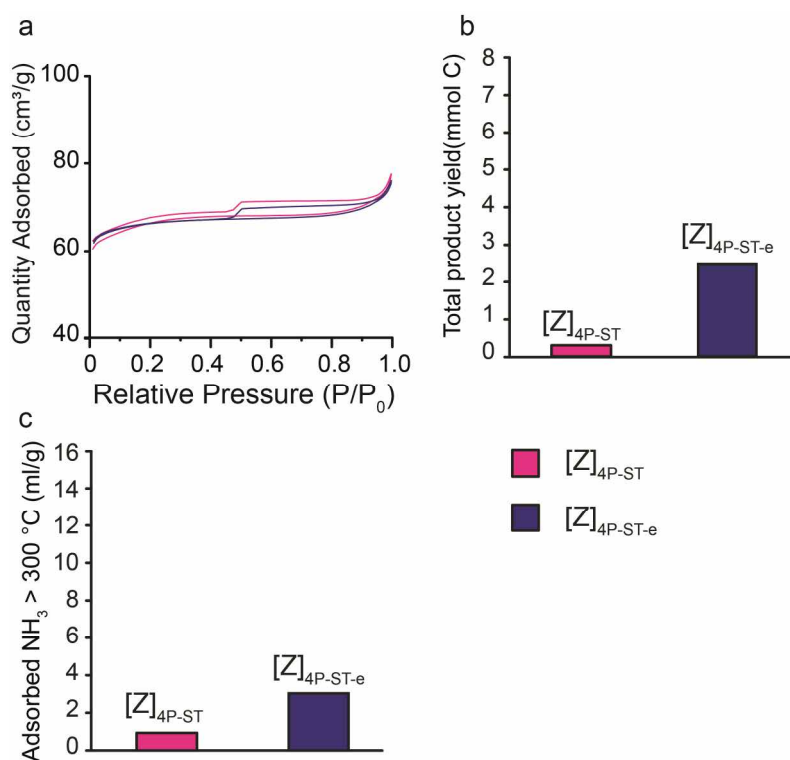
Figure 5.9 (a) N_2 physisorption data (b) total product yield of C_1-C_5 species in mmol of carbon atoms that were produced during the temperature programmed reaction (TPR) of n-hexane. (c) Amount of adsorbed ammonia above 300 °C. Samples ■ = $[Z]_{4P\text{-}ST}$ and ■ = $[Z]_{4P\text{-}ST\text{-}e}$.

5.3.4 Reversible hydrothermal stability

Hot water washing of phosphated H-ZSM-5 is known to remove non-interacting and reversibly interacting phosphate species from the zeolite, which leads to an increase in strong acid site number. [8, 10-11, 25, 56]   When phosphated and steamed H-ZSM-5 samples, such as $[Z]_{4P\text{-}ST}$, are washed with hot water, 20-30 % of the phosphorus atoms, with respect to the amount of silicon atoms, is removed, as shown in Tables 5.1 and A5.1. Elution of phosphorus from the 4 wt.% phosphorus-containing and steamed H-ZSM-5 sample, leads to formation of a sample that we denoted as $[Z]_{4P\text{-}ST\text{-}e}$. Figure 5.9b and c show that there is a factor 7.51 increase in the total C_1-C_5 product yield for the catalytic cracking of *n*-hexane and a factor 3.19 increase in the number of strong acid sites after washing sample $[Z]_{4P\text{-}ST}$. In order to assess where these renewed active sites originate from we have applied ^{27}Al MAS NMR. It can be observed in Figures 5.10 a and A5.9 that after washing the resonance at -12 ppm decreases in intensity and the resonance at 55 ppm reappears. Chemical analysis presented in Tables 5.1 and A5.1 show that no significant leaching of aluminum species takes place during the washing step.

A resonance at -10 ppm was attributed in Chapter 4 to TFAl species that are reversibly forced into a six-fold coordination by physically bonded phosphate species, shown in Schemes 5.2a and 5.3. [50] Removal of these interactions by hot water washing was shown to lead to the retrieval of
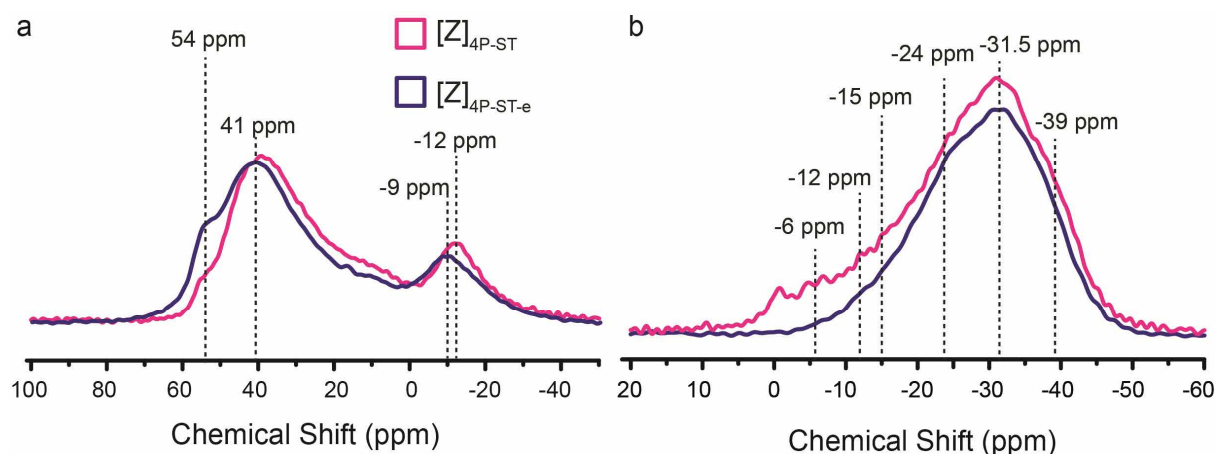
Figure 5.10 (a) ^{27}Al MAS NMR. (b) ^{31}P MAS NMR, spectral intensities are normalized to the weigh percentage of phosphorus (Table 5.1). Samples ■ = [Z]$_{4P-ST}$, and ■ = [Z]$_{4P-ST-e}$.

TFAl atoms and corresponding strong acid site number. Based on this we propose that these type of interactions also stabilize TFAl species during hydrothermal treatment. The retrieval of acid sites after washing out phosphorus from steamed H-ZSM-5, has been reported previously. [8, 10, 25] Therefore, it is important to realize that reversible interactions between phosphates and TFAl species already seem to promote hydrothermal stability of aluminum in the framework. A schematic representation of this effect is shown in Scheme 5.2a. It can be further observed in Figure 5.10a that there is a shift in the 40 ppm - 10 ppm resonance after washing, which is attributed to the removal of excess phosphorus present in the micropores.

From the ^{31}P MAS NMR in Figures 5.10b and A5.9 it can be seen that resonances at -1 ppm, -6 ppm and -12 ppm decrease in intensity after washing. These interactions correspond to

Table 5.1 ICP-OES results of the elements Si, Al and P in the zeolite H-ZSM-5 samples under investigation. [a]

Sample	Al (wt%)	P (wt.%)	Si (wt.%)	Si/Al[b]	P/Al	P/Si
[Z]	3.1	-	33.7	10.5	-	-
[ST]	2.8	-	30.0	10.2	-	-
[Z]$_{4P}$	2.5	3.4	27.7	10.8	1.2	0.11
[Z]$_{4P-ST}$	2.4	3.3	27.5	11.0	1.2	0.11
[Z]$_{4P-ST-e}$	2.4	2.7	28.0	11.2	1.0	0.09

[a] Samples are measured after drying, [b] Bulk Si/Al ratio

orthophosphates, pyrophosphates, and polyphosphates. [35-36] The resonance at -15 ppm has been attributed to phosphate species that physically interact with TFAl species, as was determined by ^{27}Al – ^{31}P heteronuclear correlation (HETCOR) NMR spectroscopy in Chapter 4. The remaining dominant resonance is at -31.5 ppm. ^{27}Al – ^{31}P HETCOR NMR experiments have shown that these phosphorus species are in very close vicinity to distorted aluminum species and ^{27}Al – ^{31}P insensitive nuclei enhanced by polarization transfer (INEPT) HETCOR spectroscopy has shown that these species correspond to Al-O-P type bonds. [35] The species are attributed to local SAPO interfaces that have a more AlPO-like character, i.e. more phosphorus species interact with the same TFAl atom, as bidentates or as branched phosphates shown in Scheme 5.3 iii and iv. [27, 38] After washing out excess phosphorus, the majority of the phosphorus species are expected to be found in the local SAPO interfaces, as shown in Scheme 5.2a.

5.3.5 Catalytic cracking of *n*-hexane

The removal of excess phosphorus from phosphated and steamed H-ZSM-5 does not only lead to a recovery of the active sites. Indeed, after phosphatation the H-ZSM-5 material also shows a different product distribution and especially an improved selectivity towards propylene during the catalytic cracking of *n*-hexane as can be seen in Figures 5.11 and A5.5. Figure 5.11a shows that while for sample [Z] 0.5 mol propylene is produced per converted *n*-hexane molecule, this is increased to 0.7 mol propylene per converted *n*-hexane molecule for sample [Z]$_{4P-ST-e}$. Furthermore, as can be seen in Figures 5.11b and A5.4, UV-Vis spectroscopy performed during the cracking reaction shows that the darkening of sample [Z]$_{4P-ST-e}$, related to coke formation [57], occurs at a lower rate than for sample [Z].

In line with the literature on phosphated H-ZSM-5, we attribute the decreased cracking activity, relative to the parent H-ZSM-5, to the overall decrease in strong acid sites. [7, 58] However, the improved selectivity towards propylene observed during temperature programmed cracking of *n*-hexane is attributed to changes in the pore dimensions of phosphated H-ZSM-5 and not necessarily to changes in acidity, as was discussed in Chapter 2. Recently, Janardhan et al. reported the formation of monolayer phosphate islands in the pores of H-ZSM-5, which changed the shape-selectivity of H-ZSM-5.[56] Furthermore, recent literature investigated the effect of channel intersections on the selectivity towards propylene during *n*-octane cracking.[59] In this study it was found that the 1-dimensional pore system of ZSM-22 showed an increase in selectivity toward propylene in comparison to the 3-dimensional pore system of ZSM-5. In another work it was shown that when ferrierite with a 2-dimensional pore system (1-dimensional

10-MR channels and 1-dimensional 8-MR channels) is used as a catalyst in the cracking of *n*-hexane, a higher selectivity toward methane, ethane propylene and butylene was found, while H-ZSM-5 showed higher selectivity towards ethylene, propane and butane.[60]

As can be seen from Figure 5.11 c, sample [Z]$_{4P-ST-e}$ shows a similar selectivity pattern as ferrierite in comparison to parent H-ZSM-5, i.e. a higher selectivity toward methane, ethane, propylene and butylene, and a lower selectivity towards ethylene, propane and butane. It has been reported that this difference in selectivity follows from the ability of a zeolitic framework to stabilize carbenium ions, which are the intermediate species in the bimolecular cracking mechanism. [61-62] For unmodified H-ZSM-5, the channel intersections can more successfully stabilize these voluminous carbenium ions. [62-63] Therefore, it has been reported that small channel zeolites show a preference for monomolecular cracking, while large channel zeolites prefer bimolecular cracking. [42] The monomolecular reaction pathway leads to the formation of methane, ethane and propylene, while the bimolecular cracking pathway promotes the formation of higher paraffins [42] and possibly ethylene. [60]
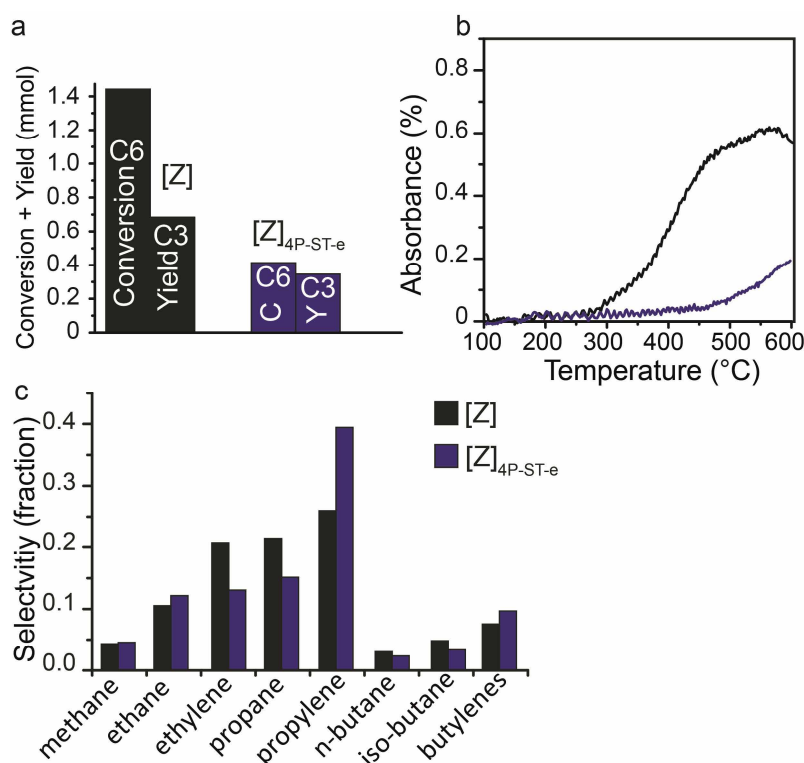
Figure 5.11 (a) The total yield of produced propylene vs. the total amount of converted n-hexane at temperatures above 350 °C. ■ = [Z] (mmol) ■ = [Z]$_{4P-ST-e}$. (mmol) (b) Evolution of the 1100 nm band measured by UV-Vis spectroscopy showing the overall darkening of the sample, corresponding to coke formation. ■ = [Z] ■ = [Z]$_{4P-ST-e}$. (c) Selectivity in moles of the main products formed during the catalytic cracking of n-hexane over a full temperature program ■ = [Z] ■ = [Z]$_{4P-ST-e}$.

Based on our results and those reported in the literature, we suggest that the phosphates in local SAPO interfaces located at channel intersections, as presented in Scheme 5.2b and c, act as a steric impediment for the formation of bulky carbenium ions, suppressing the bimolecular cracking mechanism. This leads to a product distribution that is more similar to zeolites with no internal cavities, e.g. zeolite H- ferrierite and H-ZSM-22. Further studies would be needed to substantiate the proposed model.

5.4 Conclusions

The physicochemical origins of the promotional effect of phosphorus on the catalytic performance and hydrothermal stability of zeolite H-ZSM-5 have been studied using a combination of soft X-ray tomography and solid-state NMR spectroscopy. It was found that the hydrothermal stabilization effect of phosphorus appears to originate mainly from two types of phosphorus-framework aluminum interaction.

The first origin is the presence of local framework silico-aluminophosphate (SAPO) interfaces, which form when phosphate species bind with partially dislodged framework aluminum species that form during thermal treatment. These local SAPO interfaces are still partially connected to the zeolitic framework through Si-O-Al bonds, and are distributed throughout the whole zeolite particle. It was found that hydrothermal treatment has no strong effect on these species. Therefore, the local SAPO interfaces remain fixed in the zeolite lattice for longer periods during steaming, preserving the framework Si/Al ratio and the pore structure of H-ZSM-5. Framework aluminum that is not stabilized by phosphorus is more easily expelled during hydrothermal treatment and migrate to the external surface where a reaction with phosphate species takes place and $AlPO_4$ is formed.

The second cause for hydrothermal stabilization by phosphorus comes from reversible phosphorus-aluminum interactions. Phosphorus can interact reversibly with TFAl atoms, forcing them into six-fold coordination. It appears these interactions remain unaffected during steam treatment as well. Furthermore, removing these reversible interactions after hydrothermal treatment by washing out phosphorus with hot water, leads to the retrieval of classic TFAl atoms and corresponding Brønsted acid sites.

The retrieval of acid sites after the elution of phosphorus leads to an increase in catalytic cracking activity for *n*-hexane. Furthermore, phosphated and steamed samples show an increase

in propylene selectivity as the formation of propane and ethylene decreases. This effect is suggested to arise from the presence of local SAPO interfaces located in the channel intersections, which suppress the formation of intermediate species of the bimolecular cracking mechanism that normally form in the internal cavities of the H-ZSM-5 framework.

Therefore, we propose that local framework SAPO interfaces play a role in both catalyst stabilization, improving lifetime under steaming conditions, and in boosting the catalyst selectivity towards propylene.

Acknowledgements

References

[1] J. E. Otterstedt, S. B. Gevert, S. G. Jääs and P. G. Menon, *Appl. Catal.* **1986**, *22*, 159-179.

[2] C. S. Triantafillidis, A. G. Vlessidis, L. Nalbandian and N. P. Evmiridis, *Micropor. Mesopor. Mater.* **2001**, *47*, 369-388.

[3] W. F. Lai, M. A. Hamilton and S. J. Mccarthy in *Process for producing phosphorus modified zeolite catalysts*, Patent WO2013059176 A1, **2013**.

[4] G. Burghels, E. Corresa Mateu, S. Klingelhofer, J. Martinez-Triguero, M. Frauenrath, A. Corma in *Process for manufacture of a zeolite based catalyst for the conversion of methanol to olefins*, Patent WO2012123558 A1, **2012**.

[5] A. K. Ghosh, N. Kulkarni and P. L. Harvey in *Method of making a catalyst and catalyst made thereby and its use in aromatic alkylation*, Patent WO2014025371 A1, **2014**.

[6] L. A. Chewter, W. J. Van Westrenen and F. Winter in *Process for the manufacture of a formulated oxygenate conversion catalyst, formulated oxygenate conversion catalyst and process for the preparation of an olefinic product*, Patent WO2010133643 A2, **2010**.

[7] G. Caeiro, P. Magnoux, J. M. Lopes, F. R. Ribeiro, S. M. C. Menezes, A. F. Costa and H. S. Cerqueira, *Appl. Catal. A-Gen* **2006**, *314*, 160-171.

[8] T. Blasco, A. Corma and J. Martínez-Triguero, *J. Catal.* **2006**, *237*, 267-277.

[9] A. Corma, J. Mengual and P. J. Miguel, *Appl. Catal. A-Gen* **2012**, *421*, 121-134.

[10] D. Liu, W. C. Choi, C. W. Lee, N. Y. Kang, Y. J. Lee, C.-H. Shin and Y. K. Park, *Catal. Today* **2011**, *164*, 154-157.

[11] M. Derewinski, P. Sarv, X. Sun, S. Müller, A. C. van Veen and J. A. Lercher, *J. Phys. Chem. C* **2014**, *118*, 6122-6131.

[12] D. L. Johnson, K. E. Nariman and R. A. Ware in *Catalytic production of light olefins rich in propylene*, Patent WO2001004237 A2, **2001**.

[13] D. H. Harris in *Novel catalyst to increase propylene yields from a fluid catalytic cracking unit*, Patent WO2014042641 A1, **2014**.

[14] M. S. Al-Ghrami and C. Ercan in *Catalyst for enhanced propylene in fluidized catalytic cracking*, Patent WO2013177388 A1, **2013**.

[15] J. C. Védrine, A. Auroux, P. Dejaifve, V. Ducarme, H. Hoser and S. Zhou, *J. Catal.* **1982**, *73*, 147-160.

[16] A. Rahman, G. Lemay, A. Adnot and S. Kaliaguine, *J. Catal.* **1988**, *112*, 453-463.

[17] A. Rahman, A. Adnot, G. Lemay, S. Kaliaguine and G. Jean, *Appl. Catal.* **1989**, *50*, 131-147.

[18] S. M. Abubakar, D. M. Marcus, J. C. Lee, J. O. Ehresmann, C. Y. Chen, P. W. Kletnieks, D. R. Guenther, M. J. Hayman, M. Pavlova, J. B. Nicholas and J. F. Haw, *Langmuir* **2006**, *22*, 4846-4852.

[19] J. Liu, C. Zhang, Z. Shen, W. Hua, Y. Tang, W. Shen, Y. Yue and H. Xu, *Catal. Commun.* **2009**, *10*, 1506-1509.

[20] P. Li, W. Zhang, X. Han and X. Bao, *Catal. Lett.* **2010**, *134*, 124-130.

[21] G. Jiang, L. Zhang, Z. Zhao, X. Zhou, A. Duan, C. Xu and J. Gao, *Appl. Catal. A-Gen* **2008**, *340*, 176-182.

[22] N. Xue, X. Chen, L. Nie, X. Guo, W. Ding, Y. Chen, M. Gu and Z. Xie, *J. Catal.* **2007**, *248*, 20-28.

[23] N. Xue, L. Nie, D. Fang, X. Guo, J. Shen, W. Ding and Y. Chen, *Appl. Catal. A-Gen* **2009**, *352*, 87-94.

[24] G. Zhao, J. Teng, Z. Xie, W. Jin, W. Yang, Q. Chen and Y. Tang, *J. Catal.* **2007**, *248*, 29-37.

[25] G. Lischke, R. Eckelt, H. G. Jerschkewitz, B. Parlitz, E. Schreier, W. Storek, B. Zibrowius and G. Öhlmann, *J. Catal.* **1991**, *132*, 229-243.

[26] G. Yang, J. Zhuang, Y. Wang, D. Zhou, M. Yang, X. Liu, X. Han and X. Bao, *J. Mol. Struc.* **2005**, *737*, 271-276.

[27] J. Zhuang, D. Ma, G. Yang, Z. Yan, X. Liu, X. Liu, X. Han, X. Bao, P. Xie and Z. Liu, *J. Catal.* **2004**, *228*, 234-242.

[28] M. J. B. Cardoso, D. D. O. Rosas and L. Y. Lau, *Adsorption* **2005**, *11*, 577-580.

[29] W. W. Kaeding and S. A. Butter, *J. Catal.* **1980**, *61*, 155-164.

[30] J. A. Lercher and G. Rumplmayr, *Appl. Catal.* **1986**, *25*, 215-222.

[31] M. Göhlich, W. Reschetilowski and S. Paasch, *Micropor. Mesopor. Mater.* **2011**, *142*, 178-183.

[32] A. Jentys, G. Rumplmayr and J. A. Lercher, *Appl. Catal.* **1989**, *53*, 299-312.

[33] P. Tynjälä, T. T. Pakkanen and S. Mustamaki, *J. Phys. Chem. B* **1998**, *102*, 5280-5286.

[34] G. Seo and R. Ryoo, *J. Catal.* **1990**, *124*, 224-230.

[35] K. Damodaran, J. W. Wiench, S. M. Cabral de Menezes, Y. L. Lam, J. Trebosc, J. P. Amoureux and M. Pruski, *Micropor. Mesopor. Mater.* **2006**, *95*, 296-305.

[36] J. Caro, M. Bülow, M. Derewinski, J. Haber, M. Hunger, J. Kärger, H. Pfeifer, W. Storek and B. Zibrowius, *J. Catal.* **1990**, *124*, 367-375.

[37] V. N. Romannikov, A. J. Tissler and R. Thome, *React. Kinet. Catal. Lett.* **1993**, *51*, 125-134.

[38] S. M. Cabral de Menezes, Y. L. Lam, K. Damodaran and M. Pruski, *Micropor. Mesopor. Mater.* **2006**, *95*, 286-295.

[39] L. R. Aramburo, Y. Liu, T. Tyliszczak, F. M. F. de Groot, J. C. Andrews and B. M. Weckhuysen, *ChemPhysChem* **2013**, *14*, 496-499.

[40] N. Xue, R. Olindo and J. A. Lercher, *J. Phys. Chem. C* **2010**, *114*, 15763-15770.

[41] www.iza-structure.org.

[42] A. F. H. Wielers, M. Vaarkamp and M. F. M. Post, *J. Catal.* **1991**, *127*, 51-66.

[43] J. Rouquerol, F. Rouquerol, P. Llewellyn, G. Maurin and K. S. Sing, *Adsorption by powders and porous solids: principles, methodology and applications*, Academic press London, **1999**, pp. 389-396.

[44] V. Mayagoitia, F. Rojas and I. Kornhauser, *J. Chem. Soc. Faraday Trans.* **1985**, *81*, 2931-2940.

[45] P. L. Llewellyn, Y. Grillet, J. Patarin and A. C. Faust, *Micropor. Mater.* **1993**, *1*, 247-256.

[46]   L. R. Aramburo, E. de Smit, B. Arstad, M. M. van Schooneveld, L. Sommer, A. Juhin, T. Yokosawa, H. W. Zandbergen, U. Olsbye, F. M. F. de Groot and B. M. Weckhuysen, *Angew. Chem. Int. Ed.* **2012**, *51*, 3616-3619.

[47]   P. Ildefonse, D. Cabaret, P. Sainctavit, G. Calas, A. M. Flank and P. Lagarde, *Phys. Chem. Miner.* **1998**, *25*, 112-121.

[48]   J. Klinowski, *Prog. Nucl. Mag. Res. Sp.* **1984**, *16*, 237-309.

[49]   G. L. Woolery, G. H. Kuehl, H. C. Timken, A. W. Chester and J. C. Vartuli, *Zeolites* **1997**, *19*, 288-296.

[50]   J. A. van Bokhoven, A. M. J. van der Eerden and D. C. Koningsberger, *J. Am. Chem. Soc.* **2003**, *125*, 7435-7442.

[51]   J.-P. Gilson, G. C. Edwards, A. W. Peters, K. Rajagopalan, R. F. Wormsbecher, T. G. Roberie and M. P. Shatlock, *J. Chem. Soc. Chem. Comm.* **1987**, 91-92.

[52]   J. Sanz, V. Fornés and A. Corma, *J. Chem. Soc. Faraday Trans.* **1988**, *84*, 3113-3119.

[53]   E. Brunner, H. Ernst, D. Freude, T. Fröhlich, M. Hunger and H. Pfeifer, *J. Catal.* **1991**, *127*, 34-41.

[54]   A. Corma, V. Fornes, W. Kolodziejski and L. J. Martineztriguero, *J. Catal.* **1994**, *145*, 27-36.

[55]   L. R. Aramburo, L. Karwacki, P. Cubillas, S. Asahina, D. A. M. de Winter, M. R. Drury, I. L. C. Buurmans, E. Stavitski, D. Mores, M. Daturi, P. Bazin, P. Dumas, F. Thibault-Starzyk, J. A. Post, M. W. Anderson, O. Terasaki and B. M. Weckhuysen, *Chem. Eur. J.* **2011**, *17*, 13773-13781.

[56]   H. L. Janardhan, G. V. Shanbhag and A. B. Halgeri, *Appl. Catal. A-Gen* **2014**, *471*, 12-18.

[57]   D. Mores, E. Stavitski, M. H. F. Kox, J. Kornatowski, U. Olsbye and B. M. Weckhuysen, *Chem. Eur. J.* **2008**, *14*, 11320-11327.

[58]   H. Vinek, G. Rumplmayr and J. A. Lercher, *J. Catal.* **1989**, *115*, 291-300.

[59]   F. Bager, N. L. Salas and S. Ernst, Oil Gas Eur. Mag. **2012**, 38, 107-111.

[60]   R. Bastiani, Y. L. Lam, C. A. Henriques and V. Teixeira da Silva, Fuel **2013**, 107, 680-687.

[61]   A. Corma and A. V. Orchillés, Micropor. Mesopor. Mater. **2000**, 35–36, 21-30.

[62]   N. Rahimi and R. Karimzadeh, Appl. Catal. A-Gen **2011**, 398, 1-17.

[63]   O. Bortnovsky, P. Sazama and B. Wichterlova, Appl. Catal. A-Gen **2005**, 287, 203-213.

[64]   H. Wang and T. J. Pinnavaia, Angew. Chem. Int. Ed. **2006**, 45, 7603-7606.

[65]   S. van Donk, A. H. Janssen, J. H. Bitter and K. P. de Jong, Catal. Rev. **2003**, 45, 297-319.
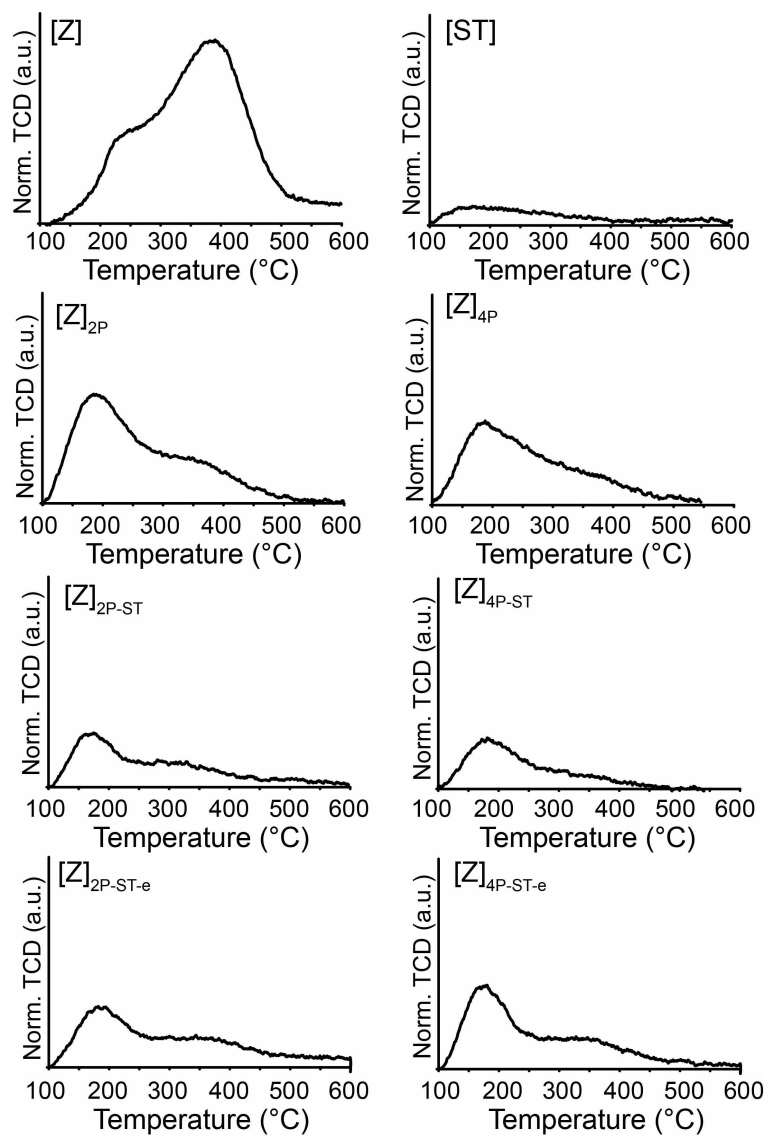
5.5 Appendix

Figure A5.1 Temperature programmed desorption profiles of ammonia. The TCD signal is normalized to the weight of the sample. Increased adsorption temperatures correlate with increased acid site strength.
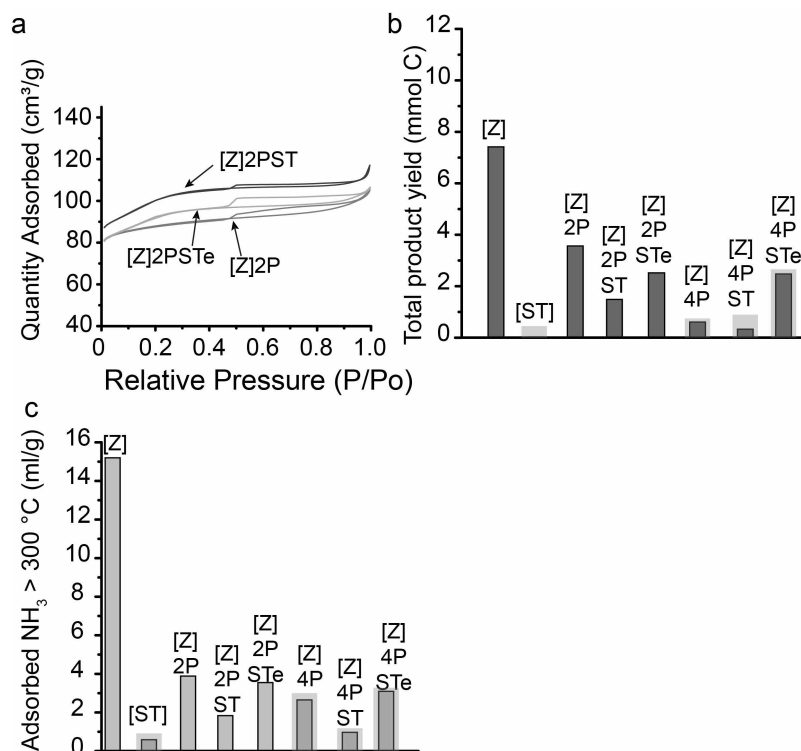
Figure A5.2 (a) N_2 physisorption profiles of the zeolite samples = [Z]2P, [Z]2P-ST, and [Z]2P-ST-e. The near-linear uptake of nitrogen in the 0 to 0.3 P/P_0 region in sample [Z]2P PS is indicative for the formation of small mesopores.[64] (b) Total product yield in mmol of carbon atoms that is converted during one temperature programmed reaction. Highlighted samples are discussed in the main text. It can be observed that sample [Z]4P has relative low catalytic activity in comparison to its strong acid site number. We attribute this to pore blockage by excess phosphorus species. Figure A5.8 clearly shows the that sample [Z]4P has a high concentration of phosphorus species on the external surface. (c) Overview of the concentration of adsorbed ammonia above 300 °C. Left axis in green bars shows the concentration of adsorbed NH_3 at temperatures above 300 °C.
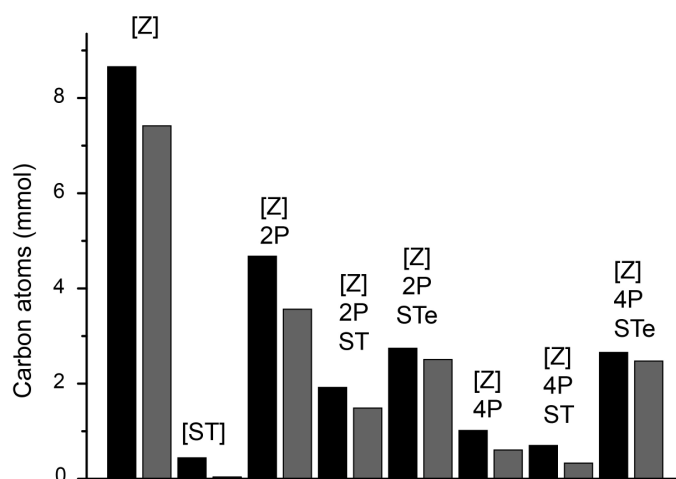
Figure A5.3 Comparison showing the total amount of carbon atoms consumed (black) during the temperature programmed catalytic cracking of *n*-hexane and the total amount of carbon atoms detected in the product yield (grey). It should be noted that the values for the hexane conversion are somewhat unreliable, as a saturator was used to introduce *n*-hexane into the feed. Small fluctuations in temperature and flow make it difficult to exactly determine the ingoing amounts of *n*-hexane, as well as to determine the outgoing amounts. This error is expected to increase with lower *n*-hexane conversions.
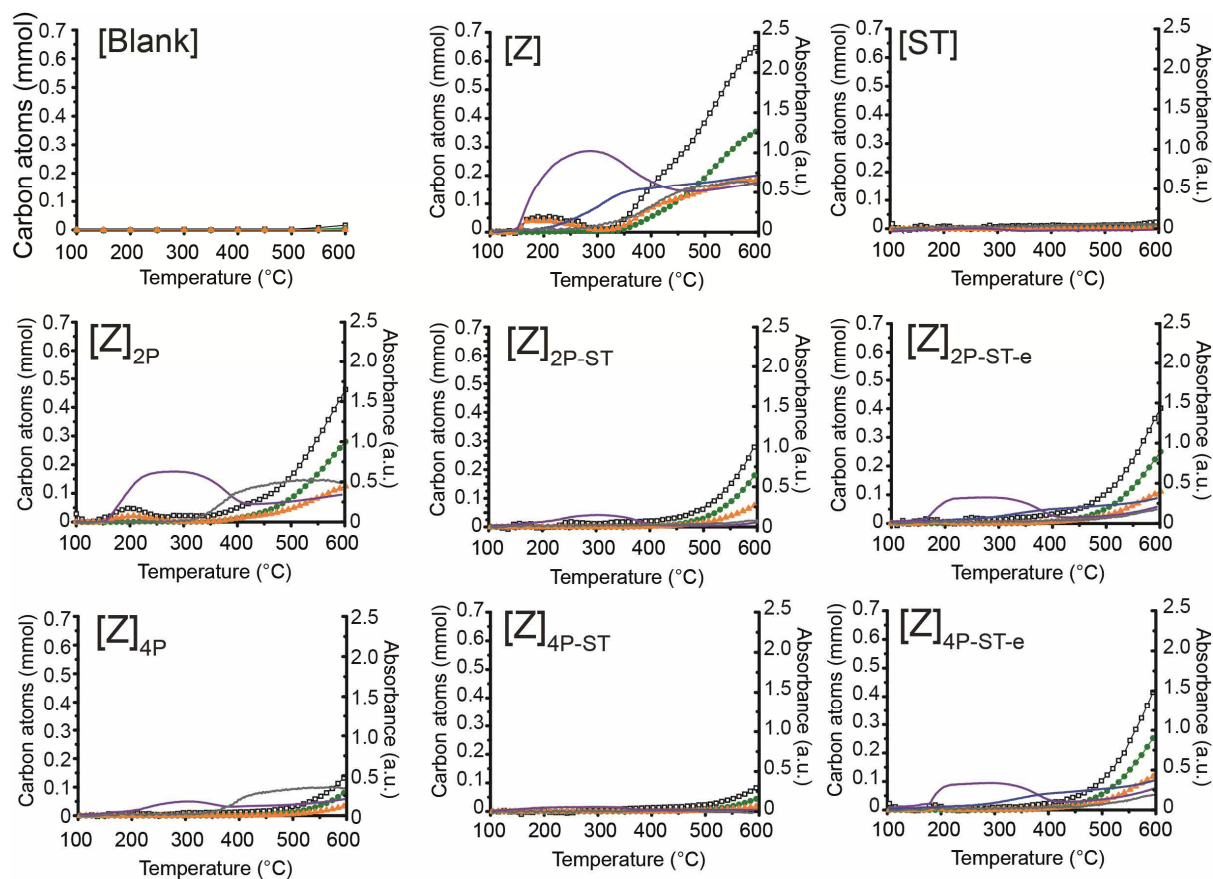
Figure A5.4 Temperature programmed catalytic cracking of *n*-hexane Left axis shows the □ = conversion of *n*-hexane (μmol C), ■ = yield of paraffins (μmol C), and ■ = yield of olefins (μmol C). Right axis shows the evolution of the UV-Vis bands. Solid line ■ = Coke formation (1100 nm).
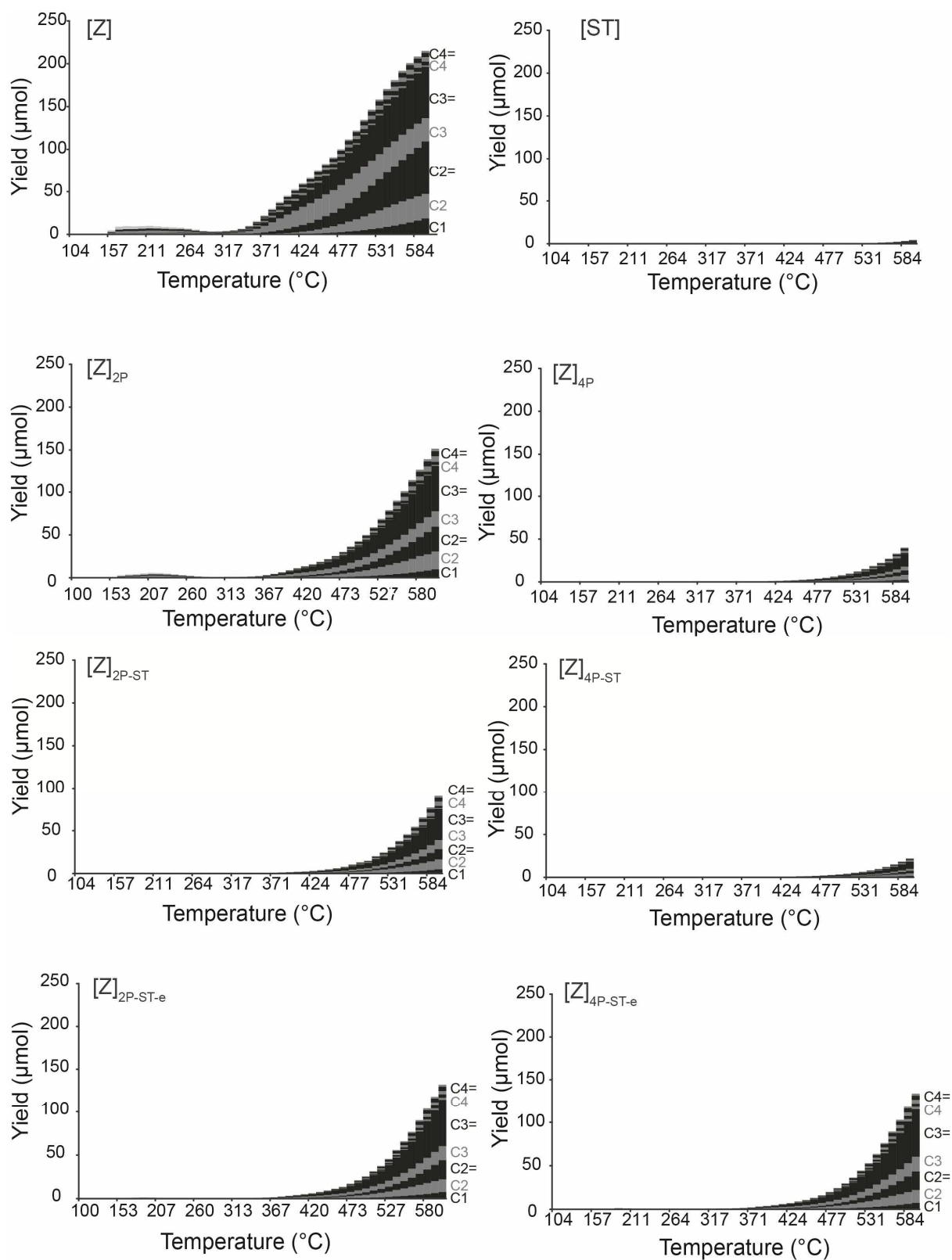
Figure A5.5 Yield profiles during the temperature programmed catalytic cracking of *n*-hexane. The yields are given in μmol of product.
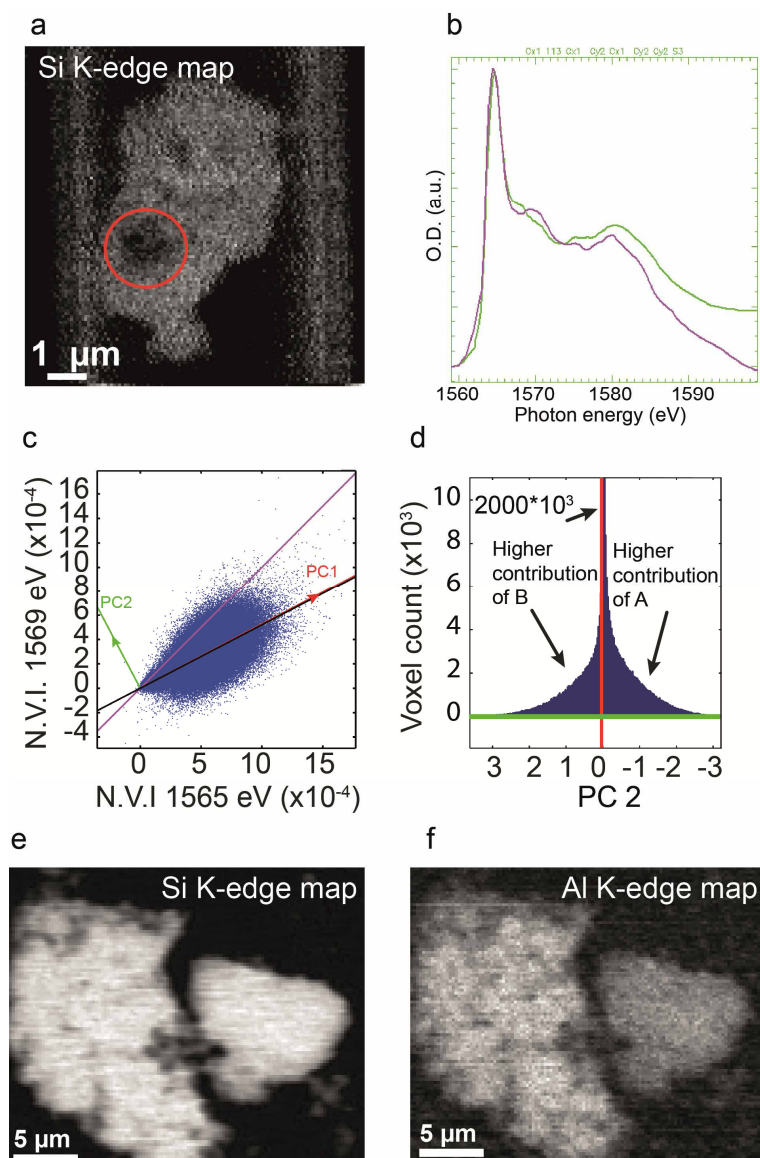
Figure A5.6 Additional information on the sample measured by soft X-ray tomography. (a) Silicon map of the aggregate on which soft X-ray tomography was performed. The dark spot marked by the red circle is not due low silicon concentration, but due to oversaturation. The 30 wt.% of silicon (Tables 5.1 and A5.1) and the use of a borosilicate capillary as a sample holder leads to attenuation of X-rays at the Si K-edge at high particle densities. (b) Al K-edge XANES, of the particle measured in tomography (magenta) and four-coordinated aluminum in NH_4-ZSM-5 (green) (c) Correlation plot of voxels intensities of volume A (Figure 5.2 b iv) and volume B (Figure 5.2 b v) as shown in the main text in Figure 5.4 b. (d) Histogram along the second principle component (PC2) axis shown in this Figure in c and in the main text in Figure 5.4 b. The deviation of voxels from the first principle component indicates changes in the A/B peak ratio of the Al K-edge XANES. Negative values correspond to a higher contribution of A and positive values to a higher contribution of B. The variance captured by PC2 is only 3%, indicating only a very small number of voxels are found to deviate from the average A/B ratio. Therefore, any changes in A/B peak ratio are probably below noise level. (e) Particles of Figure 5.6 (main text), showing the Si K-edge map and (f) Al K-edge map.
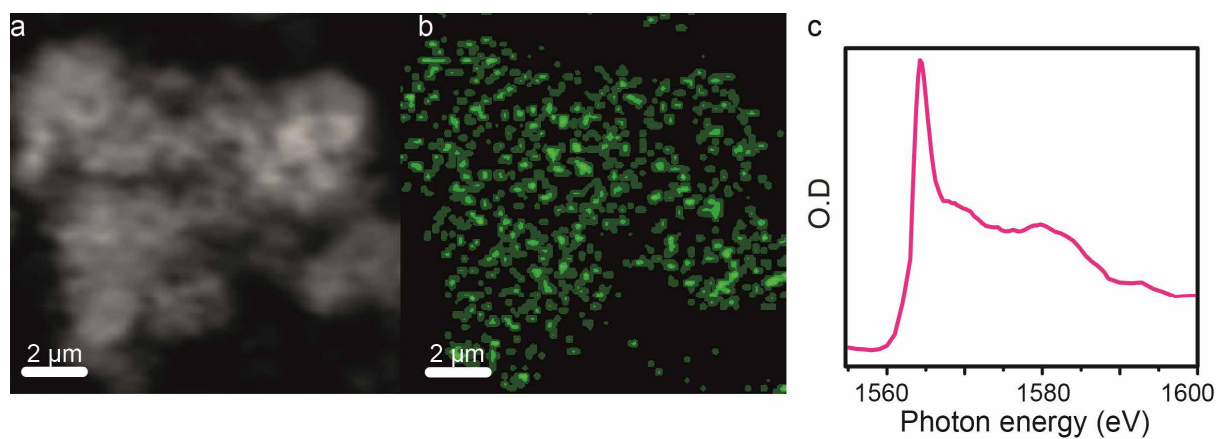
Figure A5.7 (a) Al K pre-edge X-ray absorption map of sample [Z]$_{4P-ST}$. (b) Distribution of phosphorus species within sample [Z]$_{4P-ST}$. The map has been reconstructed using the P K-edge stacks. (c) Al K-edge XANES of sample [Z]$_{4P-ST}$ corresponding to the aggregate in (a) and (b).

Table A5.1 ICP-OES results of the elements Si, Al and P in the zeolite H-ZSM-5 samples under investigation.[a]

Sample	Al (wt.%)	P (wt.%)	Si (wt.%)	Si/Al[b]	P/Al	P/Si
[Z]$_{2P}$	2.9	1.7	31.7	10.5	0.5	0.05
[Z]$_{2P-ST}$	2.9	1.8	32.5	10.7	0.5	0.05
[Z]$_{2P-ST-e}$	2.9	1.2	32.3	10.8	0.4	0.03

[a] Samples are measured after drying, [b] Bulk Si/Al ratio
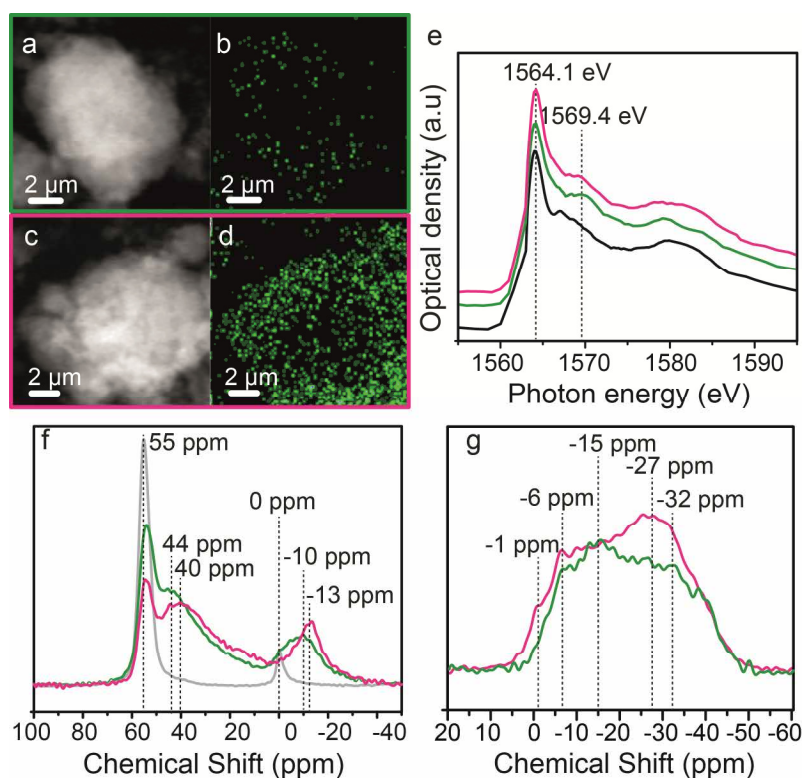
Figure A5.8 (a and c) Al K pre-edge X-ray absorption maps of samples (a) [Z]$_{2P}$ and (c) [Z]$_{4P}$. Samples contain 2 wt.% and 4 wt.% P respectively. (b and d) Distribution of phosphorus species on samples (b) [Z]$_{2P}$ and (d) [Z]$_{4P}$. Maps have the same optical density scale and have been reconstructed using P K-edge stacks. (e) Al K-edge XANES of samples ■ = [Z], ■ = [Z]$_{2P}$, and ■ = [Z]$_{4P}$. (f) ^{27}Al MAS NMR of samples ■ = [Z] (spectral intensity has been reduced by 0.5), ■ = [Z]$_{2P}$, and ■ = [Z]$_{4P}$. (g) ^{31}P MAS NMR of samples ■ = [Z]$_{2P}$, and ■ = [Z]$_{4P}$. ^{31}P spectra are not quantitative. Increasing the amount of phosphorus leads to an increased coverage of the zeolitic external surface. However, phosphorus also migrates further into the micropores, as can be observed in Figure 5.3 and A5.2. From the ^{31}P MAS NMR spectra of the samples [Z]$_{2P}$ and [Z]$_{4P}$ in Figure A5.8 g, it can be noticed that the sample [Z]$_{4P}$ has a more intense resonance around -27 ppm, attributed to phosphorus in close vicinity to aluminum, as was also observed by HETCOR NMR in Chapter 4.[35] This indicates that a higher amount of phosphorus species is interacting with, or is close to aluminum species. We expect that higher loadings of phosphorus lead to more local SAPO interfaces with phosphate bidentate interactions and branched phosphate species as shown in Scheme 5.3 iii and iv (main text). These different types of local SAPO interfaces have previously been studied in detail by Damodaran and co-workers. [35]
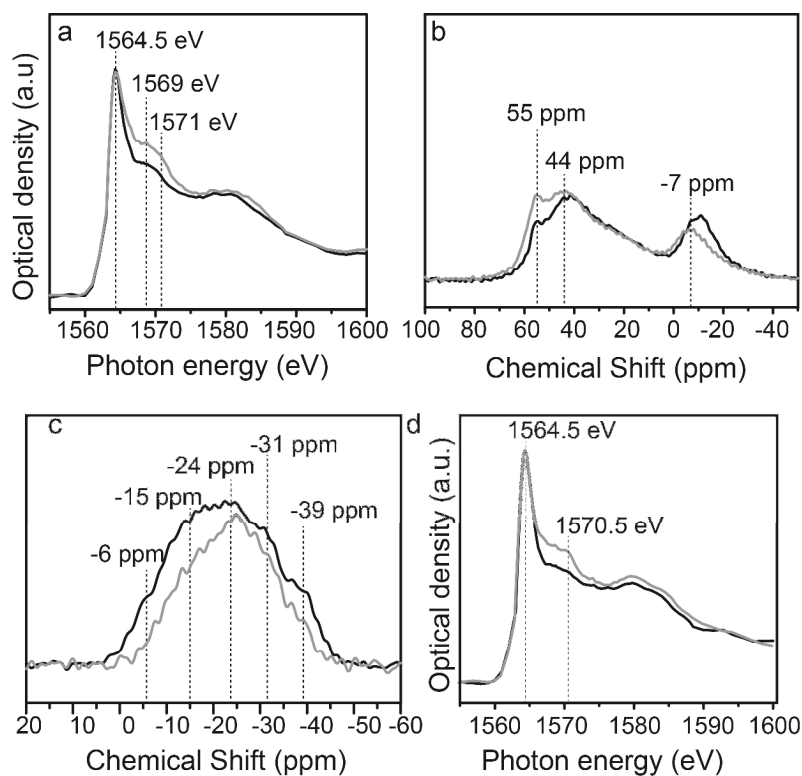
Figure A5.9 Samples black = $[Z]_{2P\text{-}ST}$ and gray= $[Z]_{2P\text{-}ST\text{-}e}$. (a) Al K-edge XANES (b) ^{27}Al MAS NMR. (c) ^{31}P MAS NMR. Spectral intensities have been normalized to the wt.% of phosphorus. For sample $[Z]_{2P\text{-}ST}$ it can be observed that the resonance between 44 ppm to 10 ppm increases in intensity at lower chemical shifts, after steam treatment, which has previously been shown to be an increase in the quadrupolar coupling constant of these resonances.[27, 38] ^{31}P MAS NMR in Figure A5.9 c shows that a broad resonance centered around -24 ppm forms for sample $[Z]_{2P\text{-}ST}$, while for sample $[Z]_{4P\text{-}ST}$ a resonance around -31 ppm appears. These results have been reported in previous works and would indicate the formation of Al-O-P monodentate species as shown in Scheme 5.3 ii for sample $[Z]_{2P\text{-}ST}$, and bidentate and branched polyphosphate species for sample $[Z]_{4P\text{-}ST}$. [27, 38] (d) Al K-edge XANES of samples black = $[Z]_{4P\text{-}ST}$, and gray = $[Z]_{4P\text{-}ST\text{-}e}$. It is interesting to see an increase of the post-edge feature in the Al K-edge XANES of (a) and (d) after washing. From the bulk ^{27}Al MAS NMR and NH$_3$-TPD data it appears that tetrahedrally coordinated framework aluminum (TFAl) species and Brønsted acid sites are retrieved. Therefore, it seems possible that the post-edge feature has some relation with the TFAl atoms and acid sites. However, further investigations will be necessary to corroborate this suggestion.

Aluminum-Phosphate Binder Formation in Zeolites as Probed with X-ray Absorption Microscopy

In this work, three industrially relevant zeolites with the framework topologies MOR, FAU and FER have been explored on their ability to form an $AlPO_4$ phase by reaction of a phosphate precursor with expelled framework aluminum. A detailed study was performed on zeolite H-mordenite, using *in situ* STXM

and soft X-ray absorption tomography, complemented with ^{27}Al and ^{31}P MAS NMR spectroscopy, XRD, FT-IR spectroscopy, and N_2 physisorption. Extra-framework aluminum was extracted from steam-dealuminated H-mordenite and shown to dominantly consist of amorphous AlO(OH). It was found that H_3PO_4 readily reacts with the AlO(OH) phase in dealuminated H-mordenite, and forms an extra-framework amorphous $AlPO_4$ phase. It was found that while $AlPO_4$ crystallizes outside of the zeolitic channel system forming $AlPO_4$ islands, $AlPO_4$ that remains inside tends to stay more amorphous. In the case of ultra-stable zeolite Y the FAU framework collapsed during phosphatation, due to extraction of framework aluminum from the lattice. However, using milder phosphatation conditions an extra-framework $AlPO_4$ α-cristobalite/tridymite phase could also be produced within the FAU framework. Finally, in steamed zeolite ferrierite with FER topology the extra-framework aluminum species were trapped and therefore not accessible for phosphoric acid, hence no $AlPO_4$ phase could be formed within the structure. Therefore, the parameters to be taken into account in $AlPO_4$ synthesis are the framework Si/Al ratio, stability of framework aluminum, pore dimensionality and accessibility of extra-framework aluminum species.
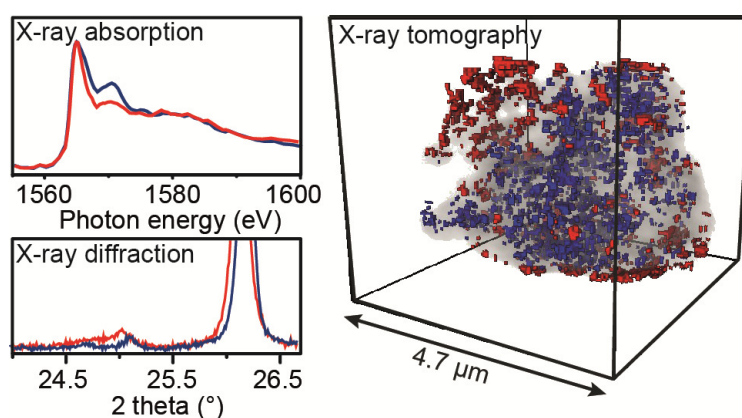
Chapter 6

6.1 Introduction

As was discussed in Chapter 1, catalysis performed over zeolites is of enormous importance to the oil and gas industry as their use saves (petro-) chemical companies billions of dollars in process and energy costs.[1] Zeolites as catalysts are primarily used in the field of catalytic cracking, i.e. the cracking of long chain hydrocarbons into smaller more valuable fractions, e.g. fluid catalytic cracking and hydrocracking.[2-3] However, besides their use as cracking catalysts, zeolites have (potential) applications in e.g. catalytic fast pyrolysis of biomass, (bio-) alcohol dehydration and (bio-) alcohol conversion to hydrocarbons.[4-7] Due to this wide and valuable application range, there is a great academic interest in zeolites as heterogeneous catalysts. However, as was recently pointed out in two reviews, the academic world focusses strongly on the performance of pure zeolite materials, while in industry the application of binders and matrices used in catalyst bodies exert a huge influence on performance as well. [8-9]

Binders are generally inorganic oxides, such as silica-alumina, aluminum-phosphate, natural clays and alumina, which are mixed with the zeolite catalysts and increase the mechanical strength and attrition resistance of the catalyst during industrial operation. [8-9] An example of the interaction between binder and zeolite is aluminum-phosphate ($AlPO_4$). [10-14] Especially in the field of catalytic hydrocarbon cracking, the addition of $AlPO_4$ to zeolites, often in combination with a zeolite phosphatation step, leads to improved light olefin selectivity, hydrothermal stabilization, improved mechanical strength and attrition resistance. [10-14]

Aluminum-phosphate is an interesting binder for another reason as well, as we have seen in Chapter 3 that $AlPO_4$ can form from a zeolite's own aluminum supply by applying a dealumination and subsequent phosphorus modification (phosphatation) step. Previous studies have shown that the formation of crystalline $AlPO_4$ upon the addition of a phosphate precursor is possible within zeolite H-ZSM-5 (with MFI topology), H-USY (with FAU topology), H-mordenite (with MOR topology) and H-beta (with BEA topology). [15-18]

The formation of an $AlPO_4$ binder by using part of the framework aluminum supply is an interesting method for multiple reasons. First, it requires zeolites with high aluminum content, which are cheaper and more environmentally friendly to produce, since the use of organic templates is not required.[19-20] Second, the pre-dealumination step leads to the formation of mesopores, creating a hierarchical material, facilitating access to reactant and product molecules during catalysis.[21-22] And third, a thorough understanding of the formation of $AlPO_4$ from extra-

framework aluminum (EFAl) should allow one to form $AlPO_4$ species inside the zeolite channel/cage system, altering its shape selective effects.[23]

However, the exact nature of this $AlPO_4$ phase has not yet been studied in great detail. Corma and co-workers found that the extra-framework aluminum EFAl present in H-USY readily reacted with phosphoric acid and formed amorphous $AlPO_4 - Al_2O_3$.[15] Upon hydrothermal treatment the phase partially formed crystalline $AlPO_4$. It was suggested that the $AlPO_4$ phase had a tridymite structure and was located both on the external surface and the zeolite interior, but direct evidence was not provided. Lischke et al. observed the formation of a crystalline $AlPO_4$ phase for a hydrothermally treated and subsequently phosphorus-modified H-ZSM-5 zeolite with the MFI topology.[17] In the work of Costa and co-workers, the zeolites H-mordenite and H-beta showed the spectroscopic signatures of $AlPO_4$ formation after phosphorus modification and hydrothermal treatment.[16] However, the authors attributed the signals to framework connected Al-O-P interactions.

In Chapter 3, we have observed the formation of an extra-framework $AlPO_4$ phase in dealuminated and subsequently phosphorus-modified H-ZSM-5 with X-ray absorption microscopy. It was found that the Al K-edge X-ray absorption near edge structure (XANES) of the phase resembled that of tridymite. However, X-ray diffraction (XRD) patterns that could confirm this peculiar observation could not be obtained. Furthermore, although $AlPO_4$ islands were formed, it could not be elucidated whether these islands were present within the zeolite channel system or not.

In order to shed light on these fundamental questions, and to establish whether this approach is extendable to other zeolite topologies besides 10-member ring (MR) H-ZSM-5, this Chapter studies the phenomena of $AlPO_4$ formation in more detail by using a multi-pronged characterization approach. This Chapter aims to provide a fundamental understanding on the nature of EFAl, its reactivity towards phosphoric acid and the eventual formation of an $AlPO_4$ phase within zeolite materials. We have studied the formation of the $AlPO_4$ phase in 1-dimensional 8-, and 12-MR zeolite H-mordenite, 2-dimensional 8-, and 10-MR zeolite H-ferrierite (with FER topology) and 3-dimensional 12-MR zeolite H-USY, using a combination of scanning transmission X-ray microscopy (STXM), and ^{27}Al and ^{31}P magic angle spinning nuclear magnetic resonance (MAS NMR) spectroscopy, complemented with Fourier-transform infrared (FT-IR) spectroscopy, XRD and N_2-physisorption. Our group has pioneered and developed the use of STXM in the field of zeolite chemistry and catalysis.[24-26] Using this experience it was possible to observe the crystallization of the extra-framework $AlPO_4$ phase of H-mordenite in

space and time by application of an *in situ* nanoreactor. [27] X-ray tomography was used to create a 3-D nanoscale chemical representation of the $AlPO_4$ phase in a single H-mordenite aggregate for the first time.

6.2 Experimental methods

6.2.1 Sample preparation

Table 6.1

Sample[a]	Parent	Treatment	Sample	Parent	Treatment
CBV 21A (NH_4-mordenite)	-	-	CBV 500 (NH_4-USY)	-	-
[MOR]	CBV 21A	Calcined 550 °C, 10 h	[USY]	CBV 500	Calcined 550 °C, 10 h
[MOR]$_{400}$	[MOR]	Steamed 400 °C, 4 h	[USY]$_{P-ST}$	[USY]	Refluxed in HNO_3 and H_3PO_4, dried, Steamed 600 °C, 2 h
[MOR]$_{400-P}$	[MOR]$_{400}$	Refluxed in HNO_3 and H_3PO_4, dried	[USY]$_{P-WI-ST}$	[USY]	Wet impregnation H_3PO_4, dried, Steamed 600 °C, 2 h
[MOR]$_{400-P-ST}$	[MOR]$_{400-P}$	Steamed 470 °C, 2 h	CP914 (NH_4-ferrierite)	-	-
[MOR]$_{400-L}$	[MOR]$_{400}$	Leached with HNO_3, filtered, dried	[FER]	CP914	Calcined 550 °C, 10 h
[MOR]$_{400-L-P-ST}$	[MOR]$_{400-L}$	Refluxed in HNO_3 and H_3PO_4, dried. Steamed 470 °C, 2 h	[FER]$_{500}$	[FER]	Steamed 500 °C, 4 h
[MOR]$_{400-P-TT}$	[MOR]$_{400-P}$	Calcined, 400 °C, 4 h.	[FER]$_{500-P}$	[FER]$_{500}$	Refluxed in HNO_3 and H_3PO_4, dried
Filtrate	[MOR]$_{400-L}$	Filtrate obtained from leaching	[FER]$_{500-P-ST}$	[FER]$_{500-P}$	Steamed 600 °C, 2 h
Filtrate + P	Filtrate	H_3PO_4, dried, steamed 600 °C, 2 h	[FER]$_{600}$	FER	Steamed 600 °C, 4 h
			[FER]$_{600-P}$	[FER]$_{600}$	Refluxed in HNO_3 and H_3PO_4, dried
			[FER]$_{600-P-ST}$	[FER]$_{600-P}$	Steamed 600 °C, 2 h

[a] Abbreviations: ST = steam treated, TT = thermal treated, P = phosphated, L = acid leached

Details on the samples under study and related treatments are presented in Table 6.1. Commercially available zeolites from Zeolyst, zeolite NH_4-USY (CBV 500 Si/Al = 2.55), zeolite NH_4-mordenite (Zeolyst CBV 21A = 10), and zeolite NH_4-ferrierite (CP914 Si/Al = 10) were heated in a tubular oven with 20 °C/min to 550 °C and calcined for 10 h in a 180 ml/min flow of dry air. The obtained samples were labeled [USY], [MOR], and [FER], respectively. In order to obtain sample [MOR]$_{400}$, part of sample [MOR] was steamed at 400 °C for 4 h and sample [FER] was steamed at 500 °C for 4 h in 80 vol.% of steam with N_2 as a carrier gas to form [FER]$_{500}$.

Acid leaching was performed by suspending 1 g of [MOR]$_{400}$ into 200 ml H$_2$O and 0.7 ml HNO$_3$ mixture. The sample was stirred at 80 °C for 14 h and subsequently filtered and washed. The residue was labeled [MOR]$_{400-L}$. The filtrate was retrieved by removing H$_2$O by rotary evaporation and was labeled Filtrate. Both samples were dried overnight at 150 °C. Phosphatation was performed on samples [USY], [FER]$_{500}$, [MOR]$_{400}$, [MOR]$_{400-L}$ and Filtrate. Samples [MOR]$_{400-P}$, [FER]$_{500-P}$ and [USY]$_P$ were prepared by suspension of sample [MOR]$_{400}$, [FER]$_{500}$ and [USY] into 250 ml H$_2$O, 0.5 ml HNO$_3$ and an appropriate amount of H$_3$PO$_4$ (P/Al ratio = 1).

The suspension was stirred for 14 h at 80 °C (pH below 0.89) after which the solvent was evaporated by rotary evaporation and the sample was dried overnight at 150 °C. Sample [MOR]$_{400-L-P}$ was prepared in an identical way as sample [MOR]$_{400-P}$, except that no HNO$_3$ was added to the solution. The Filtrate + P was prepared by stirring 0.2 g of Filtrate in 10 ml of H$_2$O and 0.2 g of H$_3$PO$_4$ after which the sample was dried at 150 °C and subsequently steamed at 600 °C for 2 h. Samples [MOR]$_{400-P-ST}$ and [MOR]$_{400-L-P-ST}$ were prepared by a steam treatment at 470 °C for 2 h in 80 vol.% steam of samples [MOR]$_{400-P}$ and [MOR]$_{400-L}$, respectively. Sample [MOR]$_{400-P-TT}$ was prepared by calcination of sample [MOR]$_{400-P}$ at 400 °C for 4 h in static air. Samples [FER]$_{500-P}$ and [USY]$_P$ were subjected to a post-steam treatment at 600 °C for 2 h and denoted [FER]$_{500-P-ST}$ and [USY]$_{P-ST}$. Alternatively, sample [FER] was steamed at 600 °C for 4 h, phosphated and post-steamed using identical conditions as mentioned above for [FER]$_{500}$. These samples were named [FER]$_{600}$, [FER]$_{600-P}$, and [FER]$_{600-P-ST}$. Furthermore, sample [USY] was phosphated by wet impregnation, where 200 mg of [USY] was suspended in 0.5 ml H$_2$O containing an appropriate amount of H$_3$PO$_4$ (P/Al = 0.5). Next, the sample was placed in a sonication bath for 15 min after which the sample was dried at 120 °C overnight and post-steamed at 600 °C for 2 h. This sample is named [USY]$_{P-WI-ST}$.

6.2.2 Ammonia temperature programmed desorption

Ammonia temperature programmed desorption (NH$_3$ - TPD) experiments were performed on a Micromeritics Autochem II. Samples were dried in a He flow at 600° C for 15 min and cooled to 100° C, after which ammonia was introduced in loops. Once the sample was saturated the temperature program was started. Under a flow of He the sample was heated with 5 °C /min to 600° C. Outgoing NH$_3$ was detected by a TCD detector.

Chapter 6

6.2.3 N$_2$-physisorption

Isotherms were recorded using a Micromeritics Tristar 3000 setup operating at -196 °C. Prior to physisorption measurements, all samples were dried overnight at 500 °C under a N$_2$ flow.

6.2.4 Fourier transform infrared spectroscopy

Fourier transform infrared (FT-IR) spectroscopy measurements were performed on self-supporting zeolite wafers. 15 mg of sample was pressed with 3 tons for 10 s into a thin disk of 13 mm in diameter. The sample was evacuated to 10^{-6} bar and heated with 7 °C/min to 600 °C and immediately cooled to 150 °C. IR spectra were taken with a Perkin-Elmer FT-IR instrument with an optical resolution of 4 cm^{-1} and 12 accumulations with wavenumbers ranging from 4000 cm^{-1} to 1000 cm^{-1}. For pyridine adsorption experiments the sample was evacuated to 10^{-2} bar and heated with 7 °C/min to 600 °C and immediately cooled with steps of 25 °C to 50 °C taking a spectrum at every interval. Pyridine was introduced in the vapor phase for 15 min and physisorbed pyridine was removed by outgassing at 150 °C and 10^{-2} bar for 30 min. TPD was performed by increasing the temperature in steps of 25°C to 600°C. For each step IR spectra were taken with a Perkin-Elmer FT-IR instrument with an optical resolution of 4 cm^{-1} and 12 accumulations with wavenumbers ranging from 4000 cm^{-1} to 1000 cm^{-1}. Spectra were baseline corrected and normalized using the bands corresponding to zeolitic framework vibrations found at 1967 cm^{-1}, 1873 cm^{-1}, and 1637 cm^{-1}.

6.2.5 Solid-state nuclear magnetic resonance spectroscopy

The solid-state nuclear magnetic resonance (NMR) spectroscopy experiments were performed at 11.7 T on a Bruker Avance III 500 MHz spectrometer using a 4 mm magic angle spinning (MAS) probe at room temperature. The MAS rate was 15 kHz for all experiments. The ^{27}Al NMR spectra were obtained using $\pi/12$ pulses, 1000 scans and a recycling delay of 0.5 s at a rf-field of 94 kHz. The ^{31}P spectra were obtained using a pulse length of 1.8 μs, 64 scans and with a recycle delay of 60 s. The chemical shifts of ^{27}Al, and ^{31}P were externally referenced to 1M Al(NO$_3$)$_{3(aq)}$, and 85% H$_3$PO$_{4(aq)}$, respectively.
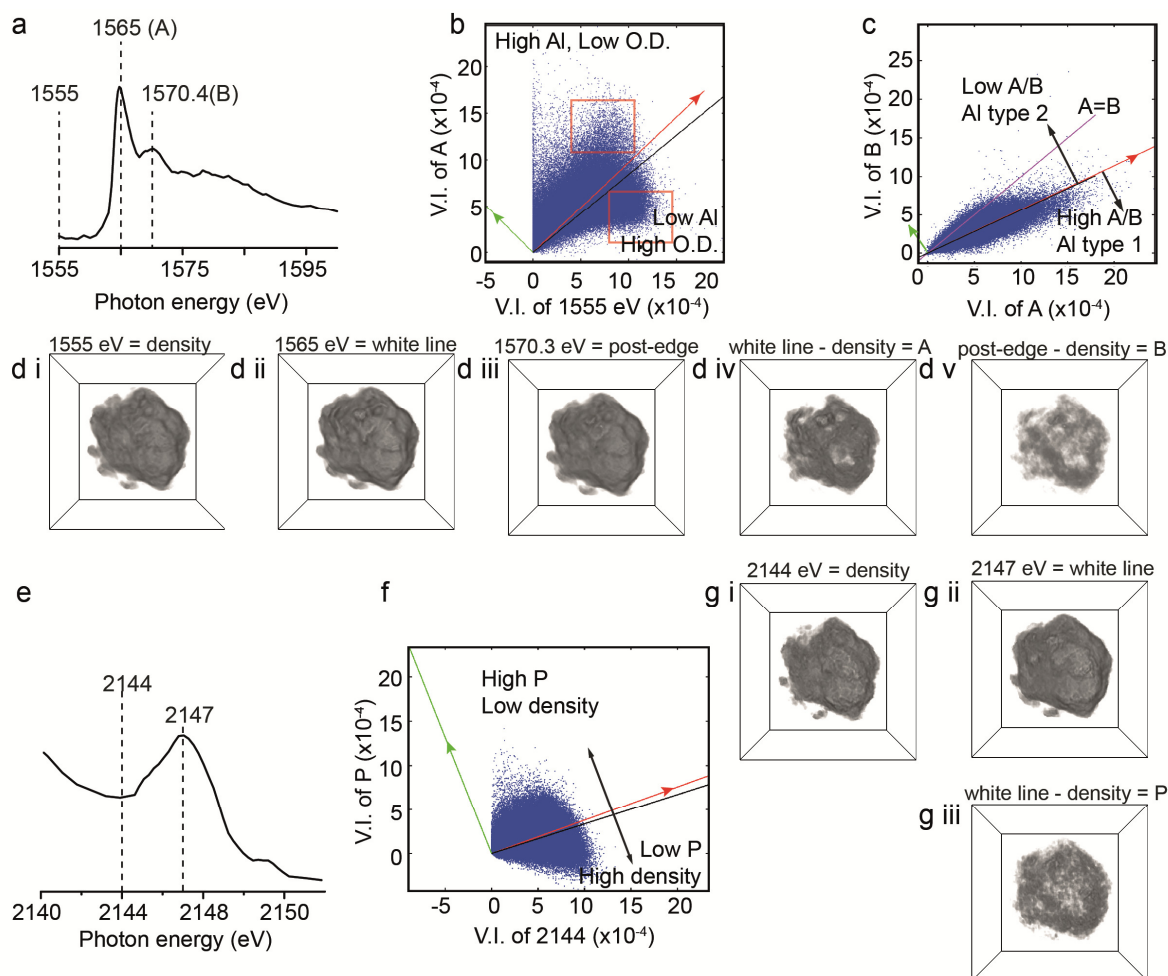
Figure 6.1 Explanation of the tomography data analysis. (a) Al K-edge XANES, obtained by 2-D STXM. (b) Correlation plot of particle density (d i) *vs.* the aluminum concentration (d iv). If there would be a homogenous distribution of Al throughout the particle there should be a positive linear correlation. The black line is the linear regression fit, indicating there is indeed a positive correlation between aluminum and the particle density. The red vector indicates the positive direction of the first principle component (PC1), along this vector aluminum and density increase with similar ratios. The positive correlation further confirms that aluminum is distributed throughout the whole particle. However, there are deviations from PC1, marked by red boxes. These deviations are described by the second principle component (PC2, green vector) and moving along this vector separates the contribution of voxels with high density and low aluminum intensities, from voxels with low density and high aluminum intensities. Moving along the PC2 axis shows changes in Al/density ratio. This PC2-axis is the y-axis of the plot in Figure 6.3 e. (c) Correlation plot of volume A (d iv) and volume B (d v). The magenta line corresponds to A=B and the black line to the linear regression fit. The red vector indicates the positive direction of the first principle component (PC1). The PC1 corresponds to the aluminum concentration, as along this axis the A/B ratio does not change, confirmed by the linear regression fit (black). Therefore, peak A and B rise uniformly along PC1 with increasing optical density. The axis of PC1 is the y-axis in Figure 6.3 c. The second principle component (PC2, green line) shows changes in A/B ratio and is used as the x-axis in Figure 6.3 e. (d) 3-D representation of the X-ray absorption tomography data of the three measured energies at the Al K-edge. (d i) 1555 eV, corresponds to particle density. (d ii) 1565 eV, Al white line, (d iii) 1570 eV, post-edge feature. (d iv) 1565 eV volume, subtracted by the 1555 eV volume, corresponds to aluminum concentration, denoted as A. (d iv) 1570 eV volume, subtracted by the 1555 eV volume, corresponds to aluminum concentration, denoted as B. (e) P K-edge XANES. (f) Correlation plot of (g i) particle density vs. (g iii) P concentration. The positive correlation indicated by the linear regression fit (black line) and the PC1 (red vector) indicate that phosphorus is found throughout the particle. However the triangular shape of the scatter plot means that there is a spread in distribution. High phosphorus intensities are found at low density and vice versa. Moving along the PC2 (green vector) axis shows the changes in P/density ratio. The PC2 axis is used as the x-axis in Figure 6.3 c. (g i-ii) 3-D reconstruction of the X-ray absorption tomography data of the two measured energies at the P K-edge. (g iii) 2147 eV volume subtracted by the 2144 eV volume, corresponds to phosphorus concentration, denoted as P.

Chapter 6

### 6.2.6 Scanning transmission X-ray microscopy

Scanning transmission X-ray microscopy (STXM) experiments were performed at the Canadian Light Source (CLS) Beamline 10ID-1. Samples were dispersed in H_2O and a droplet was placed on a silicon nitride window. After drying in air the sample was placed in the STXM chamber, which was subsequently evacuated to 10^{-1} mbar. For the in-situ measurements a micro-electromechanical system (MEMS) designed nanoreactor was used.[27] The nanoreactor contains a micrometer-sized platinum heating element which, allows to heat a sample to 400 °C. The sample is supported on silicon nitride window of 1.2-mm in thickness. At specific regions, the silicon nitride window was etched down to 10 nm thickness, forming windows of 5.5 mm in diameter. At these specific windows soft X-rays are able to pass through without suffering from severe attenuation. The in-situ experiment was performed as follows: Sample $[MOR]_{400-P}$ was dispersed on the nano-reactor window in a similar manner as described above, followed by evacuation of the STXM chamber to 10^{-1} mbar. A polarized X-ray beam was obtained using a 1.5 m long, 75 mm period Apple II undulator. The X-ray beam was focused to ~30 nm spot size on the sample plane using a Fresnel zone plate (ZP). The beam from the ZP passed through a molybdenum-based order-sorting aperture (OSA), with a 50 μm pinhole. The OSA allowed only first-order ZP diffracted light to pass. Spectral image sequences (stacks) are measured by recording images over a range of photon energies. After this step the STXM chamber was filled with air to 1 bar and the sample was heated to 400 °C for 1 h. As the reactor was not closed, air was able to reach the sample. After this step the chamber was evacuated to 10^{-1} mbar, the temperature was decreased to room temperature and another image stack was recorded, using the same range of photon energies. After aligning the image sequence, spectra of the whole or a sub-region were extracted for comparison. In addition, spectra were fit to reference spectra of the components using linear regression. All STXM data analysis was performed using aXis2000.[28] The white-line of framework alumina was calibrated to 1565 eV. X-ray tomography experiments were performed by mounting sample $[MOR]_{400-P-ST}$ in a borosilicate capillary. The capillary had a 1 mm external diameter and was heated and pulled by a micropipette puller. The sample under investigation was present in a part of the capillary where the capillary had an external diameter of 10 microns and a wall thickness of approximately 1 micron. The capillary was placed in a tomography sample stage. For the measurement, the sample was rotated 180° in 36 steps, with a 5° step size. More information on the tomography setup can be found in Chapter 5. At each step three energies were measured, i.e. 1555 eV, 1565 eV and 1570.3 eV. After the sample was rotated the full 180°, the sample was rotated back to 0° in 36 steps with a 5° step size. At each step two energies were measured, i.e. 2144 eV and 2147 eV. Sinograms and

binslices were constructed and reconstructed using the TXM-Wizard software [29] and using the iterative Algebraic Reconstruction Technique (iART) algorithm. The 3-dimensional data was analyzed using Avizo 8.0 and MATLAB.

6.2.7 X-ray diffraction

X-ray diffraction (XRD) diffractograms were obtained with a Bruker D2 X-ray powder diffractometer equipped with a Co Kα X-ray tube ($\lambda = 1.7902$ Å).

6.3 Results and Discussion
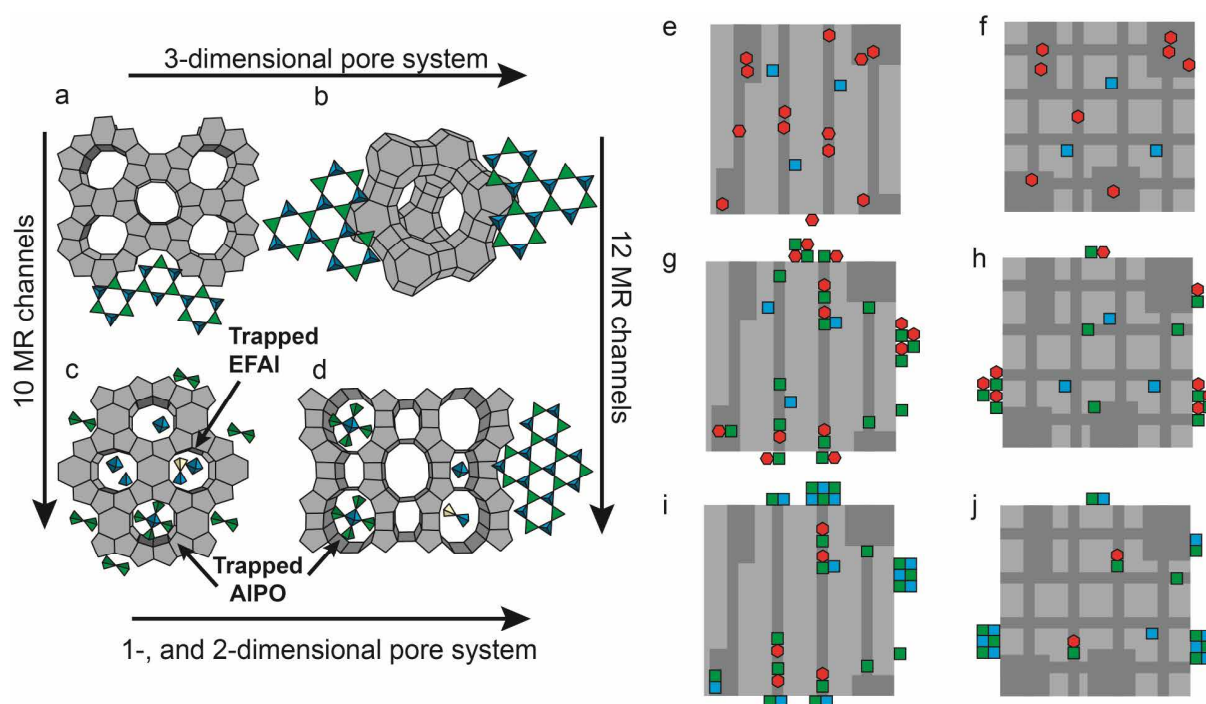
Scheme 6.1 Simplified representation of the concepts proposed in this work. (a-d) location and type of extra-framework aluminum (EFAl) species and aluminum-phosphate (AlPO$_4$) species for the framework topologies (a) MFI, (b) FAU, (c) FER, and (d) MOR. Green = phosphorus, blue = aluminum, yellow = silicon. (e-j) Different stages in the formation of AlPO$_4$ for a 1-dimensional framework (left), and a 3-dimensional framework (right). Blue = aluminum (4), red = aluminum (6), green = phosphorus. (e-f) Zeolites after hydrothermal treatment. (g-h) Formation of amorphous AlPO$_4$ phase. (i-j) crystallization of AlPO$_4$ after post-steam treatment. Frameworks are adapted from the International Zeolite Association Database (MOR, FER, MFI) and from ref. 30-31 (FAU).

Three different zeolite framework topologies have been studied in this work, i.e. MOR (mordenite), FAU (zeolite USY) and FER (ferrierite). First, we start by presenting the results of AlPO$_4$ formation in H-mordenite as measured by soft X-ray tomography and bulk-spectroscopy. The second part consists of an *in-situ* study where the crystallization of an amorphous AlPO$_4$ phase in H-mordenite is monitored in space and time by scanning transmission X-ray microscopy (STXM). Third, we show the nature of extracted extra-framework aluminum (EFAl) and its reactivity towards phosphoric acid, and in a fourth part it is shown that lack of EFAl in H-mordenite prevents the formation of AlPO$_4$. We close the studies on H-mordenite with an inspection of the acid site number and accessibility of the material. After that, the results on AlPO$_4$ formation in zeolite H-USY and zeolite H-ferrierite are presented. Finally, we end with a comparison of the results found for the different zeolite topologies. Previous results obtained for the MFI framework in Chapter 3 (H-ZSM-5) are included in that discussion as well. Based on the results we will point out which different synthesis parameters should be taken into account when

Table 6.2

Type of species	Description	Spectroscopic signals
TFAl	Tetrahedrally coordinated framework Al and corresponding bridging hydroxyl groups	[1565 eV][a], [55 ppm][b], [3603 cm^{-1}][e]
OFAl	Octahedrally coordinated triple-bound framework Al physically coordinated to three H_2O molecules	[0 ppm][b]
EFAl	Extra-framework aluminum, amorphous AlO(OH)	[1568.6 eV][a], [62 ppm, 30 ppm, 5 ppm][b], [3650-3660 cm^{-1}][e]
Al(PO$_4$) • 2 H_2O	Amorphous (or semi-crystalline) aluminum-phosphate	[1570.4][a], [-12 ppm][b], [-15 ppm, -23ppm][c],
AlPO$_4$	Crystalline α-cristobalite/tridymite aluminum-phosphate	[1565 eV, 1571.2 eV][a], [39 ppm][b], [-30.5 ppm][c], [24.8-25.1° 2θ][d]
Excess phosphates	Non-interacting ortho-, pyro-, and polyphosphates	[1.5 ppm, -6 ppm, -12 ppm][c]

[a] Al K-edge, [b] ^{27}Al MAS NMR, [c] ^{31}P MAS NMR, d) XRD, [e] FT-IR.

preparing an AlPO$_4$ phase from framework aluminum in zeolite materials. In Table 6.2 different species with their corresponding spectroscopic signatures are presented.

6.3.1 Mordenite

6.3.1.1. *Nanoscale soft X-ray tomography*

Sample [MOR]$_{400-P-ST}$ was prepared by applying a subsequent pre-steam treatment, phosphatation, and post-steam treatment to zeolite H-mordenite. More information on sample preparation and abbreviations can be found in Table 6.1. Using soft X-ray tomography, a set of images of the sample was collected at different photon energies during a 180° rotation. The 3-D representation of the soft X-ray absorption data is presented in Figure 6.2 and more information can be found in Figures 6.1 and A6.1. From Figure 6.2 it can be observed that the a single zeolite particle of sample [MOR]$_{400-P-ST}$ consists of an aggregate of smaller crystals [32] and contains specific islands that have a high concentration of phosphorus and aluminum. These islands appear to be located on the external surface of the zeolite material. Inside the aggregate, phosphorus and aluminum are also present, but in lower concentrations. The aluminum K-edge spectra that are presented in Figures 6.1-6.2 and A6.1-A6.2, show the absorption white-line at 1565 eV (peak A), which is typical for AlO$_4$ species found in aluminosilicates.[33] The post-edge feature at 1570.4 eV (peak B) is normally not observed in protonated zeolites as can be seen for the Al K-edge XANES of parent sample [MOR] in Figure A6.2. [34]

The 2-D STXM results shown in Figure A6.1, reveal that at specific regions different types of Al K-edge XANES can be found. The post-edge feature at +5.5 eV from the white-line has a
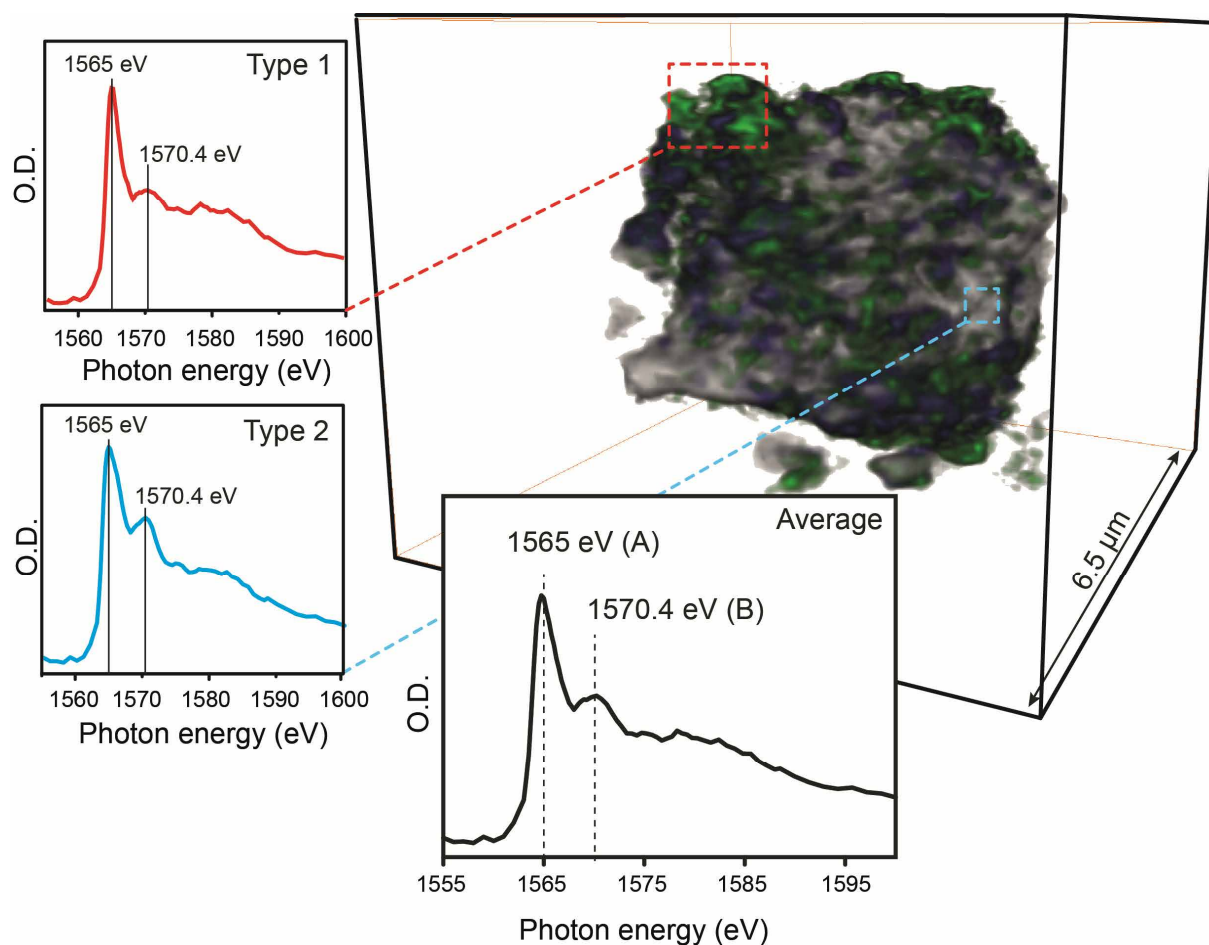
Figure 6.2 3-D representation of a steamed, phosphated, and subsequently post-steamed H-mordenite aggregate, ([MOR]$_{400\text{-P-ST}}$), reconstructed from the soft X-ray tomography data. Voxel size is 63x63x63 nm^3. Grey colored voxels correspond to data collected at an energy measured before the aluminum K-edge (1555 eV) and relates to the particle density. Blue colored voxels represent the aluminum distribution (Figure 6.1 d iv) and green colored voxels the phosphorus distribution (Figure 6.1 g iii). Low intensity voxels are not shown. The average Al K-edge XANES is shown in black, and was obtained by 2-D STXM of the particle. It should be noted that voxels do not contain a full Al K-edge XANES. Tomography data was collected only at 1555 eV (particle density), 1565 eV (peak A) and at 1570.4 (peak B). The ratios between the recorded peak A and peak B intensities were used to identify corresponding Al phases (Type 1 and Type 2). The blue box highlights a high aluminum and high phosphorus island on the surface with corresponding Al K-edge XANES, while the red box highlights aluminum present in the crystal interior. More information on reconstruction and XANES can be found in Figures 6.1 and A6.1.

higher intensity in parts of the zeolite where the average aluminum and phosphorus concentration is low. This type of aluminum was indicated as Type 2 and the corresponding Al K-edge XANES is shown in Figure 6.2. The Type 1 aluminum XANES, which has a low contribution of the post-edge feature at +5.5 eV, is present in regions of the zeolite where the concentration of aluminum and phosphorus is high.

Statistical analysis performed on the 3-D rendered particle confirm these results. Figure 6.3 a shows the correlation between particle density and aluminum concentration. It can be seen that aluminum is found throughout the whole aggregate. However, there is a relative decrease in Al

concentration in dense parts and a higher Al concentration at lower particle densities. In Figure 6.3 b these areas are presented in three dimensions, and it can be observed that aluminum rich zones are present as clusters on the external surface, while inside the denser parts of the crystal the concentration of aluminum is lower. The correlation plot between phosphorus, particle density and aluminum in Figure 6.3 c-d, unequivocally show that the aluminum rich zones at the surface also contain high concentrations of phosphorus, while dense regions of the crystals have lower aluminum and low phosphorus concentrations. Finally, Figure 6.3 e-f shows that the Al K-edge XANES A/B peak ratio increases for aluminum found at the external surface. This indicates that Al Type 1 is more dominant in low particle density, high aluminum and high phosphorus clusters on the external surface, while Al Type 2 is more dominant in high particle density, low aluminum and low phosphorus regions deeper inside the zeolite aggregate.

The nature of the high aluminum and high phosphorus islands on the external surface was determined by inspection of the Al K-edge spectra, ^{27}Al and ^{31}P MAS NMR spectra, and XRD. In Figure 6.4a the ^{27}Al MAS NMR spectra of [MOR]$_{400-P-ST}$ is presented. It can be observed that there is a sharp dominating resonance at 39 ppm. This resonance is attributed to crystalline AlPO$_4$.[17, 35-38] The corresponding ^{31}P MAS NMR resonance at -30.5 ppm correlates with this assignment.[35-36] Furthermore, XRD data shows a peak around 24.8° 2θ, which only appears after a steam- or thermal treatment of sample [MOR]$_{400-P}$. This XRD peak is attributed to α-cristobalite, a berlinite polymorph.[14] Also, there is a shift to slightly lower 2θ values, indicating unit cell contraction, which follows from the removal of Al atoms from the framework. [39-40] Besides the resonance for AlPO$_4$, the ^{27}Al MAS NMR spectra of sample [MOR]$_{400-P-ST}$ shows resonances at 55 ppm and -11 ppm. The resonance at 55 ppm is attributed to tetrahedrally coordinated framework aluminum (TFAl) species [41-42] and the -11 ppm peak to six-coordinated aluminum in amorphous AlPO$_4$, e.g. Al(PO$_4$) • 2 H$_2$O.[18] This latter assignment is in agreement with the post-edge feature at + 5.5 eV, found in the Al K-edge spectra of sample [MOR]$_{400-P-ST}$, as it has been attributed to six-coordinated aluminum in aluminum phosphate and can also be observed in the Al K-edge XANES of tridymite structured AlPO$_4$ and AlPO-11.[43-45]

By combining the X-ray tomography results with those from bulk spectroscopy it appears that for zeolite mordenite sample [MOR]$_{400-P-ST}$, (i) crystalline α-cristobalite/tridymite AlPO$_4$ is present on the external surface, while (ii) inside the zeolitic framework more six-coordinated aluminum in amorphous AlPO$_4$ phase is found. The latter observation is in accordance with the N$_2$-physisorption data in Figure A6.3. There is a decreased micropore volume of sample [MOR]$_{400-P-ST}$, compared to that of its parent sample [MOR]$_{400}$, which points to the filling of micropores. Scheme 6.1a and i give a simplified representation of these findings.
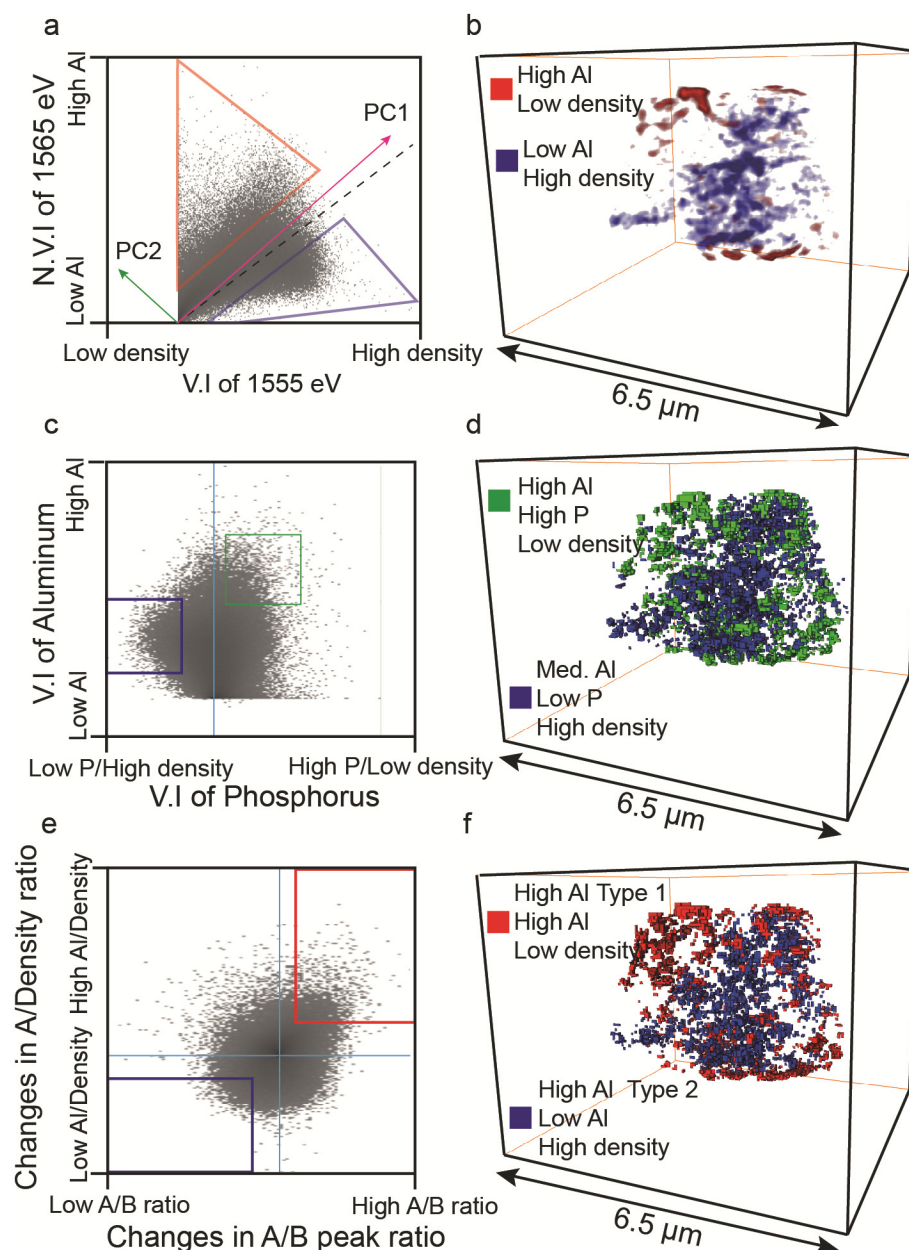
Figure 6.3 Statistical analysis of the particle presented in Figure 6.2. (a) Correlation plot of the voxel intensities (V.I) at the energy at 1555 eV (corresponding to particle density) and the normalized voxel intensities (N.V.I) at energy 1565 eV (peak A), corresponding to Al (Figure 6.1d iv). The red vector indicates the positive direction of the first principle component (PC1). All voxels that lie along this line evolve in a similar manner, i.e. a linear correlation between the increase in intensity of Al and particle density. Therefore, the linear regression fit (dotted black line) has a similar slope. Any deviation from PC1 is described by the second principle component (PC2, green vector) that runs perpendicular to PC1. The red triangle indicates voxels with high Al intensity and low density, while the blue triangle indicates voxels with low Al intensity and high density. (b) 3-D representation of the voxels found along the second principle component axis that fall in the corresponding colored triangles in (a). (c) Second order correlation plot of the V.I. of phosphorus correlated with particle density (PC2 in Figure 6.1 f) vs. aluminum (PC1 in Figure 6.1 c). The blue box indicates a region with medium aluminum intensities, high density and no or low phosphorus. The green box indicates a region with high aluminum, low density and high phosphorus intensities. (d) 3-D representation of the voxels found in the boxed regions indicated in (c). (e) Second order correlation plot of the changes in the ratio of the peaks A and B, as indicated in Figure 1 (PC2 of Figure 6.1 c) vs. the A/density ratio (PC2 of Figure 6.1b and 6.3a). High A/B ratios indicate Al Type 1, and low A/B ratios indicate Al Type 2 (Figure 6.2). The red box indicates a region where voxels have high aluminum, low density and high Al Type 1 intensities. The blue box indicates a region where voxels have low aluminum, high density and high Al Type 2 intensities. (f) 3-D representation of the voxels found in the boxed regions indicated in (e). More information on the construction of this Figure is shown in Figure 6.1.
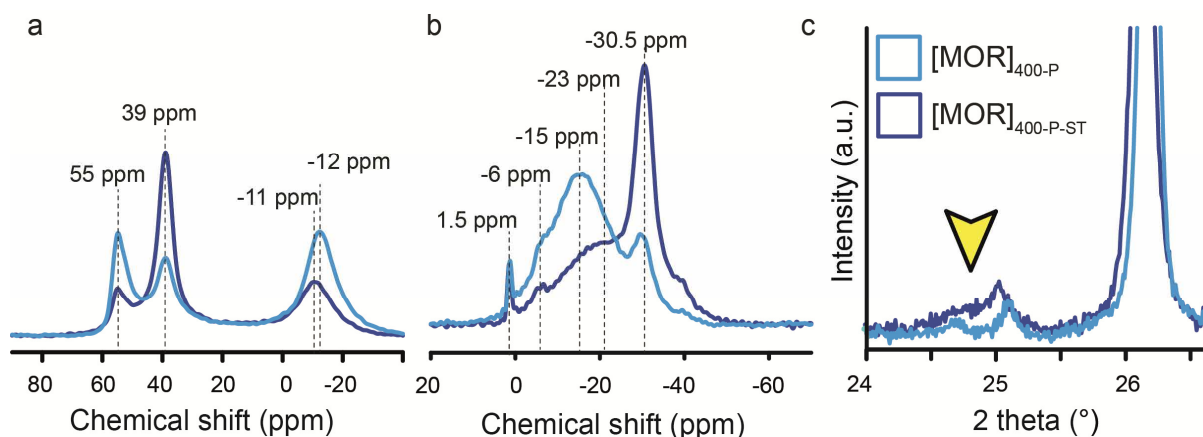
Figure 6.4 Sample [MOR]$_{400-P}$ ■ = before and [MOR]$_{400-P-ST}$ ■ = after steam treatment (a) ^{27}Al MAS NMR. (b) ^{31}P MAS NMR. (c) XRD.

While parent [MOR] forms a very fine powder that is easily suspended in water, the formation of the AlPO$_4$ phase in sample [MOR]$_{400-P-ST}$ leads to the formation of millimeter-sized clusters that prove to be very hard to crush by hand. Suspension in water is extremely difficult, indicating that the hydrophobicity of the material has increased with the formation of AlPO$_4$.

6.3.1.2 *In-situ STXM shows the crystallization of AlPO$_4$ islands*

Before the post-steam treatment, as can be observed in Figure 6.4a, the crystalline AlPO$_4$ phase is only present in low concentrations. This follows from the ^{27}Al MAS NMR spectrum of sample [MOR]$_{400-P}$ in Figure 6.4a, as it shows a low intensity for the 39 ppm resonance. Furthermore, the ^{27}Al MAS NMR spectrum of sample [MOR]$_{400-P}$ shows that the resonances at 55 ppm and -12 ppm have higher intensities than after hydrothermal treatment. ^{31}P MAS NMR in Figure 6.4b, shows a broad resonance centered around -15 ppm and smaller resonances at -30.5 ppm, -6 ppm and 1.5 ppm. The latter two resonances can be attributed to orthophosphate and pyrophosphate species.[46] The resonance at -15 ppm has been attributed to not fully condensed phosphates interacting with aluminum in alumina oxide hydroxide phosphate gels.[35] The smaller contribution of the resonance at -30.5 ppm, which corresponds to fully crystalline AlPO$_4$, correlates well with the smaller contribution of the ^{27}Al 39 ppm signal. [35-36]

After steam treatment there is a strong decrease in intensity of the ^{31}P -15 ppm resonance and for the ^{27}Al -12 ppm and 55 ppm resonances. The decrease in the intensities of resonances attributed to amorphous AlPO$_4$, coincides with the increase in intensity of the resonances at ^{27}Al 39 ppm and ^{31}P -30.5 ppm. Beside the ^{31}P -30.5 ppm resonance there is also a broad resonance at ^{31}P -23 ppm after steam treatment, which are attributed to semi-crystalline AlPO$_4$ domains. [35]
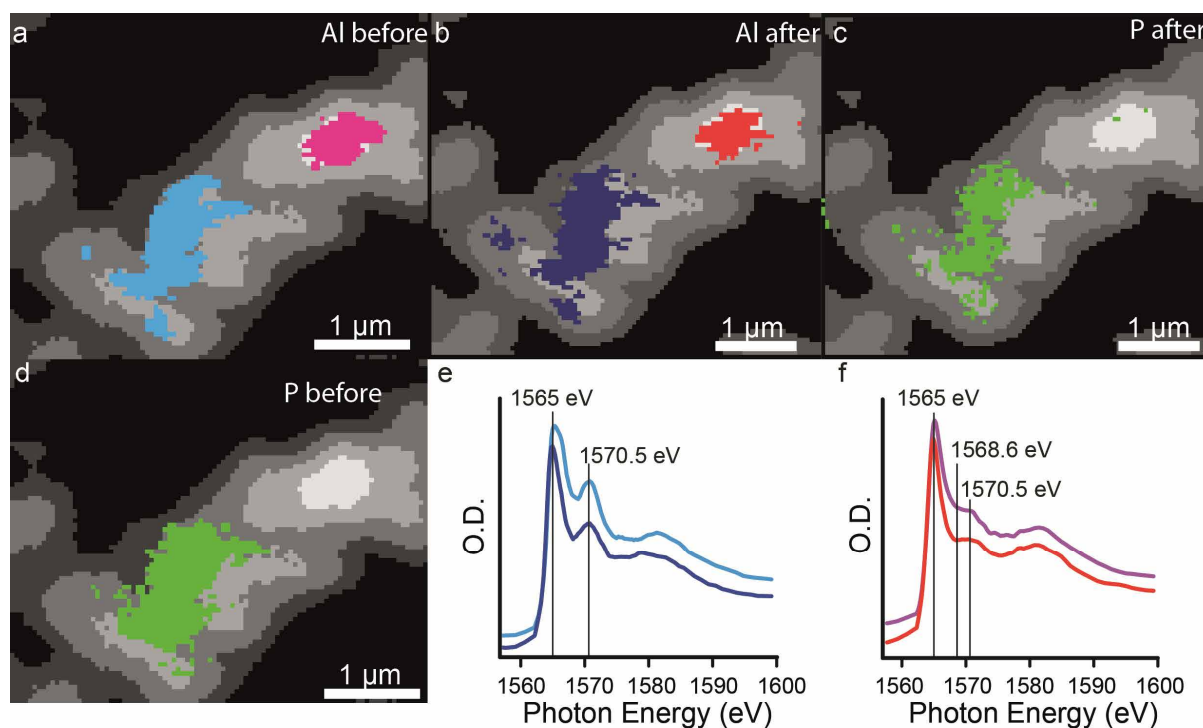
Figure 6.5 *In-situ* crystallization of the aluminum-phosphate ($AlPO_4$) phase within H-mordenite monitored by scanning transmission X-ray microscopy (STXM). Chemical maps of sample [MOR]$_{400-P}$ (a and d) before and (b and c) after heating at 400 °C. Greyscale masks are constructed from the Si map and indicate the particle area. Brighter regions have a higher optical density. The colored Al K-edge XANES in (e) and (f) correspond to the colored masks in (a) and (b). (c-d) mask of the highest phosphorus optical density. Detailed depiction of elemental distribution can be found in Figure A6.5.

Therefore, during steam treatment amorphous $AlPO_4$ crystallizes and forms α-cristobalite/tridymite $AlPO_4$ and semi-crystalline $AlPO_4$ domains. The latter conclusion corresponds with the fact that the ^{27}Al -12 ppm resonance, corresponding to aluminum in amorphous $AlPO_4$, does not disappear completely. Furthermore, the decrease in intensity of the ^{27}Al 55 ppm resonance after steam treatment indicates that TFAl species are expelled from the framework. These species are expected to react with phosphate species to form (amorphous) $AlPO_4$, as was discussed in Chapter 5.[16, 47] Although we do not see the appearance of new NMR resonances and therefore no sign of EFAl, it is possible that the resonances corresponding to these species are superimposed.

In order to see if the amorphous $AlPO_4$ phase migrates during crystallization, we performed an *in situ* crystallization of sample [MOR]$_{400-P}$ by heat treatment in a micro-electromechanical system (MEMS) nanoreactor [27] monitored by STXM. XRD experiments showed that a heat treatment performed at 400 °C already leads to the formation of crystalline α-cristobalite as can be seen by the formation of the 24.8° 2θ peak in Figure A6.4. From the X-ray absorption elemental maps shown in Figures 6.5 and A6.5 it can be observed that the $AlPO_4$ phase is already present on the outer surface of the zeolite aggregate as the concentrations of silicon and

aluminum do not correlate. The corresponding Al K-edge spectra show a contribution of the +5.5 eV peak. The part of the aggregate that is low on phosphorus shows an Al K-edge XANES that has almost no contribution of the +5.5 eV peak.

After the heat treatment it can be observed that the +5.5 eV peak decreases in intensity. This effect has been described previously as the annealing of $(Al-O-P)_n$ linkages leading to the formation of α-cristobalite/tridymite $AlPO_4$.[43] It can be observed that the phase remains stationary during crystallization. A simplified representation of these results is shown in Scheme 6.1g and i. There is also a decrease in the post-edge feature at 1568.6 in the Al K-edge XANES of the region that is high in aluminum content, but low in phosphorus, which is attributed to coordination changes induced by dehydration. It has been shown previously that the coordination of aluminum in H-ZSM-5, H-beta and H-mordenite changes upon dehydration as octahedrally coordinated aluminum is reverted into three- or four-coordination.[24, 48-49]

6.3.1.3 *Reaction between extra-framework aluminum oxide hydroxide and phosphoric acid*

The previous results suggest that phosphoric acid reacts with aluminum in steam-treated H-mordenite to form amorphous $AlPO_4$ species. It is expected that a steam-treatment of H-mordenite leads to the formation of EFAl. As this steam-treated zeolite is subsequently phosphated in an acidic medium, the EFAl species dissolve and react with phosphoric acid.[50-51] To determine which aluminum species are affected, we performed an acid leaching step where HNO_3 was used to leach out EFAl from the steam-treated H-mordenite sample, $[MOR]_{400}$.[40]

From Figure 6.6 it can be observed that before the acid leaching step, sample $[MOR]_{400}$ shows all spectroscopic signatures of a partial dealuminated material. ^{27}Al MAS NMR spectra in Figure 6.6 a show a decrease in the resonance at 55 ppm, which indicates a decrease in TFAl atoms. There is the appearance of a broad resonance at 30 ppm, which corresponds to five-coordinated or four-coordinated EFAl and a resonance at 5 ppm that corresponds to six-coordinated EFAl species. [42, 52-54] The resonance at 0 ppm is already present in the parent sample [MOR] and corresponds to framework aluminum in a six-coordinated environment due to physical coordination with water.[55] Furthermore, EFAl species can be observed as the peak at 1568.6 eV (+3.6 eV) in the Al K-edge XANES in Figure 6.6 b [24, 33] FT-IR spectroscopy shows that dealumination leads to a reduction in Brønsted acid sites as the band 3603 cm^{-1} that corresponds to bridging hydroxyl groups decreases in intensity (Figure 6.6 c).[56] The band at 3660 cm^{-1} corresponds to Al-OH groups in EFAl.[56] N_2-physisorption data presented in Figure A6.3 indicates a decreased pore volume, no indication of the formation of mesopores and XRD data
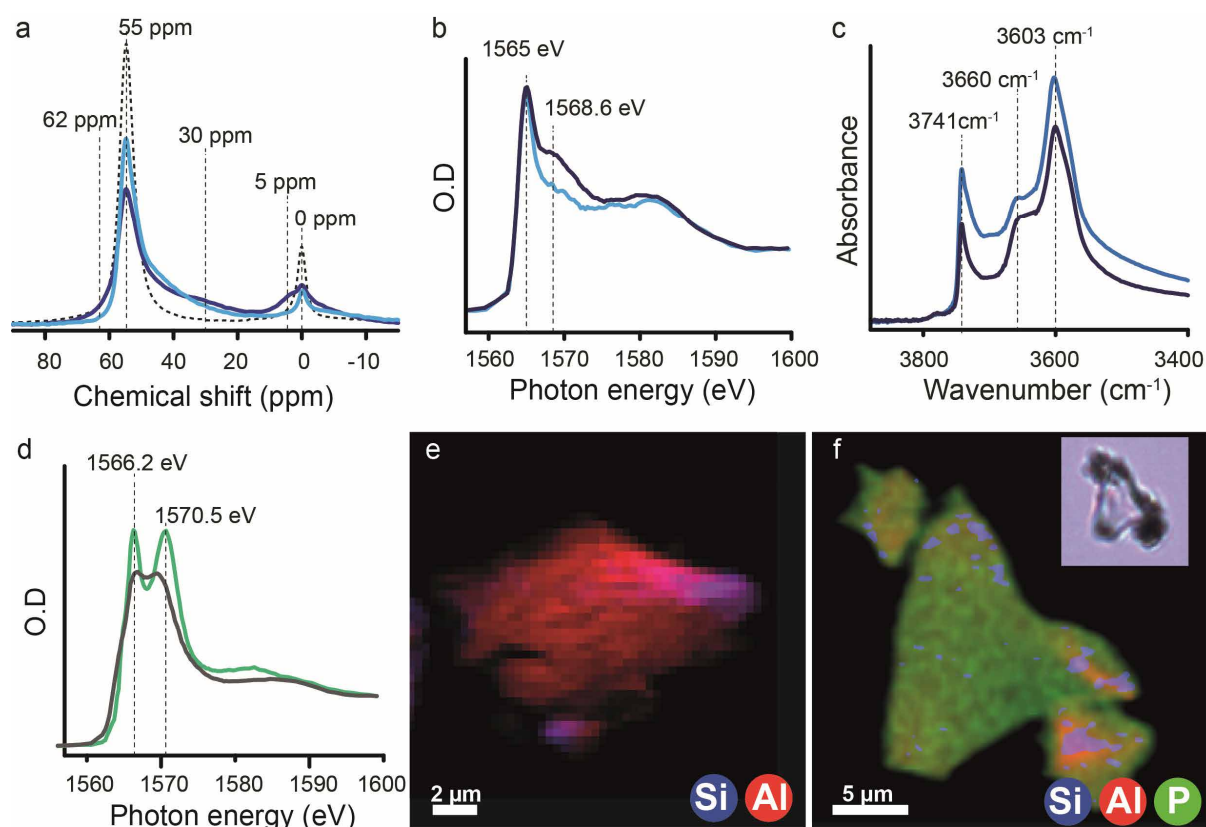
Figure 6.6 Microscopic and spectroscopic insights in the extra-framework aluminum phase and its reaction with phosphorus acid outside zeolite H-mordenite. Samples ■ = [MOR], ■ = [MOR]$_{400}$, ■ = [MOR]$_{400-L}$. (a) ^{27}Al MAS NMR spectra. Intensities are not quantitative. (b) Al K-edge XANES. (c) FT-IR spectra. (d) Al K-edge XANES of ■ = Filtrate, ■ = Filtrate + P. (e) Chemical map revealing elemental distribution in Filtrate. (f) Chemical map revealing element distribution in Filtrate + P. Inset is an optical microscopy image of the particle.

shows that the crystalline structure of the MOR framework remains intact. Therefore, although dealumination takes place, the effects are not severe, as is expected with steam-treatment temperatures of 400 °C.

By leaching the EFAl species from sample [MOR]$_{400}$ with HNO$_3$ it can be observed from the ^{27}Al MAS NMR spectrum in Figure 6.6 a that the resonances at 62 ppm, 30 ppm and 5 ppm disappear, similar to what was observed in Chapter 3. The remaining resonances are at 55 ppm, a broad tail of the 55 ppm resonance from 50 ppm to 20 ppm, and the resonance at 0 ppm. As mentioned the 55 ppm resonance and the 0 ppm resonance stem from aluminum atoms in the framework and are not expected to be leached out by acid treatment with 0.3 M HNO$_3$. [40] We attribute the 50 ppm - 20 ppm resonance to TFAl atoms in a distorted environment, i.e. partially dislodged TFAl species, which also cannot be leached out using HNO$_3$. [42]

Al K-edge XANES confirm the removal of EFAl species as the peak at 1568 eV disappears. Furthermore, there is an increase in the ratio between the 3603 cm^{-1} and 3660 cm^{-1} band in the FT-IR spectra, which is in accordance with the removal of EFAl species.[56] One could deduce

from the FT-IR spectra that sample [MOR]$_{400-L}$ contains more bridging hydroxyl groups. However, pyridine chemisorption experiments did not show an appreciable difference in the Brønsted acid site number as shown further in this Chapter in Figure 6.8. Even more, in sample [MOR]$_{400}$ not all Brønsted acid sites were accessible for pyridine. Therefore, it is unlikely that bridging hydroxyl groups are retrieved by removal of extra-framework cationic aluminum species, or the reinsertion of aluminum at defect sites. [57-59]

The extracted EFAl was characterized by XRD and STXM. The XRD patterns presented in Figure A6.4 show that the material is amorphous and the obtained patterns do not provide any information on the structure. However, by means of X-ray absorption microscopy we were able to determine that after extraction the EFAl species have an Al K-edge XANES that resembles aluminum oxide hydroxides, such as boehmite and diaspore (Figures 6.6 d and A6.2).[33] Furthermore, as shown in Figure 6.6 e, it was found that these alumina aggregates contain some silicon as well, indicating that both alumina and silica are extracted from the framework. Amorphous silica-alumina has been suggested to exist as extra-framework species in USY, to which an ^{27}Al MAS NMR chemical shift at 32 ppm was attributed.[60] However, based on the low amounts of silicon observed with STXM it seems that AlO(OH) forms the majority of the leached EFAl species. This conclusion is in accordance with the findings of Chevreau et al. who showed that Si was present in EFAl of zeolite Y in concentrations lower than 5 wt.%. [61]

To establish if AlO(OH) was found in the dealuminated material before acid leaching, linear regression fitting was applied to the Al K-edge XANES of sample [MOR]$_{400}$ using the Al K-edge XANES of samples [MOR], [MOR]$_{400-L}$ and Filtrate as references. [24] The results of this fitting procedure are presented in Figure A6.6 and it can be observed that the fit correlates quite well with the original spectra. We applied the same method to an H-mordenite sample that was steamed at more severe temperatures (500 °C) and found the fit to be good as well. The results indicate that EFAl species are present as amorphous AlO(OH) in steamed H-mordenite and not just as a product formed by acid leaching. ^{27}Al MAS NMR confirms this as the three resonances at 62 ppm, 30 ppm, and 5 ppm are also observed (at similar chemical shifts) for ground boehmite. [62] However, besides AlO(OH) it is expected that amorphous aluminum-silicate and possible other five-, and six-coordinated Al species will be present as well, as silicon is detected in sample Filtrate and the Al K-edge XANES reference spectrum for AlO(OH) cannot fully reconstruct the Al K-edge XANES of [USY] (Figure A6.6 c). This is also shown in Chapter 3, where andalusite was needed as an additional reference to obtain a good fit for steamed H-ZSM-5.

To assess what product forms after the reaction of the EFAl species with phosphoric acid, 0.2 g of Filtrate was reacted with 0.2 g of phosphoric acid in an aqueous solution, followed by a steam treatment. As sample Filtrate consists mainly of amorphous AlO(OH) it is expected to readily react with phosphoric acid.[14, 50] It can be observed in Figure 6.6 f and A6.7 that transparent tabular-shaped crystals form, which is generally the crystal habit that is described for tridymite.[63-64] From the X-ray absorption spectra in Figure 6.6 d, it becomes apparent that the coordination of aluminum changes. There is the formation of a sharp peak at 1566.2 eV and 1570.5 eV. The latter peak correlates with the peak observed in the samples [MOR]$_{400-P}$ and [MOR]$_{400-P-ST}$. When the Al K-edge XANES of sample Filtrate + P is used to fit the spectra of sample [MOR]$_{400-P}$ a reasonable fit is obtained (Figure A6.5). As mentioned, the 1570.5 eV peak was attributed to six-coordinated aluminum in AlPO$_4$. [45] The P K-edge of sample Filtrate + P shown in Figure A6.2 shows that phosphorus has a four-fold coordination. [43] The spatial distribution of phosphorus and aluminum is similar as can be seen in Figure 6.6 and A6.7.

Furthermore, it can be observed in Figure 6.6 and A6.7 that there are regions where silicon is present. In these regions, there is a high concentration of aluminum and a low concentration of phosphorus. This could indicate that there is aluminum-silicate present in the extra-framework AlPO$_4$ phase and that phosphorus does not react as easily with this phase as with the AlO(OH) species. However, we did not find different Al K-edge spectra for these regions, which would suggest the concentration of a silica-alumina phase is very low, or silicon is present in a separate silica phase.

6.3.1.4 *Effect of phosphatation on dealuminated and acid leached H-mordenite*

So far, the results in this Chapter and Chapter 3 have pointed out that extra-framework AlO(OH) present in dealuminated zeolite H-mordenite reacts with phosphoric acid to form extra-framework amorphous AlPO$_4$ and, after thermal or hydrothermal treatment, crystallizes into α-cristobalite/tridymite AlPO$_4$. Therefore, it is expected that the removal of this EFAl supply prevents the formation of AlPO$_4$ after phosphorus modification.[17] To test this hypothesis we have performed a phosphatation step followed by a post-steam treatment on acid leached sample [MOR]$_{400-L}$, which lead to the formation of sample [MOR]$_{400-L-P-ST}$.

As expected, the structural characterization results presented in Figure 6.7 show that there is no indication of the formation of crystalline AlPO$_4$ in sample [MOR]$_{400-L-P-ST}$, as the ^{27}Al MAS NMR resonance at 39 ppm, the ^{31}P MAS NMR resonance at -30.5 ppm, the Al K-edge XANES post-edge feature at +5.5 eV and the XRD 24.8° 2θ peak are not observed. However,
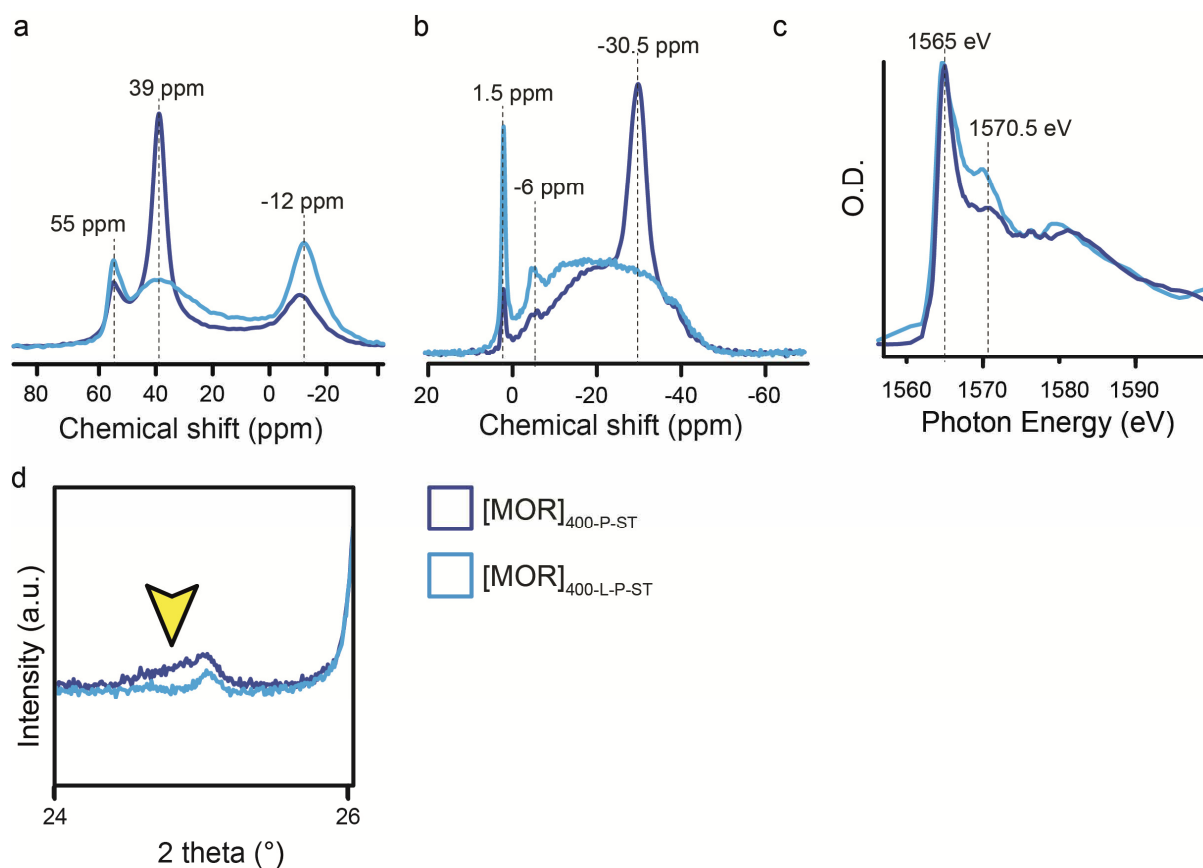
Figure 6.7 Samples ■ = [MOR]$_{400-P-ST}$, ■ = [MOR]$_{400-L-P-ST}$ (a) ^{27}Al MAS NMR spectra. Intensities are not quantitative. (b) ^{31}P MAS NMR spectra. (d) Al K-edge XANES. (d) XRD.

phosphatation still influences the remaining aluminum species, as there is a change in the ^{27}Al MAS NMR spectra in comparison to that of sample [MOR]$_{400-L}$ presented in Figure 6.6 a. There is a strong decrease in the 55 ppm peak and there is the formation of a broad band at 40 ppm. The most intense resonance of the ^{27}Al MAS NMR spectrum of [MOR]$_{400-L-P-ST}$ is at -12 ppm, which we attributed to amorphous AlPO$_4$. However, the expected corresponding ^{31}P MAS NMR resonance at -15 ppm is not observed. Also, the Al K-edge spectrum of sample [MOR]$_{400-P-ST}$ does not show the post-edge feature at 1570.5 eV and there is no strong correlation in the location of phosphorus and aluminum atoms as shown in Figure A6.8.

However, when linear regression fitting is applied using the Al K-edge XANES of Filtrate + P as a reference, it can be observed that there are regions in the sample that have a better correlation with phosphorus position and also show an Al K-edge spectra that resembles that of Filtrate + P (Figure A6.8). Therefore, it cannot be ruled out that phosphorus does form extra-framework AlPO$_4$ species. It is expected that the formation of EFAl and subsequent reaction with phosphate species during the post-steam treatment induces the formation of amorphous or

crystalline AlPO$_4$.[16] Also, since phosphoric acid is a complexing acid, it is possible that it can remove partially dislodged aluminum species from the framework which HNO$_3$ cannot.[40]

6.3.1.5 *Acidity in dealuminated and phosphated materials*

Ammonia temperature programmed desorption of sample [MOR]$_{400\text{-P-ST}}$ shows a 85 % decrease in ammonia desorbed at temperatures above 300 °C as can be seen in Figure 6.8. A similar decrease in the number of strong acid sites in comparison to parent sample [MOR] is therefore expected. Sample [MOR]$_{400\text{-P-ST}}$ has two desorption maxima, at 175 °C and 425 °C (Figure 6.8). The low temperature desorption maxima corresponds to weak acid sites that are not observed in the parent sample, while the high desorption maxima corresponds to strong acid sites. FT-IR infrared is in accordance with the observation of strong acid sites, as there is still a band present at 3603 cm^{-1} that corresponds to bridging hydroxyl groups, shown in Figure 6.8 and A6.9. However, the accessibility of these acid sites is limited for pyridine, as the FT-IR spectrum in Figure 6.8 does not show the formation protonated pyridinium ions and the bridging hydroxyl are not affected. Furthermore, it can be observed that this effect is observed for all phosphated samples, indicating that a 4 wt.% loading of phosphorus effectively blocks the 1-dimensional pore system of the mordenite framework.

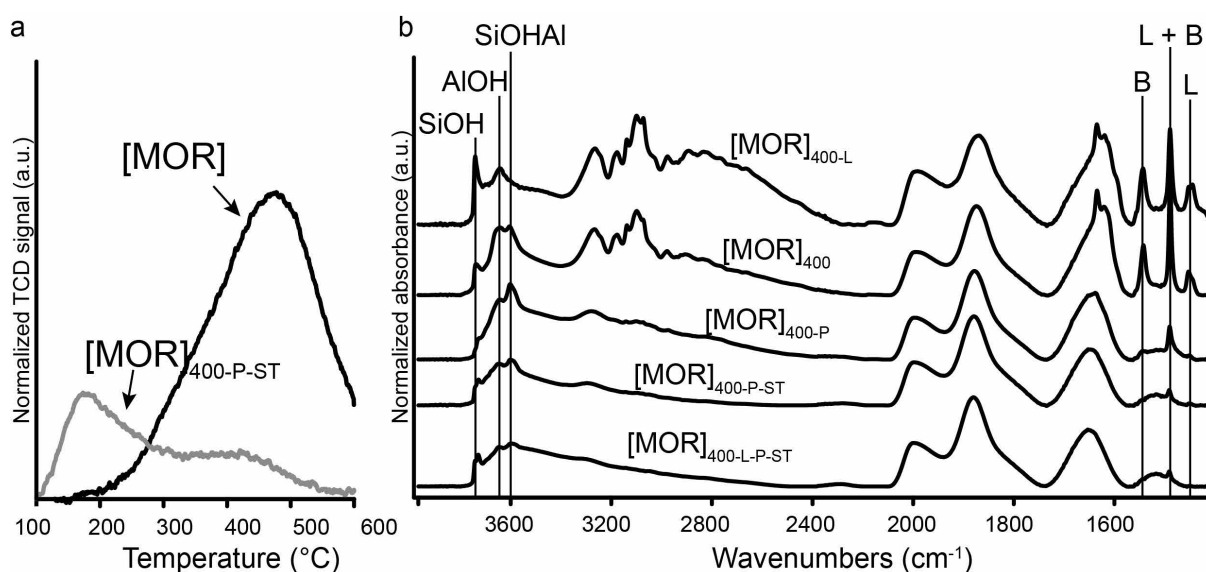**Figure 6.8** (a) Ammonia TPD profiles of samples [MOR] and [MOR]$_{400\text{-P-ST}}$. (b) FT-IR spectra of the samples under study after adsorption and subsequent removal of physisorbed pyridine at 150 °C *in vacuo*. Only chemisorbed pyridine remains. The OH-stretch region of the samples, without probe addition is shown in Figure A6.9.

6.3.2 Extension of the phosphatation method to other zeolite framework topologies

6.3.2.1 *Faujasite*

As zeolite H-USY with FAU topology already contains an EFAl supply, it was not necessary to apply a pre-steam treatment. [15] When the H-USY sample was treated with phosphoric acid and HNO_3 under reflux conditions, XRD data presented in Figure A6.10 showed that the material became amorphous. It is assumed that the use of additional HNO_3 caused the collapse of the framework structure and an amorphization of the material. [65] An acid treatment without phosphoric acid leads to severe amorphization as well (Figure A6.10). Interestingly, the XRD patterns of sample $[USY]_{P-ST}$, which are presented in Figure A6.10, do not show the formation of crystalline $AlPO_4$. Therefore, it appears that the amorphous aluminosilicate phase that is expected to form after the framework collapse, does not react with phosphoric acid. This is supported by the results of Filtrate + P shown in Figure 6.6, where regions of silicon and aluminum was found in the sample, but not phosphorus.

In order to prevent excessive leaching of framework aluminum, the phosphatation was performed by wet impregnation with an aqueous solution containing only H_3PO_4. The phosphorus P/Al ratio was decreased from 1 to 0.5. This approach was effective, as it did not lead to total framework collapse as can be observed from the XRD diffractogram in Figure 6.9c. STXM and XRD results clearly show the formation of an extra-framework $AlPO_4$ phase. As can be seen in Figure 6.9, the presented $[USY]_{P-WI-ST}$ aggregate shows a large concentration of aluminum and phosphorus that is located around the central part of the aggregate. The Al K-edge XANES Al Type 3, which corresponds to this $AlPO_4$ cluster is significantly different from the Al K-edge XANES Al Type 4, found in the zeolitic silicon rich regions. Spectra Al Type 3 resembles that of crystalline $AlPO_4$ as has been previously observed for the sample $[MOR]_{400-P-ST}$ and tridymite in $AlPO_4$ thin-films.[43] The crystallinity of the $AlPO_4$ phase is even higher for the sample $[USY]_{P-WI-ST}$ than for sample $[MOR]_{400-P-ST}$ as can be seen by the distinct post-edge feature at 1571.2 eV. The large crystalline $AlPO_4$ clusters are confirmed by the sharp XRD peak around 25.1°, which corresponds to the α-cristobalite phase.[14] The crystallite sizes range between 30 nm to 40 nm, as determined by the Scherrer equation. The large crystal sizes and the clearly observable $AlPO_4$ phase with STXM can in part be attributed to the fact that H-USY has a much larger aluminum supply, due to its low Si/Al ratio of 2.55, in comparison to H-mordenite.

These results are in full accordance with the study performed by Corma and co-workers.[15] It was found that phosphoric acid readily reacts with the EFAl species in zeolite H-USY to form an amorphous $AlPO_4$ phase. After steam treatment it was found that the phase crystallizes into
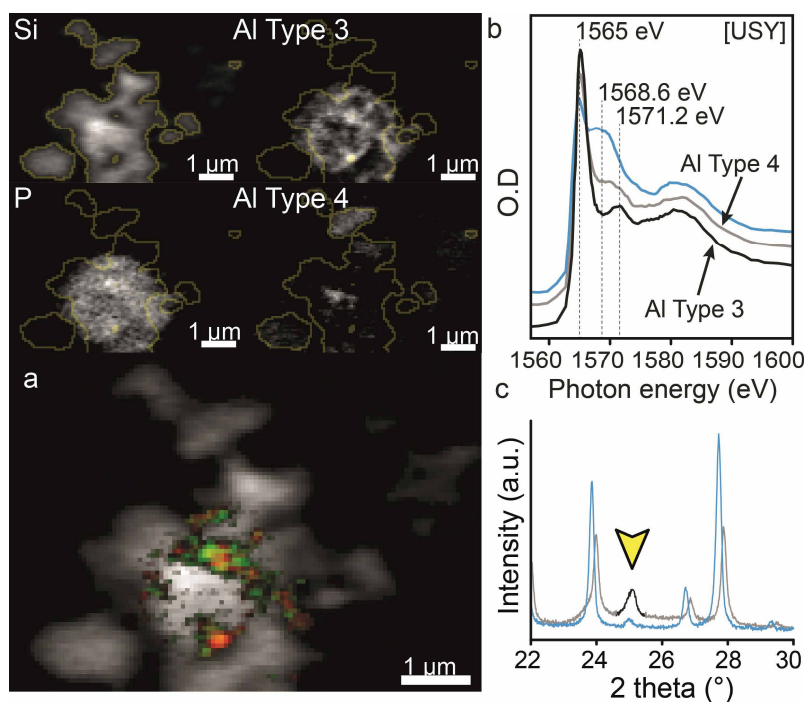
Figure 6.9 Scanning transmission X-ray microscopy (STXM) maps of different elements in phosphated H-USY. It can be seen that there are two types of aluminum present, i.e. Al Type 3, which is sited at similar positions as phosphorus and Al Type 4, which is located at similar positions as silicon atoms. (a) The highest optical densities found for P (green) and Al Type 4 (red) in respect to Si (grey). (b) Al K-edge XANES corresponding to ■ = USY, ■ = [USY]$_{P-WI-ST}$, Al Type 3 and ■ = [USY]$_{P-WI-ST}$, Al Type 4.

AlPO$_4$. The authors suggested that the phase was tridymite and, based on N$_2$ physisorption data, it was postulated that the phase could be found on the external surface of the zeolite. Using X-ray absorption microscopy and X-ray diffraction there is now direct prove for these suggestions.

6.3.2.2 *Ferrierite*

From the previous results would appear that an extra-framework AlPO$_4$ phase can be created from a zeolite's own supply by simply applying a dealumination step followed by a phosphatation step. However, the results obtained for phosphated zeolite H-ferrierite show that this assumption is not necessarily correct. As can be observed in Figure 6.10, the ^{27}Al MAS NMR and ^{31}P MAS NMR spectra show no indication on the formation of crystalline AlPO$_4$, as a sharp and intense resonance at 39 ppm would be expected in the ^{27}Al MAS NMR spectra and one at -28 ppm or -31 ppm for the ^{31}P MAS NMR.[15-16, 18]

However, in contrast to acid-leached H-mordenite, the lack of the AlPO$_4$ cannot be attributed to the absence of an EFAl phase. From Figure 6.10 it can be observed that H-ferrierite steamed at 500 °C, shows a strong contribution of the ^{27}Al MAS NMR resonance at 32 ppm,
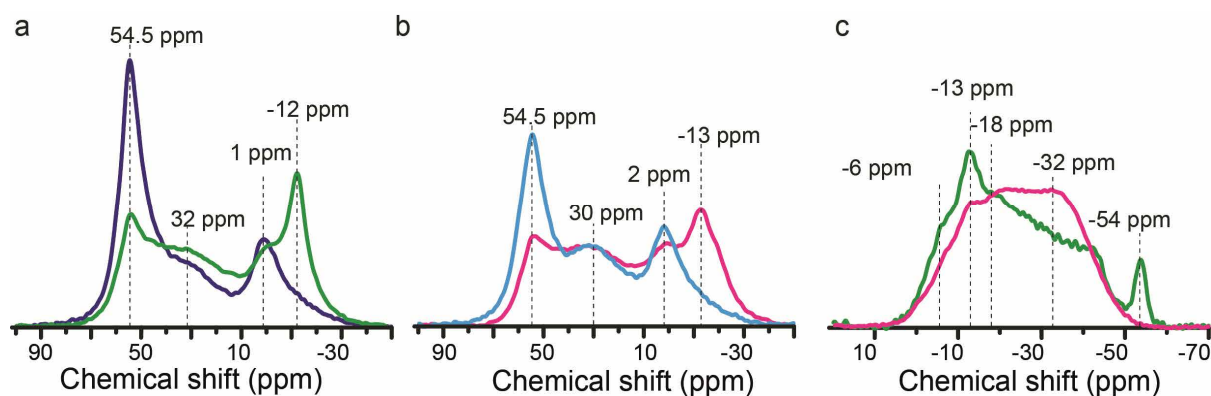
Figure 6.10 (a) ^{27}Al MAS NMR of sample ■ = [FER]$_{500}$, ■ = [FER]$_{500\text{-P-ST}}$. (b) ^{27}Al MAS NMR of sample ■ = [FER]$_{600}$, ■ = [FER]$_{600\text{-P-ST}}$. (c) ^{31}P MAS NMR of sample ■ = [FER]$_{500\text{-P-ST}}$, ■ = [FER]$_{600\text{-P-ST}}$.

corresponding to EFAl species. [66-67] The resonance at 30 ppm is even more pronounced for H-ferrierite steamed at 600 °C. Furthermore, in Figure 6.11, the Al K-edge XANES of steamed H-ferrierite shows a peak at 1568.6 eV, corresponding to EFAl species and the FT-IR band of steamed H-ferrierite at 3650 cm^{-1} corresponds to Al-OH species in EFAl. [24, 33, 67] Therefore, the presence of EFAl species can be confirmed. It is reported in the literature that leaching out EFAl from zeolite H-ferrierite after steam treatment is very difficult.[66-67] It has been suggested that EFAl species in H-ferrierite are trapped in the structure as migration of aluminum to the surface has not been observed, while at the same time EFAl species were detected, which could not be washed out. [66] Although the exact origins of the trapped EFAl species is not well understood, one of the suggestions was that this type of EFAl was trapped in the 8-ring channels and resistant to acid washing.[66]

The inaccessible nature of these EFAl species follows from our results as well. First, it can be observed in Figure 6.10 that the ^{27}Al MAS NMR resonances at 32 ppm and 0 ppm remain almost unaffected after phosphatation. The only observable change is a decrease in intensity of the 54.5 ppm resonance and the appearance of a new resonance at -12 ppm, which would indicate that the latter forms at the cost of the former. Second, the FT-IR spectra shown in Figure 6.11 c show that while the intensity of the band for external Si-OH groups at 3745 cm^{-1} decreases sharply, the intensity of the band at 3650 cm^{-1}, corresponding to Al-OH groups, is not affected. In contrast, we have seen that the intensity of the bands corresponding to terminal Al-OH groups decrease after the phosphatation of H-ZSM-5 in Chapter 3. From the X-ray absorption maps in Figure 6.11 it follows that location of phosphorus and aluminum does not correlate, which further indicates that most phosphorus does not interact with aluminum in zeolite H-ferrierite. A schematic representation of this effect is shown in Scheme 6.1 c.
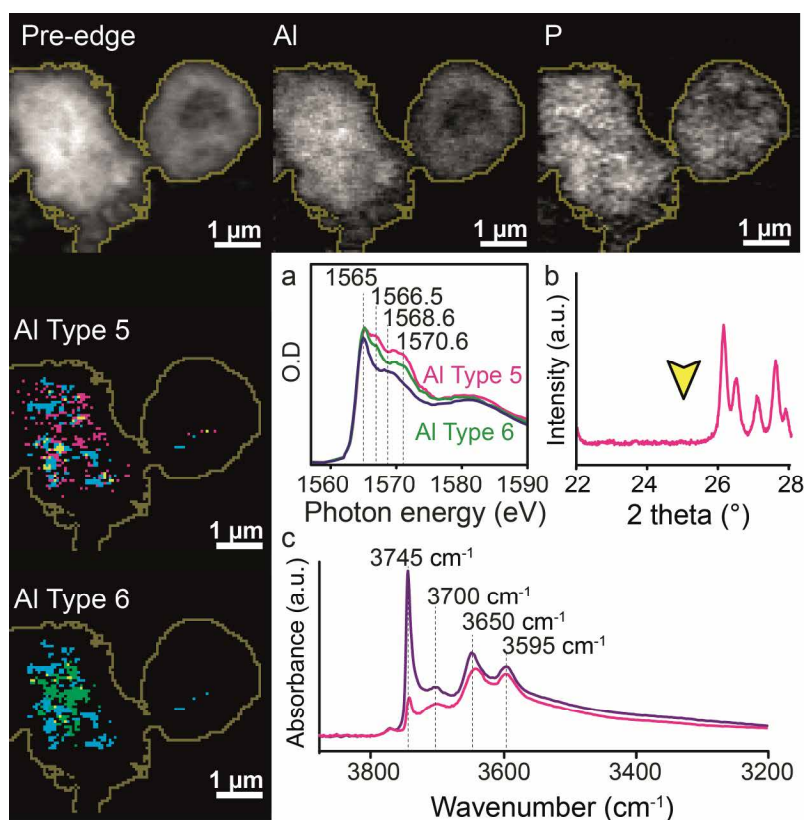
Figure 6.11 Scanning transmission X-ray microscopy (STXM) maps of different elements in phosphated FER ST 500. Scale bar is 1 μm. Using a linear regression fitting, Al Type 5 and Al Type 6 can be distinguished. It can be observed that the distribution of high concentrations of P (cyan) and Al Type 6 (green) hardly overlap (yellow). There is slightly more overlap (yellow) between P (cyan) and Al Type 5 (magenta), however there is no clear correlation. (a) Corresponding Al K-edge XANES of ■ = [FER]$_{500}$, ■ = [FER]$_{500-P-ST}$ Type 5, and ■ = [FER]$_{500-P-ST}$ Al Type 6. (b) XRD data of sample ■ [FER]$_{600}$, and ■ = [FER]$_{600-P-ST}$. (c) FT-IR data of ■ = [FER]$_{600}$, and ■ = [FER]$_{600-P-ST}$.

Finally, the Al K-edge XANES presented in Figure 6.11 do not show a decrease in the 1568.6 eV peak as was observed for sample [MOR]$_{400-P}$ for steamed H-ZSM-5. However, there is a new spectrum that contributes to the overall XANES as two peaks at 1566.5 eV and 1570.6 eV appear. These values correspond to those of Filtrate + P. Linear regression fitting of the [FER]$_{500-P-ST}$ XANES, shown in Figure A6.11, using the Al K-edge XANES of Filtrate + P as a reference indicate the latter spectrum has a contribution to the overall spectrum.

6.3.3 Influence of zeolite topology on AlPO$_4$ formation

From the results described in the previous sections and from the results obtained in Chapter 3, we are now in the position to discuss some of the parameters that should be taken into account in the synthesis of AlPO$_4$ from the framework aluminum of zeolite materials. The most important factor is the availability of reactive aluminum. A steam treatment is an effective route to obtain reactive aluminum, since during steam treatment aluminum is expelled from the

framework and forms dominantly extra-framework AlO(OH), as shown in Scheme 6.1e-f. These species are very reactive towards H_3PO_4 and form amorphous $AlPO_4$.[15, 17] However, aluminum that is still connected to the zeolitic framework is not able to form $AlPO_4$, as long as there are still framework Si-O-Al bonds left, as can be observed in Scheme 6.1g-h. We also expect $AlPO_4$ not to form by reaction of amorphous silica-alumina with phosphoric acid.[68] Therefore, the tendency of framework aluminum to be hydrolyzed under steaming conditions is an important factor that determines if reactive aluminum is formed or not. Unfortunately, to our best knowledge, not many studies on the exact effect of framework topology on hydrothermal stability have been reported in the literature. In the works of Costa and Caeiro et al. it is reported that identical hydrothermal treatments on zeolites with comparable Si/Al ratios, lead to an 80% loss of TFAl atoms in H-mordenite, 60% loss in H-ZSM-5, and 15 % in H-beta.[16, 69] Therefore, it is clear that the hydrothermal stability of framework aluminum is different for different zeolite topologies. If formed EFAl species are trapped in the framework, as for H-ferrierite, they are inaccessible to phosphoric acid and $AlPO_4$ will not form. [66-67]

Depending on the framework type, framework aluminum and partially dislodged framework aluminum can also be dissolved by mineral acids and extracted from the framework, allowing these species to react with phosphoric acid. It has been shown that dissolution of framework aluminum is possible in framework structures such as H-mordenite and aluminum rich H-USY [51, 61, 65], but more difficult in materials such as zeolite H-beta, [70] H-ZSM-5, [71] and H-ferrierite.[72] Therefore, even for a mildly steamed sample, such as H-mordenite, most of the aluminum present in the zeolite is extracted from the framework and a high amount of crystalline $AlPO_4$ is formed, as was shown in this Chapter. For H-ZSM-5 we did observe the formation of an $AlPO_4$ phase in Chapter 3, although the amount was lower than for H-mordenite. As a consequence the XRD patterns of the former sample did not show a peak for α-cristobalite. However, the P/Al ratio used in that study was 0.5 instead of P/Al = 1 which is used in the current study and no additional HNO_3 was added. Therefore, the phosphorus content and acidity of the solution used in phosphatation is also a factor that should be considered.

This follows from the results on H-USY from this study, which show that if the framework Si/Al ratio is very low (Si/Al bulk ratio = 2.55), the extraction of framework aluminum destabilized the framework and led to a collapse of the structure. When HNO_3 was left out of the phosphatation step and the P/Al ratio was decreased to 0.5, the framework structure was better preserved and crystalline $AlPO_4$ was formed.

It has been reported that oxalic acid, being a complexing agent, is more effective in dissolving framework aluminum from zeolites H-mordenite and H-beta than mineral acids.[40, 73] Therefore, it is possible that phosphoric acid, which is also a chelating agent for aluminum cations, is capable of extracting more framework aluminum from the zeolite than HNO_3.

During thermal or hydrothermal treatment of the amorphous $AlPO_4$ phase $(Al-O-P)_n$ linkages anneal, which leads to the crystallization of the amorphous $AlPO_4$ phase as shown in Scheme 6.1i-j. In order for the $AlPO_4$ phase to grow as 3-dimensional crystal structures, sufficient space is needed. Therefore, it is assumed that if $AlPO_4$ is located inside the zeolite micropores, crystallization is inhibited, which could explain the higher concentration of amorphous $AlPO_4$ found inside the zeolite H-mordenite. Such an effect was not observed for zeolite H-USY, as for the samples under study the $AlPO_4$ phase was found exclusively outside of the crystal. Al K-edge XANES of silicon rich parts showed a spectrum that resembled four-coordinated aluminum in aluminum-silicates, as can be seen in Figure 6.9. [33] The results reported by Corma and co-workers are in accordance with this observation, as they showed by ^{27}Al MAS NMR that the -12 ppm resonance for amorphous $AlPO_4$ had almost disappeared after the crystallization of the $AlPO_4$ phase in H-USY.[15] For dealuminated, phosphated and post-steamed H-ZSM-5, we observed a decrease in mesopore volume after phosphorus introduction, which could indicate the presence $AlPO_4$ in the interior parts of zeolite H-ZSM-5. However, we did not find indications the $AlPO_4$ phase was more amorphous. We postulate that the pore dimensionality of the framework plays a role. The 1-dimensional pore structure of zeolite H-mordenite is prone to pore-blockage (Scheme 6.1i), leading to the parts of the $AlPO_4$ phase to be trapped inside the channel system, hindering subsequent crystallization. In the 3-dimensional channel system of zeolite H-Y and H-ZSM-5, these constrains are not as dominant and a stronger segregation between (i) $AlPO_4$ outside the zeolite and (ii) framework aluminum inside the zeolite is expected (Scheme 6.1j). Zeolite H-USY, with the largest and most interconnected channels, should have the least diffusion limitations. However, further studies will be necessary to fully substantiate these claims.

Besides crystallization of the $AlPO_4$ phase, the post-steam treatment also leads to further dealumination. The formed EFAl species are expected to react with phosphate species to form additional $AlPO_4$, as could be observed for zeolite H-mordenite and presented in Scheme 6.1i-j. Costa and co-workers showed that the addition of phosphates to fresh and unmodified zeolite H-beta and H-mordenite, followed by a steam treatment (800 °C, 5 h) converted the majority of the framework aluminum into crystalline extra-framework $AlPO_4$. Also, Zhuang et al. obtained similar results for phosphated H-ZSM-5 after a steam treatment (800 °C, 10 h). It is interesting

how this relates to the promotional effect of phosphorus on the hydrothermal stability H-ZSM-5, which will be discussed in more detail in Chapter 7.[17, 69, 74]

In the case of H-ferrierite, due to the inaccessible nature of the EFAl species, the formation of a crystalline $AlPO_4$ phase is unlikely to take place. However, we suggest that the applied post-steam treatment leads to further dealumination, as expelled aluminum species react with the phosphates that are present in the channel system, to form amorphous $AlPO_4$. The spectroscopic signals found at -12 ppm in ^{27}Al MAS NMR spectroscopy and 1566.5 eV and 1570.6 eV in Al K-edge XANES microscopy support this hypothesis. We further postulate that these $AlPO_4$ species become trapped in the framework similar to the EFAl species, as N_2-physisorption data in Figure A6.3 shows that the pore volume decreases further after post-steam treatment.

As this is, to our best knowledge, one of the few studies that explores the creation of a zeolite binder material made from components of the zeolite itself, it is too premature to present a fully unified view on $AlPO_4$ formation in zeolite materials. However, we do hope that this work may stimulate future characterization studies that further explore these promising avenues.

6.4 Conclusions

A detailed study has been performed on the formation of an aluminum-phosphate ($AlPO_4$) binder from the framework aluminum supply of three industrially relevant zeolites; H-USY, H-mordenite and H-ferrierite. It has been found that the dealumination of the zeolite materials by hydrothermal treatment has an extra-framework aluminum (EFAl) phase, with amorphous $AlO(OH)$ phase as the main component. The presence of small traces of silicon implied that amorphous silica-alumina was also present in the EFAl phase. When the dealuminated zeolite sample was suspended in an acidic aqueous solution containing phosphoric acid, the $AlO(OH)$ species readily reacted with phosphoric acid and an amorphous extra-framework $AlPO_4$ phase was formed. If the EFAl species were trapped in the framework, as was the case for zeolite H-ferrierite, they remained inaccessible to phosphoric acid and an $AlPO_4$ phase could not form. Extra-framework amorphous silica-alumina and framework-connected aluminum were not found to participate in the formation of $AlPO_4$. However, acid leaching of framework aluminum was observed in H-USY, leading to a collapse of the framework and severe amorphization.

The amorphous $AlPO_4$ phase was found to consist of four-, and six-coordinated aluminum connected to PO_4^- units. Silicon was found in the $AlPO_4$ phase as well, although indications for an interaction with phosphorus or $AlPO_4$ have not been observed. The amorphous $AlPO_4$ phase was found to be heterogeneously distributed on the external zeolitic surface. The phase was found to be located in the zeolitic interior as well, but at lower concentrations. It is suggested that the $AlPO_4$ phase is more likely to become trapped in an 1-dimensional channel system, than in a 3-dimensional channel system.

During a subsequent thermal or hydrothermal treatment the amorphous $AlPO_4$ phase crystallizes into $AlPO_4$ with an α-cristobalite/tridymite structure. The phase was not observed to migrate during crystallization. The crystalline α-cristobalite/tridymite $AlPO_4$ forms islands, which are located at the external surface of the zeolite materials. The $AlPO_4$ phase that was present in the crystal interior was found to consist of more aluminum atoms with a six-fold coordination. It was suggested that $AlPO_4$ located in the zeolite channel system has the tendency to remain more amorphous due to spatial constraints inhibiting crystallization. Besides crystallization of the $AlPO_4$ phase, a post-steam treatment leads to progressed dealumination of the zeolite material. The EFAl that is formed subsequently reacts with phosphate species to form additional (amorphous) $AlPO_4$. After the crystalline $AlPO_4$ phase was formed in H-mordenite, the samples form millimeter-sized clusters with an increased hydrophobicity.

Acknowledgements

References

[1]   W. Vermeiren and J. P. Gilson, *Top. Catal.* **2009**, *52*, 1131-1161.

[2]   J. E. Otterstedt, S. B. Gevert, S. G. Jääs and P. G. Menon, *Appl. Catal.* **1986**, *22*, 159-179.

[3]   S. Mohanty, D. Kunzru and D. Saraf, *Fuel* **1990**, *69*, 1467-1473.

[4]   M. Guisnet and J.-P. Gilson, *Zeolites for cleaner technologies*, Imperial College Press London, **2002**.

[5]   U. Olsbye, S. Svelle, M. Bjørgen, P. Beato, T. V. W. Janssens, F. Joensen, S. Bordiga and K. P. Lillerud, *Angew. Chem. Int. Ed.* **2012**, *51*, 5810-5831.

[6]   J. Caro, M. Noack and P. Kölsch, *Adsorption* **2005**, *11*, 215-227.

[7]   J. Jae, R. Coolman, T. J. Mountziaris and G. W. Huber, *Chem. Eng. Sci.* **2014**, *108*, 33-46.

[8]   S. Mitchell, N.-L. Michels and J. Perez-Ramirez, *Chem. Soc. Rev.* **2013**, *42*, 6094-6112.

[9]   J. S. J. Hargreaves and A. L. Munnoch, *Catal. Sci. Tech.* **2013**, *3*, 1165-1171.

[10]   G. Cao, L. R. M. Martens, J. L. White, T. J. Chen and M. J. Shah in *Zeolite catalyst activity enhancement by aluminum phosphate and phosphorus*, Patent US6080303 A, **2000**.

[11]   A. Corma in *Catalyst composition comprising a molecular sieve and an aluminum phosphate containing matrix*, Patent WO1999002260 A1, **1999**.

[12]   G. W. Kirker, M. E. Landis and J. H. Yen in *Hydrogenation catalyst*, *Vol.* US4724066 A, **1988**.

[13]   T. G. Roberie and F. T. I. I. John in *Catalytic cracking utilizing a zeolite and aluminum phosphate-containing catalyst*, Patent US5286369 A, **1994**.

[14]   Y.-J. Lee, Y.-W. Kim, N. Viswanadham, K.-W. Jun and J. W. Bae, *Appl. Catal. A-Gen* **2010**, *374*, 18-25.

[15]   A. Corma, V. Fornes, W. Kolodziejski and L. J. Martineztriguero, *J. Catal.* **1994**, *145*, 27-36.

[16]   A. F. Costa, H. S. Cerqueira, J. M. M. Ferreira, N. M. S. Ruiz and S. M. C. Menezes, *Appl. Catal. A-Gen* **2007**, *319*, 137-143.

[17]   G. Lischke, R. Eckelt, H. G. Jerschkewitz, B. Parlitz, E. Schreier, W. Storek, B. Zibrowius and G. Öhlmann, *J. Catal.* **1991**, *132*, 229-243.

[18]   J. Zhuang, D. Ma, G. Yang, Z. Yan, X. Liu, X. Liu, X. Han, X. Bao, P. Xie and Z. Liu, *J. Catal.* **2004**, *228*, 234-242.

[19]   G. Majano, L. Delmotte, V. Valtchev and S. Mintova, *Chem. Mater.* **2009**, *21*, 4184-4191.

[20]   F. J. Machado, C. M. López, M. a. A. Centeno and C. Urbina, *Appl. Catal. A-Gen* **1999**, *181*, 29-38.

[21]   M. Hartmann, *Angew. Chem. Int. Ed.* **2004**, *43*, 5880-5882.

[22]   J. Perez-Ramirez, C. H. Christensen, K. Egeblad, C. H. Christensen and J. C. Groen, *Chem. Soc. Rev.* **2008**, *37*, 2530-2542.

[23]   H. L. Janardhan, G. V. Shanbhag and A. B. Halgeri, *Appl. Catal. A-Gen* **2014**, *471*, 12-18.

[24]   L. R. Aramburo, E. de Smit, B. Arstad, M. M. van Schooneveld, L. Sommer, A. Juhin, T. Yokosawa, H. W. Zandbergen, U. Olsbye, F. M. F. de Groot and B. M. Weckhuysen, *Angew. Chem. Int. Ed.* **2012**, *51*, 3616-3619.

[25]   L. R. Aramburo, Y. Liu, T. Tyliszczak, F. M. F. de Groot, J. C. Andrews and B. M. Weckhuysen, *ChemPhysChem* **2013**, *14*, 496-499.

[26]   F. M. F. de Groot, E. de Smit, M. M. van Schooneveld, L. R. Aramburo and B. M. Weckhuysen, *ChemPhysChem* **2010**, *11*, 951-962.

[27]   J. Creemer, S. Helveg, G. Hoveling, S. Ullmann, A. Molenbroek, P. Sarro and H. Zandbergen, *Ultramicroscopy* **2008**, *108*, 993-998.

[28]   A. P. Hitchcock, **2008**. aXis2000 is written in Interactive Data Language (IDL). It is available free for non-commercial use from http://unicorn.mcmaster.ca/aXis2000.html (last accessed on July 26, **2014**).

[29]   Y. Liu, F. Meirer, P. A. Williams, J. Wang, J. C. Andrews and P. Pianetta, *J. Synchrotron Radiat.* **2012**, *19*, 281-287.

[30]   B. Boddenberg, G. U. Rakhmatkariev, S. Hufnagel and Z. Salimov, *Phys. Chem. Chem. Phys.* **2002**, *4*, 4172-4180.

[31]   www.iza-structure.org.

[32]   A. N. C. van Laak, S. L. Sagala, J. Zečević, H. Friedrich, P. E. de Jongh and K. P. de Jong, *J. Catal.* **2010**, *276*, 170-180.

[33]   P. Ildefonse, D. Cabaret, P. Sainctavit, G. Calas, A. M. Flank and P. Lagarde, *Phys. Chem. Miner.* **1998**, *25*, 112-121.

Chapter 6

[34]   K. Shimizu, Y. Kato, H. Yoshida, A. Satsuma, T. Hattori and T. Yoshida, *Chem. Commun.* **1999**, 1681-1682.

[35]   Y. Huang, R. Richer and C. W. Kirby, *J. Phys. Chem. B* **2003**, *107*, 1326-1337.

[36]   C. S. Blackwell and R. L. Patton, *J. Phys. Chem.* **1984**, *88*, 6135-6139.

[37]   G. Liu, M. Jia, Z. Zhou, W. Zhang, T. Wu and D. Jiang, *Chem. Commun.* **2004**, 1660-1661.

[38]   J. Sanz, J. M. Campelo and J. M. Marinas, *J. Catal.* **1991**, *130*, 642-652.

[39]   K. Reddy and C. Song, *Catal. Lett.* **1996**, *36*, 103-109.

[40]   R. Giudici, H. W. Kouwenhoven and R. Prins, *Appl. Catal. A-Gen* **2000**, *203*, 101-110.

[41]   J. Klinowski, *Prog. Nucl. Mag. Res. Sp.* **1984**, *16*, 237-309.

[42]   T.-H. Chen, B. H. Wouters and P. J. Grobet, *Eur. J. Inorg. Chem.* **2000**, *2000*, 281-285.

[43]   S. Daviero, A. Ibanez, C. Avinens, A. Flank and E. Philippot, *Thin Solid Films* **1993**, *226*, 207-214.

[44]   M. Fröba and M. Tiemann, *Chem. Mater.* **1998**, *10*, 3475-3483.

[45]   Y. Aoki, S. Hirata and H. Habazaki, *J. Electrochem. Soc.* **2011**, *158*, P41-P44.

[46]   J. Caro, M. Bülow, M. Derewinski, J. Haber, M. Hunger, J. Kärger, H. Pfeifer, W. Storek and B. Zibrowius, *J. Catal.* **1990**, *124*, 367-375.

[47]   M. J. B. Cardoso, D. D. O. Rosas and L. Y. Lau, *Adsorption* **2005**, *11*, 577-580.

[48]   A. Omegna, R. Prins and J. A. van Bokhoven, *J. Phys. Chem. B* **2005**, *109*, 9280-9283.

[49]   J. A. van Bokhoven, A. M. J. van der Eerden and D. C. Koningsberger, *J. Am. Chem. Soc.* **2003**, *125*, 7435-7442.

[50]   J. V. Bothe and P. W. Brown, *J. Am. Ceram. Soc.* **1993**, *76*, 2353-2358.

[51]   S. van Donk, A. H. Janssen, J. H. Bitter and K. P. de Jong, *Catal. Rev.* **2003**, *45*, 297-319.

[52]   J.-P. Gilson, G. C. Edwards, A. W. Peters, K. Rajagopalan, R. F. Wormsbecher, T. G. Roberie and M. P. Shatlock, *J. Chem. Soc. Chem. Comm.* **1987**, 91-92.

[53]   E. Brunner, H. Ernst, D. Freude, T. Fröhlich, M. Hunger and H. Pfeifer, *J. Catal.* **1991**, *127*, 34-41.

[54]   J. Sanz, V. Fornés and A. Corma, *J. Chem. Soc. Faraday Trans.* **1988**, *84*, 3113-3119.

[55]   G. L. Woolery, G. H. Kuehl, H. C. Timken, A. W. Chester and J. C. Vartuli, *Zeolites* **1997**, *19*, 288-296.

[56]   M. Hunger in *Catalytically active sites: generation and characterization*, *Vol. 2* Wiley-VCH: Weinheim, **2010**, pp. 493-546.

[57]   P. Wu, T. Komatsu and T. Yashima, *J. Phys. Chem.* **1995**, *99*, 10923-10931.

[58]   N. Y. Chen and F. A. Smith, *Inorg. Chem.* **1976**, *15*, 295-297.

[59]   J. Jiao, S. Altwasser, W. Wang, J. Weitkamp and M. Hunger, *J. Phys. Chem. B* **2004**, *108*, 14305-14310.

[60]   S. M. C. Menezes, V. L. Camorim, Y. L. Lam, R. A. S. San Gil, A. Bailly and J. P. Amoureux, *Appl. Catal. A-Gen* **2001**, *207*, 367-377.

[61]   T. Chevreau, A. Chambellan, J. Lavalley, E. Catherine, M. Marzin, A. Janin, J. Hemidy and S. Khabtou, *Zeolites* **1990**, *10*, 226-234.

[62]   K. J. D. MacKenzie, J. Temuujin, M. E. Smith, P. Angerer and Y. Kameshima, *Thermochim. Acta* **2000**, *359*, 87-94.

[63]   J. Oehler, *Nature* **1973**, *241*, 64-65.

[64]   O. W. Flörke and K. Langer, *Contrib. Mineral. Petr.* **1972**, *36*, 221-230.

[65]   L. Aouali, J. Teanjean, A. Dereigne, P. Tougne and D. Delafosse, *Zeolites* **1988**, *8*, 517-522.

[66]   R. Pellet, D. Casey, H. Huang, R. Kessler, E. Kuhlman, C. Oyoung, R. Sawicki and J. Ugolini, *J. Catal.* **1995**, *157*, 423-435.

[67]   D. P. B. Peixoto, S. M. Cabral de Menezes and M. I. Pais da Silva, *Mater. Lett.* **2003**, *57*, 3933-3942.

[68]   W.-G. Kim, N.-H. Kim, J.-H. Kim and G. Seo, *Kor. J. Chem. Eng.* **1999**, *16*, 392-395.

[69]   G. Caeiro, P. Magnoux, J. M. Lopes, F. R. Ribeiro, S. M. C. Menezes, A. F. Costa and H. S. Cerqueira, *Appl. Catal. A-Gen* **2006**, *314*, 160-171.

[70]   D. M. Roberge, H. Hausmann and W. F. Holderich, *Phys. Chem. Chem. Phys.* **2002**, *4*, 3128-3135.

[71]   P. J. Kooyman, P. van der Waal and H. van Bekkum, *Zeolites* **1997**, *18*, 50-53.

[72]   M. Müller, G. Harvey and R. Prins, *Micropor. Mesopor. Mater.* **2000**, *34*, 135-147.

[73]   A. Beers, J. Van Bokhoven, K. De Lathouder, F. Kapteijn and J. Moulijn, *J. Catal.* **2003**, *218*, 239-248.

[74]   T. Blasco, A. Corma and J. Martínez-Triguero, *J. Catal.* **2006**, *237*, 267-277.
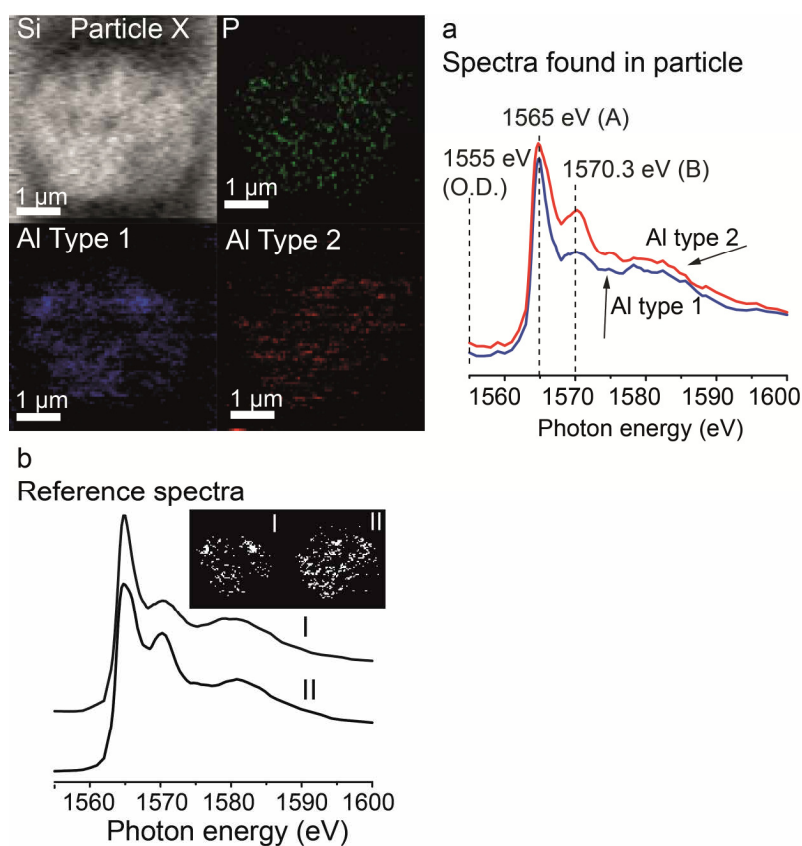
6.5 Appendix

Figure A6.1 2-D STXM results of the sample measured by soft X-ray tomography (Particle X) and presented in the main text in Figure 6.1-6.3. Top left corner shows elemental maps of the aggregate. (a) Spectra corresponding to the Al Type 1 mask (blue) and Al Type 2 mask (red). The spectra are obtained by linear regression fitting of the Al K-edge stack of Particle X using the reference spectra shown in (b). The results indicate the presence of two types of Al K-edge XANES, Al Type 1 (blue) and Al Type 2 (red). It can be observed that hotspots of Al Type 1 matches that of phosphorus hotspots. (b) Reference spectra used for the fitting. The reference spectra are taken from the *in-situ* experiment presented in the main text in Figure 6.5. I = $[MOR]_{400-P}$ after heating (more crystalline $AlPO_4$) and II = $[MOR]_{400-P}$ before heating (more amorphous $AlPO_4$). The corresponding masks were placed over the Al K-edge XANES stack map of particle X, to obtain the spectra shown in (a), by averaging XANES of pixels pooled by the masks.
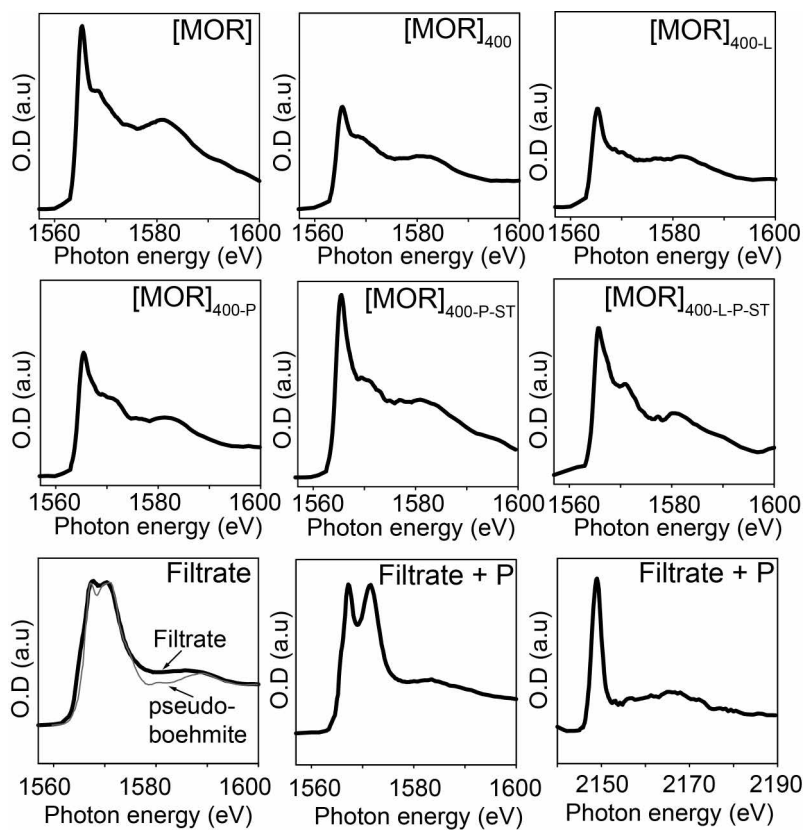
Figure A6.2 Al K-edge and P K-edge XANES of the H-mordenite samples under study.
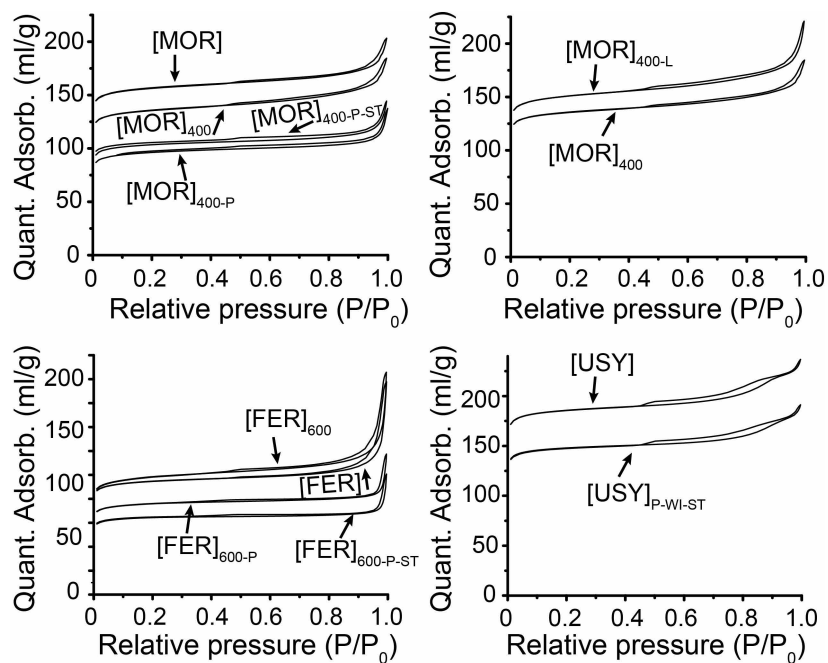
Figure A6.3 N₂ physisorption of the samples under study.
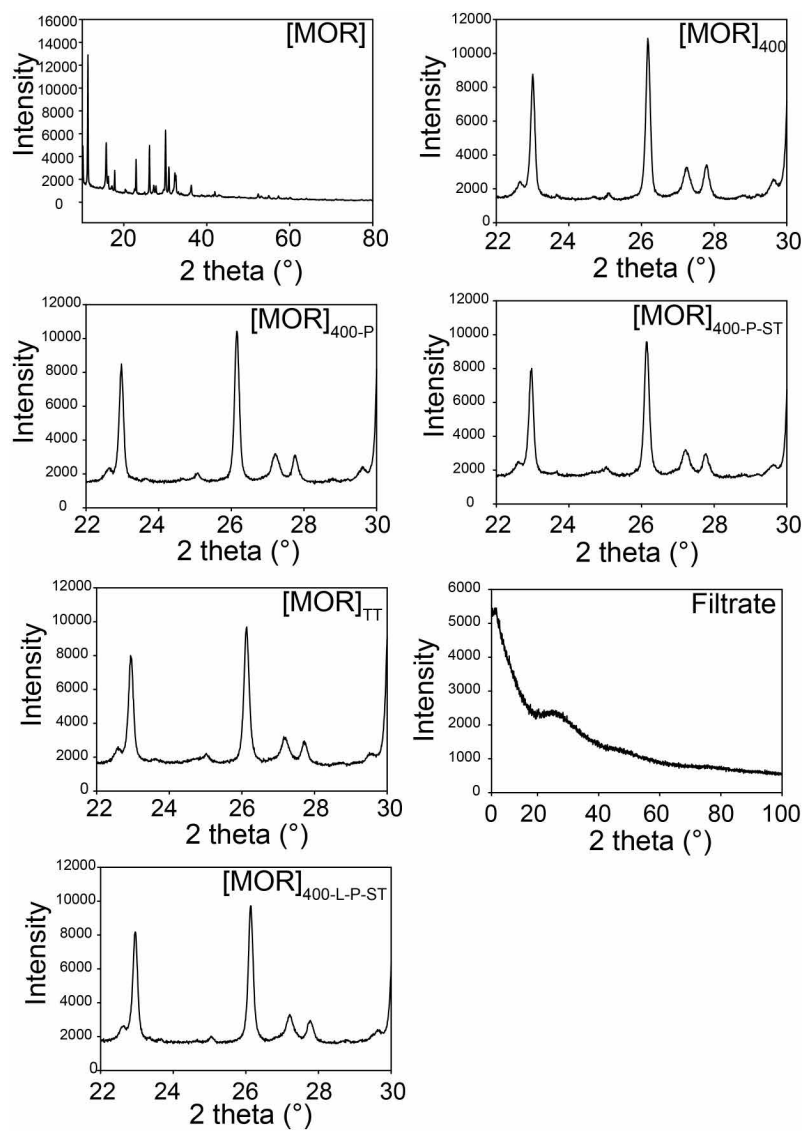
Figure A6.4 XRD diffractograms of the H-mordenite samples under study.
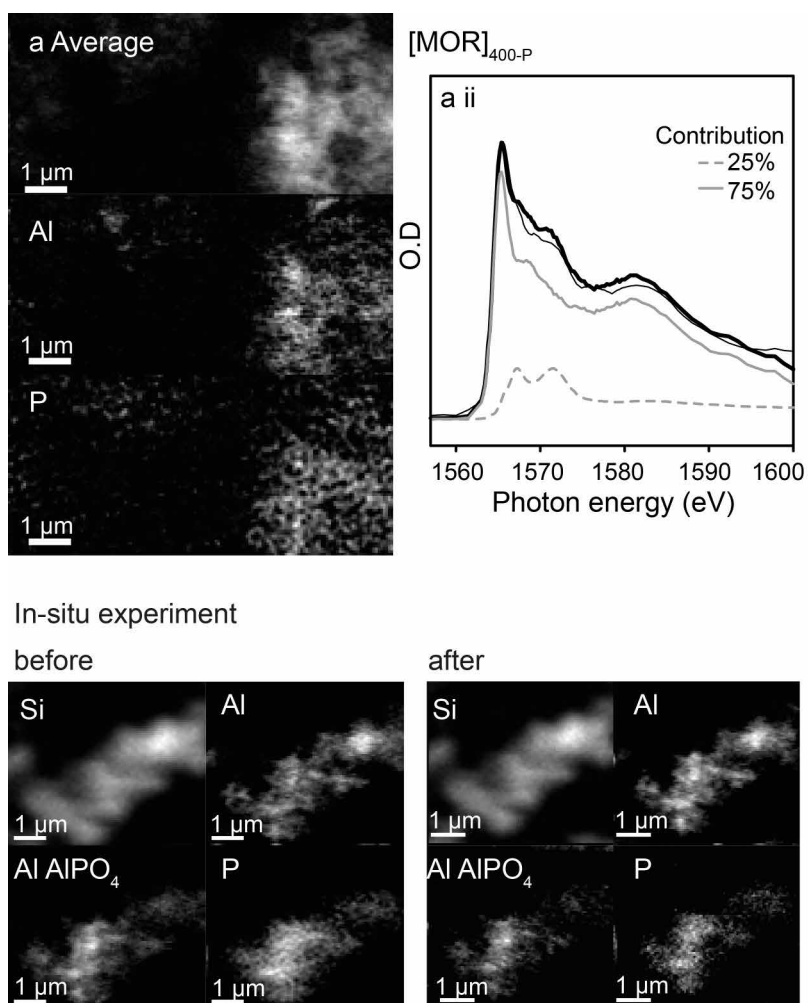
Figure A6.5 STXM results of sample [MOR]$_{400-P}$. (a) Different elemental maps. (a ii) Fit results of the Al K-edge XANES corresponding to the sample shown in (a). Fit results obtained by linear regression fitting. Thick black line = Fit result, Black thin line = Al K edge XANES, Gray = Reference 1: sample [MOR], Dashed gray = Reference 2: sample Filtrate + P. The total contribution of each spectra is given in %. (b) Overview of the elemental maps of sample [MOR]$_{400-P}$ used in the in-situ experiment after thermal treatment.
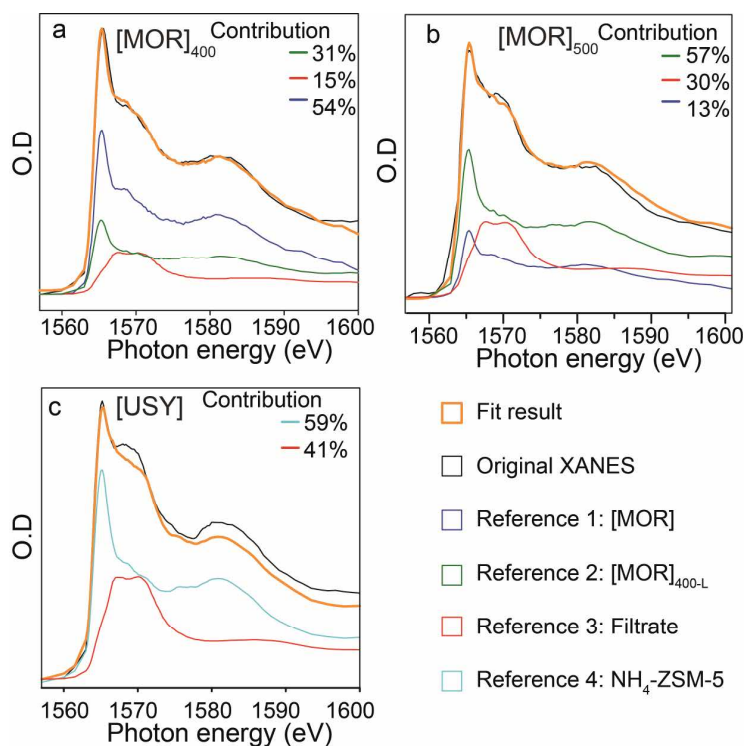
Figure A6.6 Fit results obtained by linear regression fitting the Al K- edge XANES of sample (a) [MOR]$_{400}$ and (b) H-mordenite steamed at 500 °C for 4 h. ■ = Fit result, ■ = Al K edge XANES, ■ = Reference 1: sample [MOR], ■ = Reference 2: sample [MOR]$_{400-L}$., ■ = Reference 3: sample Filtrate. The total contribution of each spectra is given in %. (c) ST[Y] ■ = Fit result, ■ = Al K edge XANES, ■ = Reference 2: sample Filtrate, ■ = Reference 4: sample NH$_4$-ZSM-5. It can be observed that while for mordenite the fits gives a good correlation, there is a component missing for [USY]. This indicates that not all EFAl in steamed zeolite Y consists of AlO(OH).
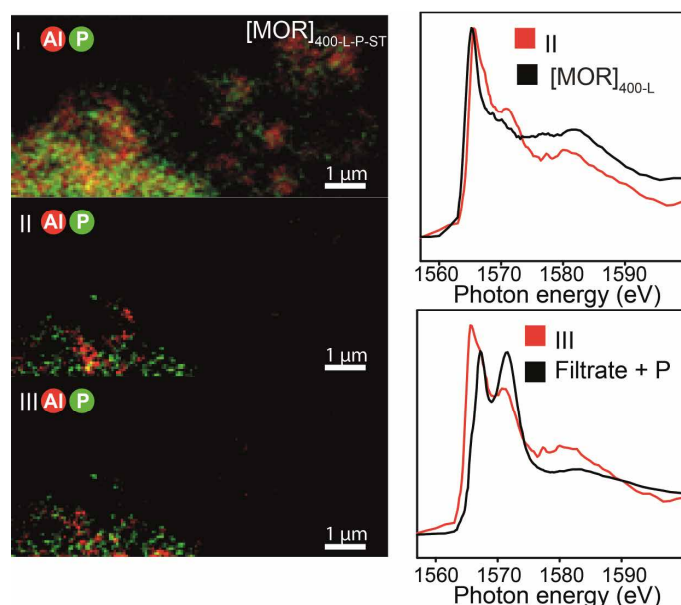
Figure A6.8 STXM elemental maps of [MOR]$_{400-L-P-ST}$. I is an overview of phosphorus and aluminum distribution. II shows only the highest optical densities of phosphorus and aluminum with a more [MOR]$_{400-L}$ character. The corresponding Al K-edge XANES to these species is shown as II. Image III shows the highest optical densities of phosphorus and aluminum with a more Filtrate + P like character. The corresponding Al K-edge XANES to these species is shown as III. Maps have been created by linear regression fitting using [MOR]$_{400-L}$ and Filtrate + P as reference spectra.
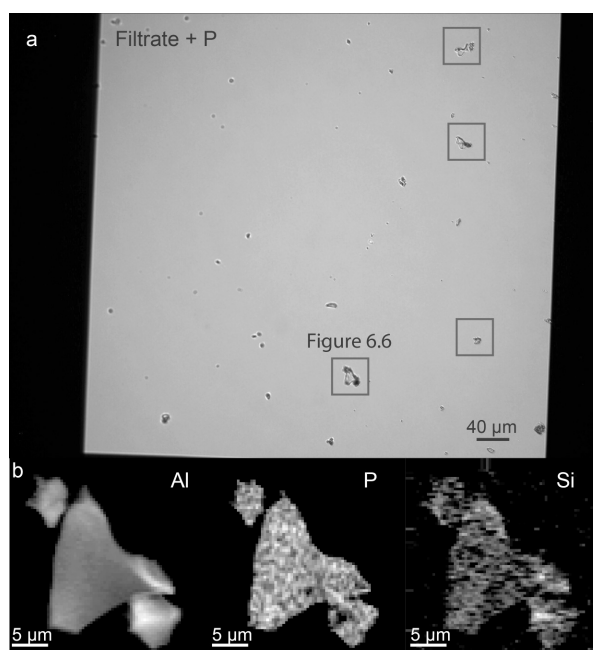
Figure A6.7 (a) Optical microscopy image of sample Filtrate + P. (b) Elemental maps of the sample in Figure 6.6.
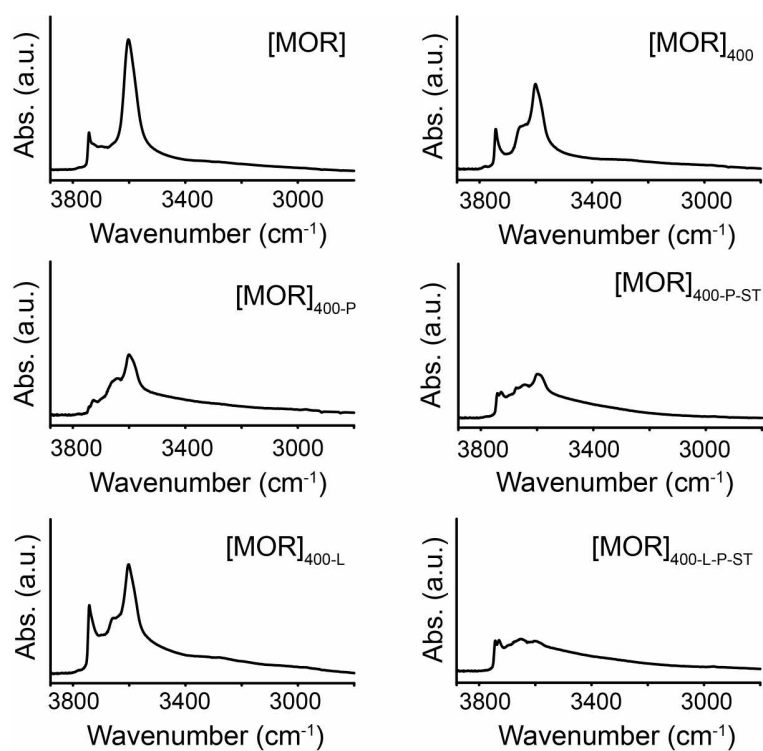
Figure A6.9 FT-IR spectra of the H-mordenite samples under study. Only the O-H stretch region is shown. Samples are baseline corrected and normalized using the zeolitic framework vibrations found at 1967 cm^{-1}, 1873 cm^{-1}, and 1637 cm^{-1}.
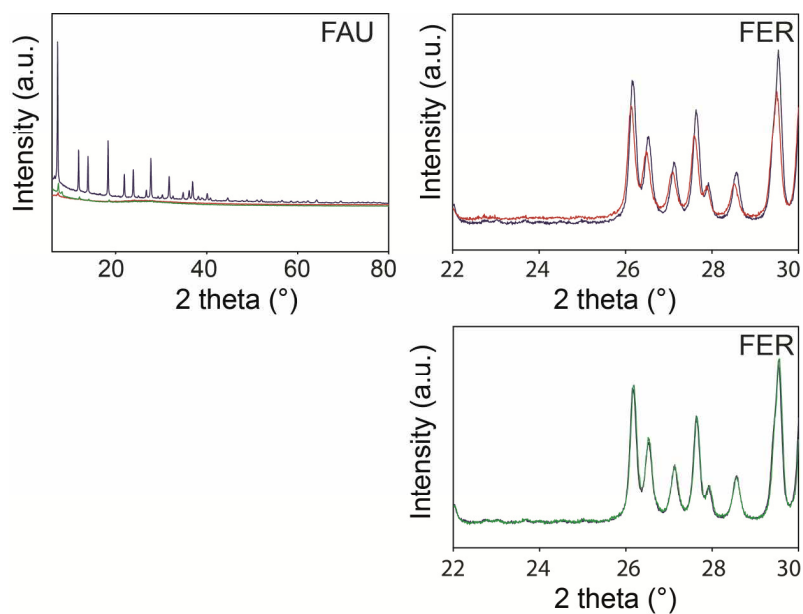
Figure A6.10 X-ray diffraction data of the materials under study. For FAU ■ = [USY], ■ = [USY]$_{P-ST}$, ■ = [USY] acid leached with 0.03 M HNO$_3$. For [FER] ■ = [FER]$_{500}$ ■ = [FER]$_{500-P-ST}$ ■ = [FER]$_{600-P-ST}$
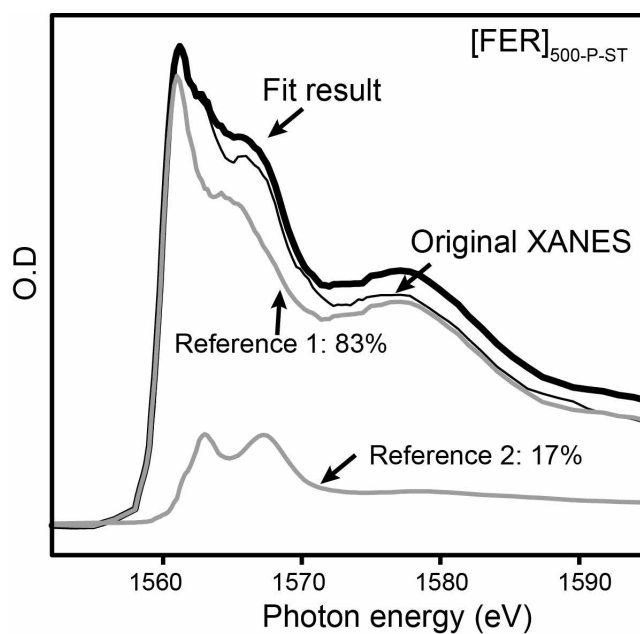
Figure A6.11 Fit results obtained by linear regression fitting the Al K- edge XANES of sample [FER]$_{500-P-ST}$. Reference 1 = sample [FER]$_{500}$, Reference 2 = sample Filtrate + P. The total contribution of each spectrum is given in %.

Summary, Concluding Remarks and Future Outlook

Biomass conversion, crude-oil cracking, and gas-to-liquid technology. Just a few of the many chemical processes where zeolites are used, or have the potential to be used as catalysts. Made from the abundant elements silicon, aluminum and oxygen, they are relatively cheap and environmentally friendly materials. In the expected transitional period where the global economy will move from fossil-based to truly sustainable resources, zeolites still have an important part to play. Therefore, it is paramount to understand the chemistry of these fascinating shape-selective 'micron-scale molecule making factories' on a fundamental level, from macro-scale to nano-scale. Insights in their morphology, accessibility, active sites, selectivity, stability and deactivation behavior will allow us to further improve and extend their use as valuable catalyst materials.

The scope of this dissertation was to elucidate only a small, but relevant part of the field of zeolite science and technology, i.e. the interaction of phosphorus with zeolites. Phosphorus can act to zeolites both as a promoter (e.g., in Fluid Catalytic Cracking (FCC) and Methanol-To-Hydrocarbons (MTH)) and as a poison (in Selective Catalytic Reduction (SCR) of exhaust gasses, such as NOx). As a promoter phosphorus is well known to improve the hydrothermal stability of zeolite H-ZSM-5. At the same time phosphorus interacts with the acid sites of zeolites, leading to a reduction in acid site number and strength. While this can be beneficial, for example in the MTH reaction, where weak acid sites are preferred, it is deleterious for SCR NOx applications. Furthermore, if phosphorus is located in the micropores of zeolites, it can either favorably alter its shape selective effects, or block micropores and reduce the overall accessibility of the zeolite material. Therefore, the main focus of this PhD thesis was to enhance the understanding of the physicochemical effects that occur upon phosphorus modification of zeolites.

More specifically, we wish to answer the following questions:

(a) What kind of bonds phosphorus forms with zeolite framework atoms?

(b) What is the nature and location of phosphorus species?

(c) How does phosphorus species influences the acidity and pore accessibility?

(d) Does the interaction between zeolites and phosphorus lead to an increased hydrothermal stability?

Answers to these important scientific questions have been sought by applying a combination of powerful characterization techniques on a wide range of differently prepared phosphated zeolite materials, including zeolite ZSM-5, Y, mordenite and ferrierite.

7.1 Summary

Many studies have already been performed on the effects of phosphorus modification of H-ZSM-5. Although there is clear consensus on the eventual decrease in strong acid site number and improved hydrothermal stability, there has been considerable ambiguity and discussion on the actual origin of these phenomena. This follows from an extensive literature survey that is presented in **Chapter 2**, where it can be read that after 30 years of research on phosphated H-ZSM-5, the existence and type of phosphorus-framework interactions are still highly debated, while the origin of newly formed weak acid sites and promoted hydrothermal stability is even more elusive. An in-depth analysis and comparison of the available characterization results is provided, which reveals universal physicochemical effects of the phosphatation process on zeolite H-ZSM-5 acid site strength, stability, accessibility and performance in hydrocarbon catalysis.

The analysis of the literature in Chapter 2 showed that most results of detailed spectroscopic investigations pointed towards interactions of phosphorus with (framework) aluminum in zeolites. Therefore, in **Chapter 3** a combined spectroscopy and micro-spectroscopy study was performed on a variety of phosphated H-ZSM-5 samples. It was found that, depending on the state of aluminum in the starting material, two clearly different interactions between phosphorus and aluminum could be observed. If aluminum was present as extra-framework aluminum (EFAl) the addition of phosphoric acid lead to the formation of an extra-framework crystalline aluminum-phosphate ($AlPO_4$) phase. However, when aluminum atoms were exclusively located

in the zeolite lattice, the presence of phosphorus would severely distort their electronic environment, possibly due to chemical interactions. Extra-framework $AlPO_4$ formation was not observed in these samples. Framework aluminum atoms that were distorted by the presence of phosphorus were not affected by a subsequent hydrothermal treatment. Phosphorus that did not interact with framework aluminum was found on the external surface as polyphosphate species that promoted zeolite aggregation.

In order to determine the nature of the interactions of phosphorus with framework aluminum, **Chapter 4** presents an extensive solid-state NMR study that was performed on H-ZSM-5, during different stages in the phosphatation process. Several interactions were identified. It was found that phosphoric acid interacts through hydrogen bonds with tetrahedrally coordinated framework aluminum (TFAl) atoms and can force TFAl atoms into an octahedral coordination. A corresponding decrease in acid site number was observed. These interactions were found to be fully reversible, as removal of phosphate species by hot water washing restored the zeolite to its original state. However, after thermal treatment irreversible phosphorus-framework bonds were formed. The gradual hydrolysis of Si-O-Al bonds during thermal treatment lead to the formation of partially dislodged $-(SiO)_{3-x}-Al-(OH)_x$ species, which reacted with H_3PO_4 to $-(SiO)_{3-x}-Al-(PO)_x$ type species. These local silico-aluminophosphate (SAPO) interfaces remain connected to the framework and could not be removed by hot water washing. As the overall charge of these species is expected to be neutral there is no need for counter-protons. Therefore, Si-O-Al bond breaking and the formation of local SAPO interfaces are the reasons for permanent acid site loss in phosphated H-ZSM-5.

With the majority of phosphorus-framework interactions being elucidated, the subsequent step was to determine if these interactions contributed to the improved hydrothermal stability in H-ZSM-5. This study is presented in **Chapter 5**. By means soft X-ray tomography and solid-state NMR spectroscopy the coordination environment and location of phosphorus and aluminum atoms in hydrothermally treated H-ZSM-5 was determined. It was established that phosphated H-ZSM-5 retains more acid sites and *n*-hexane cracking activity after steam-treatment than its non-phosphated counterpart. Additionally, there was no indication for the formation of EFAl species and the majority of the aluminum was in a highly four-coordinated state. In contrast, the hydrothermally treated H-ZSM-5 sample without phosphorus showed high amounts of EFAl species. The dealumination of steamed zeolite H-ZSM-5 resulted in an increased framework Si/Al ratio and the formation of mesopores. Conversely, no decrease in framework Si/Al ratio and mesopore formation was observed for phosphated H-ZSM-5 samples after steam treatment.

The majority of the aluminum atoms in phosphated H-ZSM-5 were found to present in the local SAPO interfaces distributed throughout the whole zeolite. Therefore, it was concluded that framework aluminum present in the local SAPO interfaces are stabilized and remain fixed in the zeolite lattice during hydrothermal treatment. Framework aluminum that was not in the vicinity of phosphorus was expelled from the framework and migrated to the external surface, where the species reacted with phosphates to form extra-framework $AlPO_4$. Washing of the sample to remove excess and reversibly interacting phosphate species lead to the retrieval of strong acid sites and renewed *n*-hexane cracking activity. Analogous to the latter effect was the disappearance of the spectroscopic signatures that correspond to TFAl species forced into octahedral coordination by phosphate species. Therefore, it appears that hydrothermal stabilization by phosphorus does not require permanent phosphorus framework interactions.

Besides an improved activity, phosphated and steamed H-ZSM-5 samples also show an increased selectivity towards propylene during *n*-hexane cracking. It is suggested that phosphate species, present in the local SAPO interfaces located in the channel intersections, form steric impediments for the formation of carbenium ions, successfully suppressing the bimolecular cracking mechanism. As a consequence, phosphated H-ZSM-5 has a product selectivity that is more similar to product distributions of medium-pore zeolites without internal cavities, such as H-ZSM-22 and H-ferrierite.

Chapter 6 focusses on the other type of phosphorus-aluminum interaction reported in Chapter 3, the formation of extra-framework $AlPO_4$ in pre-dealuminated zeolites. Moreover, in this Chapter other zeolites than H-ZSM-5 have been investigated, which are the industrially relevant MOR, FAU and FER topologies. The chapter consists of a detailed study of $AlPO_4$ formation, by means of *in-situ* scanning transmission X-ray microscopy (STXM) and soft X-ray tomography, complemented with more established bulk techniques, such as solid-state NMR. It was found that EFAl species that were extracted from steam-treated H-mordenite were amorphous aluminum oxide hydroxides. Silicon was also detected in the extra-framework aluminum phase, which indicated the presence of amorphous silica-alumina. Phosphoric acid readily reacted with the AlO(OH) species and formed an amorphous $AlPO_4$ phase. In the case of H-ferrierite, the extra-framework aluminum (EFAl) species were trapped in the ferrierite framework, and remained inaccessible to phosphoric acid. Consequently, an $AlPO_4$ phase could not form. The amorphous $AlPO_4$ phase crystalized into α-cristobalite/tridymite $AlPO_4$ during thermal treatment. It was found that while $AlPO_4$ crystallizes outside of the zeolitic channel system forming $AlPO_4$ islands, the $AlPO_4$ phase that was present in the crystal interior consisted of more aluminum atoms with a six-fold coordination. It is therefore suggested that $AlPO_4$

located in the zeolite channel system has the tendency to remain more amorphous due to spatial constraints inhibiting crystallization. Furthermore, it is proposed that the $AlPO_4$ phase is more likely to become trapped in a 1-dimensional channel system, than in a 3-dimensional channel system.

7.2 Concluding remarks

During the course of this research project a combination of spectroscopy, microscopy and catalytic testing has been performed on phosphated zeolites. Based on the results there are certain general conclusions that can be derived regarding the interplay between phosphorus and zeolite materials. First of all, the combination of soft X-ray absorption microscopy, X-ray diffraction, solid-state NMR, and FT-IR spectroscopy has resolved a number of issues in the open literature regarding the assignment of specific *spectroscopic signatures*. An overview of the signatures will be given below and will certainly be of help to researchers in the field of zeolite science and technology when interpreting their results on dealuminated and phosphated zeolites.

Secondly, a more unified view on the *various effects of phosphorus modification* on zeolites will be presented. It will be shown that the changes in the zeolite accessibility, pore-structure, acidity, stability and catalytic performance stem from (i) the presence of non-interacting phosphate species and (ii) interactions between phosphate species and the zeolitic framework. Based on this the origins of acid site loss, hydrothermal stabilization and changes in catalytic performance in phosphated zeolites will be discussed.

7.2.1 Spectroscopic signatures

Combined spectroscopy and microscopy techniques have resolved many spectroscopic signatures that are found in zeolite materials before and after phosphorus modifications. These are (1) octrahedrally coordinated framework aluminum, (2) extra-framework aluminum and (3) partially dislodged aluminum, (4) non-interacting phosphorus species, (5) extra-framework aluminum-phosphate, (6) reversible phosphorus-aluminum interactions, and (7) local silico-aluminophosphate interfaces.

7.2.1.1 *Dealuminated zeolites*

1. The combination of solid-state NMR and FT-IR spectroscopy, in addition to pyridine adsorption has shown that the octahedral aluminum that is often observed in H-zeolites is *not* extra-framework aluminum as is often suggested. As described by Woolery et al. and Van Bokhoven and co-workers these species are shown in Figure 4.15 b and d and are present at defect sites in the framework. Their octahedral coordination in hydrated form stems from a physical coordination of aluminum with three H_2O molecules and with three covalent Si-O-Al bonds. The species form Lewis acid sites when dehydrated and are located next to Si-OH groups. Therefore, the presence of these species can be deduced from (i) a sharp ^{27}Al MAS NMR resonance at 0 ppm for six-coordinated aluminum, (ii) a FT-IR band around 3720 cm^{-1}, stemming from Si-OH groups present in the channel system, (iii) an observable FT-IR band during pyridine adsorption around 1454 cm^{-1}, corresponding to coordinately bound pyridine to Lewis acid sites. Treatment with ammonia reverts the species into tetrahedrally coordinated framework aluminum as a bond with the neighboring Si-OH group is formed. Consequently, the spectroscopic signatures disappear after ammonia treatment.

2. The spectroscopic signatures for extra-framework aluminum. The results in this thesis have strongly pointed towards one dominant type of extra-framework alumina, which are amorphous aluminum oxide hydroxides. Therefore, the spectroscopic signals that are observed with ^{27}Al MAS NMR around 60 ppm, 30 ppm and 5 ppm should be attributed to amorphous AlO(OH). The resonance at 30 ppm should most likely *not* be attributed to a separate five-coordinated aluminum species as was often suggested, but to aluminum sites in AlO(OH) that are associated with H_2O.[1] Besides the three mentioned ^{27}Al MAS NMR resonances extra-framework AlO(OH) in zeolites can be recognized (i) by two peaks of equal intensity at +2.2 eV and +5 eV from the whiteline in Al K-edge XANES, and (ii) a FT-IR band at 3660 cm^{-1}. Extra-framework AlO(OH) can be removed by leaching with HNO_3 and as a consequence the spectroscopic signatures disappear.

3. The spectroscopic signatures for partially dislodged tetrahedral aluminum. Although these species are more hypothetical than the former two, there are strong indications for their existence, both experimentally and theoretically.[2] In ^{27}Al MAS NMR they can be recognized as an asymmetric resonance forming a shoulder of the resonance for TFAl species at 55 ppm. ^{27}Al MQ MAS NMR shows that the species has an isotropic chemical shift around 67 ppm with a horizontal shape along the chemical shift. This and the asymmetric shape of the 1D NMR spectra indicate that these aluminum atoms have high quadrupolar couplings and are in a highly

distorted environment. This species is different than the extra-framework Al4 (resonance 6) that can be observed in Figure 3.8 c. In FT-IR these species can be recognized as a sharp band between 3655 cm^{-1} and 3645 cm^{-1}. It is suggested the O-H stretch vibrations stem from bridging hydroxyl groups that are still present as counter charge, since in H-ZSM-5 the band is able to retain pyridine at elevated temperatures. However, in the case of H-mordenite the band has no acidic character. Al K-edge XANES resemble four-coordinated aluminum with a contribution of a peak at +6 eV and a decrease the broad peak at +15 eV, which indicates a loss of ordering of the aluminum sites. The spectroscopic signatures cannot be removed by leaching with HNO$_3$, but do disappear after phosphorus addition.

7.2.1.2 *Phosphated zeolites*

1. Spectroscopic signatures for non-interacting phosphorus species are ^{31}P MAS NMR resonances between 0 ppm and -14 ppm and resonances below -32 ppm.

2. The spectroscopic signatures of the amorphous AlPO$_4$ phases are (i) a broad ^{27}Al MAS NMR resonance around -12 ppm, (ii) a broad ^{31}P MAS NMR resonance around -15 ppm, and (iii) an Al K-edge XANES peak at +5.5 eV from the whiteline. As crystalline α-cristobalite/tridymite phase the spectroscopic signatures are (i) A sharp and symmetric ^{27}Al MAS NMR resonance around 40 ppm, (ii) a sharp ^{31}P MAS NMR resonance that can be found between -28 ppm and -31 ppm, (iii) an Al K-edge XANES with a small post-edge feature between +5.5 eV and +6.2 eV, depending on crystallinity, (iv) a FT-IR band at 3670 cm^{-1} that is attribute to P-OH groups and (v) an XRD peak around 25° 2θ.

3. Reversible phosphorus-aluminum interactions. The spectroscopic signatures for phosphorus interacting with tetrahedral framework aluminum through hydrogen bonds are (i) a broad ^{27}Al MAS NMR resonance with a chemical shift centered around 44 ppm and an identical isotropic shift as TFAl atoms at 55 ppm, (ii) a ^{31}P MAS NMR resonance at -12 ppm, (iii) a broad FT-IR band between 3520 cm^{-1} and 3200 cm^{-1}. For phosphates that replace physically coordinated H$_2$O molecules in OFAl atoms the spectroscopic signatures can be found for (i) ^{27}Al MAS NMR as sharp symmetrical resonances at -4 ppm and – 7 ppm (ii) and a ^{31}P MAS NMR resonance at -12 ppm. Finally, the ^{27}Al MAS NMR resonance at -10 ppm corresponds to TFAl atoms that are forced into an octahedral coordination by phosphate species. The ^{31}P MAS NMR signals correspond to -15 ppm. Hot water washing will remove these spectroscopic signatures.

4. The presence of local SAPO interfaces can be observed by ^{27}Al MAS NMR as a broad asymmetric resonance from 40 ppm – 10 ppm. This resonance is shown to be in a highly

distorted environment by MQ MAS NMR and has a distribution in isotropic shifts, indicating a variety of species. Al K-edge XANES micro-spectroscopy has shown that the aluminum species are in high four-coordinated environment. The resonances for ^{31}P NMR can be found between -24 ppm and -32 ppm as there is an expected variety of monodentate and bidentate phosphate interactions with aluminum. The spectroscopic signatures are not removable by hot water washing.

7.2.2 Various effects of phosphorus modification

Based on all the results obtained during the course of this PhD, supplemented with results from the open literature, we will spent the following section on discussing the overarching effects that take place during the phosphatation of zeolites.
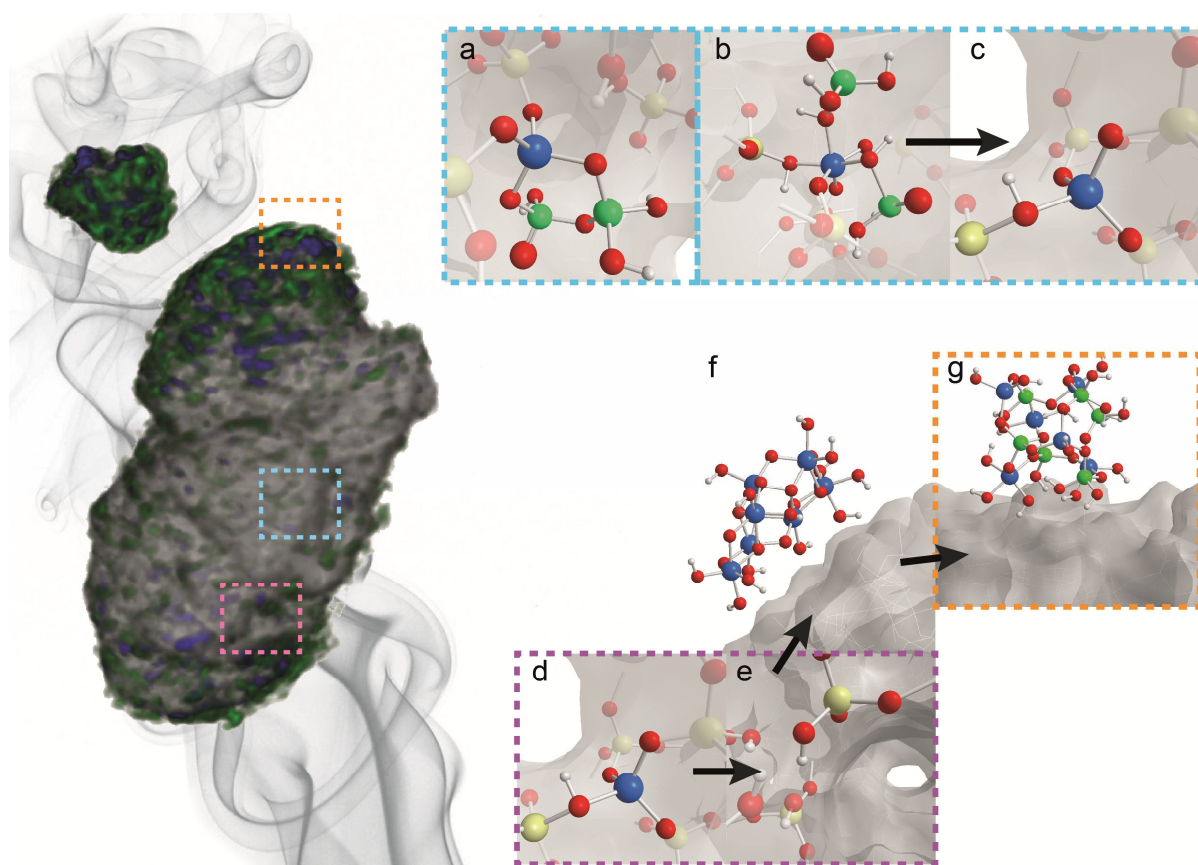
Figure 7.1 The phosphated and steamed H-ZSM-5 sample from Chapter 5 and the main effects that take place during steam treatment. (a) Local framework SAPO interfaces are not affected by steam treatment and remain in the framework. (b) Physically coordinated TFAl species are also resistant to steam, while (c) removal of the physically coordinated phosphates by hot water washing leads to acid site retrieval. (d) TFAl atoms that are not interacting with phosphorus are (e) expelled from the framework and (f) migrate as AlO(OH) species to the surface, where they (g) react with phosphates to form aluminum phosphates.

7.2.2.1 *Non-interacting phosphate species*

When there is no interaction between phosphorous and the framework, phosphorus is present as excess (poly)phosphates. These species can easily be removed by hot water washing. There is a higher amount of phosphorus present on the external surface of zeolite H-ZSM-5 and it is expected that most of these species are excess (poly)phosphates. Excess phosphorus on the external surface promotes zeolite aggregation. However, phosphorus enters micropores as well, and increased phosphorus loadings lead to a greater decrease in micropore volume. This indicates that more phosphorus enters the zeolite at higher loadings. For phosphorus weight loadings of 4 wt.%, access to acid sites is effectively blocked as followed from the results in Chapters 5 and 6. In the one-dimensional MOR topology of H-mordenite, access to all acid sites is blocked, while for the three-dimensional MFI topology of H-ZSM-5 cracking activity is lower than would be expected from the decrease in acid sites. Removal of the excess phosphorus species leads to an improved accessibility of the material as was shown in Chapter 5. Thermal treatment leads to the formation of condensed polyphosphates that are more difficult to dissolve with hot water. Therefore, high concentrations (above 4 wt.%) of excess phosphorus poisons zeolite-catalysts as these species block the accessibility of active sites.[3-5]

While non-interacting phosphorus influences the accessibility of the zeolite material, phosphorus-aluminum interactions form the key in the other physicochemical changes observed in phosphated zeolites. The following three classes in phosphorus-aluminum interactions have been found.

7.2.2.2 *Phosphorus-aluminum interactions*

1. The most well established interaction is the reaction between aluminum oxide hydroxide and phosphoric acid. The AlO(OH) species are extra-framework and form during steam treatment of zeolites in the absence of phosphorus (Figure 7.1 d-f) Phosphorus preferentially reacts with this extra-framework AlO(OH), provided the species are available and accessible in the zeolite, which leads to the formation of amorphous $AlPO_4$. This extra-framework $AlPO_4$ phase is generally found on the external surface of zeolites (Figure 7.1 g). However, in the 1-dimensional MOR framework, $AlPO_4$ is trapped in the channels, and the reduction in mesopore volume for MFI found in Chapter 3 indicates $AlPO_4$ is probably also located inside the zeolite. Thermal or hydrothermal treatment of the phase leads to the formation of crystalline $AlPO_4$.

It was shown in Chapter 3 that the H-ZSM-5 sample, which contained an $AlPO_4$ phase, was not affected by a mild hydrothermal treatment. However, if this means that $AlPO_4$ has similar

promotional effects on H-ZSM-5 as phosphates is not clear. The fact that for the studied materials AlPO$_4$ was mostly found on the external surface, would suggest the phase acts more like a binder material.

2. Reversible interactions of phosphorus with framework aluminum. We proposed three hypothetical interactions, which are (i) phosphorus-aluminum interactions through hydrogen bonds, (ii) replacement of the H$_2$O molecules by phosphates in octahedrally coordinated framework aluminum (OFAl) atoms and (iii) the physical coordination of phosphoric acid with tetrahedrally coordinated framework aluminum (TFAl) atoms, enforcing an octahedral coordination (Figure 7.1 b). It is not certain if the former two interactions have an effect on zeolite acidity or stability. However, interaction (iii) is intriguing, as it has been shown that these interactions survive thermal and severe hydrothermal treatments. Removal of these interactions leads to a reappearance of classic tetrahedrally coordinated aluminum and Brønsted acid sites (Figure 7.1 c).

3. The third and last type of interactions that were proposed are the local silico-aluminophosphate (SAPO) interfaces that form when phosphoric acid reacts with the Al-OH groups of partially dislodged aluminum species (Figure 7.1 a). These species are found throughout the whole zeolite and are expected to consist of a variety of (SiO)$_3$Al(OP(OR)), (SiO)$_2$Al(O$_2$P(OR)$_2$) or (SiO)$_2$Al(O$_2$P$_2$O$_2$(OR)$_3$) species where R = H or (poly)phosphoric acid, . Aluminum atoms in these interfaces are four-coordinated and in a highly distorted electronic environment. The results of this PhD thesis have indicated that local SAPO interfaces are partly responsible for the loss in Brønsted acid sites, the retained pore structure during hydrothermal treatment, and the change in product distribution during *n*-hexane cracking.

7.2.2.3 *Origins and consequences of the physicochemical effects of phosphatation*

We would like to argue that the attraction between phosphate and alumina is the driving force behind the loss in acid site number, the improved hydrothermal stability and changes in shape-selectivity in phosphated zeolites. Take for example, Figures 2.4 and 3.7 that are presented in Chapters 2 and 3. Here it can be observed that the presence and concentration of phosphorus has an effect on the amount of broken Si-O-Al bonds after thermal treatment, i.e. higher concentrations of phosphorus lead to more broken Si-O-Al bonds. Therefore, it appears that phosphates actively promote dealumination during thermal treatment. The loss of Si-O-Al bonds and the expected reaction of phosphorus with Si-O-Al-OH species to form neutral local SAPO interfaces leads to permanent loss of Brønsted acid sites. Furthermore, the reversible

interactions of phosphorus with framework aluminum have been shown to lead to a reduction in acid sites as well. At this moment, the exact nature of reversible acid site loss is not understood. Whether reversible or not, loss of strong Brønsted acid sites can be either promotional or poisonous, depending on the application. For metal ion-exchanged zeolites, such as Cu-SSZ-13 used in SCR of NO_x exhaust gasses in the automotive industry, the loss of Si-O-Al bonds and protons is deleterious. Due to a decrease in the overall negative charge on the framework, cationic metal species become redundant and form metal oxides.[3] However, for methanol-to-propylene applications, the decrease in acid site number and strength is beneficial. High framework Si/Al ratios have been shown to increase the propylene yield during methanol conversion and the decrease in acid site strength is thought the reduce secondary cracking reactions.[6]

The local SAPO interfaces have been found to remain unaffected during steam treatment and as aluminum remained fixed in the framework, the pore structure was better retained. However, from the literature it follows that eventually, with

Figure 7.2 (Left) different steps in the dealumination process as proposed by Malola et al.[2] (Right) Proposed steps in the dealumination process in the vicinity of phosphates, based on the suggestions of Zhuang et al. and Damodaran and co-workers.[7, 34]

prolonged steam treatments all Si-O-Al bonds of the SAPO interfaces are hydrolyzed, leading to the formation of extra-framework $AlPO_4$ (Figure 7.2). [7] Therefore, we suggest that SAPO interfaces form metastable intermediates during dealumination in the zeolite ZSM-5 channel system. We explicitly mention the zeolite ZSM-5 channel system, as it is not certain if
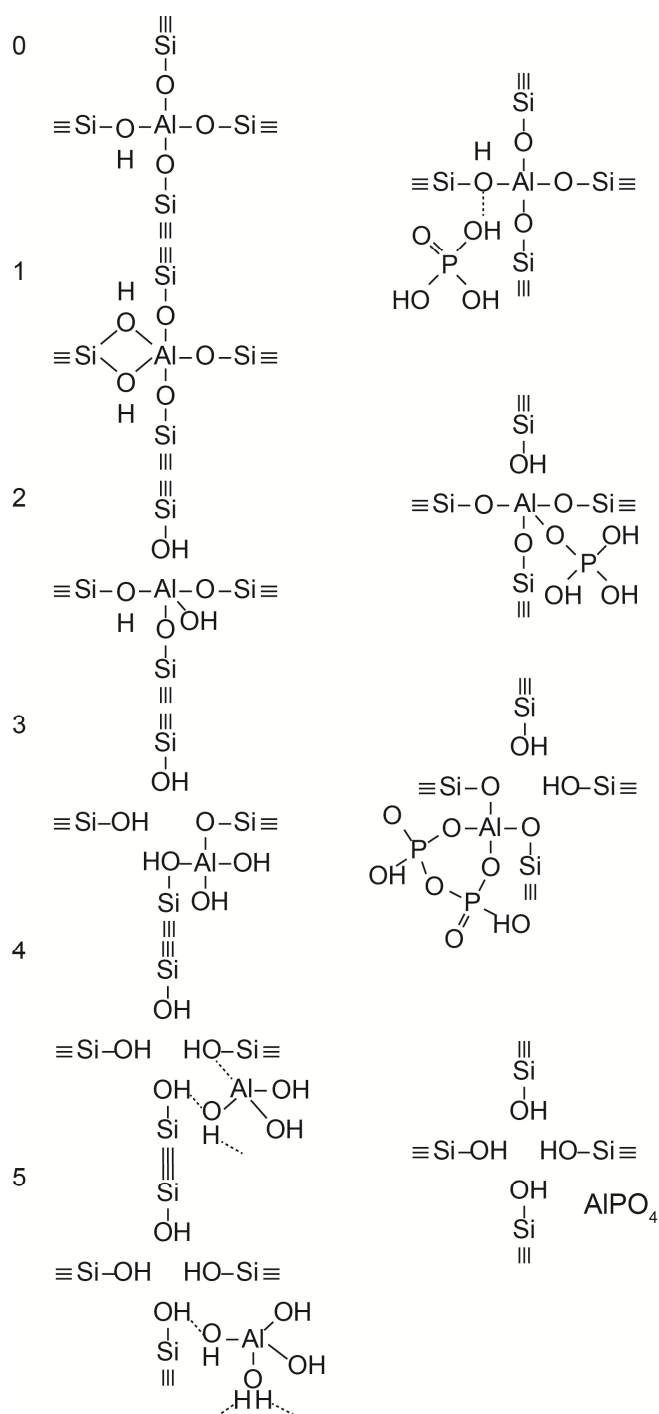
phosphorus has a similar promoting effect on different framework topologies. In a contribution from Costa and co-workers it can be seen that for zeolite H-beta and H-mordenite phosphatation followed by hydrothermal treatment only leads to extra-framework crystalline $AlPO_4$ formation, similar to the $AlPO_4$ phases we have shown in Chapter 3 and 6. Authors from the same group applied a similar steam treatment on phosphated H-ZSM-5 and the spectroscopic signatures of SAPO interfaces could be seen. This begs the question, if the local SAPO interfaces in H-ZSM-5 are inherently stabilized by the MFI channel system, while not in other topologies. It would explain why reports in the academic and patent literature on phosphorus modification are based almost exclusively on zeolite H-ZSM-5 or similar multidimensional 10-MR structures, such as ZSM-11, MCM-22, and IM-5.[8-9]

The role of reversible phosphorus-aluminum interactions on the hydrothermal stability is not clearly understood. Previous works have shown that adsorbates can change the local symmetry and coordination of T-atoms in H-ZSM-5 and $AlPO_4$ materials.[10-11] We speculate that these local changes could stabilize the T-atoms at these positions.

Phosphorus interaction with framework aluminum in H-ZSM-5 also changes the activity and product distribution in hydrocarbon cracking and the methanol-to-hydrocarbons reaction, as was discussed in Chapter 2. The decrease in the number of strong acid-sites and accessibility can be directly linked to the decrease in catalytic activity, as followed from Chapters 2 and 5. However, although the change in product distribution is often attributed to a decrease in acid site number and strength, it is likely that the shape-selective properties, which change when phosphate species are present in the micropores of zeolite ZSM-5, also have a strong effect. The product distributions found for *n*-hexane cracking in Chapter 5 resemble that of zeolites that are 1-dimensional along 10-member ring (MR) channels, such as ZSM-22 and ferrierite. Similar to these materials an increase in methane, ethane, propylene, butylene and a decrease in ethylene, butane and pentane selectivity is observed. Furthermore, if one compares the product distributions of phosphated H-ZSM-5 in the methanol-to-hydrocarbon reaction at 400 °C it can be observed that there is an increase in alkene selectivity, a decrease in aromatic selectivity and an increase in C_{3+} species.[12, 35-37] Similar results were reported for methanol-to-olefins over zeolite H-ZSM-22.[13] In the latter topology a decrease in ethylene selectivity was also observed, which was can also be found in the studies of Kaeding et al. [36] and Abubakar and co-workers [12], but not for the other works. Nevertheless, an important suggestion to make is that although phosphorus modification alters the acidity of zeolites, it appears that the change in topology plays a major role in its selective properties as well. Both for MTH and alkane cracking, phosphates present in the channel intersections - presumably connected to local SAPO

interfaces - hinder the formation of voluminous carbenium ions. In the case of the MTH process the aromatic-based hydrocarbon pool mechanism is then most probably suppressed, while in the catalytic cracking of hydrocarbons the bimolecular cracking mechanism is inhibited. Whether this is considered a promotional or poisonous effect of phosphorus depends on the desired product distributions.

7.3 Future perspectives

The concepts presented in this dissertation should allow the field to modify zeolites by phosphatation more rationally. For example, by exclusive synthesis of local SAPO interfaces in channel intersections of the MFI framework, one obtains a material that has a 3-dimensional framework structure, but not the internal cavities that promote the formation of carbenium ions. In these materials, transport of molecules is still fast, while coke formation and reaction mechanisms induced by carbenium ions are reduced.[14-15] In Chapter 4 the partially dislodged Si-O-Al-OH species formed during thermal treatment were found to act as anchoring points for phosphoric acid. Therefore, thermal treatment before phosphatation is a first step in the exclusive formation of local SAPO interfaces.

However, more precise synthesis methods should be explored than the ones applied in this PhD thesis. As we have seen in the previous Chapters, introduction of phosphoric acid under reflux conditions leads to a high concentration of (excess) phosphorus species on and close to the outer surface. Other groups have shown that hydrothermal dispersion of phosphorus leads to better distributed phosphorus species.[16-17] Janardhan et al. reported on the formation of phosphate monolayer islands, by performing phosphatation followed by an elution step.[18] The authors argued that the removal of excess phosphorus species is essential for the creation of accessible materials, with which we agree. However, elution of phosphorus by hot water washing also removes the reversible phosphorus-aluminum interactions. This can be undesirable, as we will discuss in more detail later in this section. Gas-vapor deposition as a means to introduce phosphorus has been reported to lead to more phosphorus-aluminum interactions, than a wet impregnation method [19] Furthermore, a pre-steam treatment followed by extraction of extra-framework aluminum to form mesopores, could be a method to obtain more efficient transport routes for phosphorus precursors. Extraction of extra-framework aluminum is essential in this step, if the formation of extra-framework $AlPO_4$ is not desired.
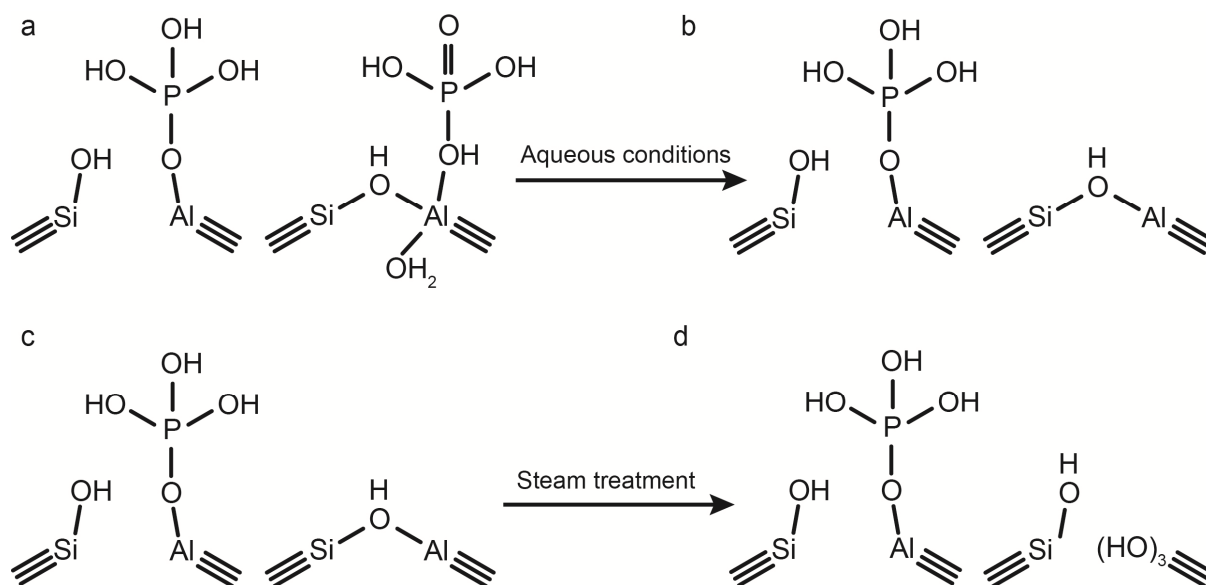
Figure 7.3 Schematic representation on the effect of aqueous conditions on permanent and reversible phosphorus-aluminum interactions

Concerning future characterization studies, we believe that the combination of soft X-ray microscopy and solid-state NMR has elucidated many phenomena, but has also reached the limits on what new information can be obtained. One of the problems is the detection limit of soft X-ray absorption microscopy for the P K-edge, which is around 2 wt.% of phosphorus. We have already seen in the previous Chapters that most of the phosphorus that could be detected was excess phosphorus, present in higher concentrations on and close to the external surface. Further investigation of samples where phosphorus is leached out, which are more relevant for catalytic applications, is therefore very difficult with soft X-ray microscopy of the P K-edge. Therefore, a suggestion would be to explore the possibility of measuring the P L_3 and L_2-edges of phosphated zeolites. The low energy of the edges (137 eV and 147 eV) allows for lower concentrations of phosphorus to be detected. However, at these low energies there is also considerable attenuation of the X-rays and it will be impossible to measure the Al K-edge and P L_3-L_2-edge in a catalyst particle of the same thickness.[20]

Another problem is considerable overlap in the spectroscopic signatures for aluminum-phosphorus types of interaction in solid-state NMR and soft X-ray absorption microscopy. For example, the ^{27}Al MAS NMR resonance of extra-framework amorphous $AlPO_4$ is at -12 ppm, while that for octahedrally coordinated framework aluminum physically coordinated to phosphates is at -10 ppm and at higher P loadings at -12 ppm. The ^{31}P MAS NMR resonances of these species are also very similar, as both are broad peaks around -15 ppm. Also 1-D ^{27}Al MAS NMR of SAPO interfaces and extra-framework $AlPO_4$ have ^{27}Al MAS NMR resonances around

40 ppm and ^{31}P MAS NMR at -30 ppm. With Al K-edge XANES it is difficult to distinguish between four-coordinated aluminum in aluminosilicate and aluminum-phosphate, as the results from Chapter 3 and 6 showed that the spectra are very similar.

In order to clearly distinguish between the phosphorus interactions with framework aluminum and extra-framework aluminum we suggest the addition of ^{27}Al $-$ ^{29}Si correlation NMR [21] in combination with ^{27}Al- ^{31}P correlation NMR. Furthermore, computational chemistry could shed new light on the actual stabilizing effect that the proposed phosphorus-aluminum interactions induce on the framework. There have been theoretical contributions to the field, but these focused on unstable Si-O-P type bonds, while Al-O-P bonds were not considered.[22-25]

Finally, besides FCC and MTH reactions, there are new promising directions where phosphated zeolites can be utilized. For example, in bio-alcohol dehydration as has been discussed in Chapter 2. By applying a phosphatation step the number and strength of acid-sites in the zeolite decreases. This makes phosphated zeolites very suitable for selective dehydration of bioalcohols to alkenes. [26-30] However, if these reactions are performed in liquid phase the reversible-interactions of phosphorus should be considered (Figure 7.3 a). The formation of H_2O during dehydration removes the reversible phosphorus-aluminum interactions, and strong acid sites will reappear, leading to undesired cracking reactions (Figure 7.3 b). A possible solution to overcome this problem is to perform a pre-leaching step followed by a post-steam treatment. In this manner, the physical interacting phosphorus is removed and the strong acid sites that form as a consequence can be removed by hydrothermal treatment (Figure 7.3 a-d). It is expected that this material has exclusively weak acid sites, which remain weak in aqueous environments.

Another key potential application for phosphated H-ZSM-5 is in catalytic fast pyrolysis of biomass.[31-32] In this process Ga-ZSM-5 is used to produce high amounts of aromatics from lignocellulosic biomass.[31] However, a major obstacle is the formation of coke during the process, which is resolved by thermal regeneration. Phosphorus stabilization could be a successful method to provide additional stability during the thermal regeneration. A study by Furomoto et al. has shown that phosphorus addition to Ga-ZSM-5 improves stability and suppresses carbonaceous deposits and gallium release from the framework during ethanol-to-propylene reactions.[33] Therefore, we hope to see future studies in the use of phosphorus as a promoter in zeolite catalyzed pyrolysis of biomass.

Chapter 7

References

[1] K. J. D. MacKenzie, J. Temuujin, M. E. Smith, P. Angerer and Y. Kameshima, *Thermochim. Acta* **2000**, *359*, 87-94.

[2] S. Malola, S. Svelle, F. L. Bleken and O. Swang, *Angew. Chem. Int. Ed.* **2012**, *51*, 652-655.

[3] I. Lezcano-Gonzalez, U. Deka, H. E. van der Bij, P. Paalanen, B. Arstad, B. M. Weckhuysen and A. M. Beale, *Appl. Catal. B-Environ* **2014**, *154*, 339-349.

[4] M. Dyballa, E. Klemm, J. Weitkamp and M. Hunger, *Chem. Ing. Tech.* **2013**, *85*, 1719-1725.

[5] G. Jiang, L. Zhang, Z. Zhao, X. Zhou, A. Duan, C. Xu and J. Gao, *Appl. Catal. A-Gen* **2008**, *340*, 176-182.

[6] J. Liu, C. Zhang, Z. Shen, W. Hua, Y. Tang, W. Shen, Y. Yue and H. Xu, *Catal. Commun.* **2009**, *10*, 1506-1509.

[7] J. Zhuang, D. Ma, G. Yang, Z. Yan, X. Liu, X. Liu, X. Han, X. Bao, P. Xie and Z. Liu, *J. Catal.* **2004**, *228*, 234-242.

[8] X. Wang, W. Dai, G. Wu, L. Li, N. Guan and M. Hunger, *Micropor. Mesopor. Mater.* **2012**, *151*, 99-106.

[9] P. Li, W. Zhang, X. Han and X. Bao, *Catal. Lett.* **2010**, *134*, 124-130.

[10] H. van Koningsveld, J. C. Jansen and H. van Bekkum, *Zeolites* **1987**, *7*, 564-568.

[11] M. P. Peeters, J. W. de Haan, L. J. van de Ven and J. H. van Hooff, *J. Phys. Chem.* **1993**, *97*, 5363-5369.

[12] S. M. Abubakar, D. M. Marcus, J. C. Lee, J. O. Ehresmann, C. Y. Chen, P. W. Kletnieks, D. R. Guenther, M. J. Hayman, M. Pavlova, J. B. Nicholas and J. F. Haw, *Langmuir* **2006**, *22*, 4846-4852.

[13] S. Teketel, S. Svelle, K.-P. Lillerud and U. Olsbye, *ChemCatChem* **2009**, *1*, 78-81.

[14] M. J. Wulfers and F. C. Jentoft, *J. Catal.* **2013**, *307*, 204-213.

[15] D. Mores, E. Stavitski, M. H. F. Kox, J. Kornatowski, U. Olsbye and B. M. Weckhuysen, *Chem. Eur. J.* **2008**, *14*, 11320-11327.

[16] X. Gao, Z. Tang, H. Zhang, C. Liu, Z. Zhang, G. Lu and D. Ji, *Kor. J. Chem. Eng.* **2010**, *27*, 812-815.

[17] X. Gao, Z. Tang, D. Ji and H. Zhang, *Catal. Commun.* **2009**, *10*, 1787-1790.

[18] H. L. Janardhan, G. V. Shanbhag and A. B. Halgeri, *Appl. Catal. A-Gen* **2014**, *471*, 12-18.

[19] Y.-J. Lee, J. M. Kim, J. W. Bae, C.-H. Shin and K.-W. Jun, *Fuel* **2009**, *88*, 1915-1921.

[20] F. M. F. de Groot, E. de Smit, M. M. van Schooneveld, L. R. Aramburo and B. M. Weckhuysen, *ChemPhysChem* **2010**, *11*, 951-962.

[21] J. W. Wiench, G. Tricot, L. Delevoye, J. Trebosc, J. Frye, L. Montagne, J.-P. Amoureux and M. Pruski, *Phys. Chem. Chem. Phys.* **2006**, *8*, 144-150.

[22] R. Lü, Z. Cao and X. Liu, *J. Nat. Gas Chem.* **2008**, *17*, 142-148.

[23] R. Lü, Z. Cao and S. Wang, *J. Mol. Struc.-THEOCHEM* **2008**, *865*, 1-7.

[24] Y. Huang, X. Dong, M. Li, M. Zhang and Y. Yu, *R. Soc. Chem. Adv.* **2014**, *4*, 14573-14581.

[25] Z. Liu, Z.-X. Chen, W. Ding, G.-J. Kang and Z. Li, *J. Mol. Struc.-THEOCHEM* **2010**, *948*, 99-101.

[26] D. Zhang, R. Wang and X. Yang, *Catal. Lett.* **2008**, *124*, 384-391.

[27] Z. Song, A. Takahashi, I. Nakamura and T. Fujitani, *Appl. Catal. A-Gen* **2010**, *384*, 201-205.

[28] K. Ramesh, L. M. Hui, Y.-F. Han and A. Borgna, *Catal. Commun.* **2009**, *10*, 567-571.

[29] N. Zhan, Y. Hu, H. Li, D. Yu, Y. Han and H. Huang, *Catal. Commun.* **2010**, *11*, 633-637.

[30] K. Ramesh, C. Jie, Y.-F. Han and A. Borgna, *Ind. Eng. Chem. Res.* **2011**, *49*, 4080-4090.

[31] J. Jae, R. Coolman, T. J. Mountziaris and G. W. Huber, *Chem. Eng. Sci.* **2014**, *108*, 33-46.

[32] G. W. Huber, S. Iborra and A. Corma, *Chem. Rev.* **2006**, *106*, 4044-4098.

[33] Y. Furumoto, Y. Harada, N. Tsunoji, A. Takahashi, T. Fujitani, Y. Ide, M. Sadakane and T. Sano, *Appl. Catal. A-Gen* **2011**, *399*, 262-267.

[34]   K. Damodaran, J. W. Wiench, S. M. Cabral de Menezes, Y. L. Lam, J. Trebosc, J. P. Amoureux and M. Pruski, *Micropor. Mesopor. Mater.* **2006**, *95*, 296-305.

[35]   J. C. Védrine, A. Auroux, P. Dejaifve, V. Ducarme, H. Hoser and S. Zhou, *J. Catal.* **1982**, *73*, 147-160.

[36]   W. W. Kaeding and S. A. Butter, *J. Catal.* **1980**, *61*, 155-164.

[37]   P. Li, W. Zhang, X. Han and X. Bao, *Catal. Lett.* **2010**, *134*, 124-130.

Nederlandse Samenvatting

Het doel van dit proefschrift was om een klein, maar belangrijk onderdeel van het zeolietchemie veld te verhelderen, namelijk de interactie van fosfor met zeolieten. In de klassieke zin zijn zeolieten mineralen die opgebouwd zijn uit tetraëders van siliciumoxide en aluminiumoxide. Typisch voor zeolieten is dat ze zeer geordende transportkanalen hebben, kleiner dan twee nanometer in diameter, zogenaamde microporiën. Hierdoor kunnen zeolieten moleculen op grootte en vorm scheiden. Daarnaast zijn zeolieten, mits ze protonen bevatten, ook zuren in vaste vorm. Door hun vormscheidende en zure eigenschappen spelen zeolieten een belangrijke rol als katalysatoren in olieraffinage. Het gebruik van zeolieten draagt bij aan een sterke verlaging van de energiekosten bij het kraken van ruwe aardolie. Ook hebben zeolieten (toekomstige) toepassingen in meer duurzame processen zoals bijvoorbeeld biomassaconversie en de omzetting van (bio)alcohol naar alkenen.

De toevoeging van fosfor aan zeolieten kan zowel een positief als negatief effect hebben op de katalytische eigenschappen van zeolieten. Zo verbetert fosfor de stabiliteit van zeolieten in kraakreacties en selectiviteit in alcohol-naar-alkeen omzetting, maar vergiftigt fosfor zeolieten bij gebruik als katalysator in de selectieve katalytische reductie van NO_x in uitlaatgassen. Het is welbekend dat de toevoeging van fosfor leidt tot een vermindering van het aantal zure groepen in een zeoliet, waarbij tegelijkertijd de gemiddelde zuursterkte van deze groepen afneemt. Ook de aanwezigheid van fosfaten in de microporiën kan leiden tot verandering in de vormscheidende eigenschappen van de zeoliet. Daarnaast leidt in een aantal gevallen de toevoeging van fosfor aan zeolieten tot een verbetering van de stabiliteit in een waterig milieu en hoge temperatuur, zogenaamde hydrothermale condities. Dit laatste effect is zeer gewenst, omdat het de katalytische levensduur van zeolieten aanzienlijk verbeterd.

Hoewel de genoemde effecten van fosfor op zeolieten bekend en uitvoerig beschreven zijn, worden de achterliggende mechanismes van fosfor-zeoliet interacties veel minder goed begrepen. Aangezien het te verwachten valt dat een fundamenteler begrip van fosfor-zeoliet interacties een verklaring biedt voor de veranderingen in eigenschappen, ligt de focus van dit proefschrift op het verhelderen van de fysicochemische effecten die optreden bij de modificatie van zeolieten met fosfor.

Om dit doel te bereiken is er een combinatie van een aantal krachtige karakteriseringstechieken toegepast op een reeks van verschillend bereide gefosfateerde zeolieten, zoals zeoliet ZSM-5, Y, mordeniet en ferrieriet.

In de uitgebreide literatuurstudie uitgevoerd in **Hoofdstuk 2**, valt te lezen dat er na meer dan 30 jaar van onderzoek op gefosfateerde zeoliet H-ZSM-5 nog steeds geen consensus is over hoe en of fosfor-zeoliet verbindingen bestaan. Daardoor blijven de oorzaken van de verbeterde hydrothermale stabiliteit en verminderde zuursterkte nog steeds ongrijpbaar. Desondanks laat de diepgaande analyse en vergelijking van de in de literatuur verkrijgbare karakteriseringsresultaten zien dat er wel degelijk universele fysicochemische effecten optreden bij de fosfatering van zeoliet H-ZSM-5. Met name op het gebied van zure groepen, zuursterkte, toegankelijkheid en werking in koolwaterstofkatalyse zijn er generieke conclusies te trekken.

De literatuurstudie van Hoofdstuk 2 liet zien dat de resultaten van de meest gedetailleerde spectroscopische onderzoeken wezen op verbindingen tussen fosfor en aluminium. Daarom is in **Hoofdstuk 3** een gecombineerde spectroscopische en micro-spectroscopische studie uitgevoerd op verschillende gefosfateerde H-ZSM-5 monsters. Hierin is gevonden dat, afhankelijk van de toestand van aluminium in het startmateriaal, twee duidelijk verschillende fosfor-aluminium verbindingen gevormd worden. Als aluminium niet meer vastzit in het zeoliet-raamwerk (*extra-framework aluminum,* ofwel EFAl) leidt de toevoeging van fosfor tot de vorming van een nieuwe kristallijne aluminium-fosfaat ($AlPO_4$) fase. Deze $AlPO_4$ fase bevindt zich buiten het zeoliet-raamwerk. Echter, als tetrahedraal geconfigureerd aluminium (*tetrahedrally coordinated framework aluminum*, ofwel TFAl) voor het toevoegen van fosfor exclusief vastzit in het zeoliet-raamwerk wordt hun elektronische omgeving wel verstoord door de aanwezigheid van fosfor (mogelijk door chemische interactie), maar wordt een $AlPO_4$ fase niet gevormd. Raamwerk-aluminium dat een verstoring ondervindt door de aanwezigheid van fosfor blijft onaangetast na een behandeling met stoom. Fosfor dat geen interactie met aluminium heeft is voornamelijk aanwezig op het externe oppervlak van de zeoliet als (poly)fosfaat verbindingen die de aggregatie van zeolietkristallen bevorderde.

Om de aard van de interacties van fosfor met raamwerk-aluminium te bepalen, is in **Hoofdstuk 4** een uitgebreide vaste-stof NMR studie verricht, waarin zeoliet H-ZSM-5 tijdens verschillende fases van het fosfateringsproces onderzocht is. Hierdoor zijn verschillende interacties gevonden. Ten eerste bleek dat fosforzuur interactie heeft met raamwerk-aluminium door middel van waterstofbruggen en dat tetrahedraal geconfigureerd raamwerk-aluminium in een octrahedrale configuratie gedwongen kan worden door fosforzuur. Een corresponderende

afname in zure groepen werd ook gevonden. Het bleek dat de interacties met fosforzuur volledig reversibel zijn, aangezien wassen met heet water de fosfaatgroepen weer verwijdert en de zeoliet laat terugkeren in zijn originele staat. Echter, na een behandeling in hoge temperatuur en lucht ontstaan er onomkeerbare interacties tussen fosfor en raamwerk-aluminium. De stapsgewijze hydrolyse van Si-O-Al bindingen tijdens de hoge temperatuurbehandeling leidt tot de vorming van gedeeltelijk loszittende $-(SiO)_{3-x}-Al-(OH)_x$ verbindingen, die vervolgens kunnen reageren met fosforzuur tot $-(SiO)_{3-x}-Al-(PO)_x$ verbindingen. Deze plaatselijke aanrakingspunten tussen fosfor, aluminium en silicium, zogenoemde silico-aluminofosfaat (SAPO) raakvlakken, blijven verbonden aan het zeoliet-raamwerk en kunnen niet verwijderd worden door wassen met heet water. Aangezien de netto lading op deze verbindingen neutraal zou moeten zijn, is het niet te verwachten dat de SAPO raakvlakken een zuur karakter hebben. De oorzaken voor het blijvende verlies van sterke zure groepen in gefosfateerde H-ZSM-5 zijn dus zowel het breken van Si-O-Al verbindingen tijdens hoge temperatuur behandeling, als de vorming van de SAPO raakvlakken.

Nadat een in Hoofdstuk 4 een deel van de fosfaat-zeoliet interacties verhelderd waren, was de volgende stap om te bepalen of deze interacties bijdragen aan de verbeterede hydrothermale stabiliteit in gefosfateerde H-ZSM-5. Deze studie is beschreven in **Hoofdstuk 5**. Door middel van Röntgenstralingstomografie en vaste stof NMR spectroscopie kon de configuratie, omgeving en locatie van fosfor en aluminium atomen in gestoomde zeoliets H-ZSM-5 bepaald worden. Er werd vastgesteld dat H-ZSM-5 meer zure groepen behoudt na een hydrothermale behandeling als deze is voorbehandeld met fosfor. Daarbij was er bij het voorbehandelde materiaal ook geen indicatie voor de vorming van EFAl verbindingen en het grootste deel van het aluminium had een coördinatiegetal van vier. Als H-ZSM-5 geen fosfor bevat leidt de stoombehandeling tot grote hoeveelheden EFAl. Deze zogenoemde dealuminering van zeoliet H-ZSM-5 resulteert in een toename van de Si/Al verhouding in het raamwerk en de vorming van mesoporiën. In de aanwezigheid van fosfor vonden laatstgenoemde effecten tijdens een stoombehandeling niet plaats.

De meerderheid van de aluminium atomen in gefosfateerde H-ZSM-5 zijn aanwezig in de SAPO raakvlakken en verspreid door het gehele kristal. Er werd geconcludeerd dat raamwerk-aluminium dat gedeeltelijk verbonden is met fosfaatgroepen gestabiliseerd wordt en in het kristalrooster blijft vastzitten tijdens hydrothermale condities. Raamwerk-aluminium dat niet in de aanwezigheid van fosfor is wordt wel uit het kristalrooster verwijderd tijdens hydrothermale condities en migreert vervolgens naar het externe oppervlak van de zeoliet waar het reageert met fosfaatgroepen tot $AlPO_4$.

Na het stomen kan een gedeelte van de fosforverbindingen verwijderd worden door te wassen met heet water. Dit leidt tot de gedeeltelijke terugkeer van sterke zure groepen en hernieuwde katalytische activiteit in het kraken van *n*-hexaan. Overeenkomend met deze laatstgenoemde effecten was de verdwijning van aluminium groepen die in een octahedrale configuratie waren gedwongen door fosfor. Deze observaties lijken erop te duiden dat de verbetering van de hydrothermale stabiliteit niet per se permanente fosfor-aluminium bindingen vereist.

Naast een verbeterde activiteit lieten de gefosfateerde en gestoomde ZSM-5 monsters ook een verbeterde selectiviteit voor propyleen zien tijdens het kraken van *n*-hexaan. De suggestie is dat fosfaatverbindingen, al dan niet in SAPO raakvlakken, die aanwezig zijn op de plekken waar zeolietkanalen elkaar kruisen, een hindernis vormen voor de vorming van carbeniumionen, waardoor het klassieke kraakmechanisme wordt onderdrukt. Hierdoor heeft gefosfateerde H-ZSM-5 een verdeling van reactieproducten, die lijkt op die van vergelijkbare zeolieten zonder kruisende 10-MR kanalen, zoals H-ZSM-22 en H-ferrieriet.

Hoofdstuk 6 richt zich op het andere type fosfor-aluminium interactie dat beschreven werd in Hoofdstuk 3, namelijk de vorming van een $AlPO_4$ fase buiten het kristalrooster van de zeoliet.. Daarbij zijn in dit hoofdstuk ook andere type zeolieten dan alleen H-ZSM-5 onderzocht, namelijk de industrieel toegepaste MOR, FAU en FER topologiën. Het hoofdstuk bevat een gedetailleerde studie naar de vorming van $AlPO_4$, door middel van *in-situ* Röntgenstraling absorptie micro-spectroscopie (STXM) en Röntgenstralingstomografie, aangevuld met meer gevestigde technieken, zoals vaste stof NMR. Er werd gevonden dat EFAl verbindingen die uit gestoomde H-mordeniet geëxtraheerd werden, bestaan uit amorfe aluminium zuurstof hydroxides. Silicium werd ook gevonden in de EFAl fase, wat de aanwezigheid van amorfe silica-alumina aangeeft. Fosforzuur reageert direct met de AlO(OH) fase tot een amorfe $AlPO_4$ fase. In het geval van H-ferrieriet zijn de EFAl verbindingen opgesloten in het FER raamwerk en zijn ze ontoegankelijk voor fosforzuur. Daardoor kon in het geval van H-ferrieriet een $AlPO_4$ fase niet gevormd worden. Tijdens verhitting op hoge temperatuur kristalliseert de amorfe $AlPO_4$ fase uit in α-cristoballiet/tridymiet $AlPO_4$. Er werd geobserveerd dat de $AlPO_4$ fase aan het externe oppervlak van de zeoliet zeer kristallijn is na verhitting, terwijl de $AlPO_4$ fase in de zeoliet meer aluminium met een amorf karakter behoudt. Een mogelijke verklaring is dat $AlPO_4$ dat aanwezig is in de zeolietkanalen de neiging heeft om amorf te blijven, doordat ruimtegebrek de kristalgroei afremt. Daarnaast werd er gesuggereerd dat het waarschijnlijker is dat de $AlPO_4$ fase vast komt te zitten in een 1-dimensionaal kanaalsystem, dan in een 3-dimensionaal kanaalsysteem.

List of Abbreviations

3Q	Triple quantum
a.u.	Arbitrary units
Al4	Four-coordinated aluminum
Al5	Five-coordinated aluminum
Al6	Six-coordinated aluminum
$AlPO_4$	Aluminum-phosphate
CLS	Canadian Light Source
CP	Cross-polarization
CPB	Cetylpyridiniumbromide
DFT	Density functional theory
DPP	Diphenylphosphine
e	(Phosphorus is) eluted
EDTA	Ethylenediaminetetraacetic acid
EFAl	Extra-framework aluminum
FAU	Framework topology of zeolite Y
FCC	Fluid catalytic cracking
FER	Framework topology of zeolite ferrierite
FID	Flame ionized detector
FT-IR	Fourier transform infrared
HETCOR	Hetero-correlation
HT	Hydrothermal treatment
ICP-OES	Inductively coupled plasma - optical emission spectrometry
INEPT	Insensitive nuclei enhanced by polarization transfer

IWI	Incipient wetness impregnation
IZA	International zeolite association
MAS	Magic angle spinning
MFI	Framework topology of zeolite ZSM-5
MOR	Framework topology of zeolite mordenite
MQ	Multiple quantum
MR	Member ring
MTH	Methanol-to-hydrocarbons
MTO	Methanol-to-olefins
NMR	Nuclear magnetic resonance
O.D.	Optical density
OAl	Octahedrally coordinated aluminum
OFAl	Octahedrally coordinated framework aluminum
P/Al ratio	Atomic phosphorus to aluminum ratio
Pyr+	Pyridinium ion
SAPO	Silico-aluminophosphate
SCR	Selective catalytic reduction
SEM	Scanning electron microscopy
Si/Al ratio	Atomic silicon to aluminum ratio
ST	Steam treated
STXM	Scanning transmission X-ray microscopy
T-atom	Tetrahedral atom in zeolite framework, e.g. silicon or aluminum
TCD	Thermal conductivity detector
TFAl	Tetrahedrally coordinated framework aluminum
TFAldis	Tetrahedrally coordinated framework aluminum in a distorted environment
TFSi	Tetrahedrally coordinated framework silicon
TMP	Trimethylphosphine

List of Abbreviations

TMPT	Ttrimethylphosphite
TPD	Temperature programmed desorption
TPP	Triphenylphosphine
TPR	Temperature programmed reaction
TT	Thermal treatment/Thermally treated
USY	Ultra-stable Y
UV-Vis	Ultra-violet and visible light
WI	Wet impregnation
XANES	X-ray absorption near-edge fine structure
XPS	X-ray photoelectron spectroscopy
XRD	X-ray diffraction
ZSM-22	Zeolite Standard Oil Company of New York Mobil 22
ZSM-5	Zeolite Standard Oil Company of New York Mobil 5

List of Publications and Presentations

This thesis is based on the following publications:

H. E. van der Bij, L. R. Aramburo, B. Arstad, J. J. Dynes, J. Wang and B. M. Weckhuysen, Phosphatation of Zeolite H-ZSM-5: A Combined Microscopy and Spectroscopy Study, *ChemPhysChem* **2014**, *15*, 283-292.

H. E. van der Bij and B. M. Weckhuysen, Local Silico-Aluminophosphate Interfaces within Phosphated H-ZSM-5 Zeolites, *Phys. Chem. Chem. Phys.* **2014**, *16*, 9892-9903.

H. E. van der Bij, F. Meirer, S. Kalirai, J. Wang and B. M. Weckhuysen, Hexane Cracking over Steamed Phosphated Zeolite H-ZSM-5: Promotional Effect on Catalyst Performance and Stability, *Chem. Eur. J.*, in press (Hot Paper, Back Cover Story)

H. E. van der Bij, D. Cicmil, J. Wang, F. Meirer, F.M.F. de Groot and B. M. Weckhuysen, Aluminum-Phosphate Binder Formation in Zeolites as Probed with X-ray Absorption Microscopy, submitted.

H. E. van der Bij and B. M. Weckhuysen, The Good or the Bad Guy? On the Chemistry between Phosphorus and Zeolite-based Catalysts?, in preparation.

Other publications by the author:

L. Karwacki, H. E. van der Bij, J. Kornatowski, P. Cubillas, M. R. Drury, D. A. M. de Winter, M. W. Anderson and B. M. Weckhuysen, Unified Internal Architecture and Surface Barriers for Molecular Diffusion of Microporous Crystalline Aluminophosphates, *Angew. Chem. Int. Ed.* **2010**, *49*, 6790-6794.

I. L. C. Buurmans, F. Soulimani, J. Ruiz-Martínez, H. E. van der Bij and B. M. Weckhuysen, Structure and Acidity of Individual Fluid Catalytic Cracking Catalyst Particles Studied by Synchrotron-based Infrared Micro-spectroscopy, *Micropor. Mesopor. Mater.* **2013**, *166*, 86-92.

Q. Qian, J. Ruiz-Martínez, M. Mokhtar, A. M. Asiri, S. A. Al-Thabaiti, S. N. Basahel, H. E. van der Bij, J. Kornatowski and B. M. Weckhuysen, Single-Particle Spectroscopy on Large SAPO-34 Crystals at Work: Methanol-to-Olefin versus Ethanol-to-Olefin Processes, *Chem. Eur. J.* **2013**, *19*, 11204-11215.

List of Publications and Presentations

I. Lezcano-Gonzalez, U. Deka, H. E. van der Bij, P. Paalanen, B. Arstad, B. M. Weckhuysen and A. M. Beale, Chemical Deactivation of Cu-SSZ-13 Ammonia Selective Catalytic Reduction (NH_3-SCR) Systems, *Appl. Catal. B-Environ.* **2014**, *154*, 339-349.

Oral presentations by the author:

H. E. van der Bij, L. R. Aramburo, B. Arstad, J. J. Dynes, J. Wang and B. M. Weckhuysen, Multi-Faceted Spectroscopy Reveals H-ZSM-5 Phosphatation Pathways, 23rd North American Catalysis Society Meeting, June **2013**, Louisville, Kentucky, USA.

H. E. van der Bij, L. R. Aramburo, B. Arstad, J. J. Dynes, J. Wang and B. M. Weckhuysen, Multi-Faceted Spectroscopy Reveals H-ZSM-5 Phosphatation Pathways, 17th International Zeolite Conference, July **2013**, Moscow, Russia.

H. E. van der Bij and B. M. Weckhuysen, Local Silico-Aluminophosphate Interfaces within Phosphated H-ZSM-5 Zeolites, Netherlands Catalysis and Chemistry Conference XV, March **2014**, Noordwijkerhout, the Netherlands.

H. E. van der Bij, B. M. Weckhuysen, Local Silico-Aluminophosphate Interfaces within Phosphated H-ZSM-5 Zeolites, British Zeolite Association Spring Meeting 2014, April **2014**, Glasgow, UK.

Poster presentations by the author:

H. E. van der Bij, L. Karwacki, J. Kornatowski and B. M. Weckhuysen, The Effect of Framework Atoms on the Intergrowth Architecture in MeAlPO-5 as Studied by Confocal Fluorescence Microscopy, Netherlands Catalysis and Chemistry Conference XV, March **2009**, Noordwijkerhout, the Netherlands.

L. Karwacki, H. E. van der Bij, J. Kornatowski, P. Cubillas, M. R. Drury, D. A. M. de Winter, M. W. Anderson and B. M. Weckhuysen, Unified Internal Architecture and Surface Barriers for Molecular Diffusion of Microporous Crystalline Aluminophosphates, International Zeolite Association Pre-Conference School, June **2010**, Maiori, Italy.

H. E. van der Bij, L. R. Aramburo, B. Arstad, J. J. Dynes, J. Wang and B. M. Weckhuysen, Phosphatation of H-ZSM-5: A combined STXM, MAS NMR and FTIR study, 7th International Symposium on Acid-Base Catalysis, May **2013**, Tokyo, Japan.

H. E. van der Bij and B. M. Weckhuysen, Local Silico-Aluminophosphate Interfaces within Phosphated H-ZSM-5 Zeolites, BASF Research Forum 2014, March **2014**, Antwerpen, Belgium.

Dankwoord

In dit laatste gedeelte zou ik graag de mensen willen bedanken die in meer of mindere mate hebben bijgedragen aan de totstandkoming van dit proefschrift.

Uiteraard mijn promotor Bert Weckhuysen. **Bert**, ontzettend bedankt voor je vertrouwen. Van jou heb ik geleerd wat het betekent om tegelijkertijd vrijheid en verantwoordelijkheid te hebben, en hoe leuk dat kan zijn. Bedankt voor al je input, het overzicht en de vergezichten. Bedankt voor je steun als de zaken minder goed liepen. Bedankt ook voor alle reizen en trips die ik mocht maken, dat waren verrijkende ervaringen. Ik vond het een zeer plezierige samenwerking, waar ik met een erg goed gevoel op terugkijk.

For their scientific contributions to this thesis I would like to thank my co-authors. **Luis**, thanks for introducing me to the world of STXM, paving the way for its use on zeolites and teaching me some important Spanish words. The smoke and coffee breaks during our night shifts were always great moments of reflection. **Bjørnar**, thanks for introducing me and helping me with all the solid-state NMR at the start of my thesis. Your enthusiastic help and experiments made the whole thesis go into the direction it eventually went. **Jian** and **Jay**, many thanks for your patience and help during the many visits I made to your beamline. Of course I also have to thank **Chithra** and **Yingshen** in this respect. Without the results from the CLS, there would simply be no thesis. **Sam**, thanks for the Avizo crash course and all the STXM feedback. On a more personal note, I think I won that fight! **Florian**, I really appreciated your help and discussions on the statistical analysis of visual data. That was really fascinating science. Too bad it was quite close to the end of my contract. **Frank**, bedankt dat ik deel kon uitmaken van het in-situ STXM team. Het behalen van resultaten was niet gemakkelijk, maar uiteindelijk is er toch wel iets moois uitgekomen. **Dimitrije**, thanks for your great help with those tedious tomography experiments. Also, thanks for all the laughs we had during the nightshifts and your healthy patriotism.

Besides the co-authors there are also other people who have contributed to the chapters in this thesis. **Inés Lezcano** thank you so much for the discussions on, and tips for the interpretation and quantification of solid-state NMR spectroscopy. **Peter de P.** hartelijk dank voor al het advies op IR gebied! All the people who accompanied me on synchrotron trips: **Korneel** ik vond onze beamtrips altijd erg gezellig, alle restaurants in Saskatoon hebben we in elk geval wel gehad. Ook nog bedankt voor het rondduwen van m'n rolstoel op het vliegveld.

Dankwoord

Mustafa, het was spannend bij de douane met onze baarden op de terugweg. Hopelijk geef je honkbal nog eens een kans. **Joe**, many thanks for your dedicated help and the jolly good fun on our beamtrips. To reminisce: Jeopardy, baseball, Outhere Brothers and Beaver creek. **Zoran,** the prince of micro-spectroscopy, thanks for all the inspiration and discussions on 'life as a PhD'. De volgende generatie zeolietenexperts: **Joris**, superbedankt! We hebben gelachen en wie weet ronden we ooit dat paper af. **Ramon**, bedankt dat je je over m'n spullen hebt willen ontfermen. Of course, I shouldn't forget to mention my first beam-team **Inge**, **Javi**, and **Fouad**. Maybe lame to say, but I thought we had some good chemistry! The trips to the USA were the highlight of course, e.g. the PT-pickup from the airport, the long waits for my Mexican food, visiting New York, nights of debauchery with cassis, modern art and the flatiron incident.

De vaste staf en andere universiteitsmedewerkers wil ik uiteraard ook graag bedanken. Van het secretariaat, **Dymph** en indertijd **Monique**, later ook nog **Inez** en **Iris**, allemaal hartelijk dank voor jullie hulp en ondersteuning. De technische staf, **Ad M.**, **Ad v/d E.**, **Marjan**, **Rien**, **Vincent** en later **Pascal**, **Herrick** en **Oscar**. Vooral **Ad M.**, erg bedankt voor je hulp bij allerhande projecten, waaronder de steam-setup en operando UV-vis/GC. De volgende heren van de glasblazerij wil ik ook nog even noemen, **Peter**, **Matthijs**, **Henkjan**, bedankt voor de koffie, de ontwikkeling van de IR-cel en alle andere keren dat jullie weer eens wat van m'n glaswerk repareereden (wat nooit lang duurde). **Harry**, hopelijk hebben onze dagjes-studeren heel wat scholieren doen besluiten om scheikunde te gaan studeren. **Paul** en **Stephan**, leuk om na practicumstudent ook practicumbegeleider te zijn geweest.

Of course thanks to **all my colleagues** from the ICC group who came and went during the last four years. It was great to meet so many nice people from all over the world, it was a truly enriching experience, which I wouldn't have want to miss. Besides working with you, the social events were also highly enjoyable, such as partaking in the two-time-champion-pub-quiz-team **Beer'ed's O' Knowledge**, futsal-team **20-22 seconds of fun**, skiing in Winterberg, the road-trip around Kentucky, the infamous LIIT borrel and of course the NAM 2013 conference dinner. De oude garde, **Jesper**, **Daniël**, **René** en **Arjen**, het waren tien mooie jaren! Die flessen Grand Prestige moeten binnenkort maar eens open. **Qingyun**, I very much enjoyed your company on the trips we made. I hope we can have some more meals in the future! **Thomas** en **Carlo**, succes met de laatste loodjes, het was gezellig! The next generation PT'ers, **Gang, Zafer,** and **Peter B.** My favorite post-docs **Elena**, **Fiona**, and **Gareth**. All the best! **Lukasz**, nice to have been colleagues (for a short while). Finally, thanks for all the insightful, friendly, funny, or pointless conversations, **Pasi, Wenhao, Ara, Fernando, Tomas, Bojang, JX, Rob, Diego, Ying, Matti, Tamara, Arjan, Jovana, Carlos, Sophie, Peter M., Matthijs, Ilona, Andy, and Manuel**.

Als laatste de mensen die niet zozeer met het werk te maken hadden, maar wel met m'n leven naast werk. Ouwe jongens krentenbrood, **Paul, Peter, Sil, Thomas** en **Tim**. Peter en Paul ook bedankt voor jullie werk als paranimfen. De schoonfamilie, **John**, **Jeannet**, **Chrissy**, **Tobias** en **Penn** & **Ravi**. Uiteraard mijn allernaaste familie, mijn ouders **Herman** en **Hermien**, mijn zusje **Anna** en als laatste natuurlijk **Kathy!**

Curriculum vitae

Hendrik Edial van der Bij was born on the 18th of December 1985 in Groningen, the Netherlands. In Spring 2004 he obtained his pre-university education diploma from OSG de Meergronden in Almere, where his chemistry teacher was Johan Le Fèvre. In September that same year he started with his undergraduate chemistry studies at Utrecht University. His bachelor thesis was titled 'The Dispersion of Cobalt Nanoparticles in Polar Solvents', which was performed at the Physical and Colloid Chemistry group under the supervision of Dr. Roberto Calderone and Prof. dr. Albert P. Philipse. He received his BSc degree in chemistry in 2008. In February 2008 he started the master 'Nanomaterials: Chemistry and Physics' at Utrecht University. He obtained his MSc degree in 2010 after finishing his master thesis titled 'Spectroscopic Investigations on Synthetic Zeolites and Zeolitic Materials - Confocal Fluorescence Microscopy as a Valuable Tool in Unraveling the Internal Architecture of Crystals', supervised by Dr. Lukasz Karwacki and Prof. dr. ir. Bert M. Weckhuysen at the Inorganic Chemistry and Catalysis group. As part of his master course, he went for a 5-month internship at the Institute of Chemical and Engineering Sciences in Singapore in 2009 under the supervision of Dr. Armando Borgna and Prof. dr. ir. Krijn de Jong.

In 2010 he started a PhD project, which resulted in the thesis titled 'Phosphatation of Zeolites: A Combined Spectroscopy, Microscopy and Catalysis Study.' His promoter was Prof. dr. ir. Bert M. Weckhuysen.

As of the 1st of October 2014, Hendrik started as an analytical scientist at Albemarle Catalysts in Amsterdam.